



University
of Glasgow

Gallagher, Andrew Patrick (1999) *Theoretical characterisation of magnetic force microscope tip stray fields*.

PhD thesis

<http://theses.gla.ac.uk/4482/>

Copyright and moral rights for this thesis are retained by the author

A copy can be downloaded for personal non-commercial research or study, without prior permission or charge

This thesis cannot be reproduced or quoted extensively from without first obtaining permission in writing from the Author

The content must not be changed in any way or sold commercially in any format or medium without the formal permission of the Author

When referring to this work, full bibliographic details including the author, title, awarding institution and date of the thesis must be given

Theoretical Characterisation of Magnetic Force Microscope Tip Stray Fields

by Andrew Patrick Gallagher

Submitted for the degree of Doctor of Philosophy at the Department of
Physics and Astronomy, University of Glasgow

September 1999

© 1999 Andrew P. Gallagher



This thesis is dedicated to
Mum and Dad and to **Catherine.**

Thanks for all the help.



Contents

Acknowledgements

Declaration

Summary

Chapter 1. Ferromagnetism and Magnetic Materials

| | |
|--|---|
| 1.1 Ferromagnetism | 1 |
| 1.2 Energy Considerations | 2 |
| 1.2.1 Exchange Energy | 2 |
| 1.2.2 Anisotropy Energy | 3 |
| 1.2.3 Magnetostatic Energy | 4 |
| 1.2.4 Zeeman Energy | 4 |
| 1.3 Domains and Domain Walls in Ferromagnetic Thin Films | 5 |
| 1.4 Scope of this Thesis | 7 |

Chapter 2. Magnetic Imaging Techniques

| | |
|--|----|
| 2.1 Introduction | 9 |
| 2.2 Optical Techniques for Magnetic Imaging | 9 |
| 2.2.1 The Bitter Technique | 9 |
| 2.2.2 Faraday and Kerr Microscopy | 10 |
| 2.3 Electron Techniques for Magnetic Imaging | 10 |
| 2.3.1 Lorentz Deflection of Moving Electrons | 10 |
| 2.3.2 Image Formation in a Conventional Transmission Electron Microscope (CTEM) | 13 |
| 2.3.3 Fresnel Mode of Lorentz Microscopy in a CTEM | 15 |
| 2.3.4 Foucault Mode of Lorentz Microscopy in a CTEM | 17 |
| 2.3.5 Image Formation in a Scanning Transmission Electron Microscope (STEM) | 19 |
| 2.3.6 DPC Mode of Lorentz Microscopy | 20 |

| | |
|---------------------------------------|----|
| 2.3.7 MDPC Mode of Lorentz Microscopy | 22 |
| 2.4 Magnetic Force Microscopy | 24 |

Chapter 3. Fundamentals of Electron Beam Tomography for the Study of Magnetic Force Microscope Tips

| | |
|--|----|
| 3.1 Introduction | 30 |
| 3.2 The General Principle of Three Dimensional Reconstruction and its Application to Determining the MFM Tip Field | 32 |
| 3.2.1 The Fourier Method | 32 |
| 3.2.2 The Radon Transform Method for 3D Reconstruction of MFM Tip Fields | 35 |
| 3.2.3 The Conventional Algebraic Reconstruction Technique | 42 |
| 3.2.4 The Magnetic Field Vector Algebraic Reconstruction Technique | 44 |
| 3.3 Experimental Implementation of Electron Beam Tomography for MFM Tip Fields | 48 |
| 3.3.1 The DPC Image Collection in the CM20 (S)TEM | 48 |
| 3.3.2 Extraction of the Input Deflection Data Sets (for tomographic reconstruction using RTM) from the DPC Image Pairs | 50 |
| 3.4 Summary | 52 |

Chapter 4. Theoretical Investigation of the Character of MFM Tip Stray Fields and Integrated Stray Fields

| | |
|--|----|
| 4.1 Introduction | 54 |
| 4.2 Calculation of Simulated Deflection Data Sets | 55 |
| 4.2.1 Calculation of the Stray Field from a Uniformly Magnetised Block | 55 |
| 4.2.2 Calculation of the Stray Field from a Sheet of Magnetic Charge Density M_s | 57 |
| 4.2.3 Calculation of Stray Field from a Triangular Thin Film | 58 |
| 4.2.4 Calculation of the Deflection Values from a Triangular Thin Film | 60 |

| | |
|---|----|
| 4.3 Tip Shape and its Effect on Stray Fields/Integrated Stray Fields | 61 |
| 4.3.1 Stray Field and Integrated Stray Field From Model Tip1 | 63 |
| 4.3.1.1 Stray Field Calculated Directly From Model Tip1 | 63 |
| 4.3.1.2 Integrated Stray Field Calculated From Model Tip1 | 67 |
| 4.3.1.3 Comparison of the Calculated and Reconstructed Stray Fields from Tip1 | 69 |
| 4.3.2 Stray Field and Integrated Stray Field From Model Tip2 | 71 |
| 4.3.2.1 Stray Field Calculated Directly From Model Tip2 | 71 |
| 4.3.2.2 Integrated Stray Field Calculated From Model Tip2 | 73 |
| 4.3.3 Stray Field and Integrated Stray Field From Model Tip3 | 74 |
| 4.3.3.1 Stray Field Calculated Directly From Model Tip3 | 74 |
| 4.3.3.2 Integrated Stray Field Calculated from Model Tip3 | 76 |
| 4.3.4 Comparison of the Simulated Integrated Field Line Scans Generated by Tips1 and 3 with the Deflection Line Scans Generated by a DI MFM Tip | 77 |
| 4.3.5 Comparison of the Stray Fields and Integrated Stray Fields from Model Tip1 with the Stray Fields and Integrated Fields from a Point Magnetic Monopole and a Point Magnetic Dipole | 80 |
| 4.4 Contribution to the Tip Stray Field and the Integrated Stray Field from Various Portions of Thin Film Tip Coating | 86 |
| 4.5 Thickness of Thin Film Coating and its Effect on Fields/Integrated Fields | 91 |
| 4.6 Summary | 94 |

Chapter 5. Individual Contributions to a Tip Assembly's Line Scan Deflection Data Set from the Tip, Cantilever and Substrate Portions of the Assembly

| | |
|--|-----|
| 5.1 Introduction | 96 |
| 5.2 Tip Contribution to the Experimental Deflection Data Set Generated by a MFM Tip Assembly | 101 |
| 5.2.1 Tip Portion of the Tip Assembly Magnetised as in the Axial Case | 101 |
| 5.2.2 Tip Portion of the Tip Assembly Magnetised as in the Transverse Case | 102 |

| | |
|--|-----|
| 5.3 Cantilever Contribution to the Experimental Deflection Data Set Generated by a MFM Tip Assembly | 107 |
| 5.3.1 Cantilever Portion of the Tip Assembly Magnetised as in the Axial Case | 108 |
| 5.3.2 Cantilever Portion of the Tip Assembly Magnetised as in the Transverse Case | 115 |
| 5.4 Substrate Contribution to the Experimental Deflection Data Set Generated by a MFM Tip Assembly | 123 |
| 5.4.1 Substrate Portion of the Tip Assembly Magnetised as in the Axial Case | 124 |
| 5.4.2 Substrate Portion of the Tip Assembly Magnetised as in the Transverse Case | 130 |
| 5.5 Summary | 133 |

Chapter 6. Investigation of the Effect on the Reconstructed Stray Field of the Cantilever and Substrate Contribution to the Tip Assembly's Line Scan Deflection Data Sets

| | |
|--|-----|
| 6.1 Introduction | 135 |
| 6.2 Comparison of Calculated and Reconstructed Stray Fields from the Model Tip | 136 |
| 6.3 Comparison of the Calculated and Reconstructed Stray Fields from the Combined Cantilever and Substrate Model | 136 |
| 6.3.1 Average Stray Field Reconstructed from the Two Rotation Data Sets | 138 |
| 6.3.2 Stray Field Reconstructed from the Rotation Data Set Sensitive to Induction Normal to the Plane of Reconstruction | 140 |
| 6.3.3 Stray Field Reconstructed from the Rotation Data Set Sensitive to Induction in the Plane of Reconstruction | 142 |
| 6.4 Comparison of the Calculated and Reconstructed Stray Fields from the Model Tip Assembly | 145 |
| 6.4.1 Average Stray Field Reconstructed from both Rotation Data Sets | 146 |
| 6.4.2 Stray Field Reconstructed from Each of the Orthogonal Rotation Data Sets | 149 |
| 6.4.3 Simple Check for the Consistency of Orthogonal Rotation Data Sets | 152 |

| | |
|--|-----|
| 6.5 Consideration of the Stray Fields Reconstructed from the Deflection Data Sets Generated by the DI MFM Tip | 153 |
| 6.6 Method to Reduce the Error in the Average Stray Field Reconstructed from Both the Rotation Data Sets Generated by the Tip Assembly | 158 |
| 6.7 Stray Field Reconstructed Using ART | 163 |
| 6.7.1 Consideration of the Accuracy of the ART Reconstructed Model Tip Field | 163 |
| 6.7.2 Consideration of the Accuracy of the ART Reconstructed Model Tip Assembly Stray Field | 168 |
| 6.8 Affect of the Electron Probe Size on the Measured Electron Beam Deflection Data and the Subsequent Accuracy of the Reconstructed Stray Field | 170 |
| 6.9 Stray Field Reconstructed from Incorrectly Aligned Integrated Field Line Scans | 175 |
| 6.10 Discussion and Summary | 178 |

Chapter 7. Characterisation of the Stray Field from Two Further MFM Tips

| | |
|--|-----|
| 7.1 Introduction | 180 |
| 7.2 The Partially Coated DI MFM Tip | 181 |
| 7.3 The Seagate Grooved Tip | 187 |
| 7.3.1 The Seagate Tip Magnetised by a Large Field Directed in the Plane of the Cantilever and Normal to the Groove | 189 |
| 7.3.2 The Seagate Tip Magnetised by a Large Field Directed Along the Cantilever Axis | 193 |
| 7.3.3 The Seagate Tip Magnetised by a Large Field Directed Along the Tip Axis | 197 |
| 7.4 Summary and Conclusions | 204 |

Chapter 8. Conclusions and Future Work

| | |
|-----------------|-----|
| 8.1 Conclusions | 205 |
|-----------------|-----|

8.2 Future Work 207

Appendix 1 209

Acknowledgements

This thesis would not have been possible without the help of many others throughout the course of this work. Foremost I would like to thank my supervisors Prof. R. P. Ferrier and Dr. S. McVitie for their patient help and invaluable discussions. Also I am grateful to Prof. J. N. Chapman for his encouragement and provision of the excellent facilities in the Solid State Group at the University of Glasgow.

Thanks also to Dr. Pat Nicholson and Dr Sam McFadden for looking after all the computing facilities.

Thanks to EPSRC for the provision of funding.

Big thanks to Peter Aitchison, Tommy Munro, Colin How, Billy Smith, Richard Lindsay, Jamie Scottand many more.... for all technical advice/football opinions/booze/etc....

Finally an enormous thanks to my Mum and Dad and to Catherine who all supported me throughout the living nightmare that is a Phd. Without all their help I can safely say that I would not have finished this thesis. Thanks again.

Declaration

This thesis is a record of work carried out by me in the Department of Physics and Astronomy at the University of Glasgow. The work described herein is my own, apart from the ART and RTM tomographic reconstruction programs which were provided by Yan Liu (ART) and colleagues at the University of Duisburg in Germany (RTM). The RTM program was further modified by Prof. R. P. Ferrier. All MFM tip experimental deflection data sets were provided by Prof. R. P. Ferrier and Dr. Steven McVitie. Some of the work given in this thesis can be found in the following paper;

'Characterisation of MFM Tip Fields by Electron Tomography', 1997, R. P. Ferrier, S. McVitie, A. Gallagher and W. A. P. Nicholson, *IEEE Trans. Mag.*, 33, pp 4064

Summary

A large part of the work described in this thesis is concerned with a theoretical characterisation of Magnetic Force Microscope (MFM) tip stray fields. The remainder of the thesis is concerned with a theoretical investigation of the accuracy of a practical method for characterising the MFM tip field - i.e. the electron tomography reconstruction method.

The thesis begins with a brief discussion of the fundamentals of ferromagnetism and the importance of being able to determine the magnetic structure of a material.

The second chapter considers several different methods which have been developed for determining the magnetic configuration of a material and particular attention is given to Differential Phase Contrast (DPC) Lorentz microscopy (this technique is the basis for three dimensional reconstruction of a MFM tip stray field using electron beam tomography) and Magnetic Force Microscopy. In the case of the latter a discussion of the need to characterise the MFM tip field is given.

The fundamental principles and the application of electron beam tomography for the investigation of MFM tip fields are discussed in Chapter 3. Two reconstruction algorithms - the Algebraic Reconstruction Technique (ART) and the Radon Transform Method (RTM) - are considered. The latter reconstruction technique is considered in more detail since it is used predominately in this thesis. The acquisition of the experimental data sets for tomographic reconstruction is also described in this chapter.

In Chapter 4 a theoretical investigation of the effect on the tip stray field of varying several physical tip characteristics is carried out. A tip model is constructed and its shape, height and the thickness of the film coating are all varied and the resulting tip stray field and line scan deflection data sets are investigated. A comparison of the deflection data generated by the tip model and that generated by a practical MFM tip is also carried out. It is found that the simulated deflection data from the tip model compared favourably with the experimental deflection data;

however there is found to be a contribution to the experimental deflection data sets for which the tip model does not account. Nonetheless, comparison of the experimental and simulated deflection data gave encouragement to extend the modelling to the cantilever and substrate portions of the tip assembly.

In Chapter 5 the deflection data sets generated by a practical MFM tip magnetised in two separate cases is considered. Tip, cantilever and substrate models were constructed for each case and the simulated deflection data was found to compare favourably with the deflection data generated by the practical tip assembly. A theoretical investigation into the character of the stray field from the cantilever and substrate portions of the tip assembly is undertaken and the conclusion is that the magnitude of the stray field from the cantilever and substrate is small in the vicinity of the tip but is spread over a large distance and as a result contributes greatly to the deflection data generated by the MFM tip assembly.

In Chapter 6, a theoretical investigation of the effect on the accuracy of the RTM reconstructed stray field that the cantilever and substrate contribution to the MFM tip assembly's deflection data set is undertaken. It is found that although the RTM reconstruction method can produce a relatively accurate representation of the MFM tip field, the cantilever and substrate contribution does reduce the accuracy of the reconstructed tip field. Two separate methods for reducing the error in the reconstructed tip field are considered. It is found that these methods produce very accurate representations of the tip field even when the exact cantilever and substrate contribution is not known. The accuracy of the tip assembly's stray field reconstructed using the ART is also considered and it is found that ART does not produce as accurate a representation of the MFM tip field as is obtained using RTM. The effect of the electron probe size and the manual alignment of the deflection line scans on the accuracy of the reconstructed stray field are also investigated.

In Chapter 7 two more MFM tips of a distinct physical character are modelled and their stray fields and deflection data sets are investigated.

Conclusions and suggestions for further work are given in Chapter 8.

Chapter 1

Ferromagnetism and Magnetic Materials

1.1 Ferromagnetism

A ferromagnetic material is one which possesses a spontaneous non-zero net magnetic moment below a well defined temperature called the Curie Temperature (T_C). Each atom of a ferromagnetic material has associated with it a magnetic dipole moment. This predominately arises from the spin of the unpaired electrons in the 3d or 4f shells - the orbital angular moment having been effectively quenched. Above the Curie Temperature the atomic magnetic moments of the material are randomly oriented due to thermal effects.

The alignment of the magnetic moments in a ferromagnetic material was suggested by Weiss^{[1][2]} to be due to a molecular field (proportional to the magnetisation of the system) within the material. However, Weiss assumed that the atomic moments were localised on the atomic cores and thus his work is strictly only correct for materials such as in the lanthanide series, since the 4f electrons which determine the magnetic properties are tightly bound to the nuclei.

The molecular field was ultimately explained by Heisenberg^[3] who proposed a quantum mechanical interaction called the exchange interaction which acts between each atom and its nearest neighbours. The Pauli exclusion principle shows that the wavefunction describing a quantum mechanical system comprising electrons must be antisymmetric. The exchange energy between two individual particles due to the interaction of their spins \underline{S}_i and \underline{S}_j is given by,

$$e_{ex} = -J(r_{ij})\underline{S}_i \cdot \underline{S}_j \quad (1.1)$$

where r_{ij} is the separation of the moments, and $J(r)$ is the exchange integral which is positive for ferromagnetic materials. The equation implies that the minimum energy state is when the atomic magnetic moments lie parallel to each other.

1.2 Energy Considerations

The magnetisation of a magnetic material will always seek to settle in a way that minimises the energy of the system^[4]. The total energy E_{tot} , is made up from several contributing energies,

$$E_{tot} = E_{ex} + E_{an} + E_m + E_z \quad (1.2)$$

where E_{ex} is the exchange energy, E_{an} is the anisotropy energy, E_m is the magnetostatic energy and E_z is the Zeeman energy. These individual energy contributions are considered in the following sections.

1.2.1 Exchange Energy

The exchange energy of a magnetic material is due to the relative orientations of neighbouring magnetic dipoles. For a cubic structure,

$$E_{ex} = A \int_V \left[(\nabla\alpha)^2 + (\nabla\beta)^2 + (\nabla\gamma)^2 \right] dV \quad (1.3)$$

where α , β , and γ are the direction cosines of the magnetisation vector (with respect to the crystal axes) and A is the exchange constant of the material given by,

$$A = \frac{nJS^2}{a} \quad (1.4)$$

In this equation a is the lattice constant of the material, n is a constant depending on the crystalline structure ($n=1$ for simple cubic, 2 for body centred cubic and 4 for face centred cubic), J is the exchange integral and S is the magnitude of the spin of the magnetic moment. Thus, the exchange energy is a minimum when the spins of the material are parallel. This results in the material displaying a non-zero magnetisation.

1.2.2 Anisotropy Energy

A magnetic material is considered to be anisotropic if the magnetisation of the material settles in a preferred direction in a zero field. This preferred direction is often called the 'easy axis' and is due to the crystalline nature of the material. Deviations of the material's magnetisation from an easy axis direction results in an increase of the anisotropy energy.

For a cubic single crystal the anisotropy energy is well defined by the first two terms of a series expansion.

$$E_{an} = \int_V \left[K_1(\alpha^2\beta^2 + \beta^2\gamma^2 + \gamma^2\alpha^2) + K_2\alpha^2\beta^2\gamma^2 \right] dV \quad (1.5)$$

where K_1 and K_2 are the anisotropy constants of the material which are dependant on temperature. For hexagonal or uniaxial crystals the anisotropy energy is given by,

$$E_{an} = \int_V \left[K_1(1-\gamma^2) + K_2(1-\gamma^2)^2 \right] dV \quad (1.6)$$

where K_1 and K_2 are again constants. The minimum anisotropy energy occurs when the magnetisation is directed along a preferred easy axis.

1.2.3 Magnetostatic Energy

A uniformly magnetised magnetic material generates a large amount of magnetic poles on its surfaces. Magnetic poles are also generated inside the material where there is a divergent component of magnetisation. Such magnetic poles generate stray fields external and internal to the magnetic material. The field is often referred to as the demagnetising field H_d , and is given by,

$$H_d = \frac{1}{4\pi} \int_v \frac{-\nabla \cdot \underline{M}}{r^2} dV + \frac{1}{4\pi} \int_s \frac{\underline{M} \cdot \underline{n}}{r^2} dS \quad (1.7)$$

where r is the position vector of the point in space at which the field is evaluated, and \underline{n} is the outward pointing unit vector normal to the surface. Note that $\nabla \cdot \underline{M}$ is equivalent to the magnetic volume charge and $\underline{M} \cdot \underline{n}$ is equivalent to the magnetic surface charge. The subsequent energy contribution from the demagnetising field is,

$$E_m = -\frac{1}{2} \mu_0 \int_v \underline{M} \cdot \underline{H}_d dV \quad (1.8)$$

where μ_0 is the permeability of free space. The magnetostatic energy is very much dependent on the geometry of the sample. This energy is a minimum when the material forms a closed domain structure with no magnetic poles on the surface.

1.2.4 Zeeman Energy

The Zeeman energy arises from the interaction of a magnetic material with an external field and is given by,

$$E_z = -\mu_0 \int_v \underline{M} \cdot \underline{H} dV \quad (1.9)$$

where H is the applied field. In the minimum energy state the magnetic moments align along the direction of the applied field.

Thus the magnetisation of a magnetic material will seek to settle in a way that minimises a combination of all the potential energy contributions described here.

1.3 Domains and Domain Walls in Ferromagnetic Thin Films

Ferromagnets are found to possess a spontaneous net magnetic moment below a well defined temperature called the Curie Temperature. To explain this Weiss^{[1][2]} suggested the existence of magnetic domains in ferromagnets, in which the atomic magnetic moments were aligned parallel over a much larger volume of solid than had previously been expected. This was indirectly confirmed by the Barkhausen^[5] effect in which the reorientation of domains caused discrete changes in the magnetic induction of a ferromagnet. Several years later Bitter^[6] directly confirmed the existence of domains from observations of patterns on the surfaces of ferromagnetic materials using a very fine magnetic powder suspended in a carrier fluid which was spread on the surface of the material .

The boundaries between domains are known as domain walls. A domain wall is therefore a region of the material where the orientation of the magnetisation rotates from one domain to the orientation of the magnetisation in a neighbouring domain. The total angular displacement across a domain wall is often 90° or 180°- particularly in cubic materials as the cubic anisotropy ensures that directions at right angles to the magnetisation in a given domain are also magnetically easy axes. Domain walls are often found to be 10 to 100nm wide. There are various types of domain wall and the type which occurs is dependent on the specimen thickness. One dimensional diagrams of the 180° Bloch wall^[7], 180° Neel wall^[8] and the 180° cross-tie wall are illustrated in fig. 1.1.

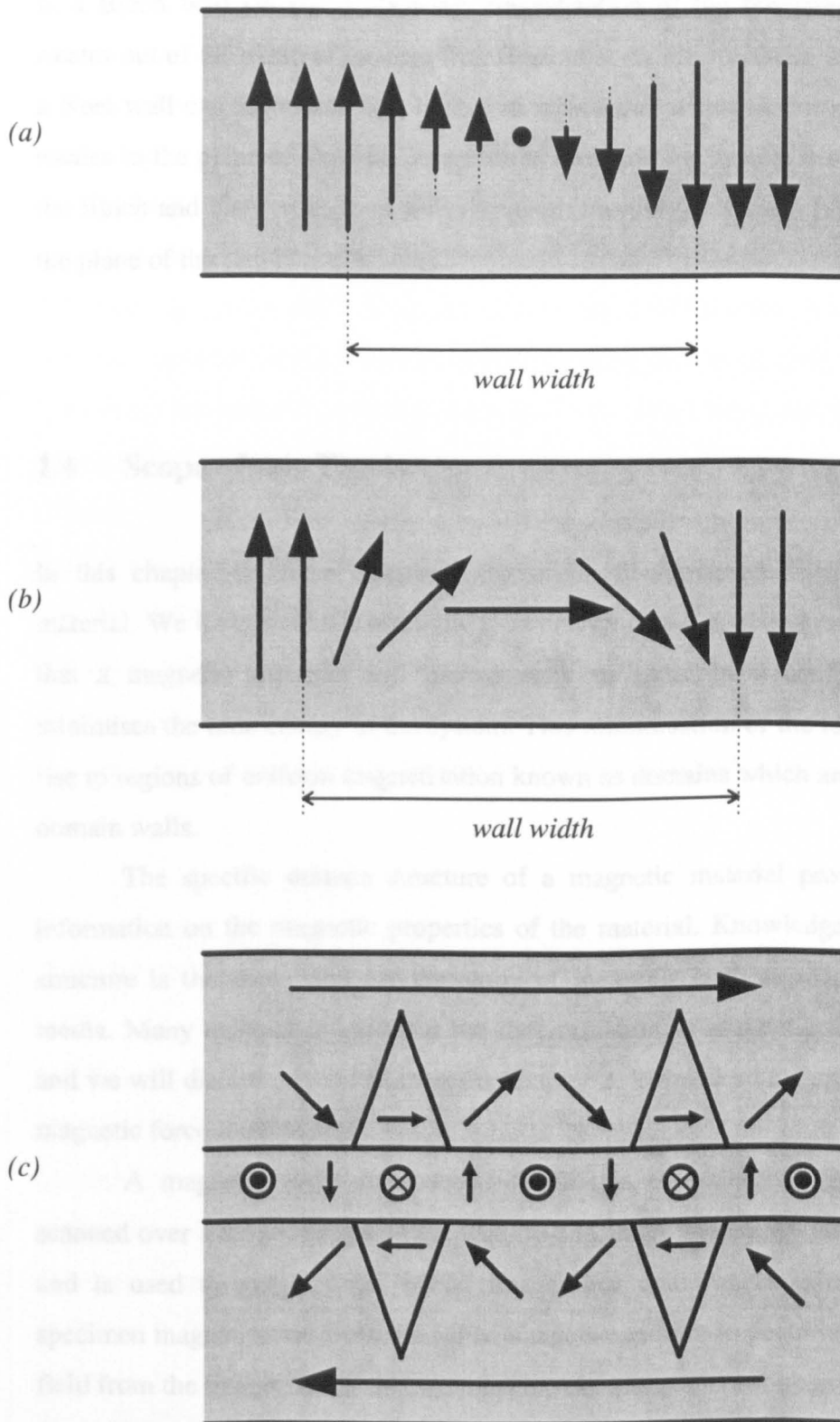


Fig. 1.1: Diagram illustrating the in-plane view of the magnetisation of a thin film.
 (a) 180° Bloch wall,
 (b) 180° Neel wall,
 (c) 180° cross-tie wall.

In a Bloch wall (in fig. 1.1(a)) the magnetisation of the ferromagnetic specimen rotates out of the plane of the thin film specimen. As the specimen thickness reduces a Neel wall can form (see fig. 1.1(b)) in which the magnetisation of the specimen rotates in the plane of the film. A cross-tie wall (see fig. 1.1(c)) is a combination of the Bloch and Neel walls in that the magnetisation vector rotates both in and out of the plane of the thin film specimen.

1.4 Scope of this Thesis

In this chapter we have discussed the origin of ferromagnetism in a magnetic material. We have also discussed the total energy of a magnetic system and the fact that a magnetic material will always seek to settle in a configuration which minimises the total energy of the system. This minimisation of the total energy gives rise to regions of uniform magnetisation known as domains which are surrounded by domain walls.

The specific domain structure of a magnetic material provides important information on the magnetic properties of the material. Knowledge of the domain structure is therefore vital for the study of materials such as magnetic recording media. Many techniques exist for the determination of magnetic domain structure and we will discuss several of these in Chapter 2. We will take a specific interest in magnetic force microscopy.

A magnetic force microscope (MFM) is essentially a ferromagnetic tip scanned over a magnetic specimen. The tip-specimen interaction force is monitored and is used to generate the MFM image. For quantitative information on the specimen magnetisation from the MFM image we require to deconvolve the tip stray field from the image. To do this we must have a quantitative measure of the tip stray field. The desire to quantitatively characterise the MFM tip field is the principal concern of this thesis. In Chapter 3 a practical technique for imaging the field from the ferromagnetic tip - called electron beam tomography - is discussed.

The main aims of this thesis are 1) to determine which physical characteristics of a MFM tip are the most important for defining the character of the tip stray field, 2) to determine the character of the stray field generated by the tip's associated structure, and 3) to determine the affect that the associated tip structure has on the tomographically reconstructed tip stray field.

In Chapter 4 we discuss the construction of a model for a ferromagnetic MFM tip. Several models are constructed and are used for a theoretical investigation into the character of the tip stray field. Following this in Chapter 5 we conduct a theoretical investigation into the character of the stray field generated by the tip's associated structure. Theoretical models constructed in Chapter 5 are then used in Chapter 6 to investigate the effect that the associated tip structure has on the tomographically reconstructed tip stray field. Comparisons between experimental and simulated reconstructed tip fields are also carried out. These allow us to comment with some authority on the accuracy (or otherwise) of the experimental reconstructed tip fields. Finally in Chapter 7 we conduct a theoretical investigation of the character of the field from two further ferromagnetic tips.

References

- [1] Weiss P, (1906), *Compt. Rend.*, 143, pp 1136
- [2] Weiss P, (1907), *J. Phys.*, 6, pp 661
- [3] Heisenberg W, (1928), *Z. Physik*, 49, pp 619
- [4] Landau L and Liftshitz E, (1935), *Phys. Z. Sowjetunion*, 8, pp 153
- [5] Barkhausen H, (1919), *Z. Physik*, 20, pp 401
- [6] Bitter F, (1931), *Phys. Rev.*, 38, pp 1903
- [7] Bloch F, (1932), *Physik*, 74, pp 295
- [8] Neel L, (1955), *Comptes Rendus*, 241, pp533

Chapter 2

Magnetic Imaging Techniques

2.1 Introduction

As stated in Chapter 1, the specific domain structure of a magnetic material provides important information on the magnetic properties of the material. Thus any technique which provides a quantitative measure of a material's domain structure is of great use and we consider several such techniques in this chapter. We begin by briefly considering optical techniques in Section 2.2. Following this we consider both electron techniques (in Section 2.3) and then Magnetic Force Microscopy (MFM) in more detail since these techniques are fundamental to this thesis.

2.2 Optical Techniques for Magnetic Imaging

2.2.1 The Bitter Technique

One of the simplest techniques developed for the observation of magnetic domains was first demonstrated by Bitter^[1]. His technique involves the use of a very fine magnetic powder suspended in a carrier liquid which is spread on the surface of the material under investigation. The fine magnetic particles of the powder accumulate at regions on the material surface where the magnetic field gradient is greatest - this occurs where domain walls meet the material surface. The patterns formed in the fine

powder can be observed through an optical microscope. With modern ferrofluid preparations a resolution of better than approximately one micron is achievable. This technique is limited by the fact that it does not give any information about the domain wall structures or the direction of magnetisation within domains.

2.2.2 Faraday and Kerr Microscopy

Two further optical microscopy techniques make use of the Faraday and Kerr effects^[2]. The Faraday effect manifests itself as the rotation of the plane of polarisation of light transmitted through a transparent medium in the presence of a magnetic field with component parallel to the direction of light propagation. The Kerr effect occurs when polarised light is reflected from the surface of a magnetic material and again results in a rotation of the polarisation of the light. Note that in both cases the rotation of the polarisation of the light is a linear function of the specimen's magnetisation. Investigations of the domain structures of magnetic samples using the Faraday effect is limited to thin transparent slices of a magnetic material. On the other hand the Kerr effect can be used for imaging domain structures on the surfaces of any magnetic sample (provided the surface is smooth). We now consider electron techniques of magnetic imaging.

2.3 Electron Techniques for Magnetic Imaging

2.3.1 Lorentz Deflection of Moving Electrons

Firstly we consider the important interaction between moving electrons and magnetic induction from a thin magnetic film^[3]. Consider fig. 2.1 which shows a diagram of a thin magnetic film illuminated by a parallel beam of electrons. Note that the incident beam of electrons is perpendicular to the plane of the film.

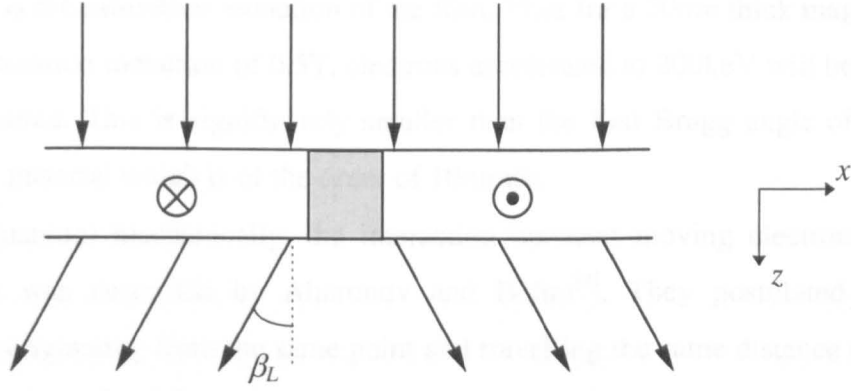


Fig. 2.1: Diagram showing the Lorentz deflection experienced by electrons passing through a magnetic thin film with a 180° domain wall.

Classically an electron moving with a velocity \underline{v} in a magnetic induction \underline{B} experiences a force \underline{F} given by,

$$\underline{F} = e\mathbf{v} \times \underline{B} \quad (2.1)$$

This is known as the Lorentz force and results in the electrons deflecting from their original path through an angle given by,

$$\beta_L = \beta_x = \frac{e\lambda}{h} \int_{-\infty}^{\infty} B_y(x,z) dz \quad (2.2)$$

where $B_y(x,z)$ is the y component of magnetic induction at point (x,z) , e is the charge of an electron, λ is the relativistically corrected electron wavelength and h is Plancks constant. In the special case that no stray field is escaping from the film and the film thickness t is constant, then equation (2.2) becomes,

$$\beta_L = \beta_x = \frac{eB_s\lambda t}{h} \quad (2.3)$$

where B_s is the saturation induction of the film. Thus for a 50nm thick magnetic film with a saturation induction of 0.5T, electrons accelerated to 200keV will be deflected by 0.015mrad. This is significantly smaller than the first Bragg angle of a typical magnetic material which is of the order of 10mrad.

Quantum mechanically, the interaction between moving electrons and the specimen was described by Aharonov and Bohm^[4]. They postulated that two electrons originating from the same point and travelling the same distance to another coincident point by different paths, have a phase difference which is proportional to the magnetic flux N enclosed by the two paths, see fig. 2.2.

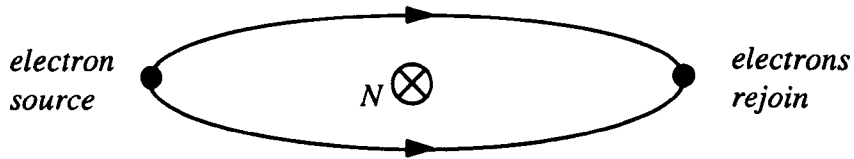


Fig. 2.2: Diagram showing two electrons originating from the same point and rejoining at another point but travelling along different paths enclosing a magnetic flux N .

The phase shift ϕ , is given by,

$$\phi = \frac{2\pi eN}{h} \quad (2.4)$$

For a plane wave incident on a thin magnetic film (as in fig. 2.1) the phase shift between two electrons at points x_1 and x_2 (on the x axis) is,

$$\phi(x_2 - x_1) = \frac{2\pi e t}{h} \int_{x_1}^{x_2} B_y(x) dx \quad (2.5)$$

A magnetic film may therefore be considered to be a strong but slowly varying phase object, and Lorentz microscopy is in fact a technique for revealing phase contrast.

2.3.2 Image Formation in a Conventional Transmission Electron Microscope (CTEM)

Fig. 2.3 shows a diagram of the essential components of a CTEM. Situated at the top of the microscope is the electron gun which is the source of the electrons in a CTEM. The Phillips CM20 (Scanning) TEM at the University of Glasgow has a thermally assisted field emission electron gun (FEG). Here electrons are drawn from a sharp tip by an anode having a potential difference of approximately 4kV. A series of accelerator rings then raise the electron voltage to 200kV. The electrons then pass through two condenser lenses and the upper portion of the objective lens which control the position and the angular convergence of the electrons at the specimen. The lower objective lens is the image forming component and the intermediate lenses magnify and project the image onto the viewing screen.

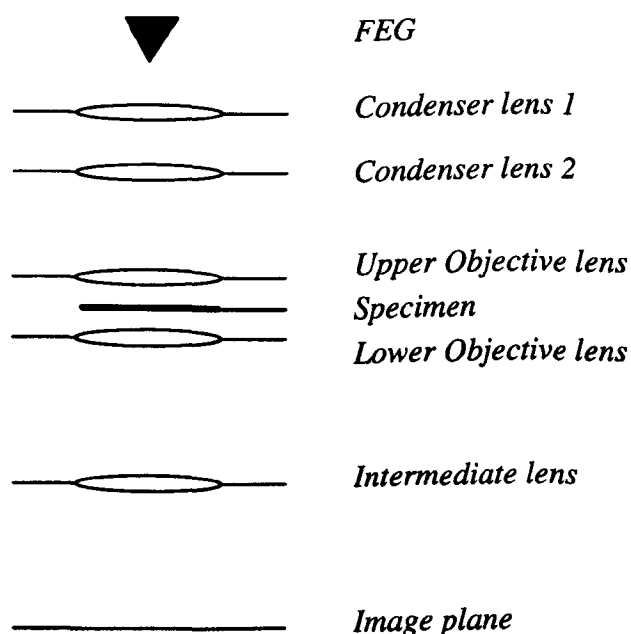


Fig. 2.3: Diagram of the essential components of a CTEM.

If we assume that the electron source is very small and is situated far away from the specimen then we may take the incident electron waves as plane waves given by $\psi_0(x, y) = e^{i2\pi kz}$ with $k = 1/\lambda$. On leaving the specimen the electron wave function becomes,

$$\psi_1(x, y) = f(x, y)\psi_0(x, y) \quad (2.6)$$

where $f(x, y)$ is the specimen transmittance function and is equal to $e^{i\phi(x, y)}$ where $\phi(x, y)$ is the two dimensional extension of equation (2.5).

At the diffraction plane the electron disturbance $g(k_x, k_y)$ is given by the Fourier Transform of the specimen's transmittance function,

$$g(k_x, k_y) = FT\{f(x, y)\} = \iint f(x, y) \exp[-2\pi i(k_x x + k_y y)] dx dy \quad (2.7)$$

The wave is then modified by the transfer function of the imaging system $t(k_x, k_y)$ given by,

$$t(k_x, k_y) = A(k_x, k_y) \zeta_a \zeta_b \quad (2.8)$$

$$\zeta_a = \exp\left[\frac{\pi i C_s \lambda^3 (k_x^2 + k_y^2)^2}{2}\right] \quad (2.9)$$

$$\zeta_b = \exp\left[\pi i \Delta z \lambda (k_x^2 + k_y^2)\right] \quad (2.10)$$

where $A(k_x, k_y)$ is the pupil function, which is equal to 1 within the objective aperture and 0 outside it, ζ_a is the contribution from the spherical aberration of the objective lens, ζ_b is the contribution from the defocus, C_s is the spherical aberration coefficient

and Δz is the defocus. Note that for magnetic imaging the spherical aberration usually makes a negligible contribution to the final image^[3] and therefore in equation (2.8) we can take $\zeta_a = 1$.

Thus the electron disturbance at the image plane $\Psi(x,y)$ is the Fourier Transform of the modified electron disturbance at the diffraction plane,

$$\begin{aligned}\Psi(x,y) &= FT\{g(k_x,k_y)t(k_x,k_y)\} \\ &= \iint g(k_x,k_y)t(k_x,k_y)\exp[2\pi i(k_x x + k_y y)]dk_x dk_y\end{aligned}\quad (2.11)$$

The intensity of the image on the image plane $I(x,y)$ is given by the modulus squared of equation (2.11),

$$I(x,y) = |\Psi(x,y)|^2 \quad (2.12)$$

This details the formation of an image on the image plane. We now consider the Fresnel and Foucault modes for magnetic imaging in a CTEM.

2.3.3 Fresnel mode of Lorentz Microscopy in a CTEM

Fig. 2.4 shows a diagram describing the nature of the contrast obtained from the Fresnel mode of Lorentz microscopy. Note that the object plane is not coincident with the specimen plane (the objective lens is focused on a plane either above or below the specimen) thus phase changes are converted into intensity changes. Domain walls will therefore be observed as bright or dark lines due to a greater or lesser number of electrons in the defocus plane. Domains will be observed as a uniform background. Note that if the electron beam is sufficiently coherent then interference fringes will be observed in the bright bands representing domain walls. This is because of the interference between the overlapping wavefronts.

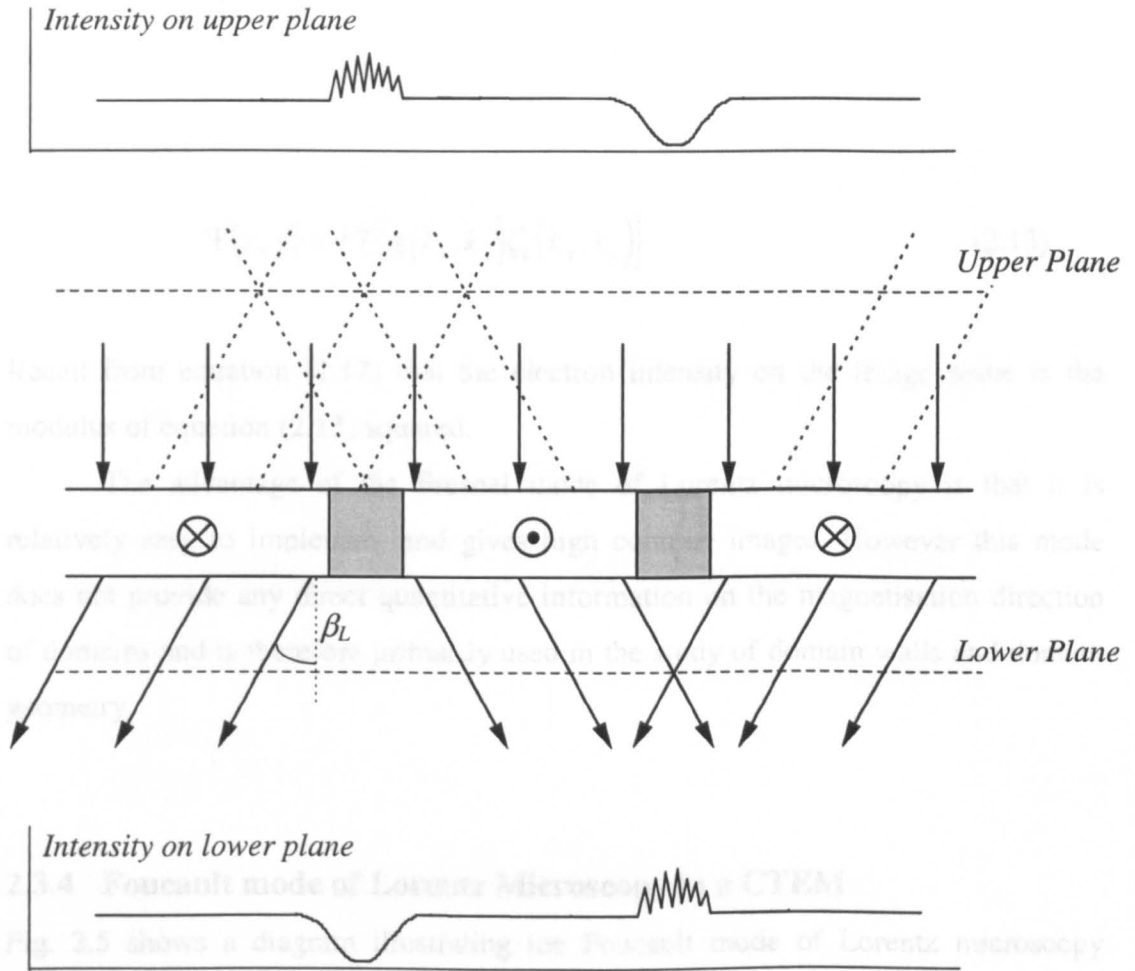


Fig.2.4: Diagram of the Fresnel mode of Lorentz microscopy. Note that the object plane is either above or below the specimen thereby converting phase changes to intensity changes.

Since the object plane is not coincident with the specimen plane then there is a non-zero defocus Δz , thus in equation (2.8) ζ_o is non zero. Also the objective aperture is generally not used in the Fresnel mode and we therefore take $A(k_x, k_y)$ in equation (2.8) to be effectively 1. Thus the electron disturbance at the image plane $\Psi(x, y)$ is given by,

$$\Psi(x, y) = FT\{g(k_x, k_y)\zeta_b(k_x, k_y)\} \quad (2.13)$$

Recall from equation (2.12) that the electron intensity on the image plane is the modulus of equation (2.13) squared.

The advantage of the Fresnel mode of Lorentz microscopy is that it is relatively easy to implement and gives high contrast images. However this mode does not provide any direct quantitative information on the magnetisation direction of domains and is therefore primarily used in the study of domain walls and domain geometry.

2.3.4 Foucault mode of Lorentz Microscopy in a CTEM

Fig. 2.5 shows a diagram illustrating the Foucault mode of Lorentz microscopy which is an in-focus imaging mode (unlike the Fresnel mode). For a specimen such as in fig. 2.5 (i.e. a thin film containing two domains with anti-parallel magnetisation) the zero order diffraction spot is split into two individual spots by the Lorentz deflections of the electrons passing through the specimen. An aperture in the back focal plane (the objective aperture) is used to hide one of the spots so that only electrons with a positive Lorentz deflection angle β_L contribute to the final image observed on the image plane. This results in the domain with magnetisation out of the page in fig. 2.5 appearing bright and the domain with magnetisation into the page appearing dark on the image plane.

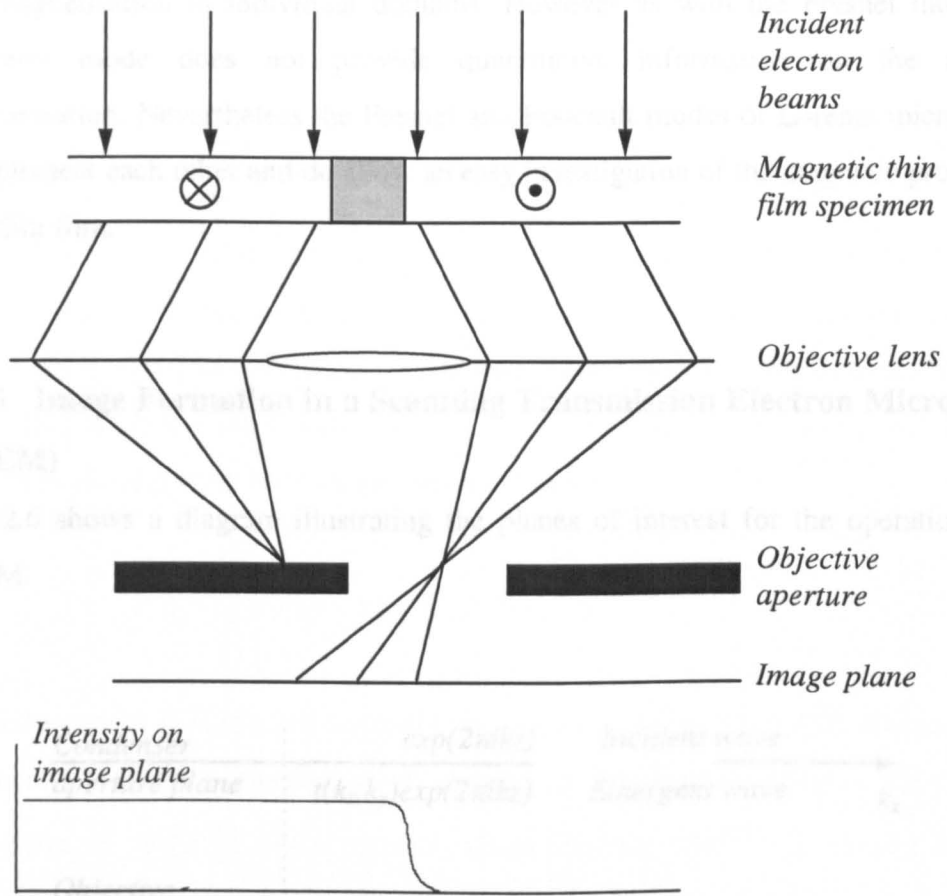


Fig. 2.5: Diagram of the Foucault mode of Lorentz microscopy.

In equation (2.8) the pupil function $A(k_x, k_y)$ will be non zero (since the objective aperture is used) and $\zeta_b = 1$ (since this is an in focus imaging mode and thus Δz is zero). Thus the electron disturbance at the image plane is given by,

$$\Psi(x, y) = FT\{g(k_x, k_y)A(k_x, k_y)\} \quad (2.14)$$

where the electron intensity at the image plane is given by equation (2.12).

The Foucault mode of Lorentz microscopy is again relatively simple to implement and is a high contrast imaging mode. The advantage this mode has over the Fresnel mode of Lorentz microscopy is that not only does it give information on the geometry of the magnetic domains but also gives information on the direction of

the magnetisation in individual domains. However as with the Fresnel mode the Foucault mode does not provide quantitative information on the sample magnetisation. Nevertheless the Fresnel and Foucault modes of Lorentz microscopy complement each other and do allow an easy investigation of the magnetic properties of a thin film.

2.3.5 Image Formation in a Scanning Transmission Electron Microscope (STEM)

Fig. 2.6 shows a diagram illustrating the planes of interest for the operation of a STEM.

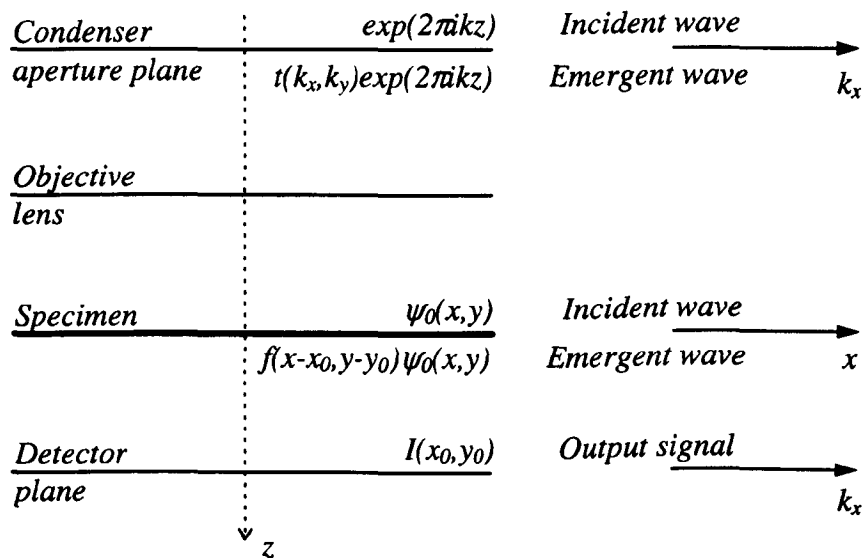


Fig. 2.6: Image formation in a STEM

Let us take the electron wave illuminating the probe forming aperture to be a plane wave. The electron disturbance incident on the specimen plane, $\psi_0(x, y)$, is the Fourier Transform of the electron wave function at the probe forming aperture,

$$\psi_0(x, y) = \iint t(k_x, k_y) \exp[-2\pi i(k_x x + k_y y)] dk_x dk_y \quad (2.15)$$

where $t(k_x, k_y)$ is as defined in equations (2.8) to (2.10) with the pupil function, spherical aberration coefficient and defocus all referring to the probe forming lens.

For reasons of mathematical expediency we assume that the electron probe remains stationary and centred on the optic axis whilst the specimen is scanned beneath it. If at a particular time a point on the specimen with coordinates (x_0, y_0) is coincident with the optic axis then the electron disturbance leaving the bottom surface of the specimen may be written in the form,

$$\psi_1(x, y) = f(x - x_0, y - y_0) \psi_0(x, y) \quad (2.16)$$

The detectors in a STEM are normally positioned in the far field with respect to the specimen so that the electron wave arriving at the detector plane is the Fourier Transform of $\psi_1(x, y)$. For a detector whose response function is $R(k_x, k_y)$ then the image signal $I(x_0, y_0)$ is given by,

$$I(x_0, y_0) = \iint R(k_x, k_y) \left| \iint \psi_1(x, y) \exp[-2\pi i(k_x x + k_y y)] dx dy \right|^2 dk_x dk_y \quad (2.17)$$

For a more detailed discussion on image formation in a STEM see Chapman^[3]. We now consider the Differential Phase Contrast (DPC) imaging mode implemented in a STEM.

2.3.6 DPC mode of Lorentz Microscopy in a STEM

The detector fitted to the JEOL 2000 and CM20 STEM's at the University of Glasgow is an eight segment photodiode made by Oxford Instruments. The geometry of the detector allows the implementation of DPC and modified DPC (MDPC) modes of Lorentz microscopy (we consider the MDPC mode in Section 2.3.7). We

begin by considering the standard DPC imaging mode which was first introduced by Dekkers and de Lang^[5] (1974) and was further developed for magnetic imaging by Chapman et al^[6] (1978). Note that DPC imaging requires a four segment detector as illustrated in fig. 2.7(a).

In the case of no specimen in the microscope column the lenses situated below the specimen (i.e. the post-specimen lenses) are used to ensure that the electron beam is centred on the detector, see fig. 2.7(a). It is clear that in this case there must be equal currents falling on each of the detector's quadrants and as a result the difference signals of the segments A-D and B-C will be zero. In the case of a magnetic specimen being present in the microscope column then the electron beam will be deflected by the specimen induction and as a result the current falling on the quadrants of the detector will not be equal, see fig. 2.7(b). Provided the deflection of the electron beam on the detector β_L is small relative to the probe angle α then the difference signals A-D and B-C will be linearly proportional to the Lorentz deflection angle β_L and thus the integrated components of magnetic induction.

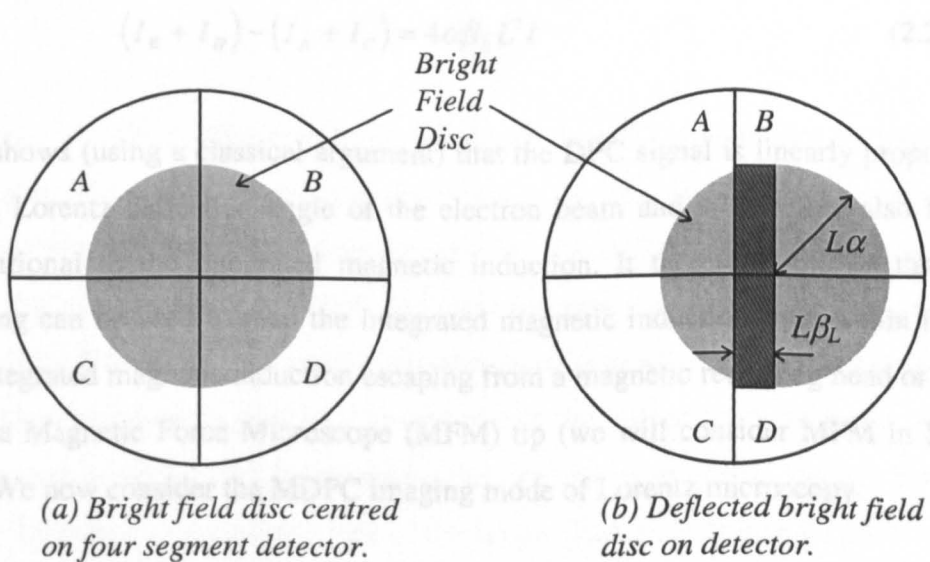


Fig. 2.7: Diagram illustrating the (a) centred and (b) deflected bright field disc on the four segment detector.

Consider fig. 2.7(b) which shows the deflected bright field disc at the detector. If we denote the effective camera length of the Image Forming lens as L , then the radius of the bright field disc on the detector will be $L\alpha$ (where α is the probe angle). If we assume that α is much larger than β_L (typically α is of the order of at least five times larger than β_L) then the signals recorded by individual quadrants of the detector will be approximately,

$$I_B = I_D = \left[\frac{\pi(L\alpha)^2}{4} + \alpha\beta_L L^2 \right] I \quad (2.18)$$

$$I_A = I_C = \left[\frac{\pi(L\alpha)^2}{4} - \alpha\beta_L L^2 \right] I \quad (2.19)$$

where I denotes the intensity of the electron beam. It follows that the difference signal between the quadrants (B+D) and (A+C) is given by,

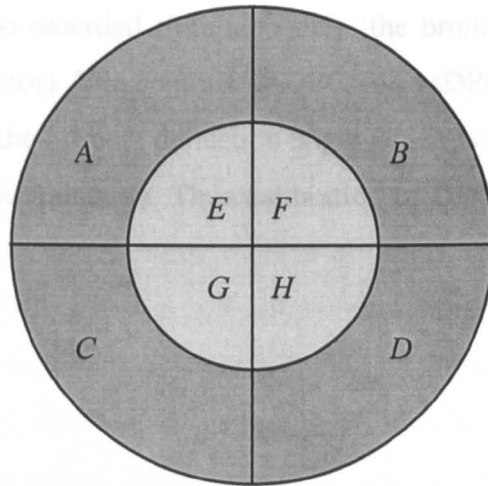
$$(I_B + I_D) - (I_A + I_C) = 4\alpha\beta_L L^2 I \quad (2.20)$$

This shows (using a classical argument) that the DPC signal is linearly proportional to the Lorentz deflection angle of the electron beam and is therefore also linearly proportional to the integrated magnetic induction. It therefore follows that DPC imaging can be used to map the integrated magnetic induction from a thin film, or the integrated magnetic induction escaping from a magnetic recording head or indeed from a Magnetic Force Microscope (MFM) tip (we will consider MFM in Section 2.4). We now consider the MDPC imaging mode of Lorentz microscopy.

2.3.7 MDPC mode of Lorentz Microscopy in a STEM

The DPC contrast from a real specimen always contains both magnetic and non-magnetic components (for example non-magnetic contrast arising from the crystalline structure of the specimen). In some cases the non-magnetic contrast from

a specimen dominates over the magnetic contrast making it almost impossible to extract any quantitative magnetic information. Since we are only interested in the magnetic contrast, the non-magnetic contrast is considered to be noise and any method for reducing this noise contribution is highly desirable.



2.4 Magnetic Force Microscopy

Fig. 2.8: Diagram of the 8 segment detector used in both STEM's at the University of Glasgow. Note that for MDPC imaging only segments A, B, C and D are used.

In 1935 Binnig and Rohrer^[6] invented the Scanning Tunneling Microscope (STM) which is capable of high spatial resolution of the order 0.2nm. The essential feature

Chapman et al^[7] (1990) introduced a simple modification to the existing DPC technique. The MDPC technique made use of an annular detector surrounding a standard four quadrant DPC detector, see fig. 2.8. MDPC images are acquired by using the annular detector which provides information about the position of the bright field disc (clearly the bright field disc must overlap onto the annular detector). The annular detector is relatively insensitive to any intensity modulations within it and as such is well suited for revealing the low spatial frequency component of the signal. Electrons in the central part of the bright field disc (detected by the standard DPC detector) contain no information about the low spatial frequency components (but do contain information about the higher spatial frequency component of the signal) and can only contribute to the noise in the image of a slowly varying object. Since the magnetic contrast of interest is of low spatial frequency and non-magnetic contrast (e.g. from the crystalline nature of the sample) is of a higher spatial

frequency then the MDPC detector detects magnetic contrast with a far higher signal to noise ratio than is possible from standard DPC imaging.

The advantage of DPC and MDPC modes of Lorentz microscopy is that they provide quantitative information on the components of magnetic induction perpendicular to the trajectory of the electrons. A standard incoherent bright field image (containing structural information about the specimen such as grain size, defects etc.) is also recorded simultaneously (the bright field image being the sum image on the detector). The contrast of DPC and MDPC images is approximately a linear function of the Lorentz deflection angle which is itself a linear function of the integrated magnetic induction. Thus calibration of DPC images is relatively simple to implement.

2.4 Magnetic Force Microscopy

In 1985 Binnig and Rohrer^[8] invented the Scanning Tunnelling Microscope (STM) which is capable of high spatial resolution of the order 0.2nm. The essential feature of the STM is that the structural character of a specimen is revealed through the interaction between a sharp needle - the tip - and a flat electrode - the specimen. An image is formed by scanning the sample under the tip (or scanning the tip over the sample) in a raster fashion. Following the introduction of the STM several variants were rapidly developed and in each case the same principle of monitoring the interaction between a tip and sample was central to their operation. We now consider one specific variant of the STM and that is the Magnetic Force Microscope^[9] (MFM).

In a MFM a sharp ferromagnetic tip is mounted on (or is sometimes part of) a sensitive cantilever. The cantilever itself is mounted on a piezoelectric bimorph which is used to control the static height of the tip or to oscillate it with a constant amplitude (typically in the range of 1 to 10nm). The magnetic specimen under investigation is scanned under the tip and the interaction force between the tip's

magnetisation and the stray field from the specimen results in the cantilever bending towards or away from the specimen. The deflection of the cantilever is measured by an optical sensor - usually an optical interferometer. This is known as the Static mode of operation of a MFM and gives a direct measurement of the interaction force between the tip and specimen. High spatial resolution has been achieved with this method (resolution of 10nm has been reported^[10]) however this mode can be influenced by thermal drift. A method which overcomes this problem is the Dynamic mode of operation of a MFM which measures the force gradient instead of the force itself.

In the Dynamic mode the cantilever is set vibrating at a frequency close to its resonant frequency (which is typically 10 to 100kHz). The specimen is again scanned under the tip and in this case the tip-specimen interaction changes the effective spring constant of the cantilever and thus alters its resonant frequency. This change in the frequency of vibration of the cantilever is reflected in a small change to the amplitude of the vibration. The change in the amplitude of vibration is measured by the optical interferometer and is included into a feedback loop which adjusts the signal to the Z piezo which maintains a constant amplitude of vibration of the cantilever. The signal to the Z piezo is used to generate the MFM image and represents a measure of the gradient of the interaction force between the tip and specimen.

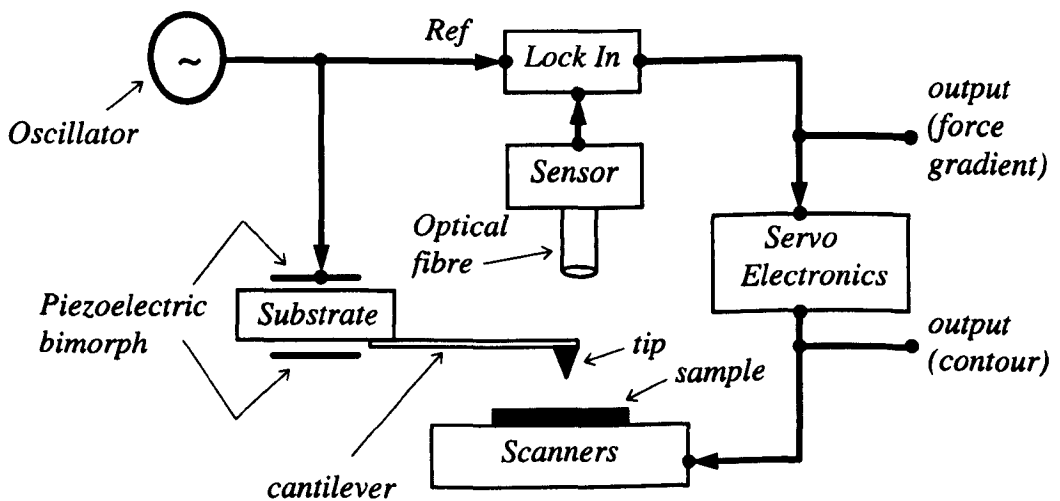


Fig. 2.9: Block diagram of a magnetic force microscope. (Rugar et al^[11])

The magnetic specimen under investigation is mounted on a stage whose in-plane position can be controlled by piezoelectric sensors (the sensors are excited to scan the specimen below the tip in a controlled manner). Fig. 2.9 shows a standard block diagram of an MFM.

Fig. 2.10 shows a MFM image of three separate tracks written in a magnetic recording media. If we assume, 1) that the recording media is smooth so that the MFM image does not include any contrast due to the topography of the specimen, 2) the tip magnetisation was not altered by the stray field from the specimen and 3) that the specimen magnetisation was not altered by the stray field from the tip (this is analogous to the tip and sample both being magnetically hard), then the MFM image represents a direct measurement of the component of the tip-specimen interaction force (or force gradient) normal to the cantilever.

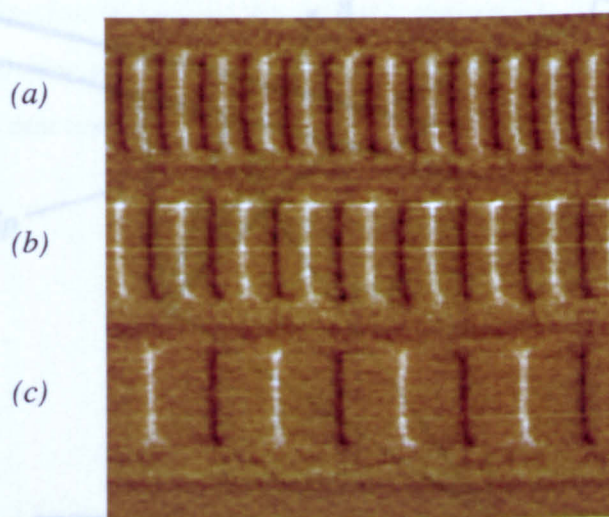


Fig. 2.10: MFM image of three separate tracks ($20\mu\text{m}$ in length) with transitions spaced every (a) $1.5\mu\text{m}$,
(b) $2.5\mu\text{m}$,
(c) $5\mu\text{m}$ apart.

The total force experienced by the tip, F_{tip} , is given by,

$$\underline{F}_{tip}(\underline{r}) = \int_{tip} \nabla \left[\underline{M}_{tip}(\underline{r}') \cdot \underline{H}_{specimen}(\underline{r} + \underline{r}') \right] dV \quad (2.21)$$

where $\underline{M}_{tip}(\underline{r}')$ is the magnetisation of the volume element in the tip and $\underline{H}_{specimen}(\underline{r} + \underline{r}')$ is the specimen stray field acting on the elemental volume, see fig. 2.11. Thus a MFM image maps the scalar component of the tip-specimen interaction, F_{MFM} , given by,

$$F_{MFM} = \underline{F}_{tip} \cdot \hat{n} \quad (2.22)$$

where \hat{n} is the unit vector normal to the cantilever (again see fig. 2.11).

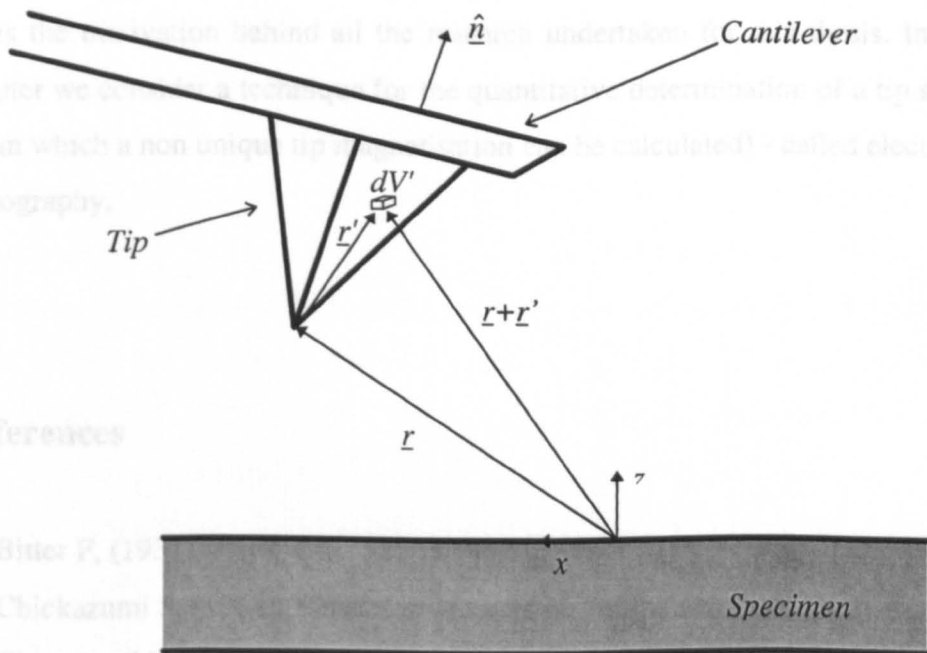


Fig. 2.11: Geometry used in calculating the tip-specimen interaction given in equations 2.22 and 2.23 (Grutter^[12]).

It is often the case that the specimen stray field is the quantity of interest - for example in magnetic recording applications. However as equation (2.22) shows, a

MFM image is a map of a convolution of the tip magnetisation and the sample stray field. It therefore follows that to extract quantitative information on the specimen stray field from a MFM image then we must have a quantitative knowledge of the tip magnetisation so that the specimen stray field may be deconvolved from the image.

In the more complex (and more realistic) non-ideal case of MFM imaging where the magnetisation of the tip is altered by the stray field from the specimen, and the magnetisation of the specimen is altered by the stray field from the tip then we still require to have a quantitative knowledge of the tip magnetisation. However in this case knowledge of the initial tip magnetisation, the shape of the tip, the nature of its magnetic structure and a correct accounting for changes in the magnetisation of the tip and/or specimen will all have to be taken into account in order that a function for determination of the required specimen stray field from a MFM image may be determined.

This requirement to characterise quantitatively the magnetisation of a MFM tip is the motivation behind all the research undertaken for this thesis. In the next chapter we consider a technique for the quantitative determination of a tip stray field (from which a non unique tip magnetisation can be calculated) - called electron beam tomography.

References

- [1] Bitter F, (1931), *Phys. Rev.*, 38, pp 1903
- [2] Chickazumi S, (1964), *Physics of Magnetism*, Wiley and Sons Inc.
- [3] Chapman J N, (1984), *J. Phys. D: Appl. Phys.*, 17, pp623
- [4] Ahaonov Y and Bohm D, (1959), *Phys. Rev.*, 115, pp 485
- [5] Cekkers N H and de Lang H, (1974), *Optik*, pp 452
- [6] Chapman J N, Batson P E, Waddell E M and Ferrier R P, (1978), *Ultramicrosc.*, 3, pp 203
- [7] Chapman J N, McFadyen I R and McVitie S, (1990), *IEEE Trans. Mag.*, 26(5), pp 1506

- [8] Binning G and Rohrer H, (1985), *Sci. Amer.*, 253, pp 50
- [9] Martin Y and Wickramasinghe H K, (1987), *Appl. Phys. Lett.*, 50, pp 1455
- [10] Grutter P, Meyer E, Heizelmann H, Rosenthaler H, Hedber H J and Guntherodt H S, (1988), *J. Vac. Sci. Tech.*, A6, pp 279
- [11] Rugar D, Mamin H J, Guthner P, Lambert S E, Stern J E and McFadyen I R, (1990), *J. Appl. Phys.*, 68, pp 1169
- [12] Grutter P, (1994), *Microsc. Soc. of America*, 24, No.1: pp 416

Chapter 3

Fundamentals of Electron Beam Tomography for the study of Magnetic Force Microscope Tips

3.1 Introduction

Tomography is the method for reconstruction of the interior of an object from its image projections obtained with a suitable radiation. Electron beam tomography is the term used when a transmission electron microscope is used to collect the projections which are then used to reconstruct the object in its entirety. Other types of tomography exist such as CAT-scan imaging (Computerised Axial Tomography) which uses density projections of biological samples obtained using X-rays, to reconstruct the original object. The only differences between electron beam tomography and CAT-scan imaging is the radiation and detectors used in the process of collecting the object's projections.

Tomography was originally developed for the three dimensional imaging of non-crystalline biological structures - for example DeRosier and Klug^[1](1968) imaged chromosomes. The emergence of tomography coincided with the development of computers which allowed the processing of large amounts of data in a suitably short time.

The three dimensional reconstruction methods used for tomography are traditionally classified into two groups - Fourier reconstruction methods and real space methods^{[2][3]}. Fourier methods are defined as algorithms which operate in Fourier space - in that the Fourier transform of the object is reconstructed from the Fourier transformations of the projections (the real space distribution of the object is then

obtained by inverse Fourier transformation). Real space methods, as the name suggests, are defined as those which carry out all reconstruction calculations in real space.

Throughout this thesis we use electron beam tomography for the determination of MFM tip fields. This technique was originally used to image magnetic recording head fields and was developed by a research group in Duisburg (Elsbrock et al.^[4], 1985; Steck et al.^[5], 1990). Significant modifications to existing tomography techniques were required so that electron beam tomography could be used for the determination of a stray field - most importantly a density function of a biological specimen is a scalar function, whereas magnetic field is a three dimensional function. The projection of a magnetic field in electron beam tomography is a planar (deflection) vector. This is due to the fact that the electron-stray field interaction deflects the beam from its original path and the final deflection represents an integral of field components along the electron beam trajectory.

The Duisburg group carried out their approach by using a scanning electron microscope (SEM) for the collection of the electron beam deflection data and a reconstruction technique based on the Fourier and Radon^[6] transforms - this technique will subsequently be referred to as the Radon Transform Method (RTM). Note that RTM allows a determination of the three dimensional stray field from either component of the deflection data and is a Fourier reconstruction method.

A separate technique for the reconstruction of recording head stray field was developed by Matsuda et al.^[7](1990). This technique is based on the Algebraic Reconstruction technique (ART), which was originally developed for the three dimensional imaging of biological structures by Gordon et al.^[8](1970) but modified to deal with a vector function instead of a scalar function. An advantage of ART is that it can produce an accurate representation of the object of measurement with fewer projections - this therefore allows an ordinary tilting stage (say $\pm 50^\circ$) to be used.

For stray field reconstruction using either the ART or RTM reconstruction techniques, the projections of the MFM tip fields are acquired in a STEM using DPC Lorentz microscopy (see Section 2.3.6). In this chapter we give a detailed introduction to the general principle, the mathematical description and the experimental implementation of electron beam tomography for the three dimensional imaging of

MFM tip fields. We consider both the ART and RTM methods but we pay special attention to the RTM method which is used extensively throughout this thesis.

3.2 The General Principle of Three Dimensional Reconstruction and its Application to Determining the MFM Tip Field

The principle of the three dimensional reconstruction of an object from its projections can be understood from the fundamental relationship between the object and its projections. In this thesis we make use of a Fourier Technique, i.e. the RTM reconstruction technique (and to a much lesser extent the ART which is a real space method), which we begin by considering in its basic scalar form - i.e. density electron beam tomography - in which a density function is suitable for defining the object of measurement. In Section 3.2.2 we discuss the derivation of the RTM tomographic algorithm for vector magnetic stray field and then we briefly consider ART in Section 3.2.3.

3.2.1 The Fourier Method

The Fourier Transform provides an alternative representation of an object by breaking it down into a series of trigonometric basis functions. In the following, we make use of complex exponential waves of the form $\exp(2\pi i \underline{k} \cdot \underline{r})$ instead of sine and cosine functions for reasons of mathematical ease. Note that $\underline{r} = (x, y, z)$ is the position vector of the object, and \underline{k} is the spatial frequency which gives the direction of the wave and its inverse wavelength. The object $f(\underline{r})$ can be built up from a series of these waves by linear superposition as,

$$f(\underline{r}) = \sum_j F(\underline{k}_j) \exp(2\pi i \underline{k}_j \cdot \underline{r}) \quad (3.1)$$

In this discrete form of the Fourier transform, the complex coefficients $F(k_j)$ contain information on the amplitude A_j , and phase (or phase shift with respect to the origin) ϕ of the associated wave

$$A_j = |F(\underline{k}_j)| \quad (3.2)$$

$$\phi_j = \tan^{-1} \left(\frac{\text{Im}\{F(\underline{k}_j)\}}{\text{Re}\{F(\underline{k}_j)\}} \right) \quad (3.3)$$

Note that $F(k_j)$ can be written in the discrete form of the inverse Fourier transform of $f(r)$ as,

$$F(\underline{k}_j) = \sum_j f(r) \exp(-2\pi i \underline{k}_j \cdot \underline{r}) \quad (3.4)$$

Thus we have a relationship between f and F .

An important result relating f and F is the Central Section Theorem which states that the two dimensional Fourier transform of the projection of an object is identical to a central section of the object's three dimensional Fourier transform (Crowther et al.^[9], 1970). It follows that the measurement of an object's projections allows a way to measure the Fourier transform of the object. Thus, by tilting the object through many different angular positions we should be able to measure its entire Fourier Transform. Fig. 3.1 shows the method by which the object of measurement is retrieved by inverse Fourier transformation from the object's projections superimposed on an array of equally spaced sampling points.

Note from fig. 3.1 that the sampling points on the object's projections become more widely spaced as they increase in distance from the centre. To ensure that their maximum separation is consistent with the required reconstruction resolution the angular spacing of the individual projections must be sufficiently small. If we assume that the resolution of the reconstructed object is set to d , then the region in Fourier

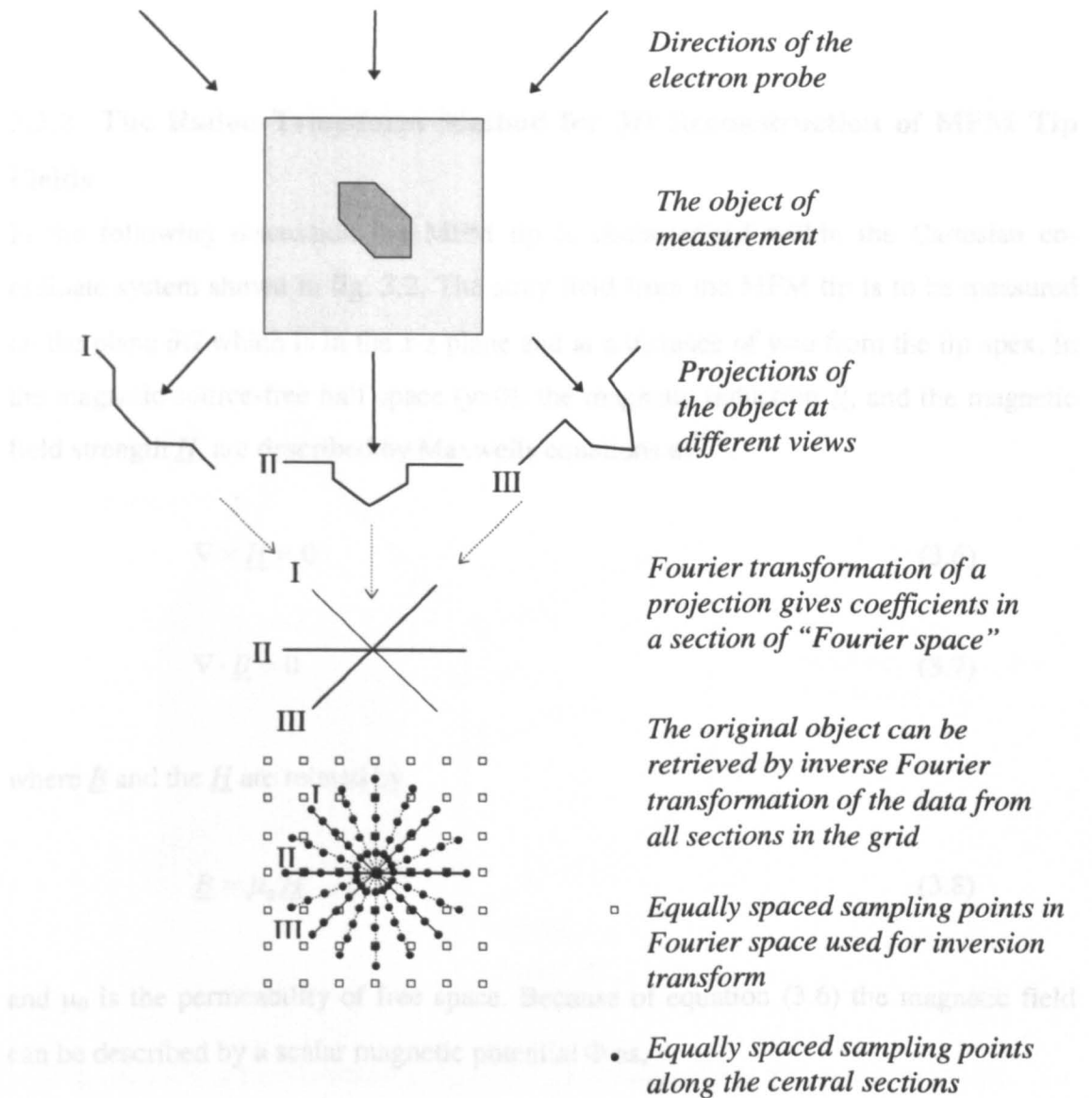


Fig. 3.1: Diagram illustrating three dimensional reconstruction using the Fourier method.

space in which the data must be acquired will be a sphere of radius $1/d$. This sphere must be larger than the size of the reconstructed object D , and so the minimum number of equally spaced projections is given as (Crowther et al.^[9], 1970; Bracewell and Riddle^[10], 1967)

with equations (3.6) to (3.10) and the theory of harmonic functions, the magnetic field in the magnetic source free half space (i.e. $y > 0$), can be written in integral form over the plane dG as

$$N = \frac{\pi D}{d} \tag{3.5}$$

We now consider the application of this theory for the determination of MFM tip fields.

3.2.2 The Radon Transform Method for 3D Reconstruction of MFM Tip Fields

In the following discussion the MFM tip is characterised within the Cartesian coordinate system shown in fig. 3.2. The stray field from the MFM tip is to be measured on the plane ∂G which is in the x - z plane and at a distance of $y=a$ from the tip apex. In the magnetic source-free half space ($y>0$), the magnetic induction \underline{B} , and the magnetic field strength \underline{H} , are described by Maxwells equations as^[11],

$$\nabla \times \underline{H} = 0 \quad (3.6)$$

$$\nabla \cdot \underline{B} = 0 \quad (3.7)$$

where \underline{B} and the \underline{H} are related by

$$\underline{B} = \mu_0 \underline{H} \quad (3.8)$$

and μ_0 is the permeability of free space. Because of equation (3.6) the magnetic field can be described by a scalar magnetic potential Φ as,

$$\underline{H} = -grad\Phi \quad (3.9)$$

and

$$\nabla^2 \Phi = 0 \quad (3.10)$$

with equations (3.6) to (3.10) and the theory of harmonic functions, the magnetic field in the magnetic source free half space (i.e. $y>0$), can be written in integral form over the plane ∂G as^[4]

$$\underline{B}(\underline{r}) = \frac{1}{2\pi} \iint_{\partial G} \frac{\underline{r} - \underline{r}_0}{|\underline{r} - \underline{r}_0|^3} B_y(\underline{r}_0) dS \quad (3.11)$$

in which \underline{r} and \underline{r}_0 are position vectors in the half space $y > 0$ and the plane ∂G respectively.

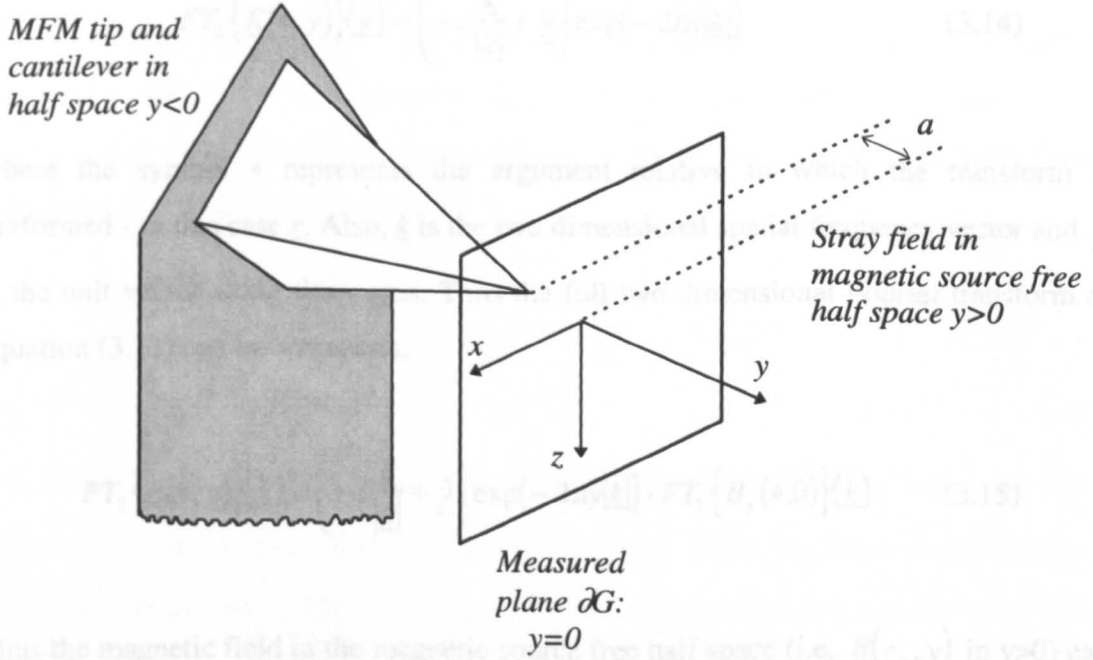


Fig. 3.2: Diagram illustrating the MFM tip relative to the measurement plane.

Now if we define the function $\underline{K}(\underline{r}, \underline{r}_0)$ as,

$$\underline{K}(\underline{r}, \underline{r}_0) = \frac{1}{2\pi} \frac{\underline{r} - \underline{r}_0}{|\underline{r} - \underline{r}_0|^3} \quad (3.12)$$

then we can regard equation (3.11) as a two dimensional convolution of the function B_y with the function \underline{K} . A two dimensional Fourier transform of equation (3.11) is now carried out. The N dimensional Fourier transform of a function f is defined as,

$$FT_n \{f\} = \int_{\mathfrak{R}^n} f(\underline{r}) \exp(-2\pi \underline{r} \cdot \underline{\xi}) d^n \underline{\xi} \quad (3.13)$$

Thus, with the help of Fourier tables (Bracewell and Riddle^[10], 1967) the two dimensional Fourier transform of \underline{K} is^[4],

$$FT_2 \{ \underline{K}(\bullet, y) \}(\underline{k}) = \left(-i \frac{\underline{k}}{|\underline{k}|} + \underline{\hat{y}} \right) \exp(-2\pi y |\underline{k}|) \quad (3.14)$$

where the symbol \bullet represents the argument relative to which the transform is performed - in this case \underline{r} . Also, \underline{k} is the two dimensional spatial frequency vector and $\underline{\hat{y}}$ is the unit vector along the y axis. Thus the full two dimensional Fourier transform of equation (3.11) can be written as,

$$FT_2 \{ \underline{B}(\bullet, y) \}(\underline{k}) = \left(-i \frac{\underline{k}}{|\underline{k}|} + \underline{\hat{y}} \right) \exp(-2\pi y |\underline{k}|) \cdot FT_2 \{ B_y(\bullet, 0) \}(\underline{k}) \quad (3.15)$$

Thus the magnetic field in the magnetic source free half space (i.e. $\underline{B}(\underline{r}_0, y)$ in $y > 0$) can be deduced if the values of the normal component of field are known in ∂G (i.e. $\underline{B}(\underline{r}_0, 0)$).

Multiplication of equation (3.15) with an arbitrary unit vector in the plane ∂G

$$\underline{\hat{e}}(\theta) = \underline{\hat{x}} \cos \theta + \underline{\hat{z}} \sin \theta \quad (3.16)$$

leads to equation (3.17), where θ is the rotation angle about the y axis.

$$FT_2 \{ \underline{B}(\bullet, y) \}(\underline{k}) = \left(\frac{\underline{k} + i|\underline{k}|\underline{\hat{y}}}{\underline{k} \cdot \underline{\hat{e}}(\theta)} \right) \exp(-2\pi y |\underline{k}|) \cdot FT_2 \{ \underline{\hat{e}}(\theta) \cdot \underline{B}(\bullet, 0) \}(\underline{k}) \quad (3.17)$$

Thus, equation (3.17) allows a determination of the magnetic field \underline{B} in the half space $y>0$ if the spectra of an arbitrary tangential (to the plane ∂G) component of the magnetic field is known.

Equations (3.15) and (3.17) therefore show that knowledge of the spectra (either of the normal component or of an arbitrary tangential component of the magnetic stray field) in the plane ∂G is sufficient to determine the whole three dimensional stray field in the magnetic source free half space defined by $y>0$.

We now introduce the Radon transform which allows the application of the theory detailed above (for determining the three dimensional stray field) via an experimental measurement in an electron microscope. The two dimensional Radon transform of a function f is defined as^[12],

$$RT_2\{f(\underline{r})\}(p, \underline{e}(\theta)) = \int \int_{\mathbb{R}^2} f(\underline{r}) \cdot \delta(p - \underline{r} \cdot \underline{e}(\theta)) d^2 \underline{r} \quad (3.18)$$

where p and $\underline{e}(\theta)$ together define a straight line ($p = \underline{r} \cdot \underline{e}(\theta)$) along which the Dirac delta function is non zero. Thus, the two dimensional Radon transform of the function f is the integral of f along the line $p = \underline{r} \cdot \underline{e}(\theta)$. In Lorentz microscopy, the electron beam is deflected by the component of magnetic field perpendicular to the direction of the electron beam. The total deflection is therefore obtained by integrating this field component along the electron beam trajectory. If the electron beam is scanned in front of the MFM tip in the plane ∂G and if the resulting electron beam deflection is small

relative to the length of the electron beam trajectory, then measurement of the deflection of the electron beam (in Lorentz microscopy) can be approximated to the Radon transform of the magnetic field component perpendicular to and along the line defined by the scanned electron beam.

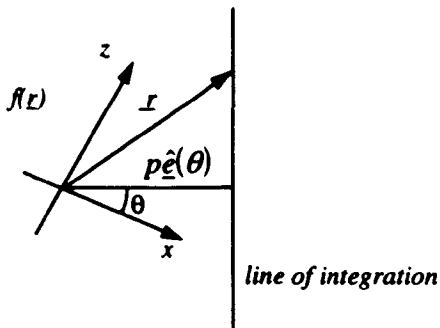


Fig. 3.3: Geometric representation of the coordinate system in the measuring plane ∂G .

An important relation between the Radon transform and the Fourier transform is^[12],

$$FT_2\{f\}(s\hat{e}) = FT_1\{RT_2[f](\bullet, \hat{e})\}(s) \quad (3.19)$$

with this relationship, equations (3.15) and (3.17) can be written using the Radon transform as,

$$FT_2\{\underline{B}(\bullet, y)\}(s\hat{e}(\theta)) = \left(-i \sin(s)\hat{e}(\theta) + \hat{y}\right) \exp(-2\pi y|s|) \cdot FT_1\{RT_2[B_y(\bullet, 0)](\bullet, \hat{e}(\theta))\}(s) \quad (3.20)$$

$$FT_2\{\underline{B}(\bullet, y)\}(s\hat{e}(\theta)) = \left(\hat{e}(\theta) + i \sin(s)\hat{y}\right) \exp(-2\pi y|s|) \cdot FT_1\{\hat{e}(\theta)RT_2[\underline{B}(\bullet, 0)](\bullet, \hat{e}(\theta))\}(s) \quad (3.21)$$

The Radon transforms $RT_2[B_y(\bullet, 0)](p, \hat{e}(\theta))$ and $\hat{e}(\theta)RT_2[\underline{B}(\bullet, 0)](p, \hat{e}(\theta))$ in equations (3.20) and (3.21) are the normal and tangential components of the deflection vector - which can be measured using DPC Lorentz microscopy. These components of the deflection vector are the input functions for determining the magnetic stray field from the MFM tip. If one of these input functions is known for all p and $\hat{e}(\theta)$ - i.e. measured along all angles of rotation - then the stray field $\underline{B}(r, y)$ can be determined in the whole half space $y > 0$ using the following method.

To reconstruct the field $\underline{B}(r, y)$ from its spectral representation in equation (3.20) or (3.21) we require to make use of the fact that the two dimensional inverse Fourier transform of a function is equivalent to a one dimensional inverse Fourier transform followed by a back projection of the function. This means that with an auxiliary function $\underline{f}(p, \hat{e}(\theta), y)$, which is defined by,

$$FT_1\{\underline{f}(\bullet, \hat{e}(\theta), y)\}(s) = |s| \cdot FT_2\{\underline{B}(\bullet, y)\}(s\hat{e}(\theta)) \quad (3.22)$$

then the original stray field $\underline{B}(r, y)$ can be obtained by back projection of the auxiliary function,

$$\underline{B}(\underline{r}, y) = BP\{f(\bullet, \bullet, y)\}(\underline{r}) \quad (3.23)$$

where BP is the back projection operator defined by the Radon Transform,

$$BP\{f(\bullet, \bullet, y)\}: \mathfrak{R}^2 \longrightarrow \mathfrak{R}^3 \quad \underline{r} \longrightarrow \int_0^\infty \int_0^\pi \underline{f}(\underline{p}, \hat{\underline{e}}(\theta), y) \cdot \delta(\underline{p} - \underline{r} \cdot \hat{\underline{e}}(\theta)) d\theta dp \quad (3.24)$$

Thus, substitution of equation (3.20) into equation (3.22) gives us,

$$FT_1\{\underline{f}(\bullet, \hat{\underline{e}}(\theta), y)\}(s) = |s|(-i \sin(s)\hat{\underline{e}}(\theta) + \hat{y}) \exp(-2\pi y|s|) \cdot FT_1\{RT_2[B_y(\bullet, 0)](\bullet, \hat{\underline{e}}(\theta))\}(s) \quad (3.25)$$

The auxiliary function $\underline{f}(\underline{p}, \hat{\underline{e}}(\theta), y)$ can then be obtained from the inverse Fourier transform (denoted $FT_1^{-1}\{\}$) of equation (3.25),

$$\begin{aligned} \underline{f}(\underline{p}, \hat{\underline{e}}(\theta), y) &= FT_1^{-1}\{\text{RHS of equation (3.25)}\} \\ &= \left[FT_1^{-1}\{|s|(-i \sin(s)\hat{\underline{e}}(\theta) + \hat{y}) \exp[-2\pi y|s|]\} * RT_2[B_y(\bullet, 0)](\bullet, \hat{\underline{e}}(\theta)) \right](\underline{p}) \end{aligned} \quad (3.26)$$

If we define the function \underline{C} (which is often referred to as the convolution kernel) as,

$$\underline{C}(\underline{p}, y) = FT_1^{-1}\{|s|(-i \sin(s)\hat{\underline{e}}(\theta) + \hat{y}) \exp[-2\pi y|s|]\} \quad (3.27)$$

then equation (3.26) becomes,

$$\underline{f}(\underline{p}, \hat{\underline{e}}(\theta), y) = [\underline{C}(\underline{p}, y) * RT_2[B_y(\bullet, 0)](\bullet, \hat{\underline{e}}(\theta))](\underline{p}) \quad (3.28)$$

The important point to note from equation (3.28) is that the auxiliary function can now be obtained from a convolution of the Radon transform $RT_2[B_y(\bullet, 0)]$ with the

convolution kernel $\underline{C}(p, y)$. Thus the combination of equation (3.28) with equation (3.23) gives the stray field $\underline{B}(r, y)$ in the half space $y > 0$ as,

$$\underline{B}(r, y) = BP\left\{\underline{C}(p, y) * RT_2\left[B_y(\bullet, 0)\right](\bullet, \hat{e}(\theta))\right\}(r) \quad (3.29)$$

Thus, equation (3.29) provides a solution for equation (3.20) in the magnetic source free half space $y \geq 0$. A solution for equation (3.21) can be obtained using a similar method but is not shown here. A flow diagram giving a summarised overview of the process to determine the three dimensional stray field is shown in fig. 3.4.

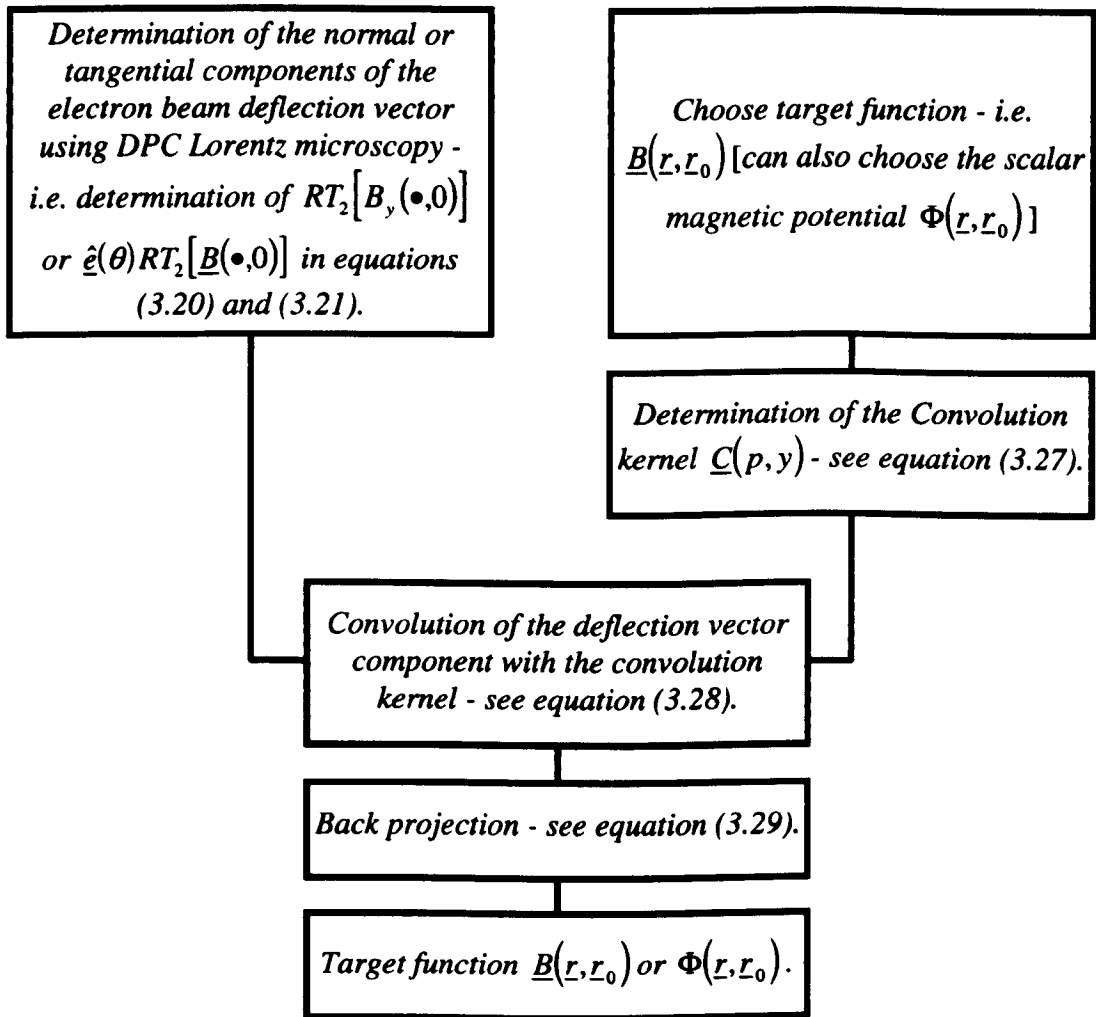


Fig. 3.4: Flow diagram illustrating a summarised overview of the process to determine the three dimensional stray field.

In Section 3.3 we consider the experimental acquisition of the input functions given by the Radon transforms $RT_2[B_y(\bullet,0)](p,\hat{e}(\theta))$ and $\hat{e}(\theta)RT_2[B(\bullet,0)](p,\hat{e}(\theta))$ in equations (3.20) and (3.21) respectively. However before this we briefly consider the scalar and vector forms of the Algebraic Reconstruction Technique.

3.2.3 The Conventional Algebraic Reconstruction Technique

In the Algebraic Reconstruction Technique (ART), the object under investigation is defined to be a density function in three dimensional space. The object can be tilted around a single rotation axis and at each angular position an electron beam (or other form of radiation - e.g. X-rays) is scanned across the object. The interaction between the object and the electron beam defines a sectional plane through the object - perpendicular to the rotation axis - and results in a projection of the plane onto a line on the detector, see fig. 3.5.

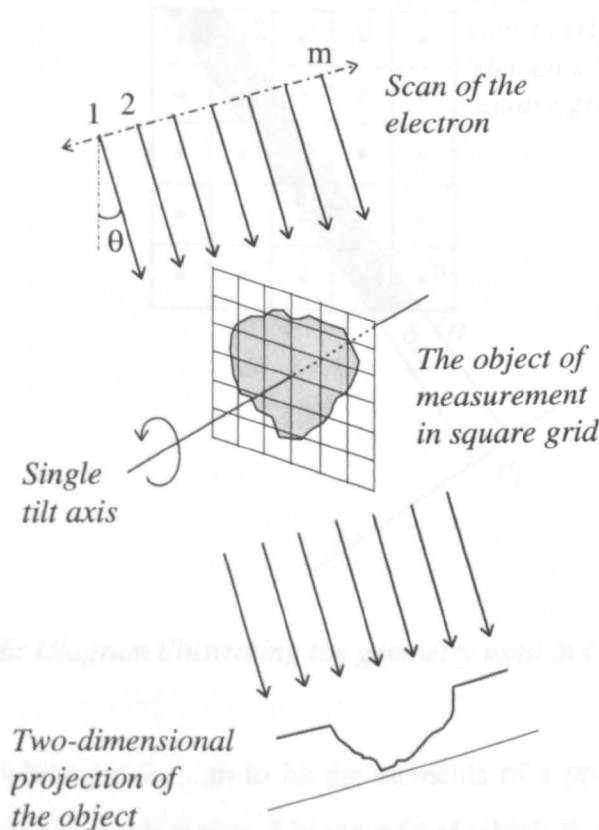


Fig. 3.5: Electron beams (or other radiation) illuminating an object and projecting the 3D object onto the detector plane.

Each sectional plane is reconstructed from the projections of different angular views of the object and the sections are combined to get the three dimensional reconstruction. The problem of reconstruction of a three dimensional density function is therefore reduced to the reconstruction of two dimensional sections of the object.

For the conventional ART algorithm we assume that the density function of the object $f(r)$ is defined on a square grid of n non-overlapping elements as shown in fig. 3.6. The discretisation of the grid should be as fine as possible and is related to the assumed spatial resolution in the projections. The object's projection is also divided into non-overlapping elements corresponding to the position of the scanning electron probe.

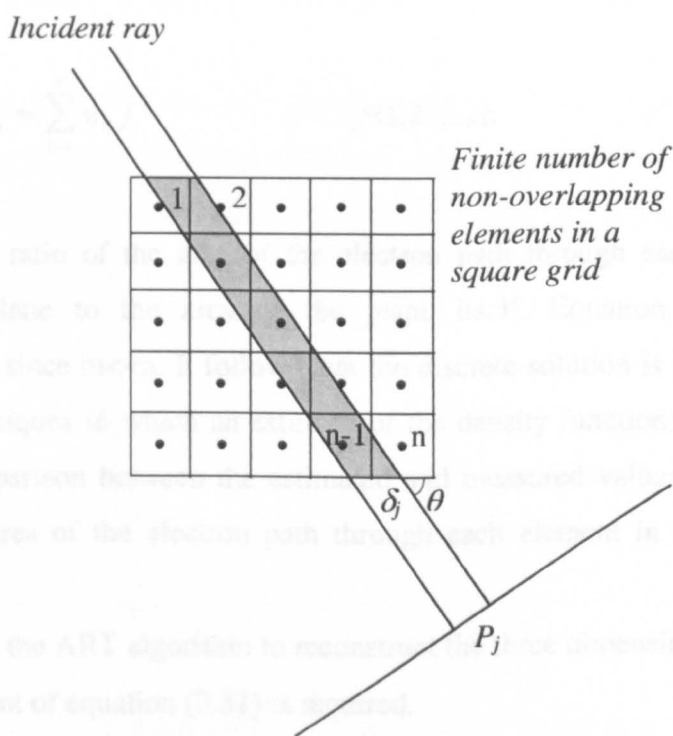


Fig. 3.6: Diagram illustrating the geometry used in conventional ART.

3.2.4 The Magnetic Field Vector Algebraic Reconstruction Technique

If we take P_j , where $j=1,2, \dots, m$ to be the elements of a projection then for every P_j there is a corresponding sub-region δ_j in the grid of which P_j is the projection. Taking r to be a point on the grid then,

$$\int_{\delta_j} f(r)dr \approx P_j \quad j=1,2, \dots,m \quad (3.30)$$

The approximation sign indicates that the process is not perfect as a result of the finite number of non-overlapping elements in the grid. This is the fundamental equation of ART from which all reconstruction algorithms for the unknown density function $f(r)$ are derived.

To determine a discrete solution for equation (3.30) we must represent the reconstruction plane in a discrete fashion - similar to the grid in fig. 3.6. In doing this and by assuming that the unknown density function $f(r)$ is a constant in each element of the reconstruction plane (and denoted f_i where $i=1,2, \dots,n$) then equation (3.30) becomes a set of simultaneous linear equations of the unknown f_i ,

$$P_j \approx \sum_{i=1}^n w_{ij} f_i \quad j=1,2, \dots,m \quad (3.31)$$

where w_{ij} is the ratio of the area of the electron path through each element of the reconstruction plane to the area of the plane itself. Equation (3.31) is highly underdetermined since $m \ll n$. It follows that the discrete solution is generally obtained by iterative techniques in which an estimate of the density functions f_i is corrected by means of a comparison between the estimated and measured values weighted to take account of the area of the electron path through each element in the reconstruction plane.

To utilise the ART algorithm to reconstruct the three dimensional tip stray field, a vector equivalent of equation (3.31) is required.

3.2.4 The Magnetic Field Vector Algebraic Reconstruction Technique

In a STEM, the interaction between a three dimensional magnetic field and moving electrons projects a two dimensional vector onto the detector plane. The derivation of the vector equivalent of equation (3.31) is now described.

We assume that the tip field is confined within the scanning area of the electron beam in the microscope. In the field-free chamber, the half space in front of the tip is divided into three regions along the electron trajectory, see fig. 3.7. In the first region (Region I) the tip stray field is zero and the incident electrons travel with a constant speed. In Region II the tip stray field is non-zero and as a result the electrons are acted on by the Lorentz force and are deflected from their incident trajectory. The Lorentz force is given by,

$$\underline{F} = e\underline{v} \times \underline{B} \quad (3.32)$$

where e is the electron charge, \underline{v} is the electron velocity and \underline{B} is the tip stray field vector.

Let s_i be a short distance in Region II and \underline{B}_i be the average value of the stray field \underline{B} in s_i along the electron beam trajectory. The components of the electron beam deflection vector (which are parallel to the ξ and η directions as the electrons traverse the distance s_i) are calculated by,

$$dD_{\xi} = \left(\frac{e}{2mE} \right)^{1/2} \frac{s_i^2}{2} B_{yi} \quad (3.33)$$

$$dD_{\eta} = - \left(\frac{e}{2mE} \right)^{1/2} \frac{s_i^2}{2} B_{xi} \quad (3.34)$$

The field in Region III is again zero and the electrons travel in a straight line to the detector plane at a distance L from the tip apex.

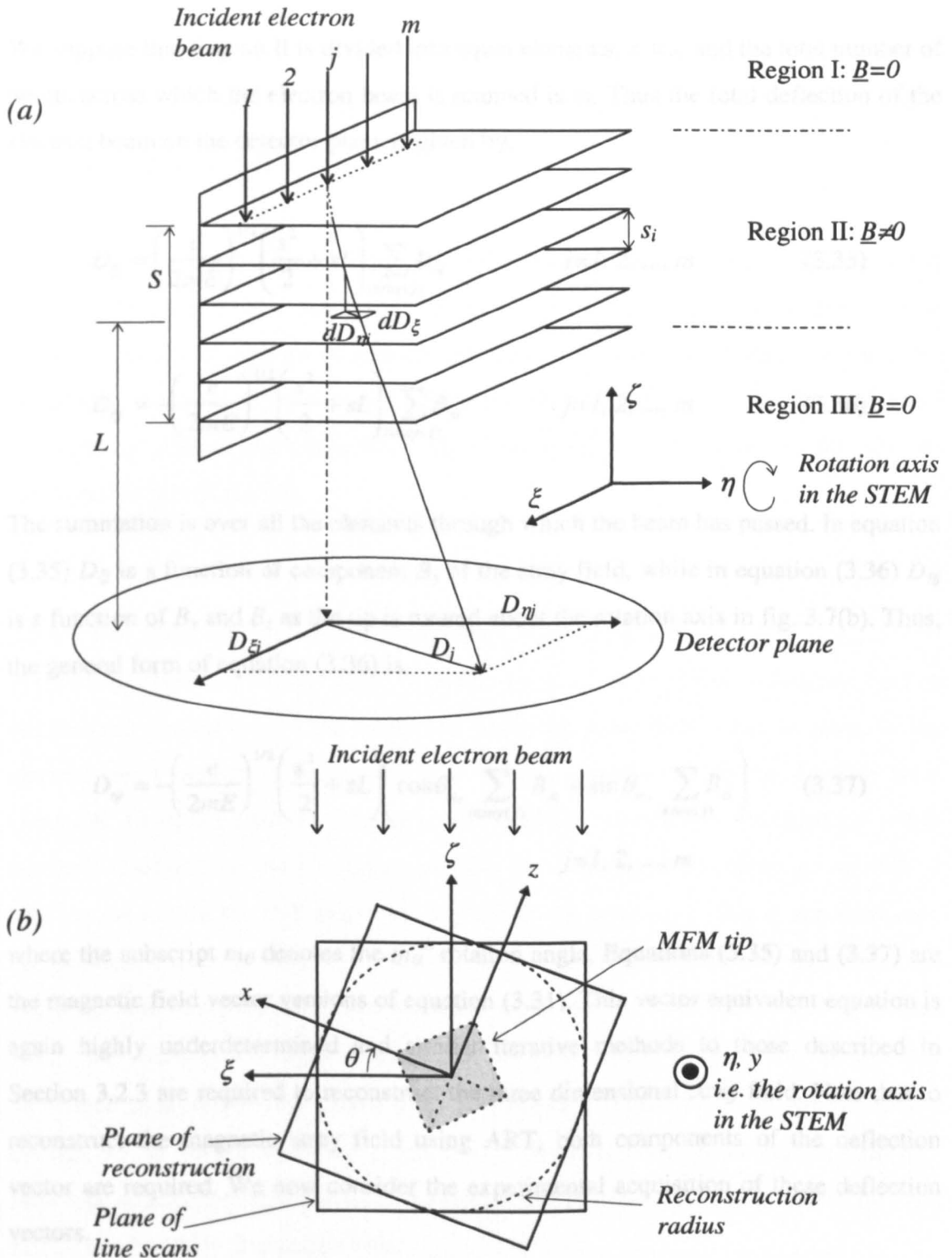


Fig. 3.7: Diagram illustrating the representation of the magnetic stray field in ART. Note that the (ξ, η, ζ) co-ordinate system is fixed and defines the microscope co-ordinates, while the (x, y, z) co-ordinate system is fixed to the MFM tip and defines the specimen co-ordinates.

We suppose that Region II is divided into equal elements, $s_i \equiv s$, and the total number of points across which the electron beam is scanned is m . Thus the total deflection of the electron beam on the detector plane is given by,

$$D_{\xi} = \left(\frac{e}{2mE} \right)^{1/2} \left(\frac{s^2}{2} + sL \right) \sum_{i \in \text{ray}(j)} B_{yi} \quad j=1, 2, \dots, m \quad (3.35)$$

$$D_{\eta} = - \left(\frac{e}{2mE} \right)^{1/2} \left(\frac{s^2}{2} + sL \right) \sum_{i \in \text{ray}(j)} B_{xi} \quad j=1, 2, \dots, m \quad (3.36)$$

The summation is over all the elements through which the beam has passed. In equation (3.35) D_{ξ} is a function of component B_y of the stray field, while in equation (3.36) D_{η} is a function of B_x and B_z as the tip is rotated about the rotation axis in fig. 3.7(b). Thus, the general form of equation (3.36) is,

$$D_{\eta} = - \left(\frac{e}{2mE} \right)^{1/2} \left(\frac{s^2}{2} + sL \right) \left(\cos \theta_{m_{\theta}} \sum_{i \in \text{ray}(j)} B_{xi} + \sin \theta_{m_{\theta}} \sum_{i \in \text{ray}(j)} B_{zi} \right) \quad (3.37)$$

$$j=1, 2, \dots, m$$

where the subscript m_{θ} denotes the m_{θ}^{th} rotation angle. Equations (3.35) and (3.37) are the magnetic field vector versions of equation (3.31). This vector equivalent equation is again highly underdetermined and similar iterative methods to those described in Section 3.2.3 are required to reconstruct the three dimensional stray field. Note that to reconstruct the magnetic stray field using ART, both components of the deflection vector are required. We now consider the experimental acquisition of these deflection vectors.

3.3 Experimental Implementation of Electron Beam Tomography for MFM Tip Fields

To reconstruct the three dimensional stray field from a MFM tip (using either the RTM or ART techniques) we require a complete set of the (digitised) electron beam deflection vector at a series of angular positions. These deflection data are extracted from DPC image pairs of the stray field (imaged in a STEM). The deflection data must be correctly aligned and taken from the same position in front of the tip prior to tomographic reconstruction.

3.3.1 The DPC Image Collection in the CM20 (S)TEM

The DPC Lorentz microscopy mode is performed in a CM20 STEM to measure the two dimensional projections of the integrated MFM tip stray field - i.e. to measure the electron beam deflection vector which is linearly proportional to the tip stray field integrated along the electron trajectory. The MFM tip assembly is mounted on a stub which is inserted into the specimen rod. The tip assembly is mounted on the stub at 77.5° to the axis of the stub and hence at 12.5° to the optic axis - this is approximately the same angle as the cantilever is mounted in the MFM- see fig. 3.8. To reconstruct the MFM tip field using the RTM reconstruction technique we must collect deflection data at 10° intervals over a rotation range of 180° . However since the specimen rod can only be rotated over $\pm 50^\circ$ this means that one change of position of the specimen stub through 90° in the specimen rod is required to determine the full deflection data sets. Note that all experimental deflection data presented in this thesis was provided by Prof. R. P. Ferrier and Dr. Steven McVitie.

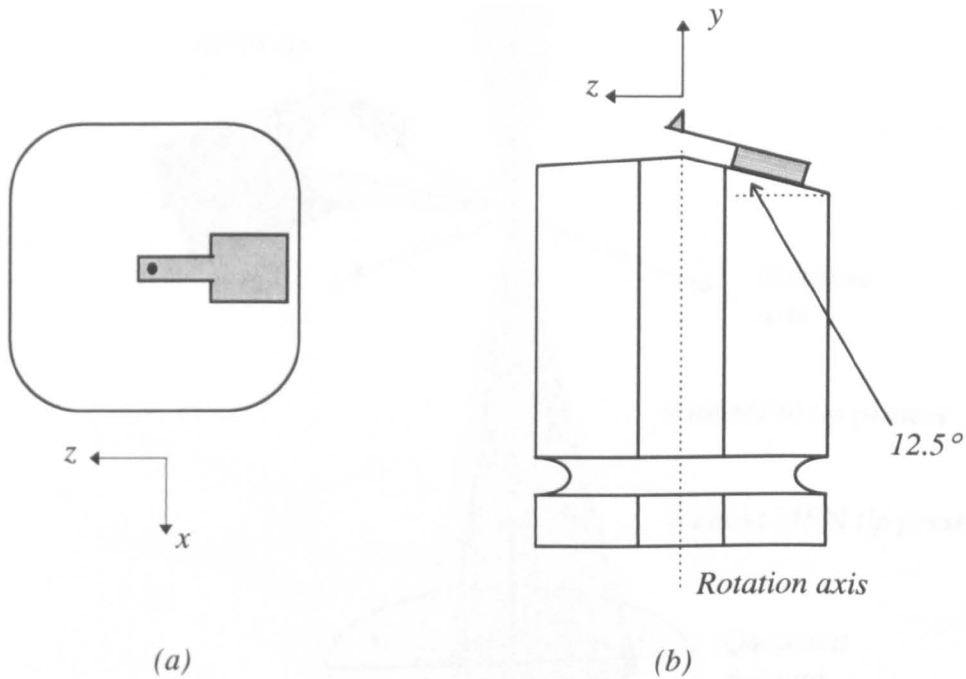


Fig. 3.8: Diagram illustrating the MFM tip mounted on stub for specimen rod in STEM. (a) View from end of specimen stub,
 (b) View from above showing the plane of reconstruction, i.e. the x - z plane.

Fig. 3.9 shows an illustration of the geometry for the electron beam deflected by the stray field from the MFM tip oriented in one angular position. The electron beam scans parallel to the x - z plane at a fixed distance in front of the tip ($y = \text{a constant}$ typically $\sim 50\text{nm}$) - this plane is the same plane on which the MFM tip field is reconstructed. The MFM tip is rotated about the y axis at 10° intervals. The two components of the electron beam deflection vector are acquired by subtracting signals from opposite segments of the DPC detector. The detector orientation relative to the rotation axis and the excitation of the image forming lenses is set so that the signal pairs (A-C) and (B-D) represent the components of the electron beam deflection vector which are perpendicular and parallel to the reconstruction plane (i.e. the x - z plane) respectively.

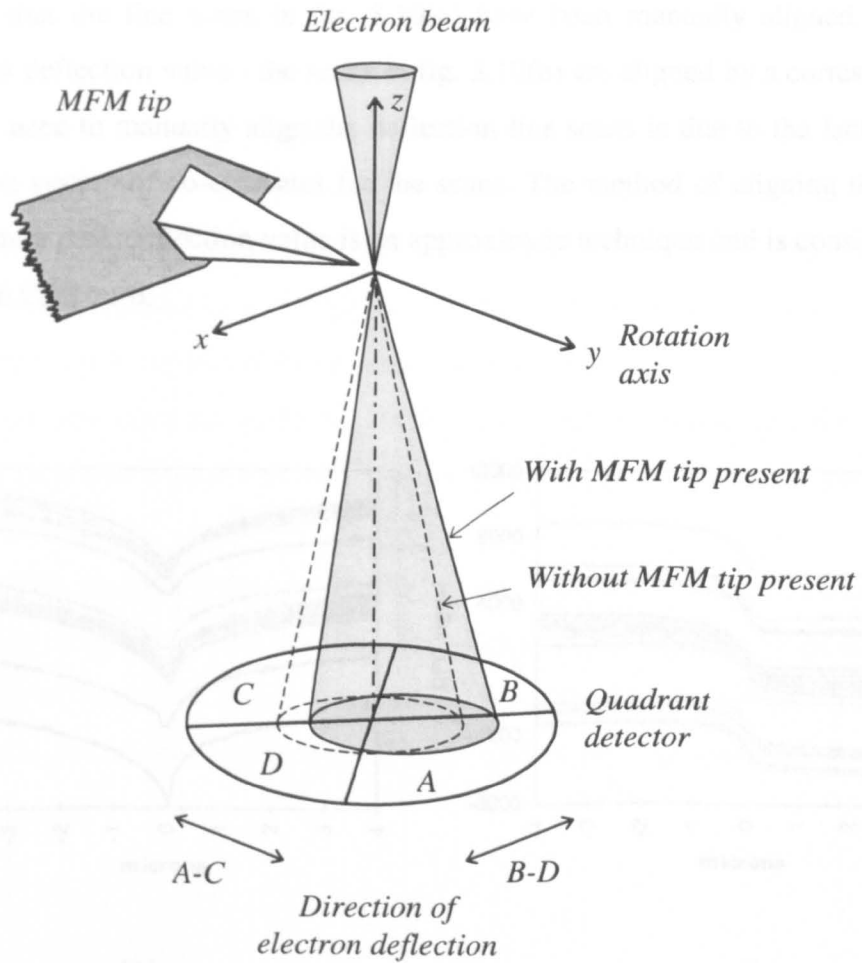


Fig. 3.9: Diagram illustrating the experimental arrangement for the implementation of DPC imaging of an MFM tip.

3.3.2 Extraction of the Input Deflection Data Sets (for tomographic reconstruction using RTM) from the DPC Image Pairs

The input data for tomographic reconstruction of the MFM tip field is a series of electron beam deflection vectors in a plane in front of the tip. A DPC image pair gives a two dimensional map of the two components of the electron beam deflection vector for the MFM tip oriented in one specific angular position. Line scans are therefore extracted from each DPC image pair perpendicular to the rotation axis and at the same distance in front of the tip. The complete set of line scans (over 180° at 10° intervals) defines the plane in which the MFM tip stray field is reconstructed, see fig. 3.10.

Note that the line scans in fig. 3.10(a) have been manually aligned about a common peak deflection value - the scans in fig. 3.10(b) are aligned by a corresponding amount. The need to manually align the deflection line scans is due to the lack of any clear common system of co-ordinates for the scans. The method of aligning the scans about a common peak deflection value is an approximate technique and is considered in more detail in Chapter 6.

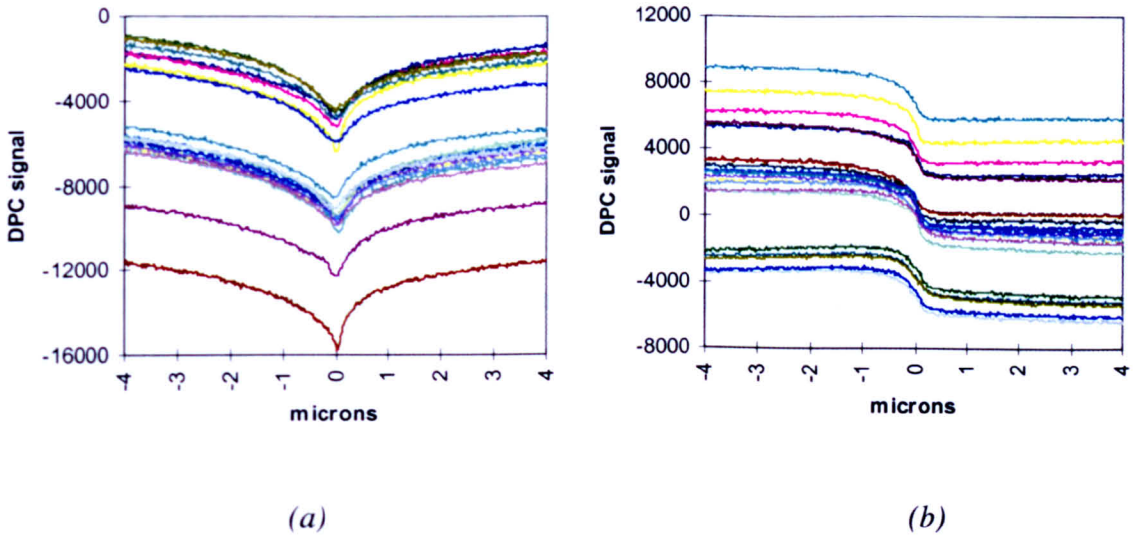


Fig. 3.10: Experimental DPC signal variation for the complete data set from a standard Digital Instruments (DI) MFM tip. (a) Line scans sensitive to induction component normal to the measurement plane. (b) Line scans sensitive to induction component in the measurement plane. These results are for a tip which has been magnetised along its axis.

Also note that the line scans extracted from the DPC images (see fig. 3.10) do not decrease to zero at the ends of the scans. The effect of this character of the deflection line scans on the ART and RTM reconstructed MFM tip field is considered in detail in Section 6.9.

3.4 Summary

The RTM reconstruction technique is based on the Fourier Transform and its relationship to the Radon Transformation. As a result the RTM technique requires input deflection data sets over a rotation range of 180° . In RTM the Radon Transform of the stray field is approximated to a straight line in the measuring plane, thus RTM is a linear technique and is subject to error when the stray field is strong - however this is not an issue for the study of MFM tip fields. The RTM reconstruction algorithm is derived for a magnetic source free half space and any reconstruction must satisfy this condition.

The ART reconstruction technique is an algebraic method. There is no limitation to the magnetic source, provided the reconstruction region is large enough to contain the full extent of its source stray field. Note that ART can provide reasonable details of the object of measurement from input deflection data sets over less than a 180° rotation range.

References

- [1] DeRosier D and Klug A, (1968), *Nature (London)*, 217, pp 130-134
- [2] Crowther R A, DeRosier D and Klug A, (1970), *Proc. R. Soc. London A*, 317, pp 319-340
- [3] Gilbert P, (1972), *Proc. R. Soc. London B*, 182, pp 89-102
- [4] Elsbrock J B. et al., (1985), *IEEE Trans. Mag.*, 21, 5, pp 1593-1595
- [5] Steck M. et al., (1990), *IEEE Trans. Mag.*, 26, 5, pp 1343-1345
- [6] Radon J, (1917), *Math. phys. Klasse*, 69, pp 262-277
- [7] Matsuda J, (1990), *IEEE Trans. Mag.*, 26, 5, pp 2061-2063
- [8] Gordon R, (1970), *J. Theor. Biol.*, 29, pp 471-481
- [9] Crowther R A, et. Al., (1970), *Nature (London)*, 226, pp 421-425
- [10] Bracewell R N and Riddle A C, (1967), *Astrophys. J.*, 150, pp 427-434

[11] Jiles D, (1991), *Introduction to Magnetism and Magnetic Materials*, Chapman & Hall

[12] Ludwig D, (1966), *Communications on pure and applied mathematics*, Vol. **XIX**, pp 49-81

Chapter 4

Theoretical Investigation of the Character of MFM Tip Stray Fields and Integrated Stray Fields

4.1 Introduction

The subject of magnetic force microscopy and the necessity to characterise the microscope's tip field have been discussed in Chapter 2. It is the purpose of this chapter to investigate - by means of computer simulation - the character of the MFM tip field and the effect on the tip field of varying certain physical parameters. The results from modelling an idealised tip uniformly magnetised in a direction pointing towards the apex of the tip are discussed.

We begin in Section 4.2 by describing the construction of a MFM tip model and the calculation of the stray field and the line scan deflection data from the model. In Section 4.3 a selection of tips of various shapes are constructed and an investigation of the effect of the tip shape on the character of the tip stray field and the line scan deflection data is undertaken. The benefits of constructing these tip models instead of using a point monopole or a point dipole approximation to the MFM tip field are also discussed. In section 4.4 the effect on the tip field and the deflection data sets of varying the parts of the tip coated with thin film is considered. In section 4.5 the effect on the tip's field and its deflection data sets of varying the thickness of the film coating the tip is investigated. Finally a summary of the results from this chapter is presented in Section 4.6.

4.2 Calculation of Simulated Deflection Data Sets

4.2.1 Calculation of the Stray Field from a Uniformly Magnetised Block

Consider a uniformly magnetised block as in fig. 4.1, with dimensions $2L_1$ by $2L_2$ by $2L_3$. The magnetic scalar potential, Φ , of such a block is given by Rhodes and Rowlands⁽¹⁾ as,

$$\Phi(x, y, z) = \frac{1}{4\pi} \int_{\text{surface}} \frac{\underline{M} \cdot \underline{n}}{|\underline{R}|} ds \quad (4.1)$$

where $\underline{M} = (0, M_s, 0)$ with M_s the saturation magnetisation of the block and \underline{n} the outward pointing unit normal vector to each face of the block. It is assumed that $\nabla \cdot \underline{M} = 0$ in the calculations. Note that the integration is over the entire surface of the block, although in this case $\underline{M} \cdot \underline{n} \neq 0$ only for the top and bottom surfaces of the block which can be considered as sheets of positive and negative surface charge of density $\underline{M} \cdot \underline{n}$. Equation (4.1) may now be written,

$$\begin{aligned} \Phi(x, y, z) = & \frac{M_s}{4\pi} \int_{-L_1}^{L_1} \int_{-L_2}^{L_2} \frac{dx' dz'}{\left[(x-x')^2 + (y-L_2)^2 + (z-z')^2 \right]^{\frac{1}{2}}} \\ & - \frac{M_s}{4\pi} \int_{-L_1}^{L_1} \int_{-L_2}^{L_2} \frac{dx' dz'}{\left[(x-x')^2 + (y+L_2)^2 + (z-z')^2 \right]^{\frac{1}{2}}} \end{aligned} \quad (4.2)$$

The magnetic field strength \underline{H} , can now be calculated simply by,

$$\underline{H}(x, y, z) = -\nabla\Phi(x, y, z) \quad (4.3)$$

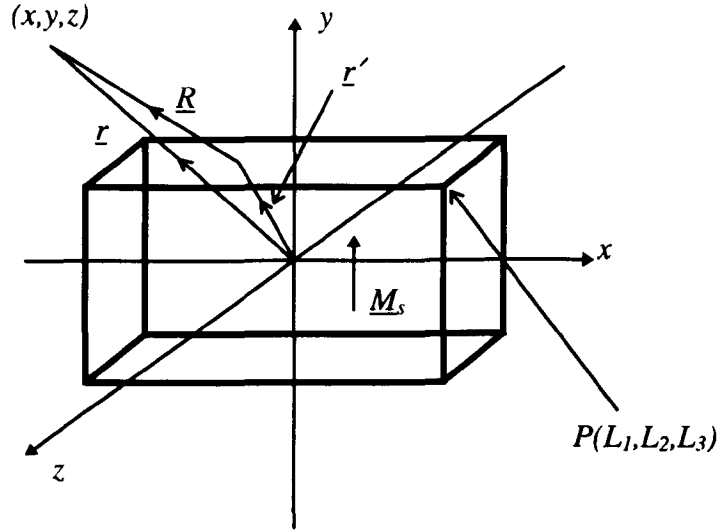


Fig.4.1: Coordinate system used for calculating the magnetic field intensity at point (x,y,z) from a uniformly magnetised block of dimensions $2L_1$ by $2L_2$ by $2L_3$. Note that \underline{r}' is the vector from the origin to the surface of the block and \underline{R} is the vector from the surface of the block to the point (x,y,z) .

the components of \underline{H} being,

$$H_x = -\frac{\partial\Phi(x,y,z)}{\partial x}, H_y = -\frac{\partial\Phi(x,y,z)}{\partial y}, H_z = -\frac{\partial\Phi(x,y,z)}{\partial z} \quad (4.4)$$

The integral in equation (4.2) is carried out over dx' and dz' which are independent of the differentiation which is performed over (x,y,z) , therefore the differential can be taken inside the integral. The resulting calculations for the magnetic field strength \underline{H} , are listed in Appendix 1.

For construction of a suitable tip model the magnetised block is not used directly, rather sheets of magnetic charge are combined together in an attempt to mimic the magnetic material attached to the tip.

4.2.2 Calculation of the Stray Field from a Sheet of Magnetic Charge Density M_s

Consider a sheet of magnetic charge of density M_s , as in fig. 4.2, with dimensions L_1 by L_3 . If we take the y -direction as the outward pointing normal, and $\underline{M}=(0,M_s,0)$, then equation (4.1) becomes,

$$\Phi(x, y, z) = \frac{M_s}{4\pi} \int_0^{L_1} \int_0^{L_3} \frac{dx' dz'}{[(x-x')^2 + y^2 + (z-z')^2]^{\frac{3}{2}}} \quad (4.5)$$

The magnetic field strength \underline{H} , can be calculated using the same method as described in the previous section. The resulting calculations for the magnetic field strength generated by a sheet of magnetic charge density M_s are similar to those listed in the appendix.

Clearly a sheet of positive magnetic charge density, as considered here, is not physically realistic. However a combination of these charge sheets can be used to calculate magnetic fields from physical objects, such as the magnetised block in the previous section. It is my intention to use this charge sheet as the building block of all models constructed. An example of calculation of the stray field from a triangular thin film is given in the next section.

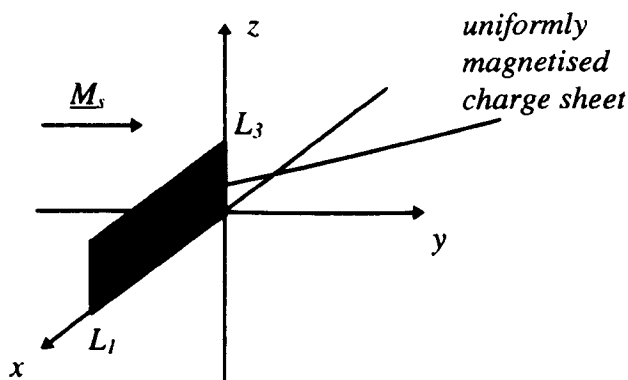


Fig.4.2: Coordinate system used for calculating magnetic field intensity in free space from a uniformly magnetised charge sheet of density M_s .

4.2.3 Calculation of stray field from a triangular thin film

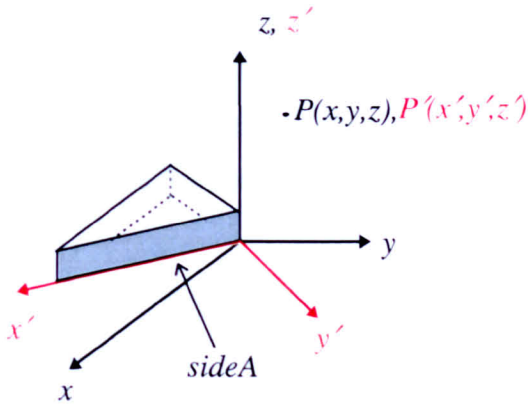
Consider a uniformly magnetised triangular shaped thin film constructed from three rectangular sheets of magnetic charge density as in fig. 4.3(a). To calculate the magnetic field strength \underline{H} , at some point P outside the volume of the thin film, requires the problem to be reduced into three manageable parts. Thus the stray field \underline{H} at point P due to each charge sheet which make up the edges of the thin film must be calculated individually and summed together to get the total field at P due to the entire thin film.

Firstly \underline{H} is calculated at point P due to side A of the thin film. To do this it is required to use a simple rotational transformation of the axes so that point P is considered relative to the primed axes of fig. 4.3(a). Once this is achieved, the stray field at point P due to charge sheet A can be calculated relative to the primed axes using the method described in section 4.2.2. Once the three components of \underline{H} have been calculated relative to the primed axes they must be transformed back relative to the original set of axes. The stray magnetic field from side A at point P relative to the (x,y,z) axes of fig. 4.3(a) has now been calculated.

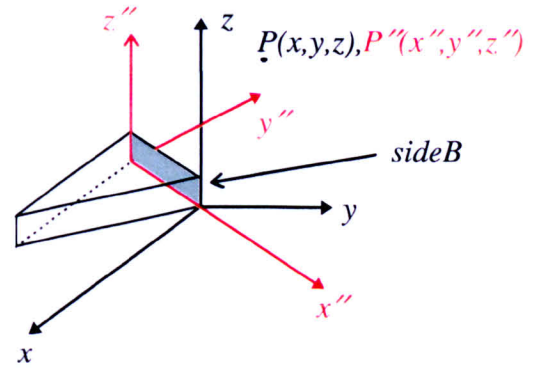
The calculations of the fields at P due to sides B and C are similar to the above description. For each side a combination of translation and rotational transformations of the axes are used to manoeuvre the axes into the correct positions to calculate the stray field \underline{H} , using the method described in section 4.2.1. Once \underline{H} has been calculated relative to the double primed axes of fig. 4.3(b) for side B, and the triple primed axes of fig. 4.3(c) for side C, the three components of \underline{H} in each case must be inverse transformed back relative to the original (x,y,z) axes of fig. 4.3(a). The three individual field contributions due to sides A, B and C at point P are then summed together to get the final field \underline{H} at point P relative to the (x,y,z) axes due to the entire triangular thin film.

The extension of this method from calculating the stray field from a triangular thin film of magnetic material to calculating the stray field from a thin film of magnetic material of arbitrary shape, is simple. The only proviso on the shape of the thin film, is that it is geometrically made up of flat surfaces or else its shape may be approximated to a combination of flat surfaces. In the following parts of this

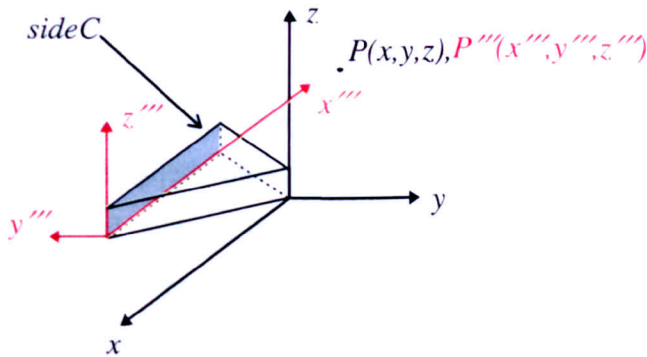
chapter and the next, this method is used to combine many different sized charged planes together in an attempt to model the stray magnetic field from the magnetic thin film material attached to the tip/cantilever/substrate structure.



(a) Coordinate system used for calculating field contribution from SideA.



(b) Coordinate system used for calculating field contribution from SideB.



(c) Coordinate system used for calculating field contributions from SideC.

Fig.4.3: Coordinate systems used for calculating magnetic field intensity in free space from a uniformly magnetised triangular shaped thin film. Sides A, B and C are shaded as indicated. The magnetisation of the film is directed along the positive y direction.

4.2.4 Calculation of the Deflection Values from a Triangular Thin Film

Consider again the triangular shaped thin film from the previous section. The method for calculating the stray field from such a thin film has been described. In this section, the method for calculating the deflection of an electron beam at the detector plane in a STEM, due to the passage of the beam through a region of space occupied by the stray field from the thin film is described.

The stray field from the film gives rise to a Lorentz force on the electron beam which is deflected from its original path. The deflection vector, d , of the electron beam from its incident path at the detector plane is given by,

$$d = \text{camera length} \times \beta_L \quad (4.6)$$

where the camera length is the effective distance between the specimen and the detector plane and the Lorentz deflection angle, β_L , is given as,

$$\beta_L = \frac{e\lambda}{h} \int B dz \quad (4.7)$$

(similar to equation 2.2) where the integral is over all z , and B represents the component of the magnetic induction normal to the electron beam trajectory.

In practical calculations of β_L , the integral in equation (4.7) was approximated to a discrete summation. Hence equation (4.7) becomes,

$$\beta_L = \frac{e\lambda}{h} \sum B \Delta z \quad (4.8)$$

Thus as $\Delta z \rightarrow 0$ the summation in equation (4.8) tends to the integral in equation (4.7). Therefore, provided the interval Δz is taken to be so small that the magnetic induction does not vary greatly over that distance then this approximation is acceptable.

It has now been detailed how to calculate the stray magnetic field strength H , from a uniformly magnetised thin film of arbitrary shape. From this it was then

described how to calculate the deflection of an electron beam from its original path due to the interaction of the electron beam with the stray field from such a film. Therefore it is now possible to simulate DPC images of the stray fields from thin films. In the following sections of this chapter, models of tips are constructed using combinations of triangular shaped thin films. The stray fields and the deflection data sets generated by the tip models are then calculated using the methods described above.

4.3 Tip Shape and its Effect on Stray Fields/Integrated Stray Fields

First we consider a perfectly smooth cone shaped tip coated with a thin film which is uniformly magnetised along the tip axis. The line scans within a deflection data set generated from such a tip mounted in a STEM and rotated about its own axis (perpendicular to the optic axis of the STEM), would be expected to be identical due to the rotational symmetry of the tip's geometry and magnetic configuration. Now consider fig. 4.4 which are SEM images of a typical Digital Instruments (DI) thin film coated MFM tip. The images appear to show the tip to be three sided at its apex, while further down it is at least four sided. It would therefore be expected that for this real MFM tip mounted in a STEM and rotated about its own axis (again perpendicular to the optic axis of the STEM), the line scans in the deflection data sets generated would not be identical due to the asymmetric nature of the tip's geometry.

Therefore it is expected that the tip shape will affect the distribution of the tip stray field and therefore the line scans within its deflection data sets. To what extent the tip shape affects the shape of the line scans within the deflection data sets is unclear. In the following sections a selection of model tips are considered in an attempt to understand the degree to which the tip shape affects the character of the stray field and integrated field.

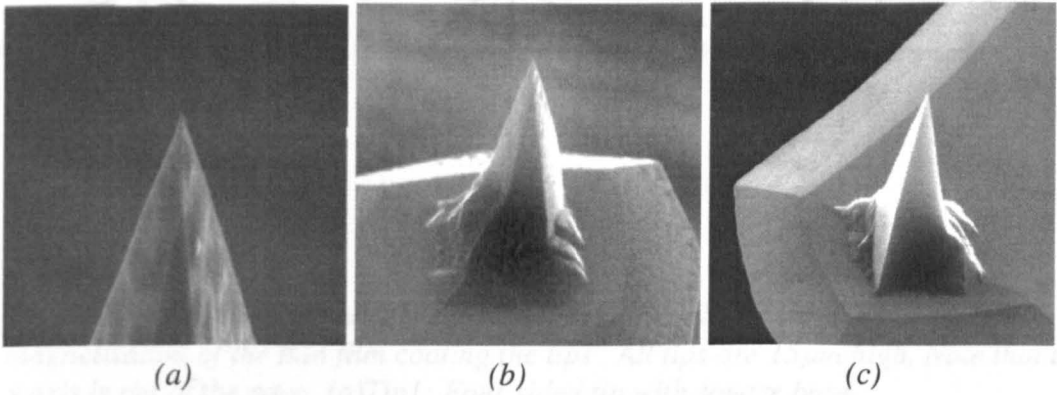


Fig. 4.4: SEM images of a typical DI MFM tip. The images show the irregular shape of the tip. In (a) the image shows the tip to be three sided at the apex and four sided further down. Notice in (b) three sides are visible, while in (c) only two sides are visible.

4.3.1 Stray Field and Integrated Stray Field from Model Tip1

The shape of each tip considered is shown in projection in fig. 4.5, and each tip is taken to be $15\mu\text{m}$ high. Tip1 is a four sided pyramid with a thin film on each face apart from its square base. Each thin film is a triangular prism of magnetic material uniformly magnetised in the plane of the film and in a direction pointing towards the apex of the tip (see Section 4.2.3). The stray field from each of the four separate thin films is calculated using a similar method to that described in the previous section (section 4.2). Tip2 is a three sided pyramid with a right angled triangular base, while Tip3 is a four sided pyramid with a kite shaped base. In both cases each face apart from the bases of the tips are coated in triangular prism shaped thin films of magnetic material uniformly magnetised in a direction pointing towards the apex of the tips.

The thin film material coating each tip model was taken to be a 40nm thick CoCr alloy with a known saturation induction of 0.5T .

Using this definition, it is found that the scans in fig. 4.7(c) have an asymmetry index of zero. In other words each scan is symmetric about the position of its peak field value. The reason for the symmetric nature of the scans is that the tip

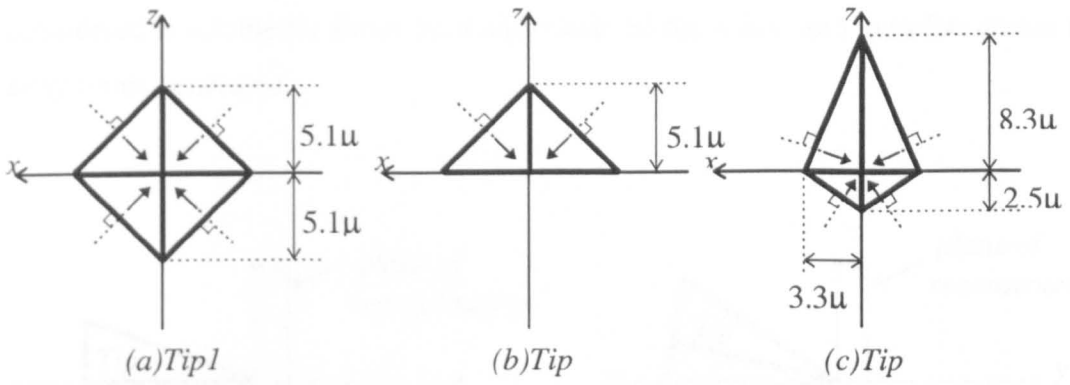


Fig.4.5: Diagram of tip models 1,2 and 3. Arrows indicate the direction of magnetisation of the thin film coating the tips . All tips are $15\mu\text{m}$ high. Note that the y axis is out of the page. (a)Tip1: Four sided tip with square base.
 (b)Tip2: Three sided tip with right angled triangular base.
 (c)Tip3: Four sided tip with a kite shaped base.

4.3.1 Stray Field and Integrated Stray Field from Model Tip1

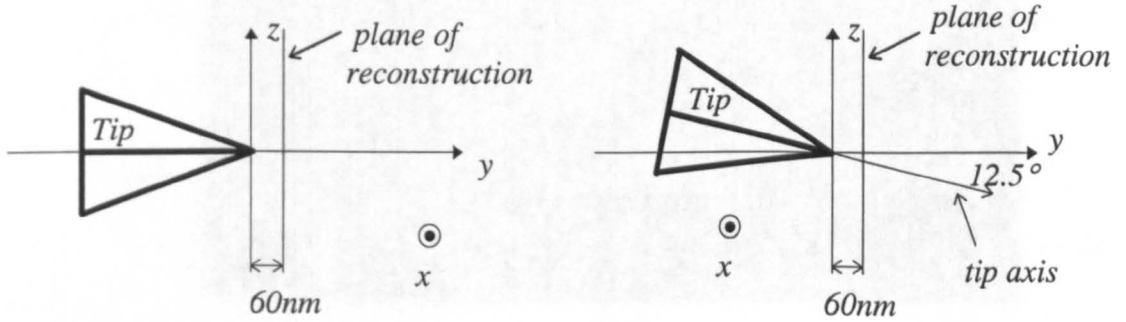
4.3.1.1 Stray Field Calculated Directly from Model Tip1

For model Tip1 oriented such that its axis was parallel to the reconstruction plane normal - see fig. 4.6(a) - the three dimensional stray field was calculated at the reconstruction plane using the method described in section 4.2.3. Fig. 4.7(a) shows grey scale images of the stray field components calculated directly from the model.

Line scans were taken horizontally and vertically (i.e. the x and z directions of fig. 4.6(a)) across the peak value of the component of field normal to the plane of reconstruction (y component) and are shown in fig. 4.7(c). For field scans such as these, the definition of the asymmetry of a scan is taken as the distance between the position of the peak field value and the centre of the FWHM as a fraction of the FWHM of the scan. The half maximum value is defined as the mid-point of the maximum and minimum values of scan, while the centre of the FWHM is taken as the midpoint between the positions of the half maximum values of the scan. In the following this fraction will be referred to as the asymmetry index of the scan.

Using this definition, it is found that the scans in fig. 4.7(c) have an asymmetry index of zero. In other words each scan is symmetric about the position of its peak field value. The reason for the symmetric nature of the scans is that the tip

considered is symmetric about the x and z axes of fig. 4.6(a) and therefore so are the stray fields generated.



(a) Tip1 oriented so that its axis is parallel with the reconstruction plane normal.

(b) Tip1 oriented so that its axis is at 12.5° to the reconstruction plane normal.

Fig. 4.6: Orientation of model Tip1 with respect to the reconstruction plane.

Now, a practical MFM tip is mounted in the MFM such that its axis is at approximately 12.5° to the normal of the sample surface. It is therefore the stray field at a plane, just in front of the tip, whose normal is at 12.5° to the tip axis that is of interest. Thus, for model Tip1 oriented such that its axis was at 12.5° to the reconstruction plane normal - see fig. 4.6(b) - the three dimensional stray field was calculated (directly from the model) at the reconstruction plane and is shown in fig. 4.7(b).

Note that the general form of each of the calculated field components in fig. 4.7(b) is similar to the corresponding component in fig. 4.7(a). Once again horizontal and vertical field scans (i.e. scans across the x and z directions of fig. 4.6(b)) were taken across the peak value of the component of field normal to the plane of reconstruction (y component) and are shown in fig. 4.7(d).

Using the definition given above for the asymmetry index of a field scan, it is found that the horizontal field scan in fig. 4.7(d) has an asymmetry index of zero (indicating that the scan is symmetric about the position of its peak field value). This

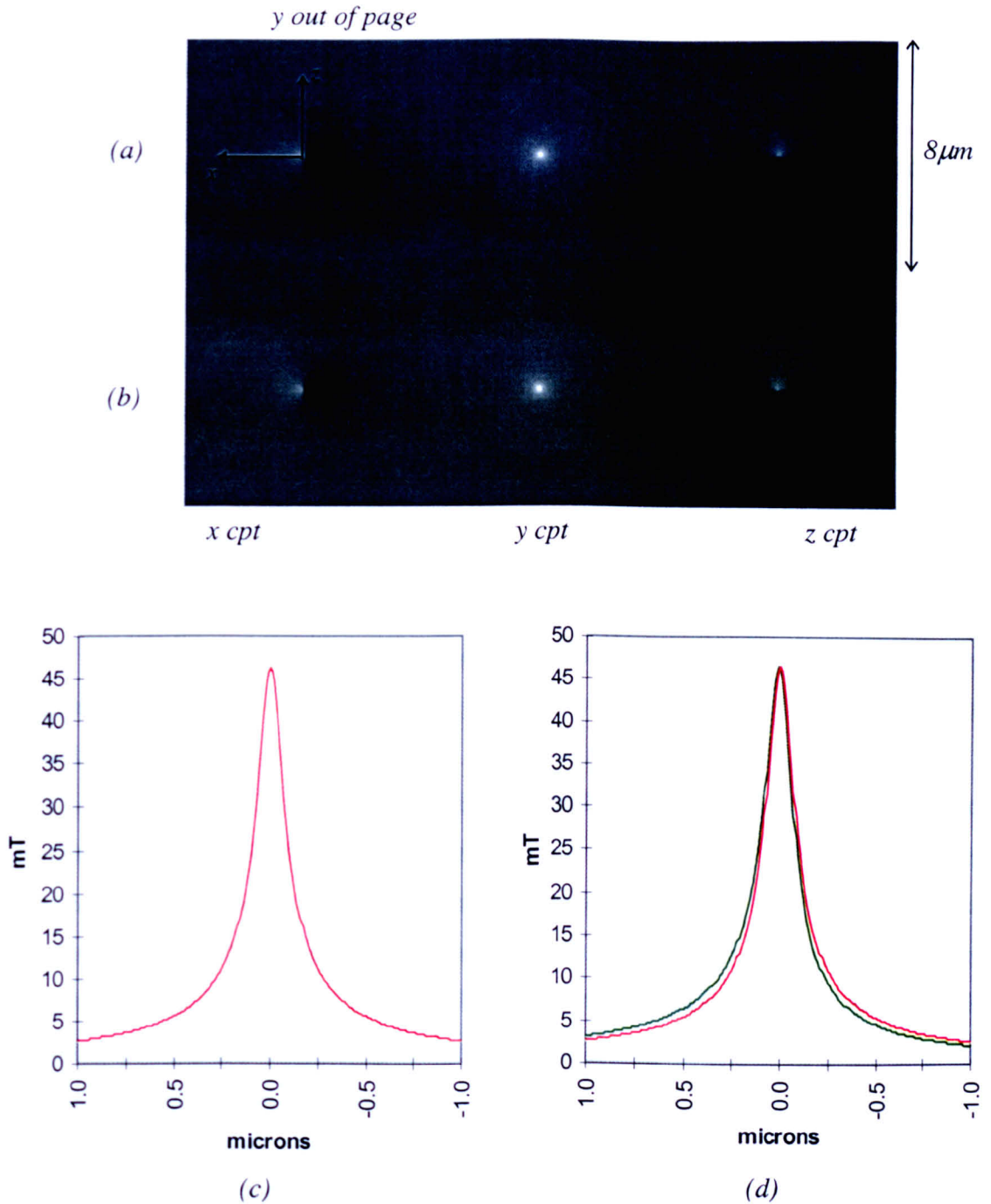


Fig. 4.7: Grey scale images of the three dimensional stray field calculated from model Tip1 oriented as in fig. 4.6(a) and (b) and field scans taken across the component of field normal to the plane of calculation.

(a) Stray field calculated from Tip1 oriented as in fig. 4.6(a).

(b) Stray field calculated from Tip1 oriented as in fig. 4.6(b).

(c) Horizontal and vertical (i.e. the x and z directions of fig. 4.6(a)) scans taken across y component of field in (a). Note that the scans are identical- thus the appearance of only one scan.

(d) Horizontal and vertical (i.e. the x and z directions of fig. 4.6(b)) scans taken across y component of field in (b).

Note that in (c) and (d) the red scans are taken horizontally (x direction) across the y component, while the green scans are taken vertically (z direction) across the y component.

is expected since the model tip is symmetric about the z axis of fig. 4.6(b) and therefore so is its stray field.

The vertical field scan in fig. 4.7(d) is found to be non symmetric about its peak field position; it has a non zero asymmetry index of 0.027. This result is also expected since the tip model oriented as in fig. 4.6(b) is not symmetric about the x axis and therefore its stray field is not expected to be symmetric either. Note that an asymmetry index of 0.027 is a small fraction of the FWHM of the scan. In fact the calculated distance between the peak field position and the centre of the FWHM of the scan is found to be 6nm. This distance is well below the resolution available from the CM20 STEM (at the University of Glasgow) operated in low mag scanning DPC imaging mode (which is of the order of 20-30nm) and in this context can be considered to be insignificant in a practical experiment.

It is therefore concluded that the symmetric nature of the stray fields (at the reconstruction plane) calculated directly from model Tip1 oriented as in figs. 4.6(a) and (b) are effectively identical.

Note that the FWHM of the horizontal field scans in figs. 4.7(c) and (d) differ by 2nm, while the FWHM of the vertical field scans in figs. 4.7(c) and (d) are identical. Furthermore, the peak value of the component of field normal to the plane (y component) is 46mT for the tip oriented as in fig. 4.6(a), and 47mT for the tip oriented as in fig. 4.6(b). These differences in the magnitude and the spatial definition of the calculated stray fields are small (being less than 2%) and may be considered insignificant in a practical experiment.

We therefore conclude that the stray field at the reconstruction plane generated by Tip1 oriented as in fig. 4.6(a) and that generated by Tip1 oriented as in fig. 4.6(b) are effectively identical since the spatial definition, the peak field values and the asymmetric nature of the stray fields differ by only a small percentage (less than 2% in each case). The suggestion is that mounting the tip on the MFM at 12.5° to the normal of the sample surface will have little effect on the character of the tip stray field at the reconstruction plane, and therefore will have little effect on the tip-sample interaction.

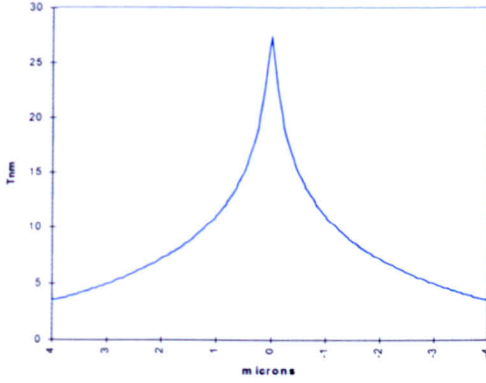
4.3.1.2 Integrated Stray Field Calculated from Model Tip1

Now consider the simulated integrated field line scan data sets generated by Tip1. Figs. 4.8(a) and (b) show the data sets generated by Tip1 rotated about an axis parallel with its own axis (i.e. the tip rotated about the y axis of fig. 4.6(a)). Figs. 4.8(c) and (d) show the data sets generated by Tip1 rotated about an axis at 12.5° to its own axis (i.e. the tip rotated about the y axis of fig. 4.6(b)).

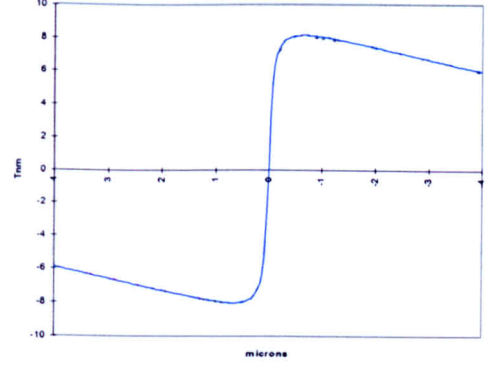
Note that although figs. 4.8(a) and (b) appear to show only one line scan for each set, there are in fact 36 scans in each set. It is found that the FWHM of the scans in fig. 4.8(a) vary in value by up to 2nm (this is due to the fact that the tip model is not fully rotationally symmetric about the rotation axis and therefore the integrated field line scans generated by the model are not identical). This variation in FWHM (of 2nm) is not large enough to be visible in the scans of 10nm resolution.

For the integrated field line scans such as in figs. 4.8(a) and (c), the definition of the asymmetry of a scan is equivalent to that for a field scan given earlier. That is, the asymmetry is defined as the distance between the peak integrated field value and the centre of the FWHM of the scan divided by the value of the FWHM of the scan. This fraction is again referred to as the asymmetry index of the integrated field scans.

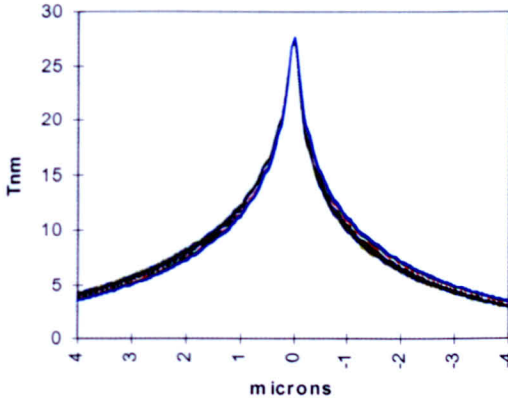
Fig. 4.8(e) plots the asymmetry index of each scan in the data sets of figs. 4.8(a) and (c). Note that for the tip rotated about its own axis (i.e. the y axis of fig. 4.6(a)) the integrated field line scans generated have an approximate asymmetry index of zero. However for the tip rotated about an axis at 12.5° to its own axis (i.e. the y axis of fig. 4.6(b)) the integrated field line scans generated have a significant non zero asymmetry index. The maximum value of the asymmetry index for the scans in fig. 4.8(c) is 0.106 which corresponds to a distance between the positions of the peak integrated field value and the centre of the FWHM of just over 10% of the value of the FWHM of the scan. The minimum value of the asymmetry index for the scans in fig. 4.8(c) is zero. The angular positions of the tip for generation of the line scans of maximum and minimum asymmetry index are separated by 90° about the rotation axis. Note that for the scans in fig. 4.8(c) the calculated distance between the position of the peak integrated field and the centre of the FWHM is 0nm at its



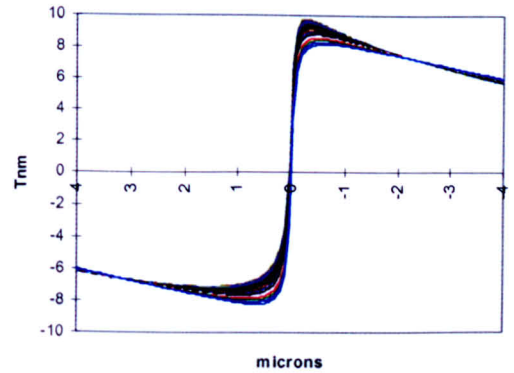
(a) Integrated field line scans sensitive to induction normal to the plane of reconstruction (i.e. along the y direction of fig. 4.6(a)) generated by Tip1 oriented as in fig. 4.6(a).



(b) Integrated field line scans sensitive to induction in the plane of reconstruction (i.e. along the x direction of fig. 4.6(a)) generated by Tip1 oriented as in fig. 4.6(a).



(c) Integrated field line scans sensitive to induction normal to the plane of reconstruction (i.e. along the y direction of fig. 4.6(b)) generated by Tip1 oriented as in fig. 4.6(b).



(d) Integrated field line scans sensitive to induction in the plane of reconstruction (i.e. along the x direction of fig. 4.6(b)) generated by Tip1 oriented as in fig. 4.6(b).

(e) Plot of the asymmetry index of the scans in (a) and (c). Note that the green points represent the asymmetric indices of scans in (a), while the red points represent the asymmetric indices of the scans in (c).

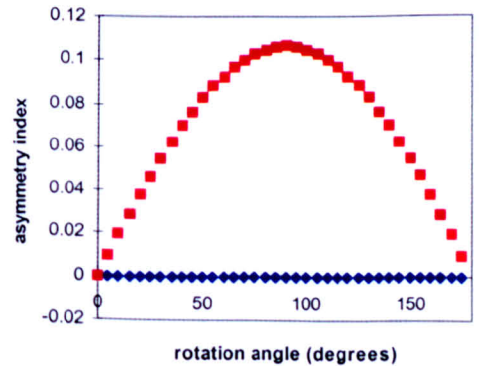


Fig. 4.8: Integrated field line scans generated by **Tip1** rotated about the y axes of fig. 4.6(a) and (b).

minimum, and 138nm at its maximum (which corresponds to 5 or 6 pixels on a real deflection line scan).

Therefore, the simulated integrated field line scans generated by Tip1 oriented as in fig. 4.6(a) and rotated about the y axis are not identical to the integrated line scans generated from the same tip model, oriented as in fig. 4.6(b) and rotated about that y axis. The difference between the asymmetric nature of the scans in each case although small would be measurable in a real experiment.

4.3.1.3 Comparison of the Calculated and Reconstructed Stray Fields from Tip1

The stray fields calculated at the reconstruction plane from model Tip1 oriented as in figs. 4.6(a) and (b) are found to be effectively identical. The corresponding integrated fields however, have been found to be clearly distinguishable from one another. Therefore, in order to determine whether the character of the stray field reconstructed from the simulated integrated field line scans (using the RTM reconstruction technique) is consistent with the field calculated directly from the tip model, a comparison of the reconstructed and calculated fields is now carried out.

The three dimensional stray field was reconstructed from each of the simulated rotation data sets in figs. 4.8(c) and (d) using the RTM tomographic reconstruction method (see section 3.4) and the average is shown in fig. 4.9(a). Fig. 4.9(b) shows the corresponding three dimensional stray field calculated directly from the tip model at the reconstruction plane. The field components in fig. 4.9(b) are the same as those shown earlier in fig. 4.7(b).

Once again horizontal and vertical field scans were taken across the component of field normal to the reconstruction/calculation plane and are shown in figs. 4.9(c) and (d). From the fact that it is difficult to separate the scans in both figs. 4.9(c) and (d) indicates that there is an excellent agreement between the normal field components calculated directly from the model and reconstructed from the simulated rotation data sets. Indeed, it is also found that the in-plane components of the calculated and reconstructed fields compare favourably. Note that this agreement is also found between the stray fields calculated directly from Tip1 oriented as in fig. 4.6(a) and the stray field reconstructed from the line scans obtained from Tip1 rotated about the y axis of fig. 4.6(a) (i.e. the line scans shown in fig. 4.8(a) and (b)).

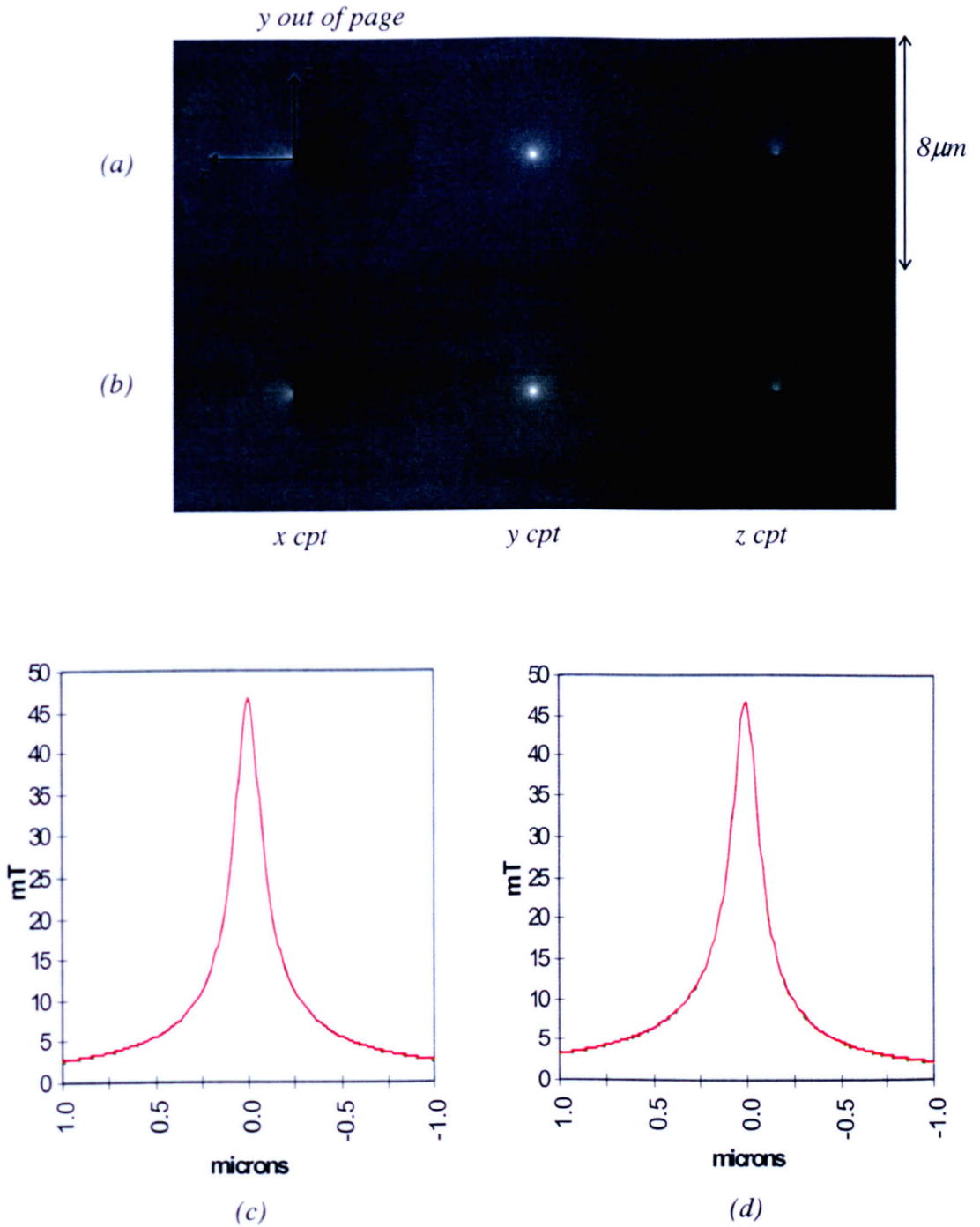


Fig. 4.9: Reconstructed and calculated fields from Tip1 oriented as in fig. 4.6(b) and scans taken across the component of field normal to the plane of reconstruction/calculation.

(a) Stray field reconstructed from integrated field line scans shown in fig. 4.8(c) and (d).

(b) Corresponding stray field calculated directly from model Tip1 oriented as in fig. 4.6(b).

(c) Horizontal scans taken across y component of field in (a) and (b).

(d) Vertical scans taken across y component of field in (a) and (b).

Note that in (c) and (d) the red scans are taken across the reconstructed field, while the green scans are taken across the calculated field. Further note that in (c) and (d) the red and green scans are almost identical.

We therefore conclude that the stray field calculated directly from the tip model is in excellent agreement with the field reconstructed (using RTM) from the simulated rotation data sets generated by the model. It follows (from Sections 4.3.1.1 and 4.3.1.2) that although the integrated stray fields generated by model Tip1 oriented as in figs. 4.6(a) and (b) are clearly distinguishable, we can still expect the stray field reconstructed from these simulated rotation data sets (i.e. in fig. 4.8) to be effectively identical. We now consider the stray fields and integrated stray fields generated by Tips2 and 3. In each case the tip models are assumed to be oriented such that the tip axes are at 12.5° to the reconstruction plane normal (similar to Tip1 oriented as in fig. 4.6(b)).

4.3.2 Stray Field and Integrated Stray Field from Model Tip2

4.3.2.1 Stray Field Calculated Directly from Model Tip2

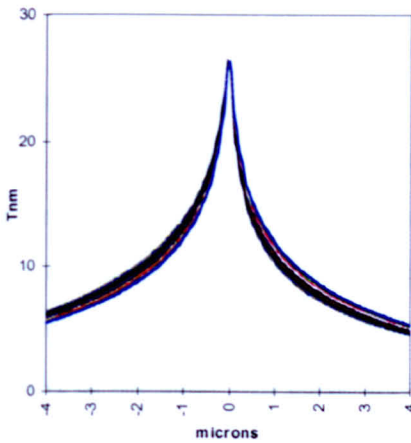
The three dimensional stray field was calculated directly from model Tip2 at the reconstruction plane and is shown in fig. 4.10(a). Once again horizontal and vertical field scans were taken across the peak value of the component of field normal to the plane of reconstruction (y component) and are shown in fig. 4.10(b). The horizontal field scan was again found to have an asymmetry index of zero, indicating that the stray field is symmetric about the position of its peak value. The asymmetry index of the vertical field scan is non zero - equalling 0.060 - corresponding to a calculated distance between the position of the peak field and the centre of the FWHM of 12nm (this distance is again below the resolution typically available from the STEM operated in DPC imaging mode). The implication is that the asymmetric character of the stray field from model Tip2 would not be resolvable when reconstructed (using RTM) from deflection line scans of 20-30nm resolution (imaged in a CM20 STEM operated in low mag scanning DPC imaging mode).

Thus the conclusion is that the asymmetric nature of the stray field generated by Tip2 would not be measurably different to the asymmetric nature of the stray field generated by Tip1 despite the fact that the magnetisation distributions are different for each tip.

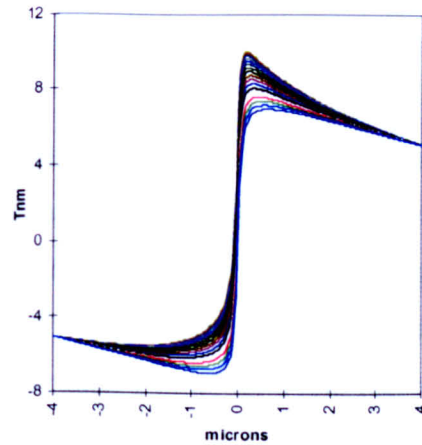
4.3.2.2 Integrated Stray Field Calculated from Model Tip2

Figs. 4.11(a) and (b) show the integrated field line scan rotation data sets generated by model Tip2. Fig. 4.11(c) plots the asymmetry index of each scan in fig. 4.11(a). The maximum value of the asymmetry index is found to be 0.162 which corresponds to a distance of 267nm between the position of the peak integrated field and the position of the centre of the FWHM of the scan. This distance is approximately equivalent to 9 or 10 pixels on a real deflection line scan. The minimum value of the asymmetry index is zero. The angular positions of the tip for the generation of line scans of maximum and minimum asymmetry index are again separated by 90° about the rotation axis.

Thus, although the asymmetric nature of the stray fields generated by Tips1 and 2 can be considered effectively identical, the integrated field line scan rotation data sets should be measurably different in a real experiment.



(a) Integrated field line scans sensitive to induction normal to the plane of reconstruction generated by Tip2.



(b) Integrated field line scans sensitive to induction in the plane of reconstruction generated by Tip2.

(c) Plot of the asymmetry index of the integrated field line scans in (a).

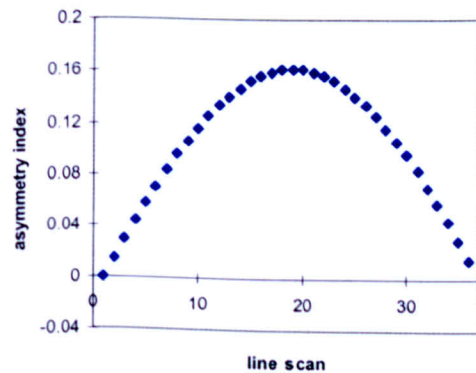


Fig. 4.11: Integrated field line scans calculated from model Tip2. Also shown is a plot of the asymmetry index of the scans in (a).

4.3.3 Stray Field and Integrated Stray Field from Model Tip3

4.3.3.1 Stray Field Calculated Directly from Model Tip3

The three dimensional stray field from Tip3 (the model which most closely resembles the DI tip shown in fig. 4.4 - if we ignore the three sided character of the tip at its apex) was calculated at the reconstruction plane and is shown in fig. 4.12(a). Once again horizontal and vertical field scans were taken across the peak value of the component of field normal to the plane of reconstruction and are shown in fig. 4.12(b). The horizontal scan was found to have an asymmetry index of zero, again indicating that the field is symmetric about the position of its peak value. The asymmetry index of the vertical field scan is again non zero, at 0.102. The calculated distance between the position of the peak field and that of the centre of the FWHM is 24nm - approximately at the limit of the resolution achievable from a STEM operated in DPC imaging mode.

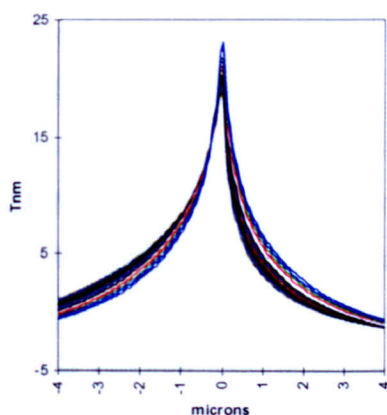
The implication is that the asymmetric character of the stray field from model Tip3 may just be resolvable when reconstructed (using RTM) from deflection line scans of 20-30nm resolution (imaged in a STEM operated in DPC imaging mode). However, the distance between the position of the peak field and the centre of the FWHM of the scan will certainly not be greater than 1 pixel on a real reconstructed field plane.

Thus the conclusion is that the asymmetric nature of the stray field generated by Tip3 may just be measurably different from the asymmetric nature of the stray field generated by Tip1 or Tip2 however the difference is small.

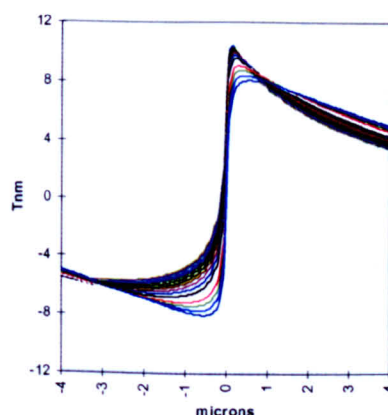
4.3.3.2 Integrated Stray Field Calculated from Model Tip3

Figs. 4.13(a) and (b) show the integrated field line scan rotation data sets generated by model Tip3. Fig. 4.13(c) plots the asymmetry index of each scan in fig. 4.13(a). The maximum value of the asymmetry index is found to be 0.244 which corresponds to a distance of 254nm between the position of the peak integrated field and the position of the centre of the FWHM of the scan. This distance is approximately equivalent to 9 or 10 pixels on a real deflection line scan. The minimum value of the asymmetry index is again zero. The angular positions of the tip for the generation of line scans of maximum and minimum asymmetry index are again separated by 90° about the rotation axis.

Thus, despite the fact that the three tip models represent three different magnetisation distributions, they have all been found to generate stray field of remarkably similar character to one another. However, although the integrated fields generated by each tip model are similar to one another, they differ to the extent that they are all distinguishable from one another in a practical experiment.



(a) Integrated field line scans sensitive to induction normal to the plane of reconstruction generated by Tip3.



(b) Integrated field line scans sensitive to induction in the plane of reconstruction generated by Tip3.

(c) Plot of the asymmetry index of the integrated field line scans in (a).

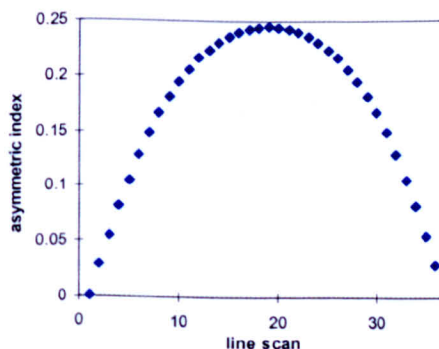


Fig. 4.13: Integrated field line scans calculated from model Tip3. Also shown is a plot of the asymmetry index of the scans in (a).

4.3.4 Comparison of the Simulated Integrated Field Line Scans Generated by Tips1 and 3 with the Deflection Line Scans Generated by a DI MFM Tip

We now compare a selection of the simulated integrated field line scans generated by Tips1 and 3 with the corresponding deflection line scans generated by the DI tip to investigate whether the character of these simulated integrated fields compare favourably with experimental deflection data.

The DI tip (coated with a CoCr alloy) was magnetised by the application of a large field directed along the tip axis. The tip assembly was mounted in the microscope such that the tip axis was at 12.5° to the rotation axis - see Section 3.4. The tip was rotated in the microscope and a full DPC deflection data set was taken. The line scans were extracted from the DPC image pairs at approximately 50nm in front of the tip. The full line scan deflection data set is not presented in this chapter (but will be introduced in Chapter 5), instead a selection of line scans from the data sets are shown in figs. 4.14 and 4.15. The corresponding simulated integrated field line scans generated by Tips1 and 3 are also shown. An indication of the relative angular position of the tip for each scan is given.

Note that the integrated field line scans generated by Tip1 have been scaled to facilitate the comparison of the asymmetric character of the simulated and experimental deflection data. Also note that the deflection line scans generated by the DI MFM tip have been modified by the subtraction of a large variable vertical shift value from each scan. The subtraction of the vertical shifts from the scans does not invalidate the comparison of the simulated and experimental deflection data since we are initially only interested in the shape character of the deflection line scans generated by the DI tip. The origin of the variable vertical shifts of the scans will be dealt with in Chapter 5.

Fig. 4.14 shows a comparison of the experimental deflection line scans (generated by the DI tip) sensitive to induction normal to the plane of reconstruction with the corresponding simulated integrated field line scans (generated by Tips1 and 3). It is clear that both sets of simulated line scans compare favourably with the experimental deflection data. In fig. 4.15 the experimental deflection line scans sensitive to induction in the plane of reconstruction generated by the DI tip are compared to the corresponding simulated integrated field line scans. In this case,

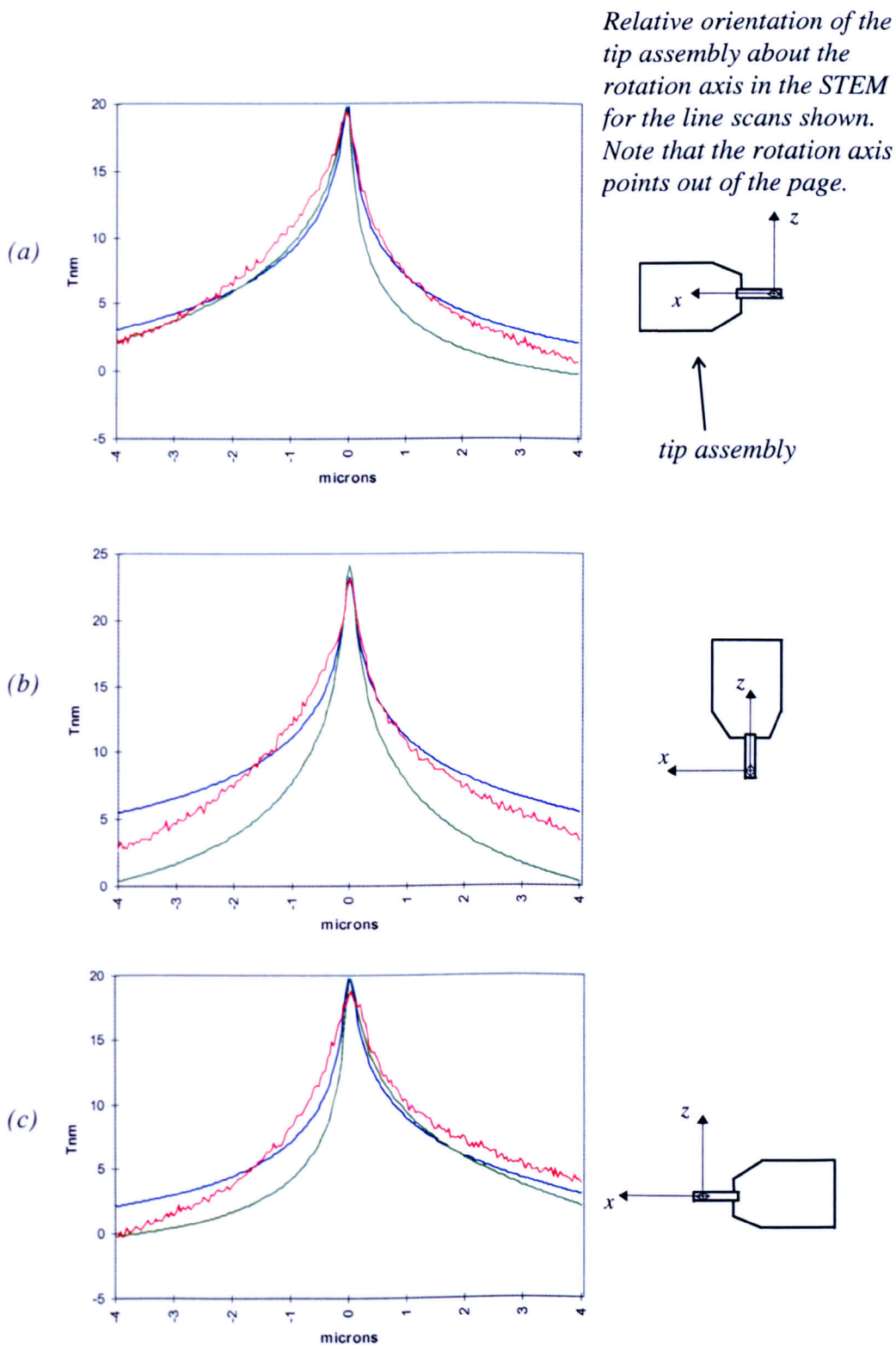


Fig. 4.14: Comparison of a selection of line scans (sensitive to induction normal to the plane of reconstruction) generated by a DI MFM tip (magnetised by the application of a large field directed along the tip axis) with simulated integrated field line scans generated by model Tips1 and 3.

Note that *the red line scans were generated by the DI tip, while the blue line scans were generated by model Tip1 and the green line scans were generated by model Tip3.*

Also note that each of the experimental deflection line scans have had a constant deflection value subtracted from them - the origin of which is considered in Chapter 5.

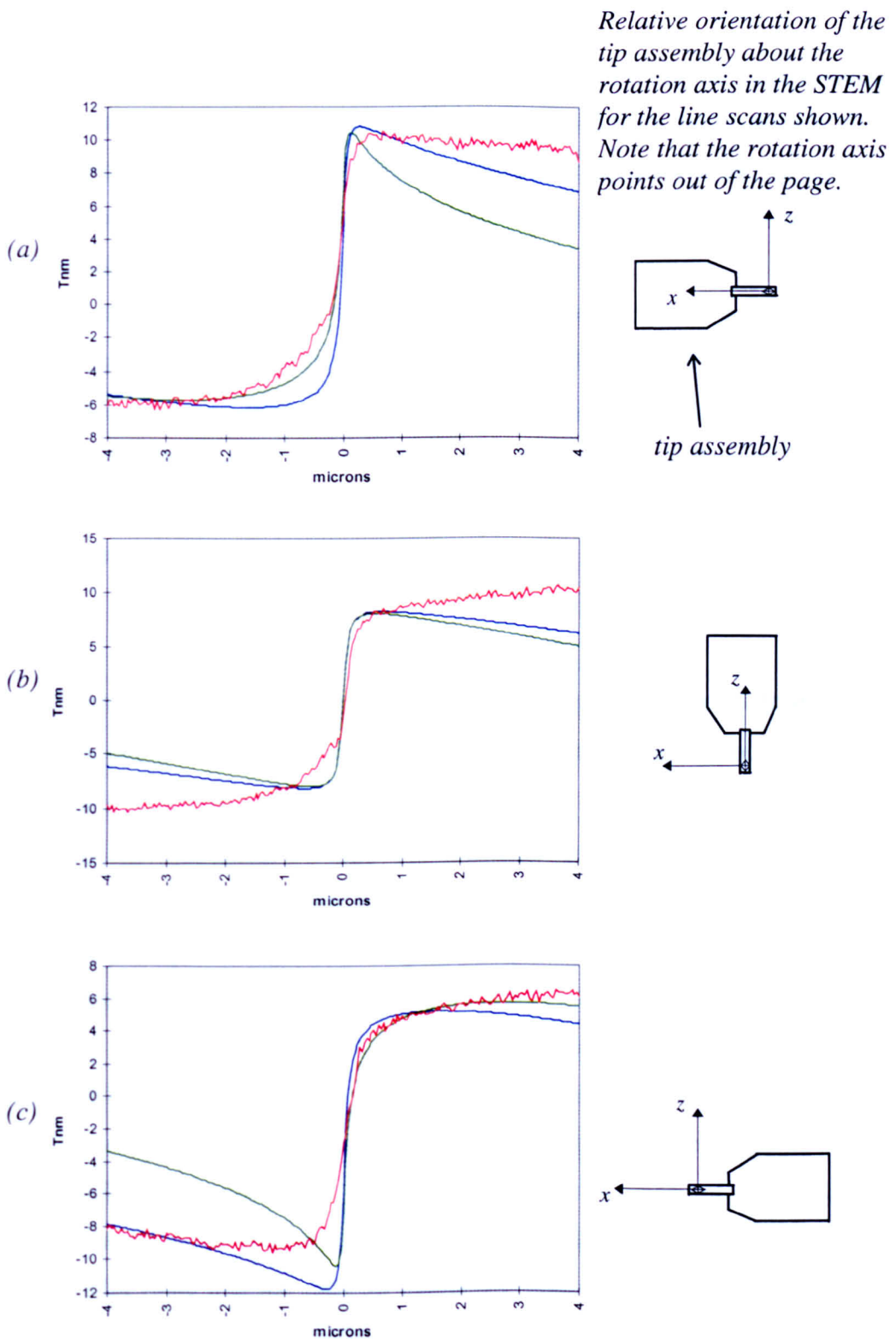


Fig. 4.15: Comparison of a selection of line scans (sensitive to induction in the plane of reconstruction) generated by a DI MFM tip (magnetised by the application of a large field directed along the tip axis) with simulated integrated field line scans generated by model Tips1 and 3.

Note that the red line scans were generated by the DI tip, while the blue line scans were generated by model Tip1 and the green line scans were generated by model Tip3.

Also note that each of the experimental deflection line scans have had a constant deflection value subtracted from them - the origin of which is considered in Chapter 5.

there is again reasonable agreement between the experimental and simulated deflection data. Note that the integrated fields calculated from the tip models do not include contributions from the cantilever and substrate portions of the tip assembly. This is a possible reason for any disagreements between the characters of the experimental and simulated integrated field.

We therefore conclude that both Tips1 and 3 are possible models for the DI MFM tip magnetised by the application of a large field directed along the tip axis. The above comparison therefore justifies the construction of these tip models to investigate the character of the MFM tip stray field. In the following section we investigate the accuracy of approximating the tip field to be the stray field from a point magnetic monopole or a point magnetic dipole.

4.3.5 Comparison of the Stray Fields and Integrated Fields from model Tip1 with the Stray Fields and Integrated Fields from a Point Magnetic Monopole and a Point Magnetic Dipole

In previous investigations^{[2][3]} into the character of the MFM tip stray field, theoreticians and experimentalists have tended to approximate the tip field to be the stray field from a point magnetic monopole or a point magnetic dipole. Using one of the tip models from the previous sections (Tips1, 2 or 3), we can investigate the accuracy of these approximations to the tip field. Firstly however, we consider the relationship between a MFM tip's net magnetic moment and its stray field.

The magnetisation of a magnetic material at a point is the magnetic moment per unit volume. Therefore the net magnetic dipole moment of a model tip is calculated as the vector sum of the products of the magnetisation and the volume of each thin film (note that for each tip model the magnetisation of each thin film is constant since they are magnetically saturated).

Using this method the (normalised) magnitude and directions of the net magnetic moments of Tips1, 2 and 3 relative to the reconstruction plane normal were calculated and are listed in Table 4.1. Also listed in this table are the asymmetry index of the stray fields calculated from the tip models (calculated from the vertical field scans taken across the peak field value of the component of field normal to the

plane of reconstruction), and the maximum asymmetry index of the integrated field line scans generated by each tip model.

Table 4.1: *Asymmetry of stray fields and integrated stray fields generated by the tip models*

| Tip Model | Normalised Net magnetic Moment of model tips | Angle between net magnetic moment of tip model and reconstruction plane normal | Asymmetric index of stray field | Max asymmetric Index of integrated field line scans |
|-----------|--|--|---------------------------------|---|
| 1 | 1 | 12.5° | 0.027 | 0.106 |
| 2 | 0.856 | 18.2° | 0.060 | 0.162 |
| 3 | 0.922 | 21.4° | 0.102 | 0.244 |

The clear suggestion from Table 4.1 is that the larger the angle between the tip's net magnetic moment and the reconstruction plane normal, then the more asymmetric the tip stray field and integrated stray field can be expected to be. In Section 4.4 the accuracy of using the character of a tip's integrated field as a guide to the character of the tip's stray field is discussed in detail.

We now compare the stray field from model Tip1 with the field from a point magnetic dipole and the field from a point magnetic monopole. Note that the dipole we will consider is of equivalent magnitude and direction to the net magnetic moment of Tip1 (given in Table 4.1), while the monopole is of an equivalent magnitude to the net magnetic charge of Tip1.

For the point monopole and dipole approximations to the model tip field we require that the monopole and dipole be positioned in space so that their individual stray fields at the reconstruction plane are of a similar magnitude and spatial distribution to the field from Tip1. In the following, the method for positioning the point dipole is described. Note that this method was also used for the point monopole approximation.

It was not clear where to position the dipole to fulfil the criteria described above and therefore the dipole was first arbitrarily positioned on the tip axis oriented in a direction parallel to the tip's net magnetic moment. The position of the dipole on

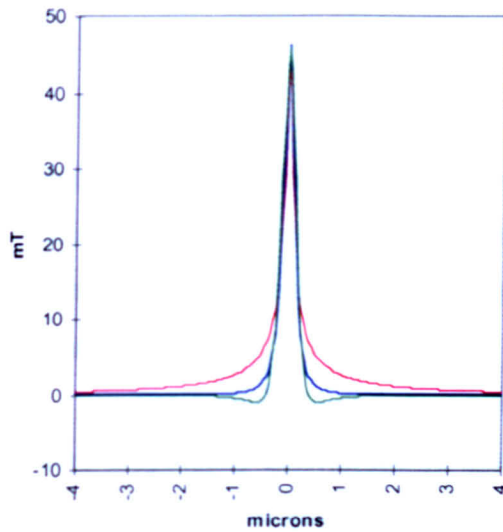
the tip axis was then altered so that the field generated by the dipole at the reconstruction plane was of a similar magnitude to the field from Tip1 (note that the dipole was moved further away or closer to the position of the tip apex depending on whether the dipole field at the reconstruction plane was respectively larger or smaller than the magnitude of the tip field). The dipole was finally positioned on the tip axis at 300nm from the tip apex (the final position of the monopole was 100nm from the tip apex).

The individual stray fields generated by the monopole and the dipole were of a similar character to the field generated by Tip1 (see fig. 4.8(b)) but are not shown here. Instead line scans taken across corresponding field components (generated by the monopole, the dipole and model Tip1) are shown in figs. 4.16(a) and (b).

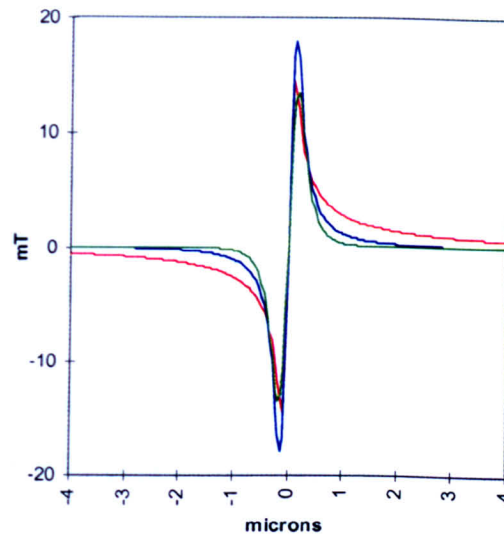
The FWHM of the field scan in fig. 4.16(a) taken across the component of the monopole field normal to the plane of reconstruction was found to be 250nm, while the corresponding FWHM of the dipole field component is 300nm. The FWHM of the scan taken across the normal component of field from Tip1 is 221nm. Furthermore, the peak value of the monopole field scan, the dipole field scan and the scan generated by Tip1 is 46mT in each case. It is therefore clear that the fields generated by each of the monopole and the dipole do compare reasonably with the field from model Tip1. We now consider the integrated fields generated from each individual magnetic source.

Figs. 4.16(c) and (d) show a comparison of corresponding integrated field line scans generated by the point monopole, the point dipole and the model tip. It is clear that there is qualitative agreement between the characters of the integrated tip field and the integrated field from the monopole and dipole. However, the magnitude and spatial definition of these integrated fields do not compare favourably with the integrated field from model Tip1.

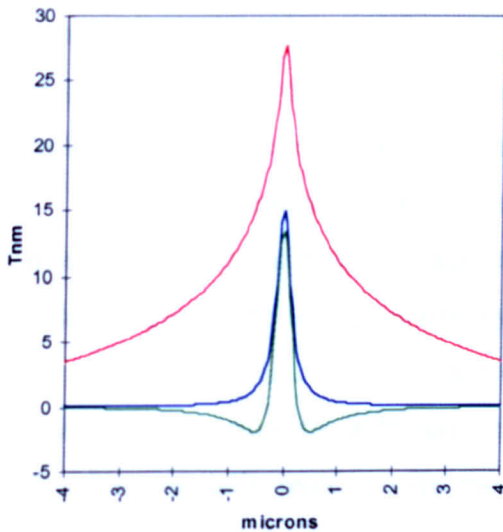
Hence, it is clear that we can determine a point monopole or a point dipole (of specific magnitude and position in space) which generates stray field at the reconstruction plane comparable to the field generated by the tip model. However, the monopole and the dipole integrated fields do not compare favourably with that from the tip.



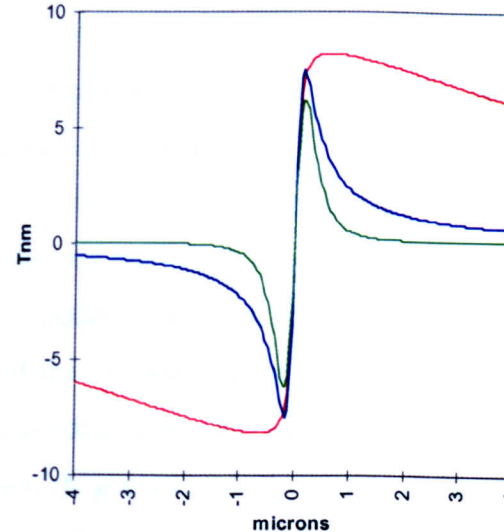
(a) Scans taken across the normal components (to the reconstruction plane) of field generated by the point monopole, the point dipole and model Tip1.



(b) Scans taken across an in-plane (reconstruction plane) component of field generated by the point monopole, the point dipole and model Tip1.



(c) Integrated field line scans (sensitive to induction normal to the plane of reconstruction) generated by the point monopole, the point dipole and model Tip1.



(d) Integrated field line scans (sensitive to induction in the plane of reconstruction) generated by the point monopole, the point dipole and model Tip1.

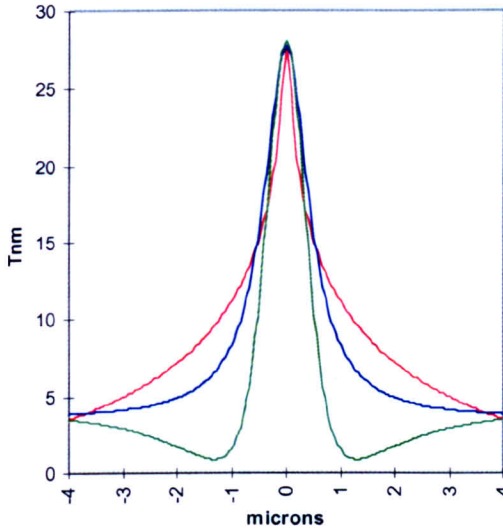
Fig. 4.16: Comparisons of the field scan components and the integrated field line scans generated by the point magnetic monopole, the point magnetic dipole and model Tip1.

Note that the red field scans/integrated field scans were generated by model Tip1, while the blue field scans/integrated field scans were generated by the point monopole, and the green field scans/integrated field scans were generated by the point dipole.

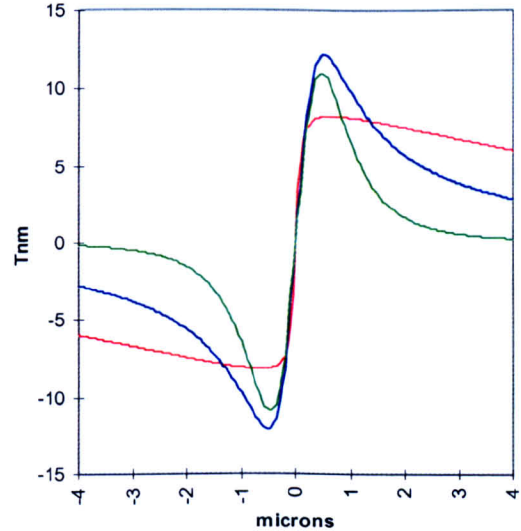
We now consider the case of a point monopole or dipole which generates integrated field line scans comparable to that from the model tip. A discussion on the agreement between the stray fields generated by the tip model and the monopole/dipole is then given.

The magnitude and the position on the tip axis of the monopole and dipole were empirically determined so that they each generated integrated field line scans comparable to that generated by the tip model, see figs. 4.17(a) and (b). In this case the monopole was positioned 450nm from the tip apex, while the dipole was positioned 750nm from the tip apex. It is clear that the integrated fields generated by each of the monopole and the dipole do compare reasonably with the integrated tip field (the monopole is arguably a more accurate approximation to the integrated tip field). However, field scans taken across corresponding components of field generated by each magnetic source - see figs. 4.17(c) and (d) - indicate that both the monopole and the dipole stray fields significantly differ from the model tip field (relative to the agreement between the integrated stray fields).

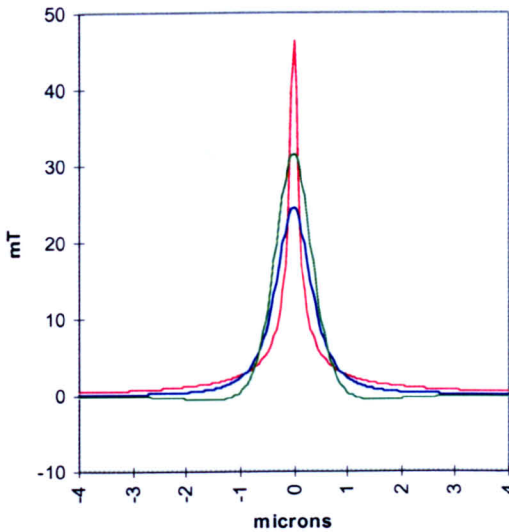
It has therefore been shown that it is not possible for a point magnetic monopole or a point magnetic dipole to generate both stray field and integrated stray field comparable to that generated by a tip model. In Chapter 5 we construct models for the cantilever and substrate portions of the tip assembly and in doing so will be guided by experimental deflection line scan data sets generated by the DI tip. We therefore crucially require a tip model which generates both a stray field and an integrated stray field which are comparable to that generated by a practical MFM tip. We therefore conclude that both the point monopole and the point dipole are not accurate approximations to the MFM tip and are not suitable for the investigations undertaken later in this thesis.



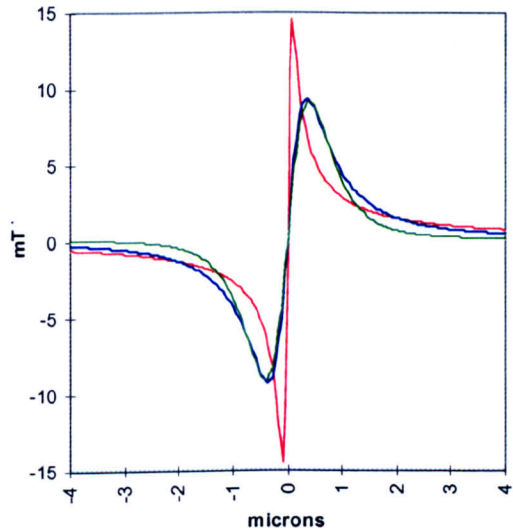
(a) Integrated field line scans (sensitive to induction normal to the plane of reconstruction) generated by the point monopole, the point dipole and model Tip1.



(b) Integrated field line scans (sensitive to induction in the plane of reconstruction) generated by the point monopole, the point dipole and model Tip1.



(c) Scans taken across the normal components (to the reconstruction plane) of field generated by the point monopole, the point dipole and model Tip1.



(d) Scans taken across an in-plane (reconstruction plane) component of field generated by the point monopole, the point dipole and model Tip1.

Fig. 4.17: Comparisons of the field scan components and the integrated field line scans generated by the point magnetic monopole, the point magnetic dipole and model Tip1.

Note that the red field scans/integrated field scans were generated by model Tip1, while the blue field scans/integrated field scans were generated by the point monopole, and the green field scans/integrated field scans were generated by the point dipole.

4.4 Contribution to the Tip Stray Field and Integrated Stray Field from Various Portions of the Thin Film Tip Coating

Previous investigations into the character of the magnetic state of MFM tips as a function of uniform external magnetic field^[4] have concluded that the magnetic material coating the top $0.7\mu\text{m}$ of the tip (i.e. film within $0.7\mu\text{m}$ from the tip apex) is the most important for defining the character of the tip field. In this section, the contribution to the stray field from different portions of a thin film MFM tip will be investigated using two models. The first tip model - which will be referred to as the Uniformly Magnetised Tip (UMT)- represents a MFM tip uniformly magnetised in a direction pointing towards the tip apex (similar to Tip1) - see fig. 4.18. The second tip model is referred to as the Non-Uniformly Magnetised Tip (NUMT) and for this model we ignore the contribution to the tip field from the magnetic charge planes at the base of each thin film - see fig. 4.18. The NUMT model represents a MFM tip predominately magnetised in a direction pointing towards the tip apex. However, the magnetic film at the base of the tip is in a domain configuration which reduces the magnetostatic energy of the system. This is analogous to an axially magnetised tip with a flux closure domain structure at its base.

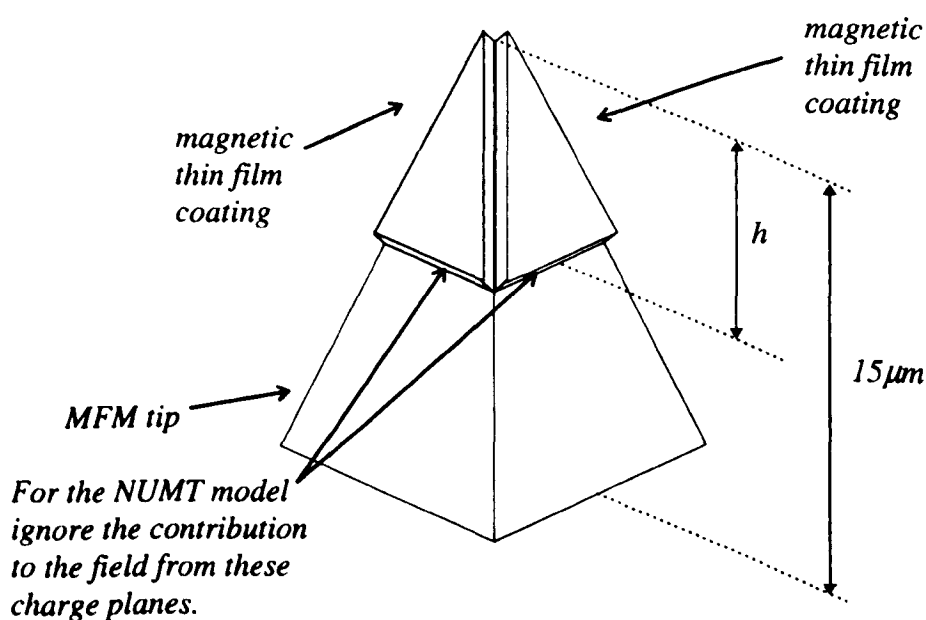


Fig. 4.18: Diagram of model Tip1 partially coated with thin film from the apex down. Note that for the NUMT model ignore the contribution to the stray field from the charge planes nearest the base of the tip.

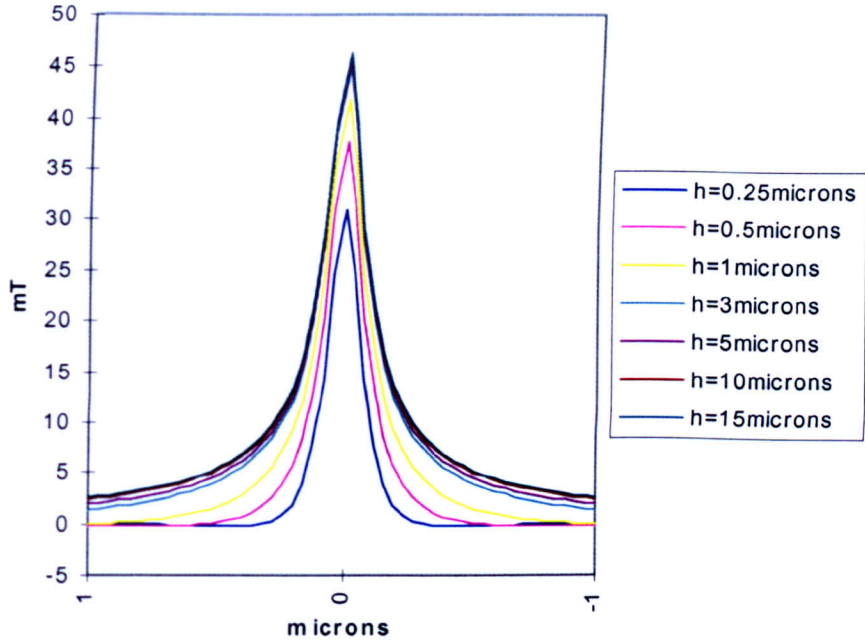
The three dimensional stray field was calculated from each tip model at the reconstruction plane for various portions of the tips coated with thin film ($h=0.25\mu\text{m}$, $0.5\mu\text{m}$, $1\mu\text{m}$, $3\mu\text{m}$, $5\mu\text{m}$, $10\mu\text{m}$ and $15\mu\text{m}$ in fig. 4.18). Field scans were then taken across the peak value of the component of field normal to the plane of reconstruction and a selection generated by the UMT model are shown in fig. 4.19(a). Fig. 4.19(b) plots the peak field values of the scans in fig. 4.19(a) and of the scans generated by the NUMT model, while fig. 4.19(c) plots the FWHM of these scans.

Note from fig. 4.19(b) that the peak value of the field generated by the UMT model with thin film coating the top $3\mu\text{m}$ of the model only (i.e. $h=3\mu\text{m}$) is 45mT , while the corresponding field value generated by the same tip model entirely coated with film (i.e. $h=15\mu\text{m}$) is 46mT . Also, the FWHM of the field scan generated by the $3\mu\text{m}$ thin film tip model is 214nm , while the FWHM of the scan generated by the fully coated tip model is 221nm . Thus, both the magnitude and the FWHM of the field scan generated by the $3\mu\text{m}$ thin film tip differ from the field scan generated by the fully coated tip by only a relatively small amount - less than 3% in each case.

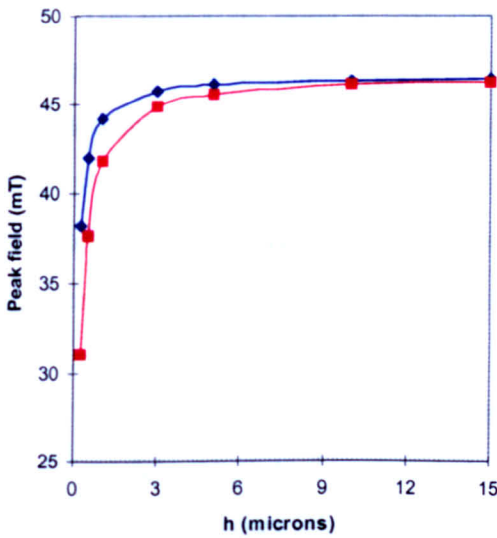
In contrast, the character (i.e. the magnitude and FWHM) of field scans generated by the UMT model with less than the top $3\mu\text{m}$ coated with film (i.e. $h<3\mu\text{m}$) differ significantly from the field generated by the fully coated tip - see figs. 4.19(b) and (c).

The suggestion therefore is that the thin film coating approximately the top $3\mu\text{m}$ of the UMT model is the most important for defining the character of the tip stray field (i.e. the magnitude and the spatial distribution of the tip field). The film coating beyond $3\mu\text{m}$ from the apex has little influence on the character of the stray field immediately in front of the tip.

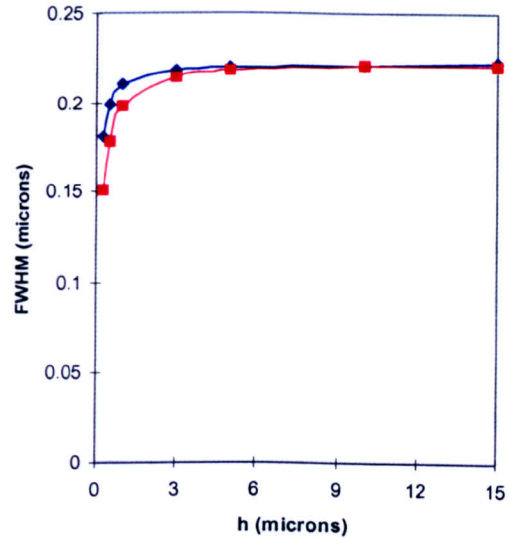
Further, from figs. 4.19(b) and (c) we find for the NUMT model, that the magnetic material within approximately $1\mu\text{m}$ from the tip apex is the most important for defining the character of this tip field. In this case, both the magnitude and FWHM of the field scan generated by the NUMT model with thin film coating the top $1\mu\text{m}$ of the model only (i.e. $h=1\mu\text{m}$) differ from the field generated by the fully coated NUMT model by less than 5% - again a relatively small difference. The NUMT models with film coating less than the top $1\mu\text{m}$ (i.e. $h<1\mu\text{m}$) generate fields



(a) Field scans taken across the normal components of field calculated from the UMT model for varying values of h .



(b) Plots of the peak field values of the scans in (a) generated by the UMT model, and of the field scans generated by the NUMT model not shown above.



(c) Plots of the FWHM of the scans in (a) generated by the UMT model, and of the field scans generated by the NUMT model not shown above.

Fig. 4.19: Field scans generated by the UMT model of varying h (see fig. 4.18). Also shown are plots of the peak field values and the FWHM of the scans generated by the UMT model and the NUMT model. Note that *red points* in (b) and (c) represent the UMT model, while the *blue points* represent the NUMT model.

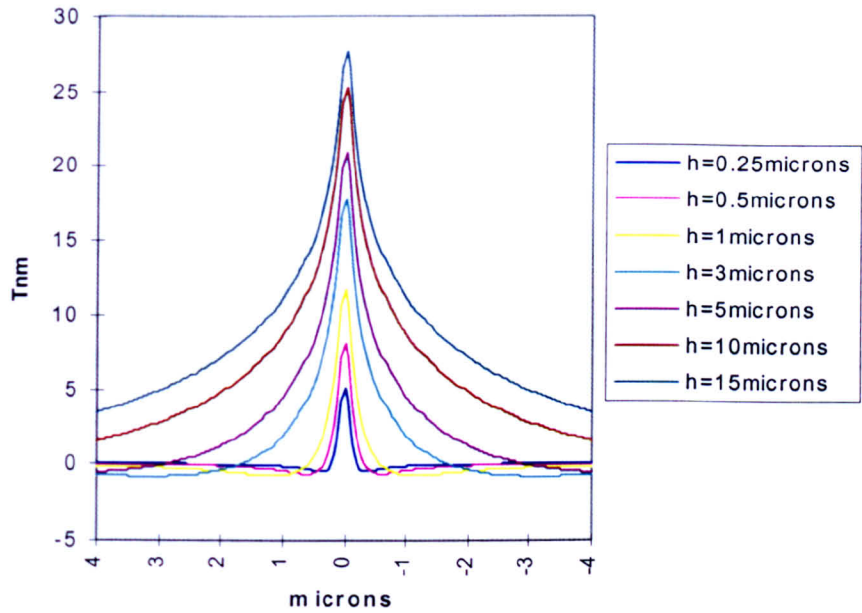
significantly different in character to the field generated by the NUMT model fully coated with film. Therefore the suggestion is that the thin film coating the top $1\mu\text{m}$ of the NUMT is the most important for defining the character of the tip field (the film beyond $1\mu\text{m}$ from the apex having little influence on the character of the field immediately in front of the tip).

The models considered above suggest that the magnetic thin film within $1\text{--}3\mu\text{m}$ of the tip apex is the most important for defining the character of the tip stray field. The portion of thin film tip responsible for the character of the field is, however, dependant on the magnetic configuration of the tip film.

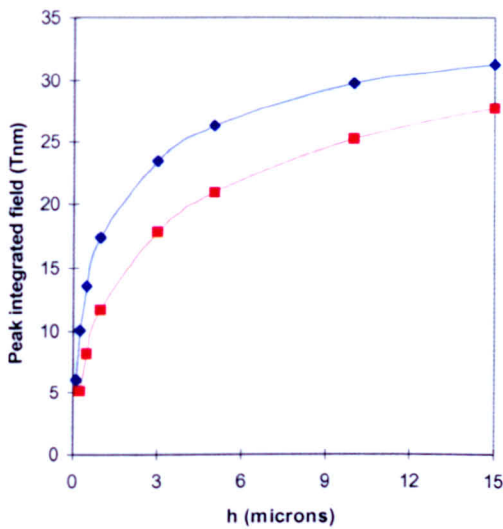
We now consider the integrated field generated by both the UMT and the NUMT models. Fig. 4.20(a) shows a selection of integrated field line scans generated by the UMT model with film coating various portions of the tip. Fig. 4.20(b) plots the peak integrated field values of the scans in fig. 4.20(a) and of the integrated field line scans generated by the NUMT model, while fig. 4.20(c) plots the FWHM of these scans.

The important point to note from figs. 4.20(b) and (c) is that the character of the integrated field (i.e. the magnitude and FWHM of the integrated field line scans) generated by the UMT model is still significantly affected as the portion of the tip coated with film increases beyond $3\mu\text{m}$ from the apex (i.e. $h > 3\mu\text{m}$). The character of the integrated field generated by the NUMT model also continues to change significantly as the portion of the tip coated with film increases beyond $1\mu\text{m}$ from the apex (i.e. $h > 1\mu\text{m}$).

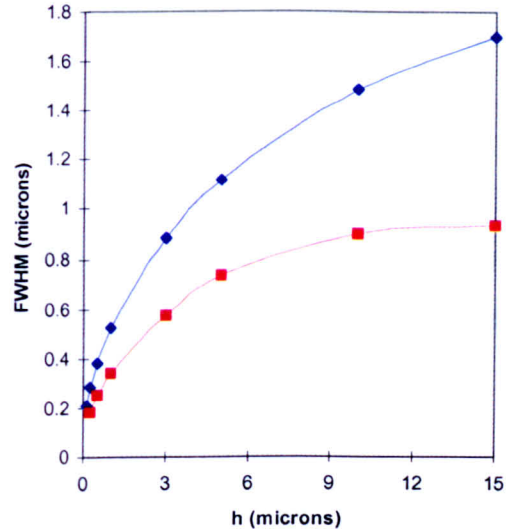
This changing nature of the integrated fields generated by the UMT and the NUMT models suggests that portions of the thin film tip which do not significantly contribute to the character of the stray field immediately in front of the tip, do however, significantly contribute to the character of the integrated field. This suggests that these portions of the thin film tip generate a smaller field over a larger distance (relative to the field from the tip film at the top of the tip) which when integrated has a significant effect on the character of the integrated tip field. This therefore implies that using the integrated field line scan data sets to assess the character of a tip field may be subject to significant error.



(a) Integrated field scans (sensitive to induction normal to the plane of reconstruction) generated by the UMT model for varying values of h .



(b) Plots of the peak integrated field values of the line scans in (a) generated by the UMT model, and of the integrated field line scans generated by the NUMT model not shown above.



(c) Plots of the FWHM of the line scans in (a) generated by the UMT model, and of the line scans generated by the NUMT model not shown above.

Fig. 4.20: Integrated field line scans (sensitive to induction normal to the plane of reconstruction) generated by the UMT model of varying h (see fig. 4.18). Also shown are plots of the peak integrated field values and the FWHM of the line scans generated by the UMT model and the NUMT model. Note that red points in (b) and (c) represent the UMT model, while the blue points represent the NUMT model.

4.5 Thickness of Thin Film Coating and its Effect on Fields/Integrated Fields

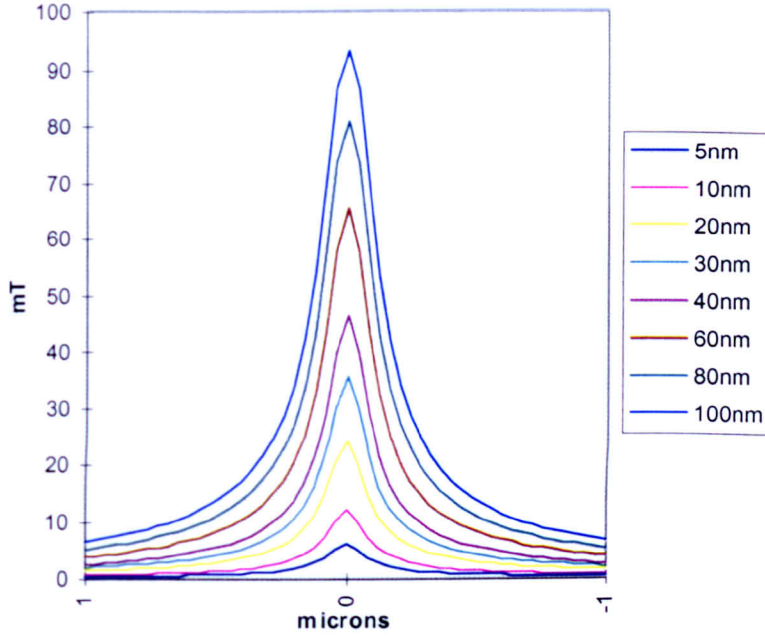
The magnetic thin film material deposited onto an MFM tip is generally sputtered or evaporated onto the tip. The resulting thickness of the film deposited is not known exactly. Therefore in this section the effect of varying the thin film coating thickness on the tip stray field and integrated field is investigated.

The three dimensional stray field was calculated from model Tip1 (coated with various thickness of film) and field scans were then taken across the peak value of the component of field normal to the plane of reconstruction and are shown in fig. 4.21(a). Fig. 4.21(b) plots the peak values of the scans in (a), while fig. 4.21(c) plots the FWHM of the scans.

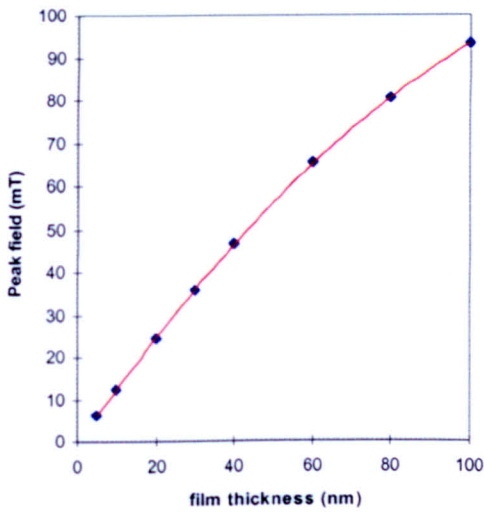
It is not clear what the exact relationship between the stray field and the tip film thickness is, however, the important point to note is that the magnitude and the FWHM of the field scans increase for increasing tip film thickness. Therefore the model suggests that not only does the magnitude of the tip field increase for thicker film coatings but the tip field also broadens for thicker film coatings.

Fig. 4.22(a) shows a selection of line scans taken from the integrated field line scan data sets generated by the tip model coated with various thickness of film. Plots of the peak integrated field values of these scans, fig. 4.22(b), and the FWHM of the scans, fig. 4.22(c), are also shown. Note that the peak integrated field values and the FWHM of the integrated field line scans increase for increasing film thickness.

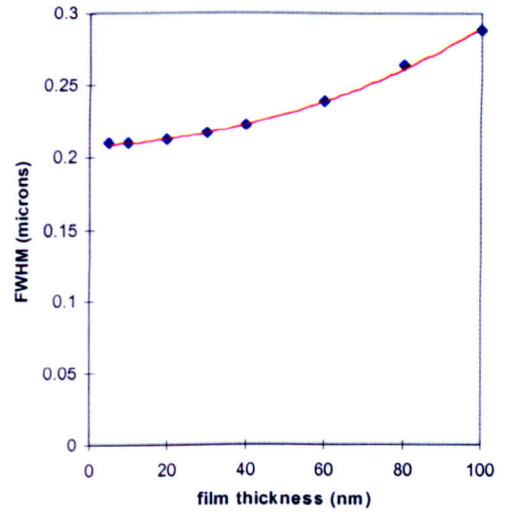
The implication from these results is that for thicker film coatings, the tip stray field (although increasing in magnitude) becomes less sharp. Therefore, since the MFM's resolution is determined by the spatial distribution of the tip field, the model suggests that for higher MFM imaging resolution the thin film tip coating should be kept to a minimum thickness (with the proviso that the tip-sample interaction can still be measured).



(a) Field scans taken across the normal components of field calculated from Tip1 for tip coated in varying film thickness (see box).

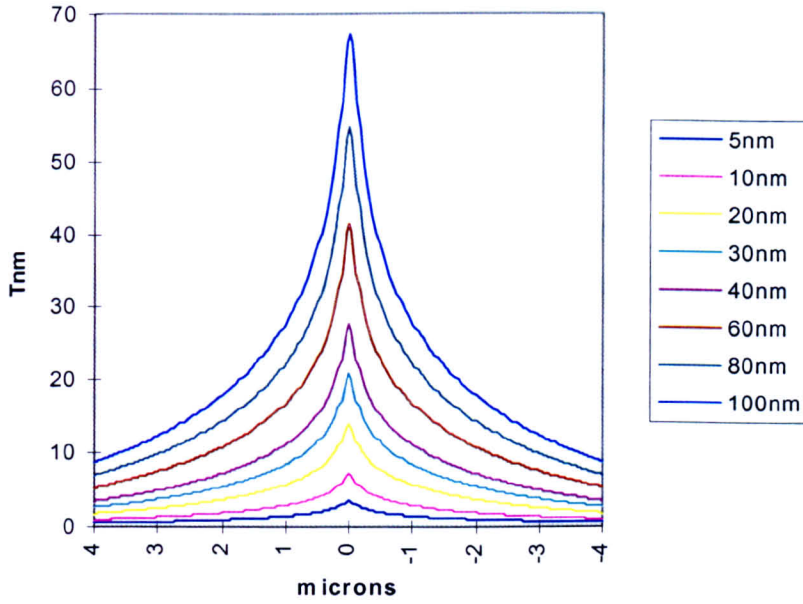


(b) Plot of the peak field values of the scans in (a).

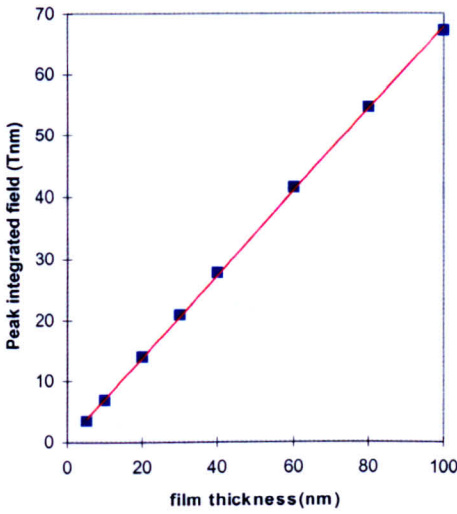


(c) Plot of the FWHM of the scans in (a).

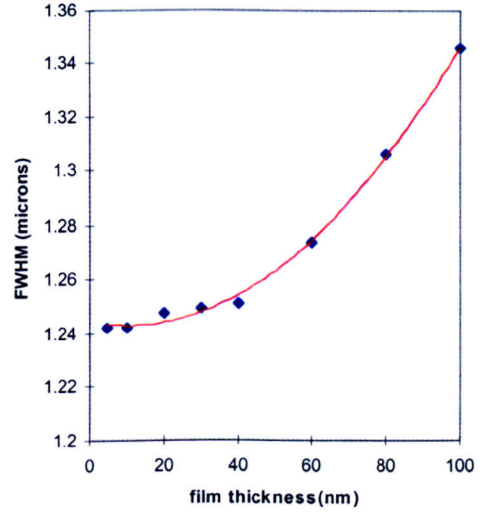
Fig. 4.21: Field scans generated by model Tip1 coated with varying thickness of magnetic film. Also shown are plots of the peak values and the FWHM of the field scans.



(a) Integrated field scans (sensitive to induction normal to the plane of reconstruction) generated by Tip1 coated with varying thickness of magnetic film (see box).



(b) Plot of the peak field values of the scans in (a).



(c) Plot of the FWHM of the scans in (a).

Fig. 4.22: Integrated field scans (sensitive to induction normal to the plane of reconstruction) generated by Tip1 coated with varying thickness of magnetic film. Also shown are plots of the peak values and the FWHM of the integrated field scans.

4.6 Summary

All the tip models considered are an approximation of the geometry of the DI MFM tip. In particular the film at the apex of the practical MFM tip is smooth, rounded and continuous (this can be deduced from any TEM images of the tip apex) while the film at the apex of each tip model is sharp and discontinuous - see fig. 4.18. Since we have concluded (in Section 4.4) that the film in the vicinity of the tip apex is the most important for defining the character of the tip field immediately in front of the tip, we might expect that a practical MFM tip will generate a broader stray field than the tip models. However, due to the fact that the three tip models - each representing a different magnetisation distribution - generate stray fields of similar character to one another, we conclude that approximating the geometry of the tip apex (which is required to construct a tip model) will not significantly affect the character of the calculated field.

Although the integrated fields generated by the tip models (Tips1, 2 and 3) are distinguishable from one another, they do all display a similar character (with Tip1 generating the least asymmetric integrated field, then Tip2 and finally Tip3 generating the most asymmetric integrated field - see Table 4.1). In Section 4.3.4, the integrated field line scans generated by model Tips1 and 3 (the tips generating the least and most asymmetric integrated field) were compared to the deflection data generated by the DI MFM tip and were found to compare favourably. This suggested that Tips1 and 3 (and therefore the intermediate case - Tip2) were possible models for the DI tip.

In contrast, in Section 4.3.5 we concluded that it is not possible to determine a point monopole or a point dipole (of specific magnitude and position in space) which generates stray field and integrated stray field comparable to that generated by a tip model. Since we require models which generate stray field and integrated fields comparable to that generated by a DI MFM tip, the monopole or dipole approximations to the MFM tip are not suitable for the following investigations. Instead, in Chapters 5, 6 and 7 we continue to use magnetic charge planes to construct models of the tip, cantilever and substrate portions of the tip assembly.

References

- [1] P. Rhodes and G. Rowlands (1954), *Proc. Leeds Phil. And Lit. Soc.*, 6, pp199
- [2] Hartmann, U (1989), *Physics Letters A*, Vol. 137, No. 9, pp 475-478.
- [3] Lohau, J; Kirsch, S; Carl, A; Dumpich, G; Wassermann, E. F (1999), *Journal of Applied Physics*, Vol. 86, No. 6, pp 3410-3417.
- [4] Babcock, K (1996), *Appl. Phys. Lett.*, 69, pp 705-707

Chapter 5

Individual Contributions to a Tip Assembly's Line Scan Deflection Data Sets from the Tip, Cantilever and Substrate Portions of the Assembly

5.1 Introduction

Using a variety of models, the previous chapter dealt with investigations of the character of the stray fields and integrated stray fields generated from the thin film material attached to an MFM tip. In reality, however, the models used in Chapter 4 are too simplistic to characterise the stray field/integrated stray field from a real MFM tip, since a real MFM tip is also attached to a cantilever and substrate. Generally the entire tip/cantilever/substrate structure, which we will refer to as the tip assembly, is sputtered with the thin film magnetic material which coats the unshielded parts of the structure equally. Therefore, it is to be expected that at any point in free space, the magnetic induction measured from the tip assembly will have contributions from the thin film material coating the cantilever and substrate in addition to that on the tip.

Fig. 5.1 shows the line scan deflection data sets generated from a Digital Instruments (DI) MFM tip coated with CoCr alloy; this was magnetised by the application of a large field ($\sim 1.0T$) directed along the tip axis. The tip assembly was rotated in the microscope about an axis at 12.5° to the tip axis (see Section 3.4). The line scans were extracted from DPC image pairs and are approximately 50nm in front of the tip. In the following this case will be referred to as the Axial Case.

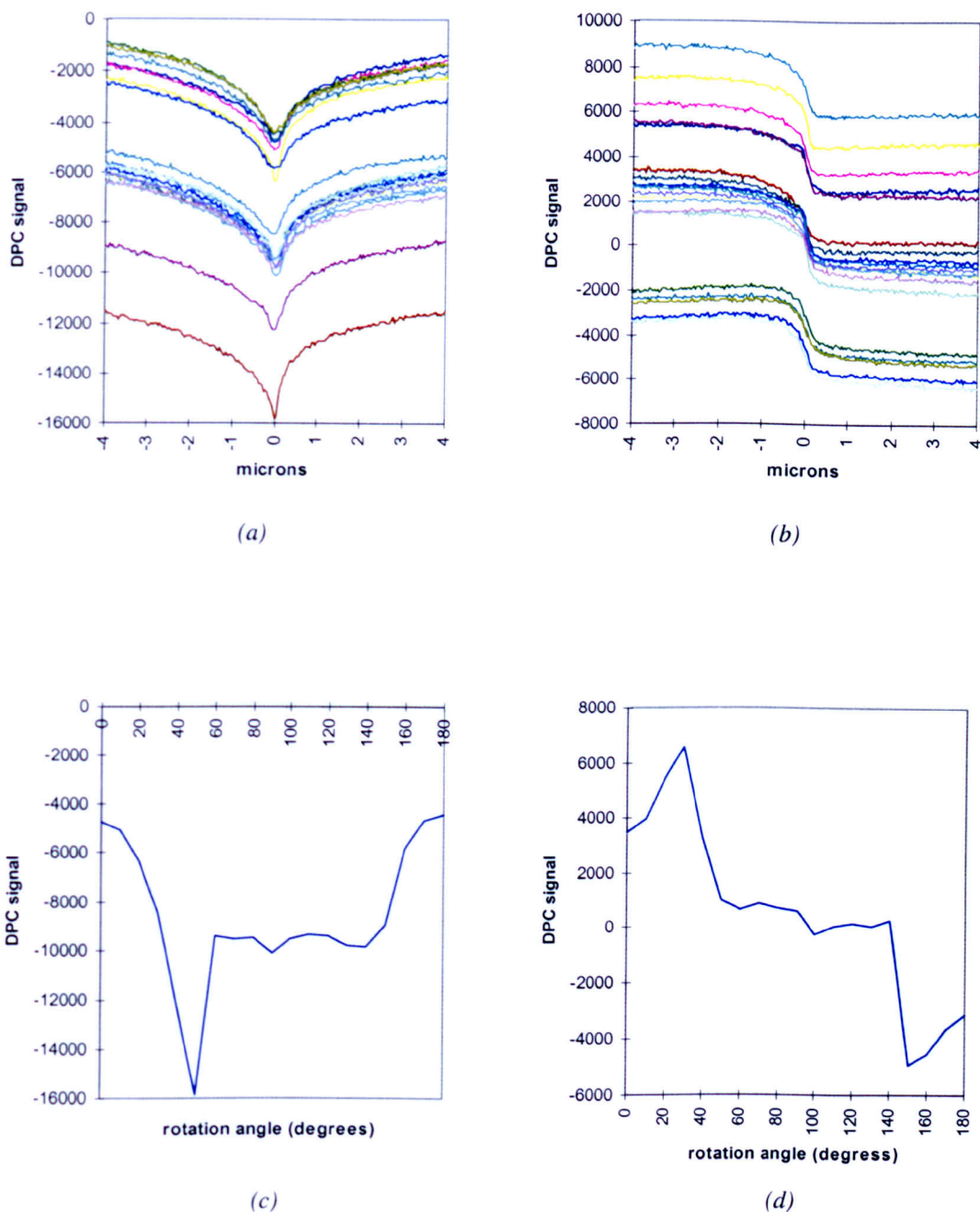
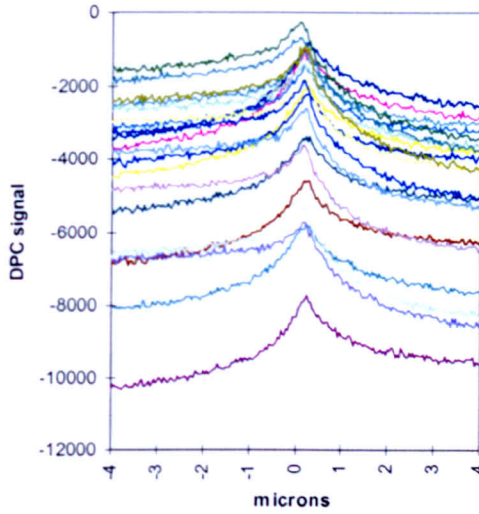
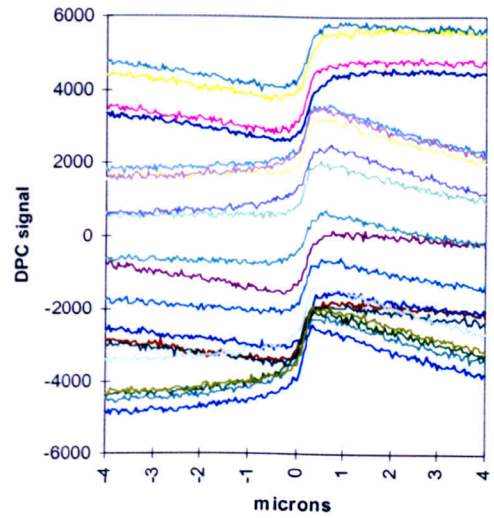


Fig. 5.1: Deflection line scan data set generated by DI MFM tip magnetised as in the **Axial Case** (i.e. tip assembly magnetised by application of a large field - $\sim 1.0T$ - directed along the tip axis).
 (a) Line scans sensitive to induction normal to the plane of reconstruction.
 (b) Line scans sensitive to induction in the plane of reconstruction.
 (c) Plot of the average value of the end-points of each scan in (a).
 (d) Plot of the average value of the end-points of each scan in (b).

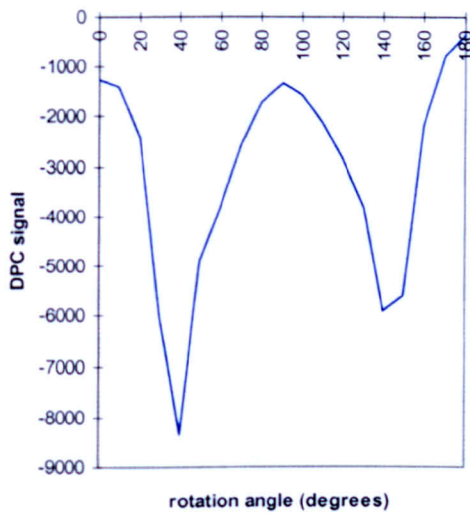
Deflection data provided by **Prof. R. P. Ferrier** and **Dr. S. McVitie**.



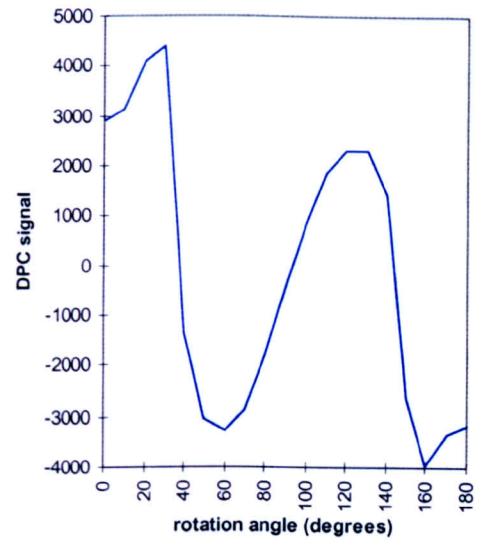
(a)



(b)



(c)



(d)

Fig. 5.2: Deflection line scan data set generated by a DI MFM tip magnetised as in the **Transverse Case** (i.e. tip assembly magnetised by application of a large field - $\sim 0.7T$ - directed along the cantilever axis).
 (a) Line scans sensitive to induction normal to the plane of reconstruction.
 (b) Line scans sensitive to induction in the plane of reconstruction.
 (c) Plot of the average value of the end-points of each scan in (a).
 (d) Plot of the average value of the end-points of each scan in (b).

Deflection data provided by **Prof. R. P. Ferrier** and **Dr. S. McVitie**.

Note the large vertical spread of line scans within each deflection data set. This behaviour is not observed in the simulated integrated field line scans generated by the tip models in Chapter 4. However there is a distinct similarity between the general shape of the scans and those generated by the tip models. This clearly suggests that the tip portion of the tip assembly is largely responsible for defining the shape of the scans in fig. 5.1, while the vertical offset arises presumably from contributions from the magnetic film on the cantilever and substrate.

The line scans shown in fig. 5.2 arise from the same tip as in fig. 5.1 but re-magnetised by the application of a large field ($\sim 0.7\text{T}$) directed along the cantilever axis. Once again a full rotation data set is shown. In the following this will be referred to as the Transverse Case.

Note the large spread of line scans within each deflection data set which are similar but not identical to the spread of scans in the data sets of fig. 5.1. Also note the similarity in shape between the line scans in fig. 5.2 and those generated by the tip models. Once again this suggests that the tip portion of the tip assembly is largely responsible for defining the shape of the scans in fig. 5.2 but that the offset in the scans originates from the magnetic material attached to the cantilever and substrate.

The shape of the scans in fig. 5.2 varies to a much greater degree than those in fig. 5.1. This may be a character of the integrated fields generated by the same part of the tip assembly responsible for the vertical shifts of the scans. Alternatively and possibly more plausibly, this may suggest that the magnetic configuration of the tip portion of the tip assembly has been modified after re-magnetisation by a field directed along the cantilever axis. Thus a further investigation into possible magnetic configurations of the tip portion of the tip assembly and its contribution to the deflection data sets is required [see Section 5.2].

Figs. 5.3(a) and (b) show a DPC image pair of the tip and cantilever portions of the tip assembly magnetised as in the Axial Case. The images are sensitive to induction in orthogonal directions and are taken from a full rotation data set of low magnification images of the tip and cantilever portions of the tip assembly. Both images show magnetic induction escaping from various regions along the tip and cantilever surfaces. These images (as indeed all the images in the full data set) clearly illustrate that there is stray field contributions from the cantilever.

Figs. 5.3(c) and (d) show a DPC image pair of the tip, cantilever and part of the substrate portion of the tip assembly (in the lower half of the images) magnetised as in the Axial Case. It is also clear that there are stray fields escaping from the surfaces of the substrate.

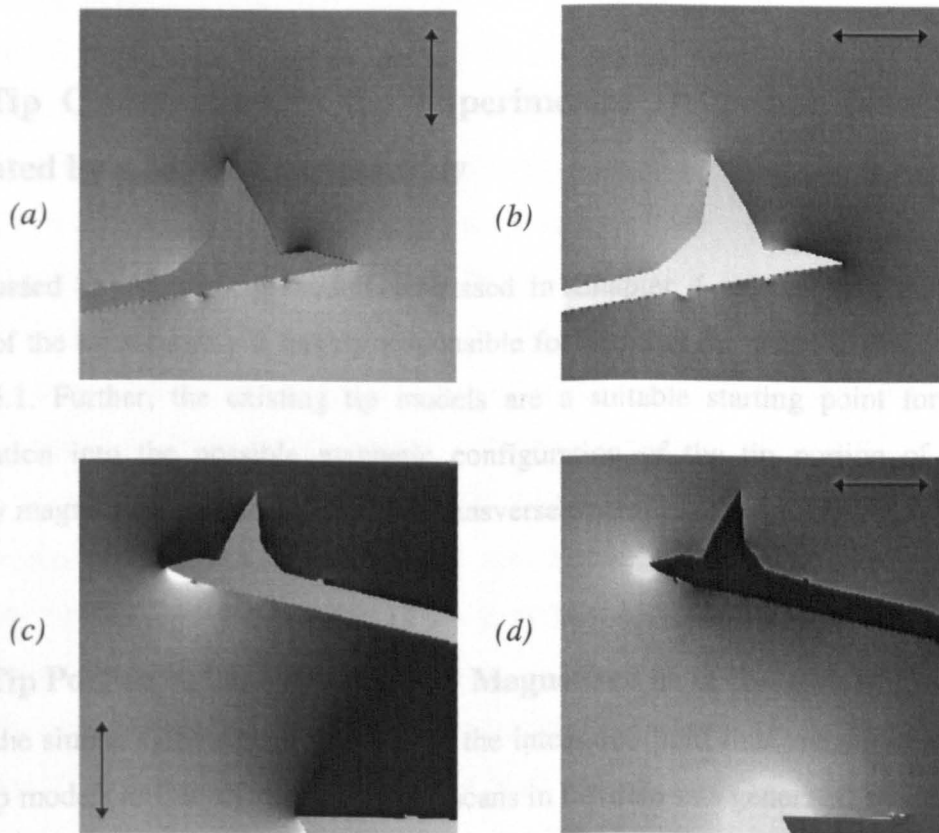


Fig. 5.3: (a) and (b) Low magnification DPC images of the tip and cantilever portions of the tip assembly magnetised as in the Axial Case. (c) and (d) Low magnification DPC images of the front edge of the substrate portion of the tip assembly (in the lower half of the images) magnetised as in the Axial Case.

Arrows indicate the direction of induction sensitivity. Images provided by **Prof. R. P. Ferrier** and **Dr. S. McVitie**.

The images of fig. 5.3 show that the thin film material attached to the cantilever and substrate portions of a real MFM tip assembly does generate stray fields. These fields contribute to the total field immediately in front of the tip portion of the assembly and therefore contribute to the character of the tip assembly's deflection data sets. Thus an investigation into the character of the stray fields and integrated stray fields generated by the cantilever (section 5.3) and substrate (section 5.4) portions is required. The investigations will consider whether the cantilever and substrate portions are responsible for the variable vertical shifting of the scans in figs. 5.1 and 5.2, and if so, what effect these have on the (ART and RTM) reconstructed tip fields (in Chapter 6). A summary of the important points to note from this chapter is given in section 5.5.

5.2 Tip Contribution to the Experimental Deflection Data Set Generated by a MFM Tip Assembly

As discussed above, the tip models discussed in Chapter 4 suggest that the tip portion of the tip assembly is largely responsible for defining the shape of the scans in fig. 5.1. Further, the existing tip models are a suitable starting point for an investigation into the possible magnetic configuration of the tip portion of the assembly magnetised as in the Axial and Transverse Cases.

5.2.1 Tip Portion of the Tip Assembly Magnetised as in the Axial Case

Clearly the similarity between the shape of the integrated field line scans generated by the tip models in Chapter 4 and the line scans in the data sets generated by the DI MFM tip assembly magnetised as in the Axial Case suggests that the tip portion of the tip assembly has a magnetic configuration similar to that of the tip models (see Section 4.3.4). In other words, the magnetic film coating the tip portion of the assembly appears to be magnetised towards the tip apex.

5.2.2 Tip Portion of the Tip Assembly Magnetised as in the Transverse Case

The shapes of the scans in fig. 5.2 vary to a much greater degree than those in fig. 5.1. As discussed above, this may suggest that the magnetic configuration of the tip portion of the tip assembly has been modified after application of the field directed along the cantilever axis. An investigation into possible magnetic configurations of the tip portion of the assembly magnetised as in the Transverse Case was undertaken.

Figs. 5.4(a), 5.5(a) and 5.6(a) show three plausible magnetic configurations for the tip (dimensions identical to Tip1 in Chapter 4) magnetised by a field applied along the direction of the cantilever axis (i.e. along the positive z direction). The corresponding integrated field line scan data sets generated by these tip models are also shown. It is clear that the shape of these line scans bear little resemblance to the scans in fig. 5.2. Thus the conclusion is that the net magnetisation of the tip portion of the assembly magnetised as in the Transverse Case does not settle along the direction of the magnetising field (i.e. along the cantilever axis).

The similarity between the shape of the integrated field line scans generated by the tip models of Chapter 4 and the scans in fig. 5.2, suggests that the tip models of Chapter 4 are possible models for the tip portion of the assembly magnetised as in the Transverse Case. However, the greater variation of the shape of the scans in fig. 5.2 than those in fig. 5.1 might suggest that the tip portion has a component of magnetisation directed along the axis of the cantilever. Thus we decided to investigate the integrated field line scans generated by tip models with a net magnetisation rotated away from the tip axis.

The model tips considered were constructed by combining the tip model magnetised as in the Axial Case (see fig. 4.5(a)) with any one of the tip models shown in figs. 5.4 to 5.6. The simulated integrated field line scans generated by these models were then compared to the deflection line scans in fig. 5.2.

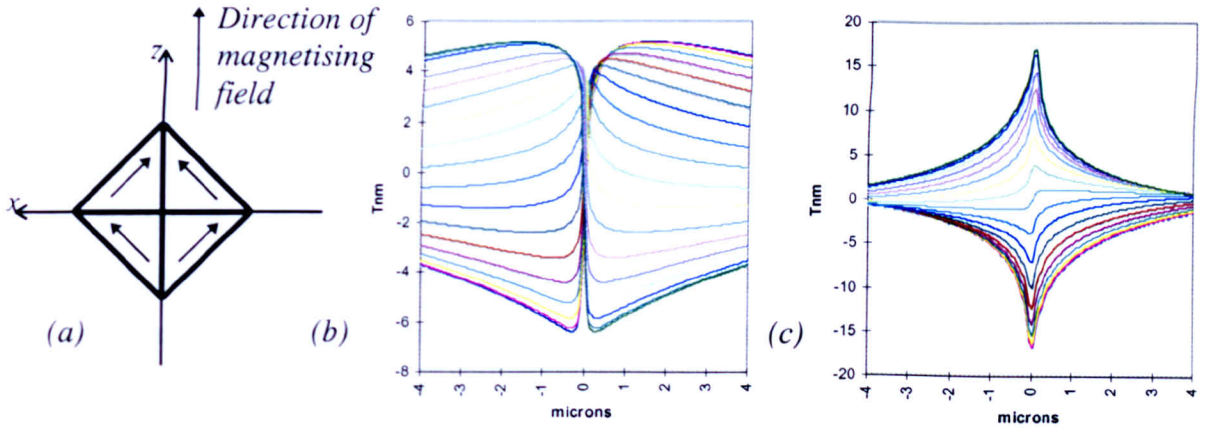


Fig. 5.4: (a) Possible magnetic configuration of the tip model magnetised as in the Transverse case. (b) Line scans sensitive to induction normal to the plane of reconstruction. (c) Line scans sensitive to induction in the plane of reconstruction.

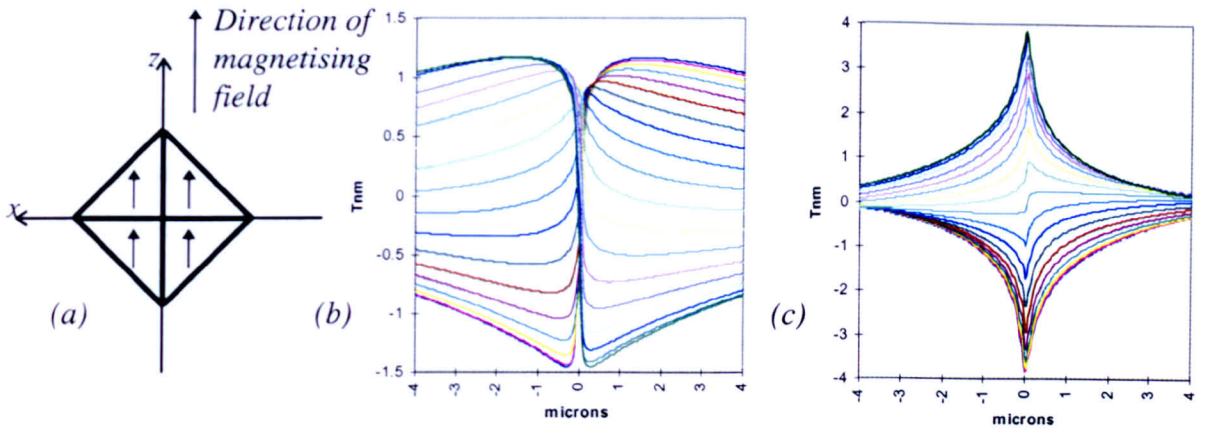


Fig. 5.5: (a) Another possible magnetic configuration of the tip model magnetised as in the Transverse case. (b) Line scans sensitive to induction normal to the plane of reconstruction. (c) Line scans sensitive to induction in the plane of reconstruction.

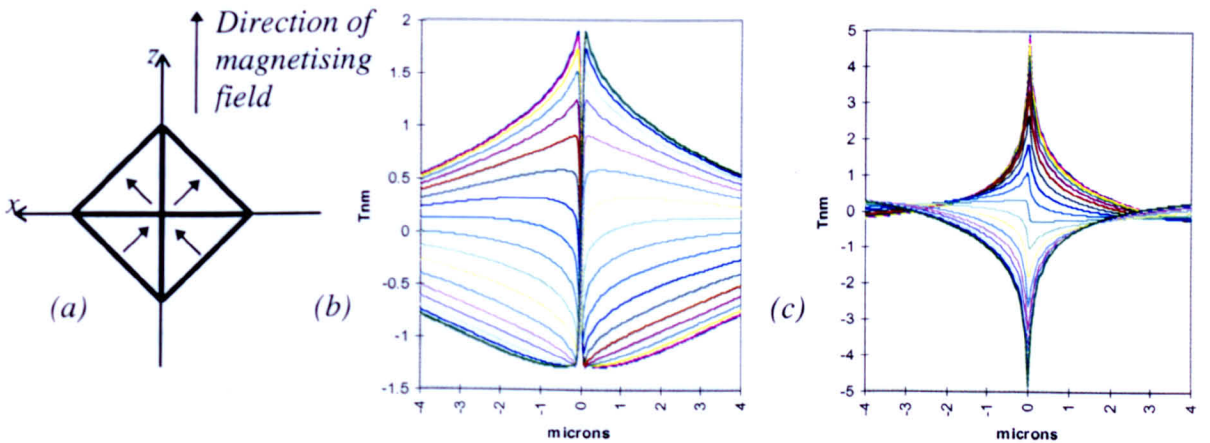


Fig. 5.6: (a) Another possible magnetic configuration of the tip model magnetised as in the Transverse case. (b) Line scans sensitive to induction normal to the plane of reconstruction. (c) Line scans sensitive to induction in the plane of reconstruction.

Fig. 5.7 shows a comparison of deflection line scans generated by the DI tip (sensitive to induction normal to the plane of reconstruction - see fig. 5.2) with the line scans generated from a tip model constructed by combining approximately 90% of the tip magnetised in the Axial Case (see Tip1 in fig. 4.5(a)) with 40% of the tip magnetised as in fig. 5.4 - these simulated contributions were combined in quadrature. Note that the size of the component contributions to the final model tip magnetisation were systematically deduced to give a best fit comparison between the simulated and experimental deflection data. An indication of the relative angular position of the tip for each line scan is given.

It is clear that the simulated line scans compare favourably with the experimental (DI tip) deflection data. Fig. 5.8 shows a comparison of the experimental deflection line scans (sensitive to induction in the plane of reconstruction) with the corresponding simulated scans generated by the same combination tip model. Once again the simulated line scans compare favourably with the experimental deflection data. Thus the suggestion is that the tip portion of the assembly magnetised as in the Transverse Case is predominately magnetised along the tip axis (even after it has been subjected to a large field applied along the cantilever axis). Our investigations suggest that the component of tip magnetisation directed along the cantilever axis is relatively small and the tip model magnetised as in fig. 5.4 is a possible model for this component.

Note that other models for the tip portion of the tip assembly magnetised as in the Transverse Case were constructed from a combination of the model tip magnetised as in the Axial Case with either of the tips in figs. 5.5 and 5.6 (these tip models are not shown here). The shapes of the simulated integrated field line scans generated again compared favourably with the experimental deflection line scans shown in figs. 5.7 and 5.8 (these simulated integrated field line scans are not shown here). We therefore conclude that the tip portion of the assembly magnetised as in the Transverse Case is predominantly magnetised along the tip axis. The component of magnetisation directed along the cantilever axis is small and it is not clear which of the models in figs. 5.4 to 5.6 best resembles this component.

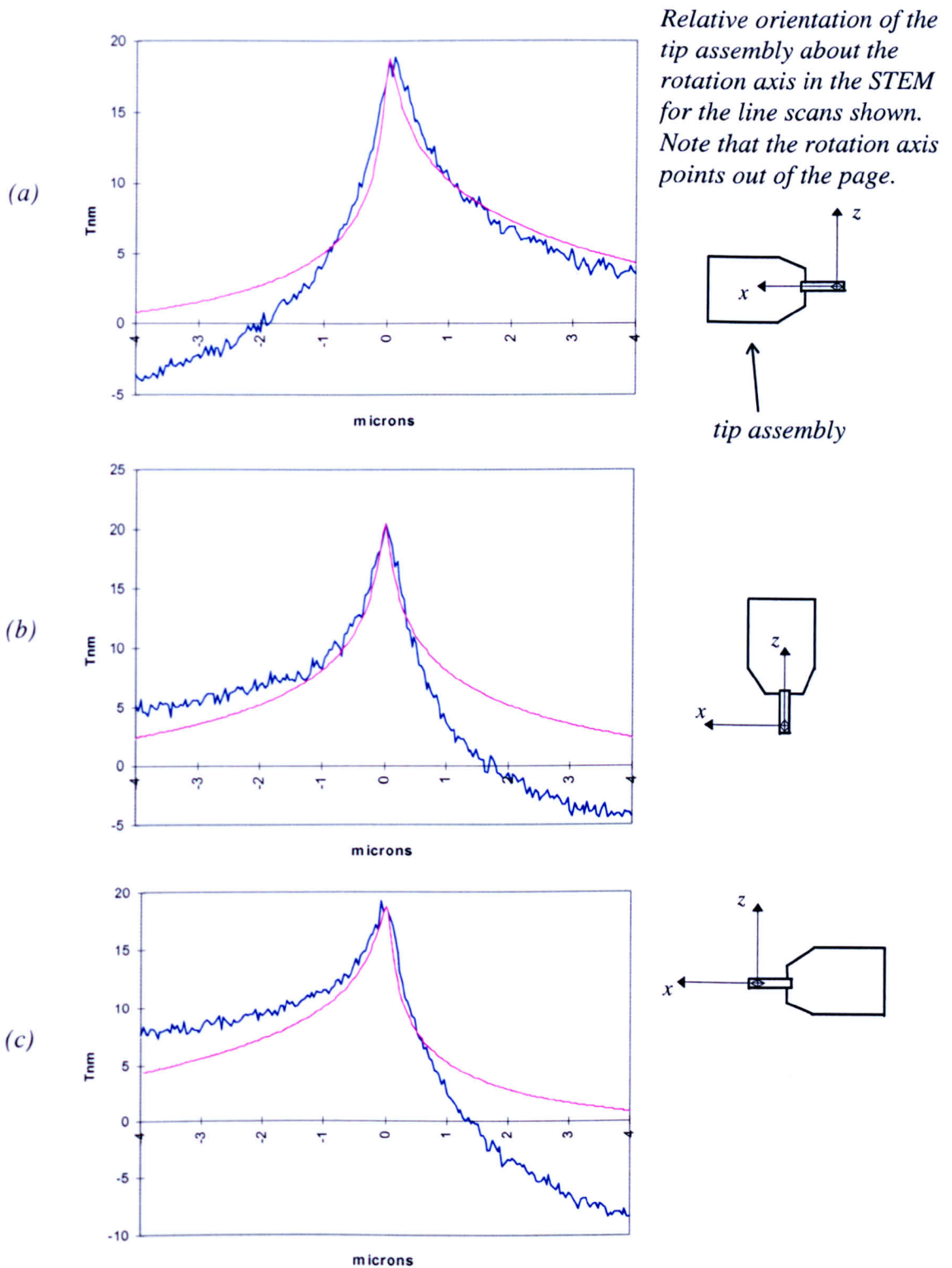


Fig. 5.7: Comparison of a selection of deflection line scans (sensitive to induction normal to the reconstruction plane) generated by the DI MFM tip assembly magnetised as in the Transverse Case with the simulated integrated field line scans generated by a model for the tip portion of the assembly also magnetised as in the Transverse Case.

The tip model was constructed by combining approximately 90% of the tip model magnetised as the Axial Case with 40% of the tip magnetised as in fig. 5.4(a). Note that the deflection line scans generated by the DI tip - which are taken from the data set in fig. 5.2(a) - have had a constant deflection value subtracted from them. The value subtracted was the average value of the end-points of the scans.

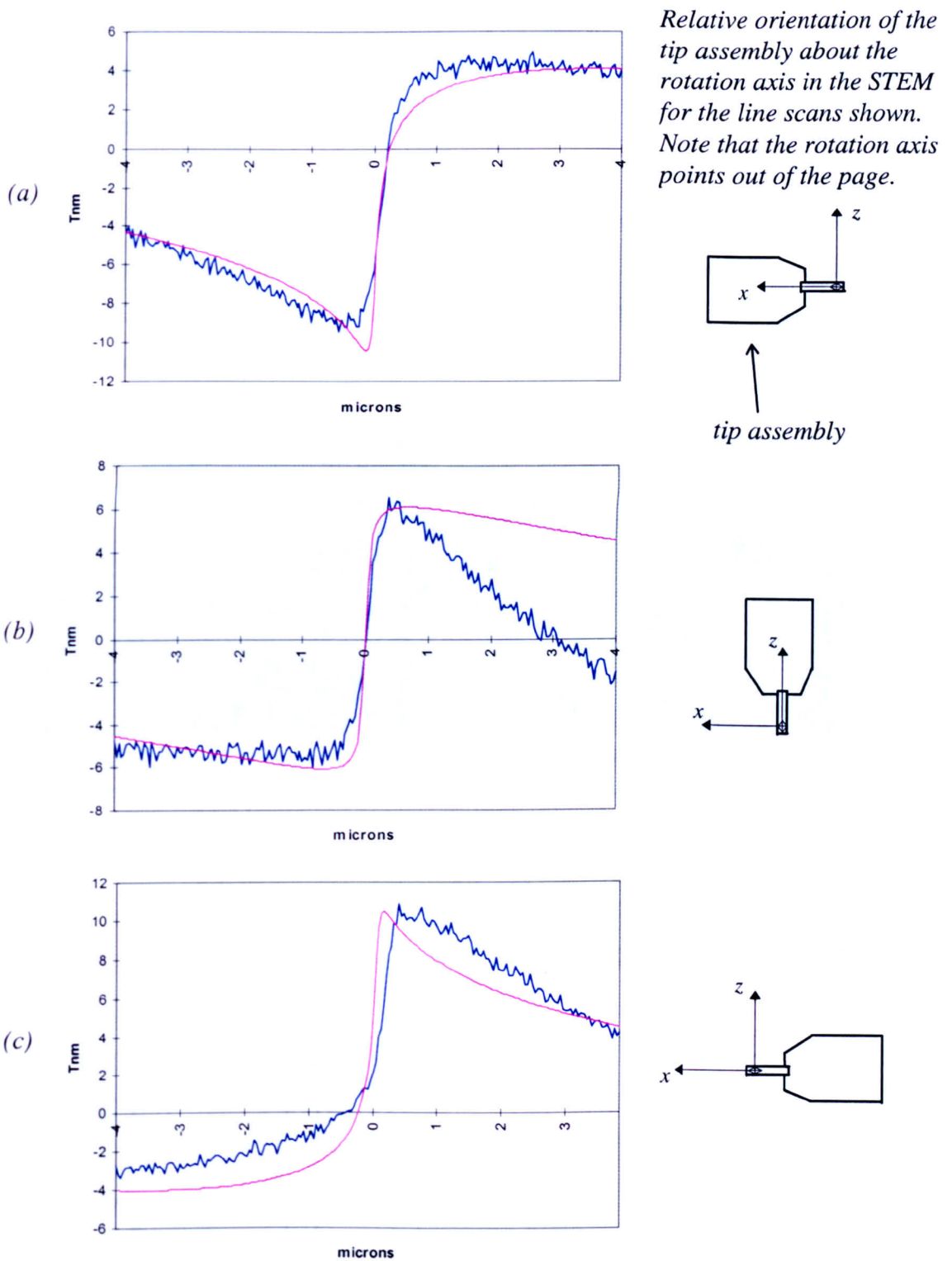
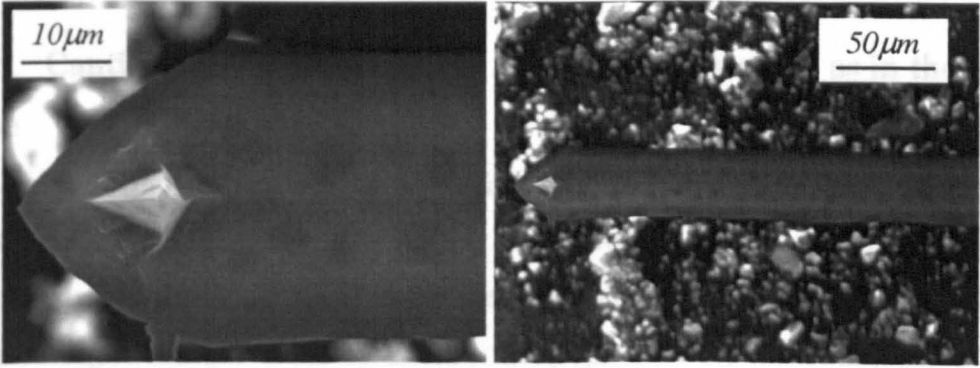


Fig. 5.8: Comparison of a selection of deflection line scans (sensitive to induction in the plane of reconstruction) generated by the DI MFM tip assembly magnetised as in the Transverse Case with the simulated integrated field line scans generated by a model for the tip portion of the assembly also magnetised as in the Transverse Case. The tip model was constructed by combining approximately 90% of the tip model magnetised in the Axial Case with 40% of the tip magnetised as in fig. 5.4(a). Note that the deflection line scans generated by the DI tip - which are taken from the data set in fig. 5.2(b) - have had a constant deflection value subtracted from them. The value subtracted was the average value of the end-points of the scans.

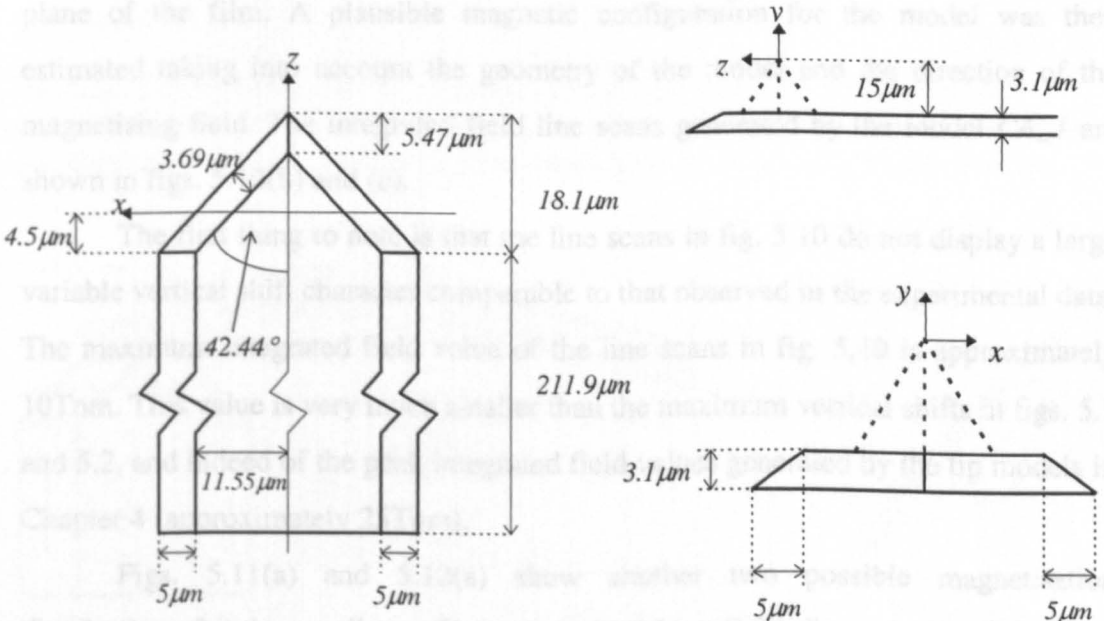
5.3 Cantilever Contribution to the Experimental Deflection Data Set Generated by a MFM Tip Assembly

In this section we consider possible magnetic configurations of the cantilever film and the stray fields and integrated stray fields which they generate. Figs. 5.9(a) and (b) show SEM images of the cantilever portion from which the dimensions of a model were determined - see fig. 5.9(c).



(a) SEM image of tip and cantilever. View looking down onto the top of the tip.

(b) Another SEM image of tip and cantilever. View looking down onto the top of the tip.



(c) Diagram of cantilever model.

Fig. 5.9: SEM images of the cantilever portion of the tip assembly and the cantilever model determined from them.

In all the following calculations it is assumed that only the top surface of the cantilever (the side with the tip attached) is coated in a CoCr alloy with a saturation magnetisation equivalent to a saturation induction of 0.5T. Therefore each of the five individual faces on the top surface of the cantilever model is coated with a thin film of the same thickness. The method used to calculate the stray field from the thin films attached to the cantilever model is similar to the method described in section 4.2.

5.3.1 Cantilever Portion of the Tip Assembly Magnetised as in the Axial Case

A number of models for the cantilever film magnetised as in the Axial Case were constructed and a selection of them are considered in the following. Fig. 5.10(a) shows one possible magnetisation for the cantilever model (i.e. model *CA_1*); the magnetising field was directed out of the page. For the determination of this magnetic configuration it was assumed that the magnetisation of each of the five individual thin films which make up the cantilever model were magnetised in the plane of the film. A plausible magnetic configuration for the model was then estimated taking into account the geometry of the model and the direction of the magnetising field. The integrated field line scans generated by the model *CA_1* are shown in figs. 5.10(b) and (c).

The first thing to note is that the line scans in fig. 5.10 do not display a large variable vertical shift character comparable to that observed in the experimental data. The maximum integrated field value of the line scans in fig. 5.10 is approximately 10Tnm. This value is very much smaller than the maximum vertical shifts in figs. 5.1 and 5.2, and indeed of the peak integrated field values generated by the tip models in Chapter 4 (approximately 25Tnm).

Figs. 5.11(a) and 5.12(a) show another two possible magnetisation distributions for the cantilever film magnetised by a field directed out of the page (i.e. models *CA_2* and *CA_3*). The same criteria as used in the construction of the previous model was also used here. Therefore the magnetic configurations of models *CA_2* and *CA_3* were again estimated taking into account the geometry of the model

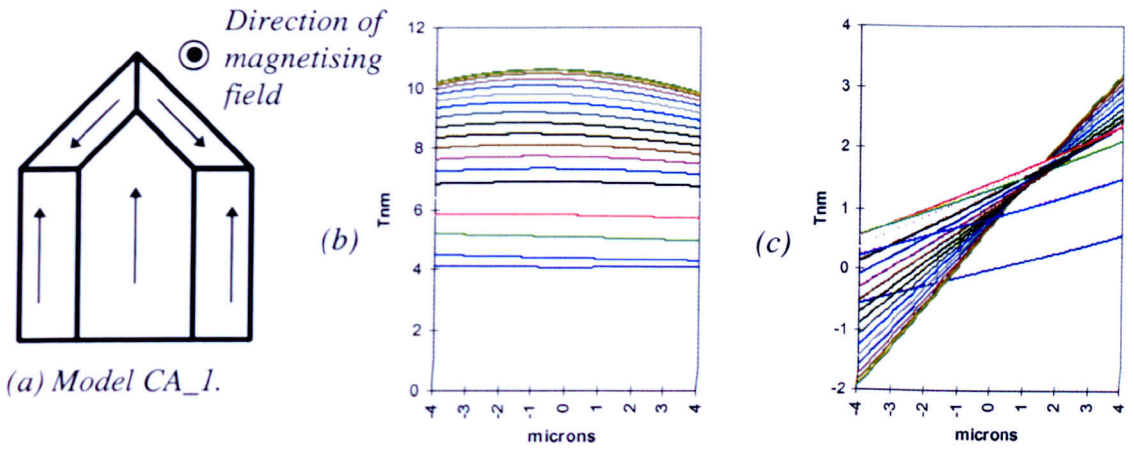


Fig. 5.10: (a) A possible magnetic configuration of the cantilever model magnetised as in Axial Case. (b) Line scans sensitive to induction normal to the plane of reconstruction. (c) Line scans sensitive to induction in the plane of reconstruction.

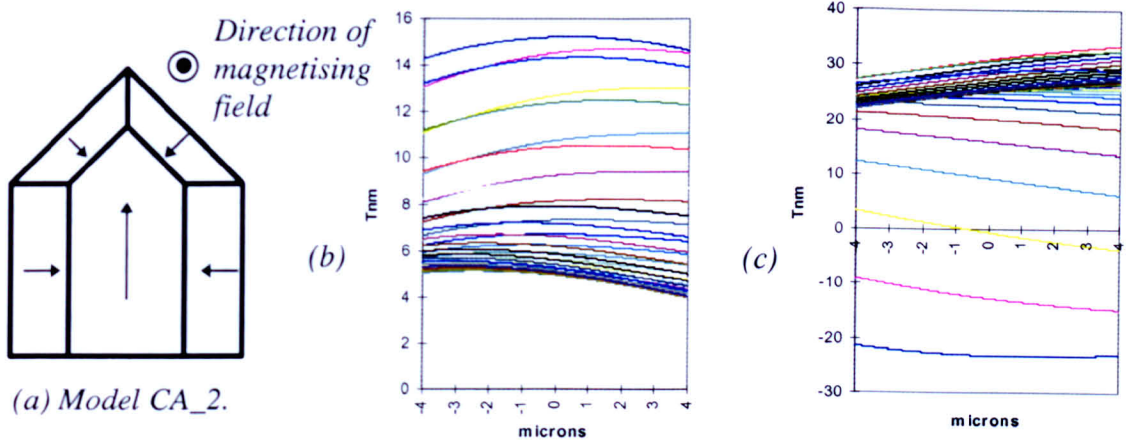


Fig. 5.11: (a) Another possible magnetic configuration of the cantilever model magnetised as in Axial Case. (b) Line scans sensitive to induction normal to the plane of reconstruction. (c) Line scans sensitive to induction in the plane of reconstruction.

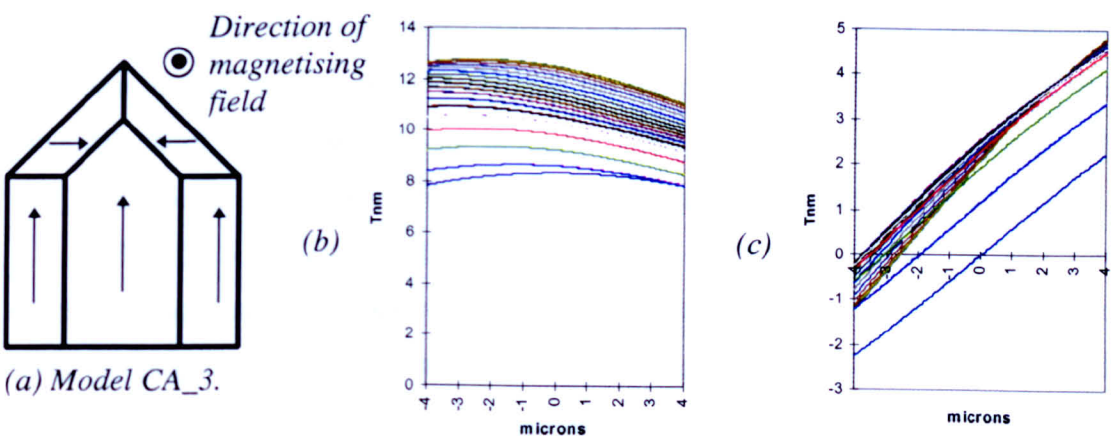


Fig. 5.12: (a) Another possible magnetic configuration of the cantilever model magnetised as in Axial Case. (b) Line scans sensitive to induction normal to the plane of reconstruction. (c) Line scans sensitive to induction in the plane of reconstruction.

and the direction of the magnetising field. The integrated field line scans generated by these models are shown in figs. 5.11(b) and (c) and figs. 5.12(b) and (c).

Once again note that in both cases the line scans generated by the models do not display a large variable vertical shift character comparable to that in figs. 5.1 and 5.2. The maximum integrated field values of the simulated line scans is again much smaller than the maximum vertical shifts in figs. 5.1 and 5.2, and of the peak integrated field values generated by the model tips in Chapter 4.

Thus the cantilever models discussed above (i.e. models *CA_1*, *CA_2* and *CA_3*) cannot explain the large vertical shifts observed in the experimental line scans and we may conclude that it must be the magnetisation of the substrate film which is responsible. Nevertheless we still need to be able to determine the contribution from the cantilever film to the tip assembly's deflection data sets and consequent reconstructed stray field. In order to help decide on the best model it was decided to simulate the 2-D distribution of integrated field in the vicinity of the tip and to compare this with the observed integrated induction.

Two DPC image pairs of part of the tip and cantilever portion of the DI tip assembly were chosen from a full rotation data set of low magnification images of the tip assembly magnetised as in the Axial Case - see figs. 5.13(a) and (c), (e) and (g). As usual the images in each pair were sensitive to induction in orthogonal directions. Investigations of the 2-D distribution of the integrated fields generated by models *CA_1*, *CA_2* and *CA_3* was undertaken. The integrated fields generated by the cantilever models *CA_1* and *CA_2* were found to compare unfavourably with the experimental deflection data (these comparisons are not shown here). This indicates that these models are not possible models for the magnetisation distribution of the practical cantilever. However, the integrated field generated by cantilever model *CA_3* was found to compare favourably with the experimental deflection data.

Fig. 5.13 shows the DPC image pairs of the DI MFM tip and the corresponding simulated images calculated from cantilever model *CA_3*. The first DPC image pair (see fig. 5.13(a) and (c) for the experimental DPC image pair and fig. 5.13(b) and (d) for the corresponding simulated DPC image pair) is of the tip and cantilever oriented such that the view is looking down the axis of the cantilever. The second DPC image pair (see fig. 5.13(e) and (g) for the experimental DPC image pair

Experimental DPC images

Simulated DPC images

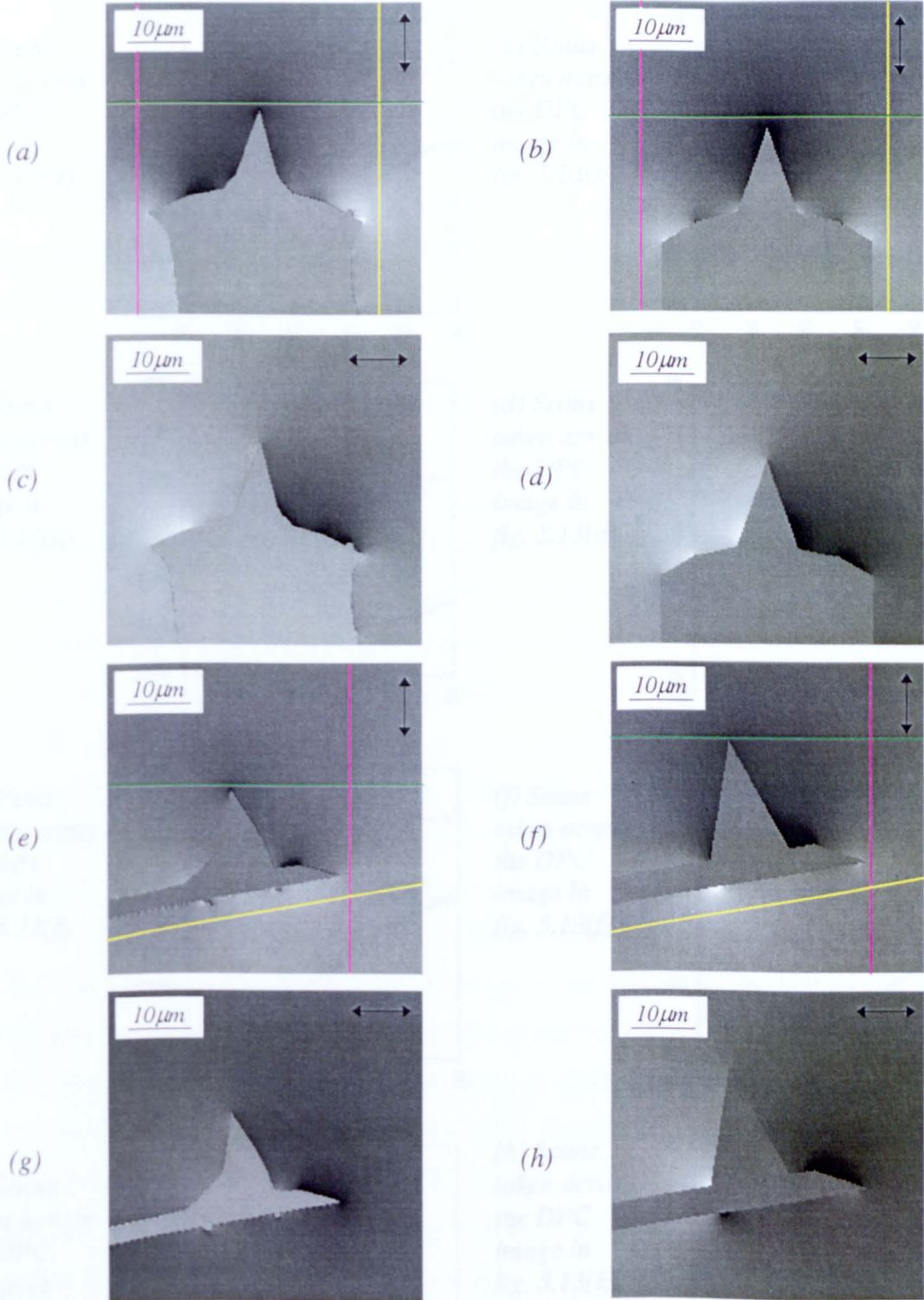


Fig.5.13: (a) and (c), (e) and (f) Low magnification DPC image pairs (separated by 90° about the rotation axis) from the full rotation data set of the tip and cantilever portions of the DI tip assembly magnetised as in the Axial Case.

(b) and (d), (f) and (h) Corresponding simulated low magnification DPC image pairs calculated from the models Tip1 and cantilever model CA_3.

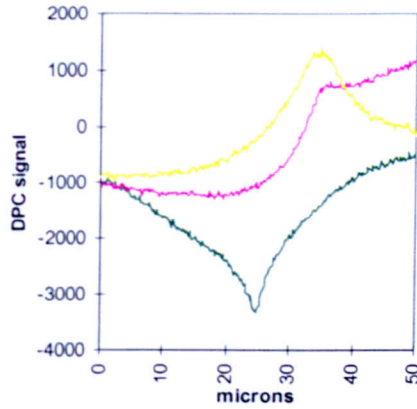
Arrows indicate direction of induction sensitivity.

Coloured lines indicate where the scans in fig. 5.14 were taken on the above images.

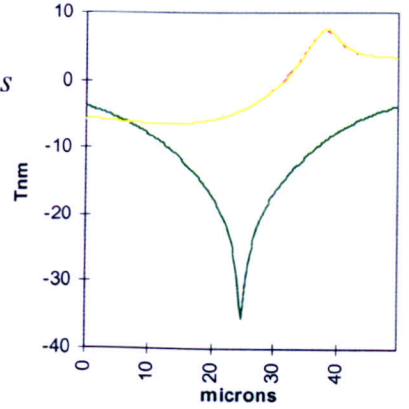
**Experimental
deflection line scans**

**Simulated
deflection line scans**

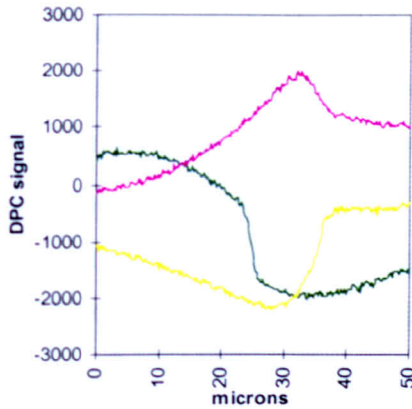
(a) Scans taken across the DPC image in fig. 5.13(a).



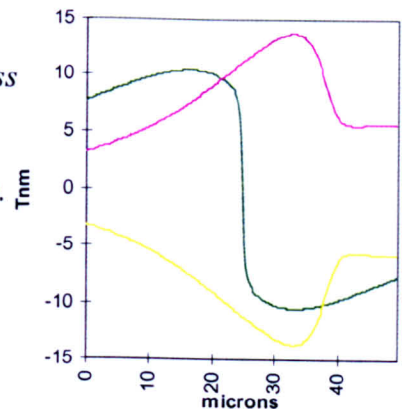
(b) Scans taken across the DPC image in fig. 5.13(b).



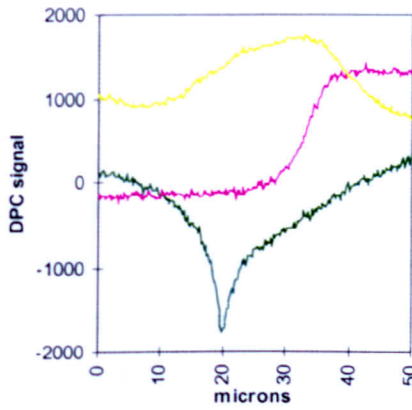
(c) Scans taken across the DPC image in fig. 5.13(c).



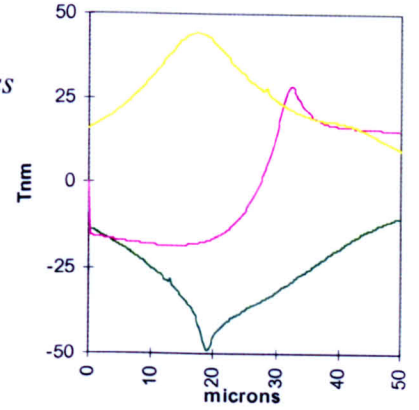
(d) Scans taken across the DPC image in fig. 5.13(d).



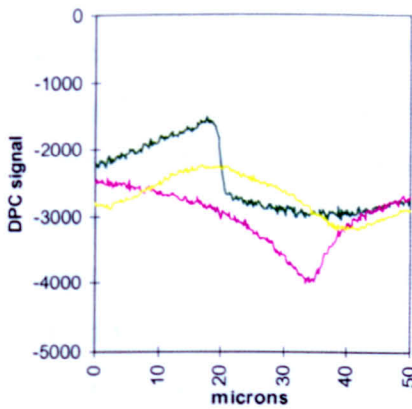
(e) Scans taken across the DPC image in fig. 5.13(f).



(f) Scans taken across the DPC image in fig. 5.13(f).



(g) Scans taken across the DPC image in fig. 5.13(g).



(h) Scans taken across the DPC image in fig. 5.13(h).

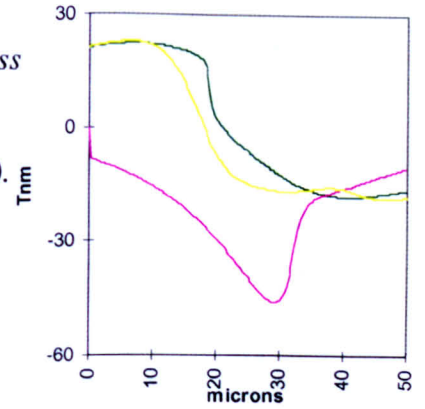


Fig. 5.14: Scans taken across the simulated and experimental DPC images in fig. 5.13. Note that the coloured lines in fig. 5.13 indicate where on the images the above scans were taken.

and fig. 5.13(f) and (h) for the corresponding simulated DPC image pair) is at 90° to this about the rotation axis. Note that the tip model used in the simulated DPC images was Tip1 from Chapter 4 (see fig. 4.5).

A visual comparison of the images in fig. 5.13 suggests that there is reasonable qualitative agreement between the corresponding simulated and experimental DPC images. For a further comparison, line scans were taken across the DPC images and are shown in fig. 5.14 (an indication of where the scans were taken on the images is given). It is clear from these scans that there is good agreement between the character of the simulated and experimental deflection data.

Note that the contribution to the experimental DPC images from the substrate portion of the DI tip assembly has not been taken into account in the simulated DPC images. Also, note that the magnetic domains in the model cantilever film are extended over a larger area than we might expect in a practical situation (notice the variation of DPC contrast along the edges of the DI cantilever in fig. 5.13 - this is consistent with what we expect from substantially smaller magnetic domains than the model cantilever domains⁽¹⁾). These are two possible reasons that the agreement between the simulated and experimental deflection data is not better. Nevertheless, we conclude that the cantilever model CA_3 is a possible model for the cantilever portion of the tip assembly magnetised as in the Axial Case.

Note that the tip model used in the simulated DPC images is coated with CoCr thin film of 40nm thickness. This tip model generates integrated field line scans of comparable magnitude and FWHM to the line scans in fig. 5.1 (ignoring the variable vertical shift). However in order to obtain simulated DPC images of comparable contrast to the experimental DPC images, the thin film coating on the cantilever model was required to be 120nm thick, that is 3 times the thickness of the thin film coating the tip. This may suggest that the sputtering of thin film onto the tip assembly is uneven. The steep sloping sides of the tip relative to the cantilever may be coated with a thinner film than the cantilever. The model therefore suggests that a further experimental investigation into the thickness of thin film coating the different portions of the tip assembly is required.

An alternative explanation for the larger than expected cantilever contribution to the tip assembly deflection data set is that (with the thickness of film coating the

tip and cantilever portions the same) the practical cantilever film has extended magnetic volume and surface charge regions not accounted for in the model. The magnetic volume charges ($\nabla \cdot \underline{M}$) arise in regions where the divergence of the cantilever film magnetisation (\underline{M}) is non zero (i.e. $\nabla \cdot \underline{M} \neq 0$). Further surface charges ($\underline{M} \cdot \underline{n}$) may arise from the fact that the practical cantilever film is not as smooth as the model film (see the underside of the cantilever in the DPC images in fig. 5.3) and as a result has a larger amount of surface charges than the model. We now briefly consider the character of the stray field generated from the cantilever model CA_3.

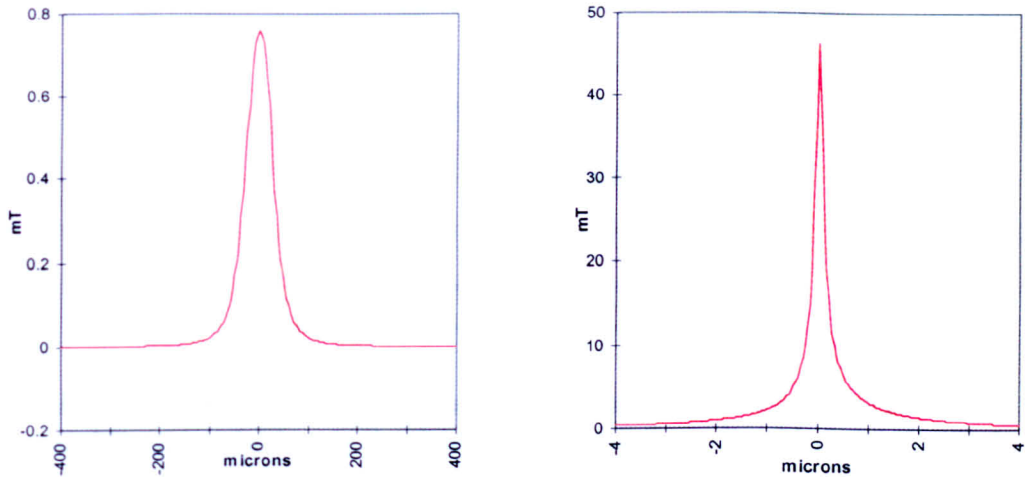
Fig. 5.15(a) shows a field scan (of the component of field normal to the plane of reconstruction) calculated directly from the cantilever model CA_3 at the plane of reconstruction. Fig. 5.15(b) shows a corresponding field scan (of the component of field normal to the plane of reconstruction) calculated directly from the tip model (i.e. model Tip1 used in the simulated DPC images in fig. 5.13) at the plane of reconstruction.

In the vicinity of the peak tip field (i.e. on the reconstruction plane), the field from the cantilever is less than 1mT and varies by less than 0.1mT. The peak tip field on the reconstruction plane is 46mT. Thus, the models suggest that the cantilever field on the reconstruction plane is small (being less than 2% of the peak tip field) and effectively constant (since changes in the cantilever field of the order of 0.1mT can be considered to be insignificant in a practical experiment).

Now consider the horizontal axes on the graphs shown in fig. 5.15. Note that in fig. 5.15(a) the field scan component calculated from the cantilever model is 800 μm in length, while the scan in fig. 5.15(b), calculated from the tip model, is only 8 μm in length. The FWHM of the field scan in fig. 5.15(a) is approximately 57 μm , while the corresponding FWHM of the scan in fig. 5.15(b) is approximately 220nm.

Thus the tip field immediately in front of the tip dominates over the field from the cantilever. However, the large spread of the cantilever field ensures its field integrals are significant as figs. 5.12(b) and (c) show. Furthermore, note that since the tip field tends to zero at infinity faster than the field from the cantilever, the cantilever field in fact becomes the dominant contribution to the stray field at

distances of greater than approximately $20\mu\text{m}$ from the tip. In Chapter 6 we consider the effect that the cantilever (and substrate) contribution to the tip assembly's deflection data sets has on the accuracy of the (ART and RTM) reconstructed tip field. Firstly however, we consider possible magnetisation distributions for the practical cantilever film magnetised as in the Transverse Case.



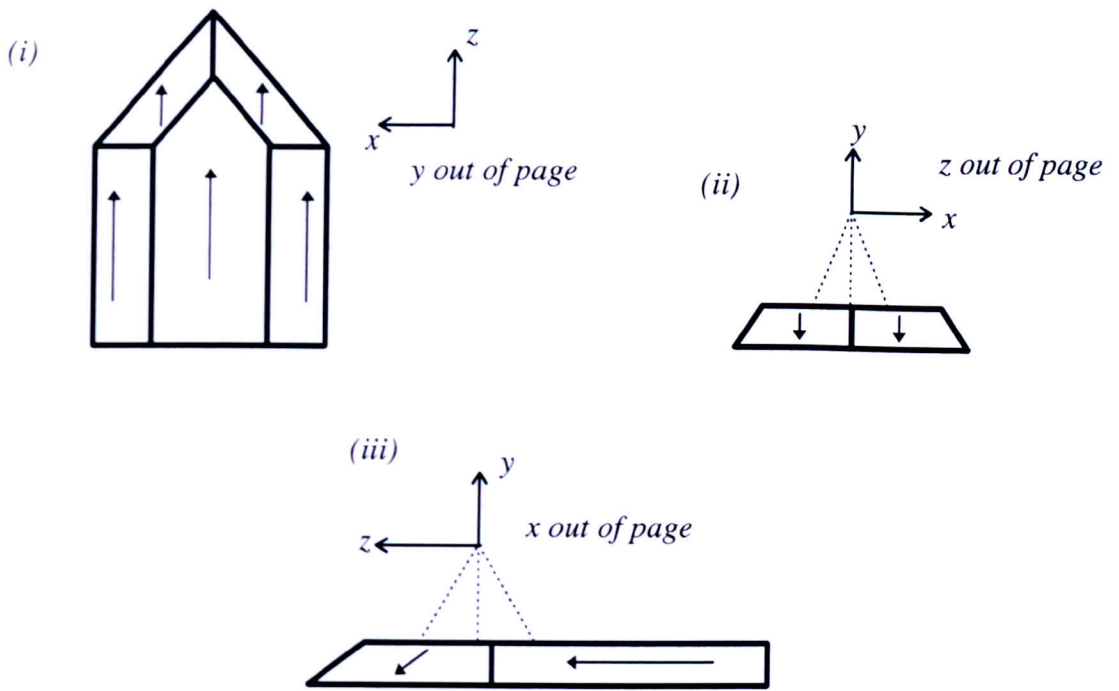
(a) Field scan calculated directly from the cantilever model at the reconstruction plane.

(b) Field scan calculated directly from the tip model at the reconstruction plane.

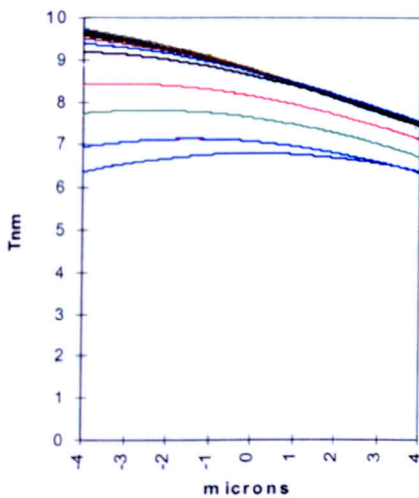
Fig. 5.15: Field scan components calculated in the plane of reconstruction from cantilever model CA_3 and model Tip1.

5.3.2 Cantilever Portion of the Tip Assembly Magnetised as in the Transverse Case

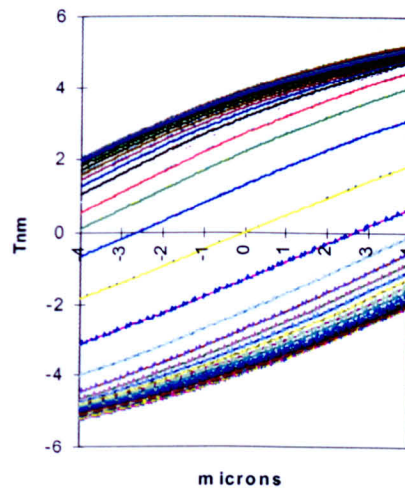
For the cantilever film magnetised as in the Transverse Case only two models were constructed. Fig. 5.16(a) shows one of these models (model CT_1); the magnetising field was directed along the cantilever axis as indicated. For the determination of this magnetic configuration it was again assumed that the magnetisation of each of the five individual thin films which make up the cantilever model were magnetised in the plane of the film. A plausible magnetisation for the model was then estimated taking into account the geometry of the model and the direction of the magnetising field. The integrated field line scans generated by model CT_1 are shown in figs. 5.16(b) and (c).



(a) Possible magnetic configuration of the cantilever portion of the tip assembly magnetised as in the Transverse Case. Note that the magnetising field is directed along the positive z direction. (i),(ii) and (iii) are different views of the cantilever magnetisation.



(b) Simulated integrated field line scans generated by the cantilever model. Scans sensitive to induction normal to the plane.



(c) Simulated integrated field line scans generated by the cantilever model, sensitive to induction in the plane of reconstruction.

Fig. 5.16: A possible magnetic configuration of the cantilever model magnetised as in the Transverse Case and the integrated field line scans generated.

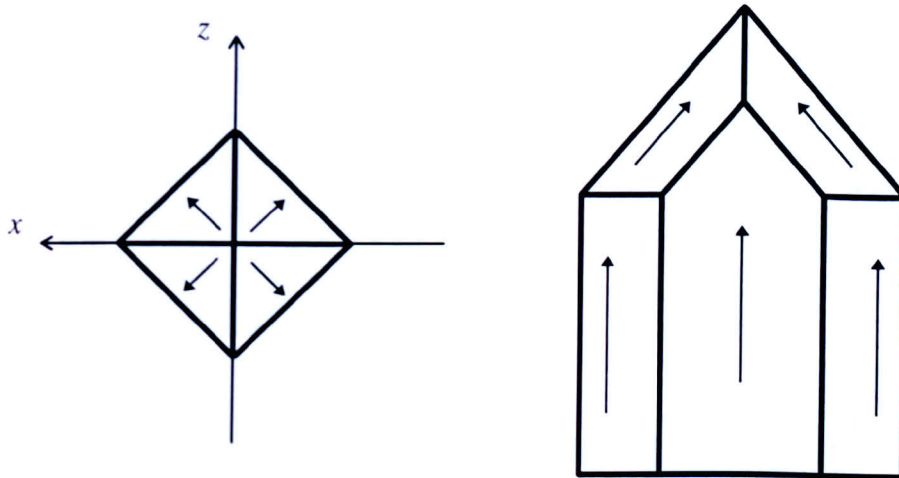
Once again the magnitude and distribution of the line scans does not compare favourably with the scans in figs. 5.1 and 5.2. A comparison of the 2-D distribution of integrated field from CT_1 with the observed induction (this comparison is not shown here) also gave poor agreement. This indicates that cantilever model *CT_1* is not a suitable model for the cantilever film magnetised as in the Transverse Case.

The second model for the cantilever film magnetised as in the Transverse Case - model *CT_2* - is shown in fig. 5.17(a). Note that the same criteria as used in the construction of the previous cantilever models was also used in this case. An investigation of the 2-D distribution of the integrated field from the model cantilever was again undertaken.

Thus once again two DPC image pairs of part of the tip and cantilever portion of the DI MFM tip assembly were taken from a full rotation data set of low magnification images of the DI MFM tip assembly magnetised as in the Transverse Case - see figs. 5.18(a) and (c), (e) and (g). As usual the images in each pair were sensitive to induction in orthogonal directions.

Fig. 5.18 shows these experimental DPC image and the corresponding simulated images calculated from cantilever model *CT_2*. The first DPC image pair (see fig. 5.18(a) and (c) for the experimental DPC image pair and fig. 5.18(b) and (d) for the corresponding simulated DPC image pair) is of the tip and cantilever oriented in such a way that the view is looking down the axis of the cantilever. The second DPC image pair (see fig. 5.18(e) and (g) for the experimental DPC image pair and fig. 5.18(f) and (h) for the corresponding simulated DPC image pair) are at 90° about the rotation axis. Note that fig. 5.17(a) shows the magnetic configuration of the tip portion of the simulated DPC images. The tip model again has identical dimensions to that of Tip1 in Chapter 4. Also, the direction of the model tip's magnetisation is reversed from the Axial Case. This is required so that the contrast in the simulated DPC images from the tip and cantilever models is consistent with the contrast observed in the experimental DPC images.

A visual comparison of the images in fig. 5.18 suggests that there is reasonable qualitative agreement between the simulated and experimental DPC images. Once again line scans were taken across the simulated and experimental



(a) Magnetic configurations of the tip and cantilever models used in the simulated DPC images of the Transverse Case in figs. 5.18. Note that the magnetising field is directed along the positive z direction.

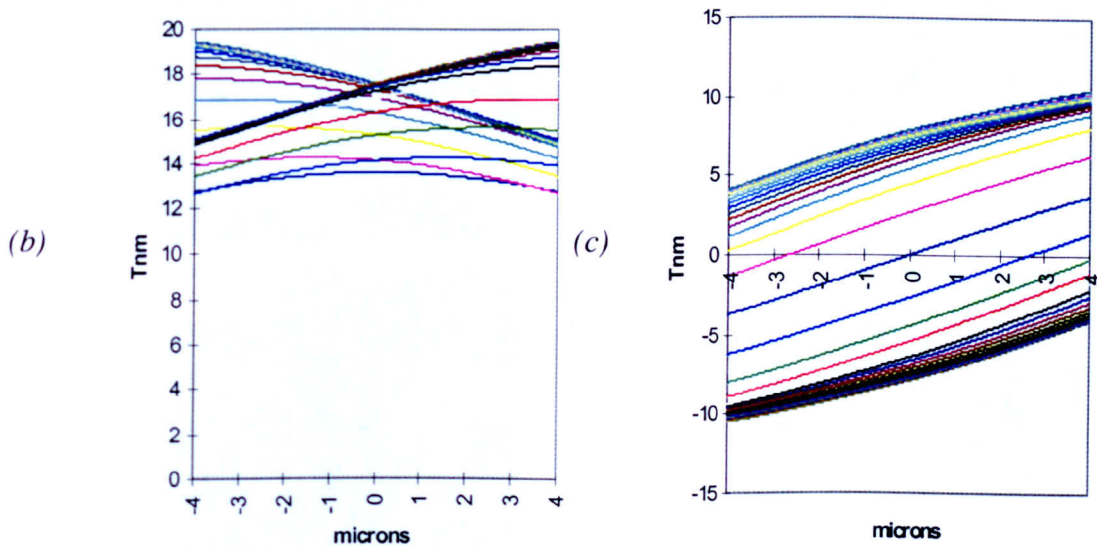


Fig. 5.17: (a) Cantilever and tip models which resemble most closely tip assembly magnetised as in the Transverse Case. (b) Line scans sensitive to induction normal to the plane of reconstruction generated by the cantilever model. (c) Line scans sensitive to induction in the plane of reconstruction generated by the cantilever model.

Experimental DPC images

Simulated DPC images

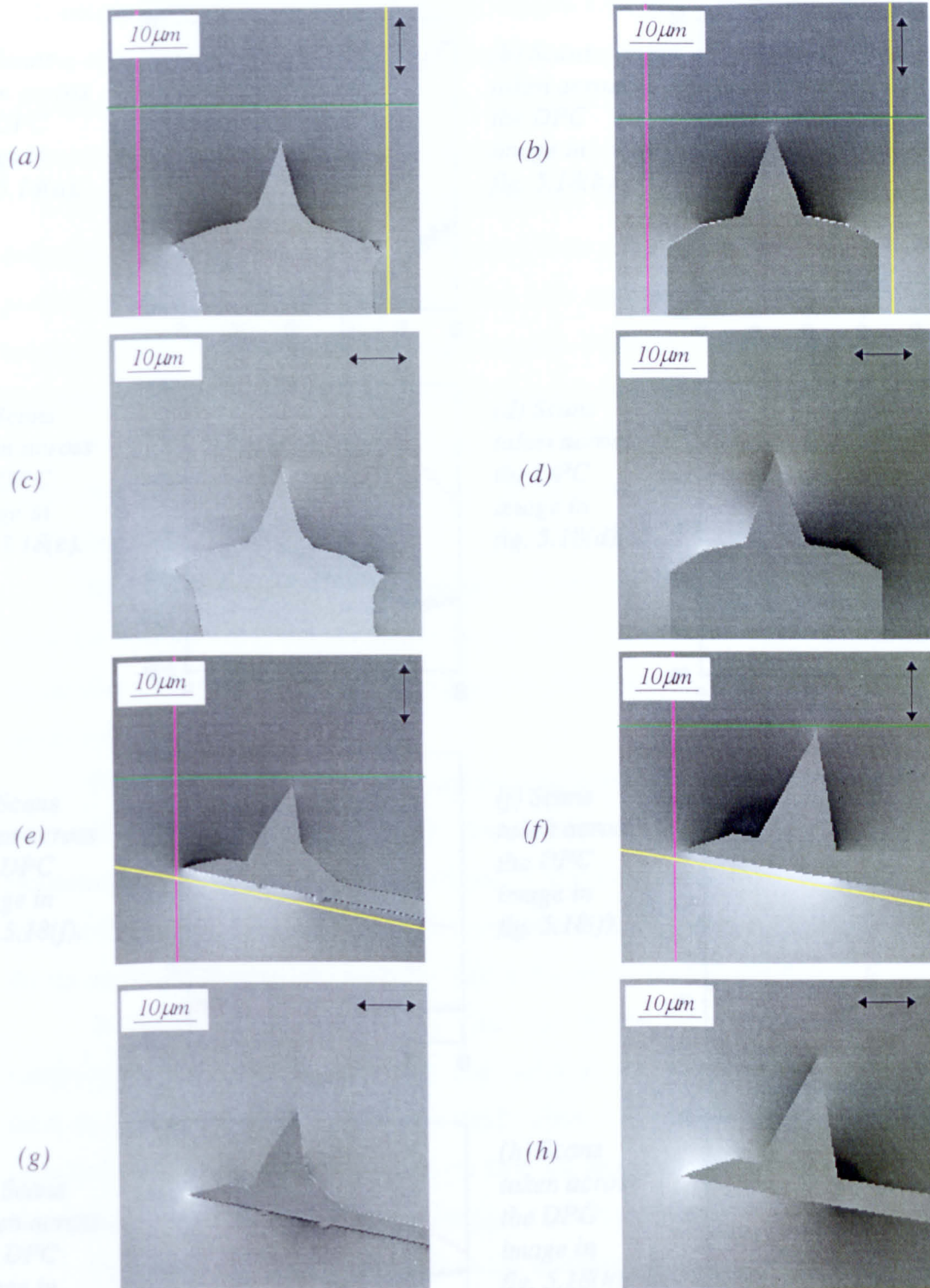


Fig.5.18: (a) and (c), (e) and (f) Low magnification DPC image pairs (separated by 90° about the rotation axis) from the full rotation data set of the tip and cantilever portions of the DI tip assembly magnetised as in the Transverse Case.

(b) and (d), (f) and (h) Corresponding simulated low magnification DPC image pairs calculated from the tip model in fig. 5.17 and cantilever model CT_1. Arrows indicate direction of induction sensitivity. Coloured lines indicate where the scans in fig. 5.19 were taken on the above images.

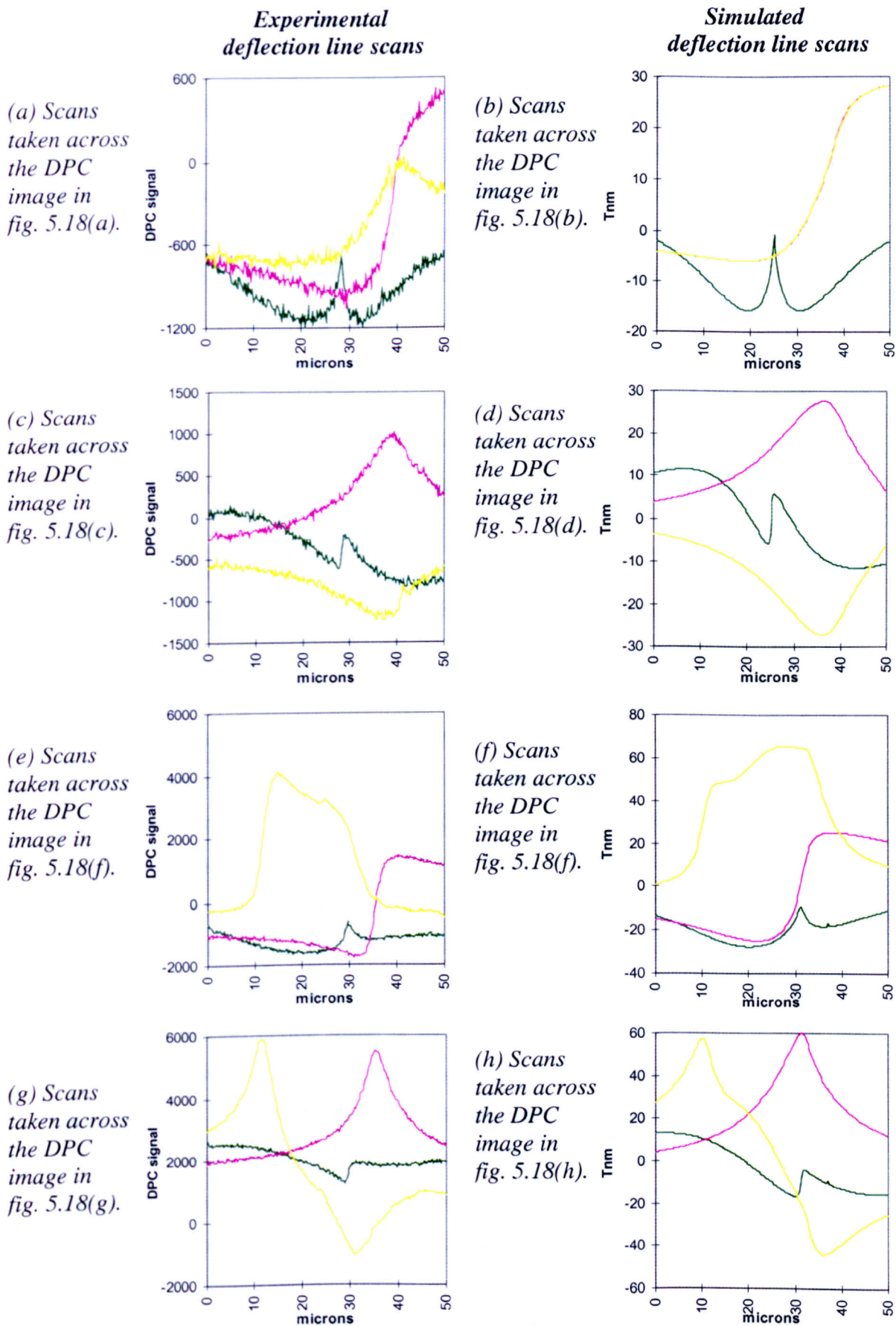


Fig. 5.19: Scans taken across the simulated and experimental DPC images in fig. 5.18. Note that the coloured lines in fig. 5.18 indicate where on the images the above scans were taken.

DPC images and are shown in fig. 5.19 (an indication of where the scans were taken on the image is given in fig. 5.18). From a comparison of the corresponding simulated and experimental scans in fig. 5.19 it is clear that there is very good agreement between the character of the simulated and experimental DPC images.

Once again note that the agreement between the simulated and experimental deflection data could have been improved upon if the contribution from the substrate portion of the tip assembly had been taken into account in the simulated DPC images. Further modification of the large magnetic domains of the model cantilever film may also have improved the agreement between the simulated and experimental deflection data^[1]. Nevertheless, cantilever model *CT_2* is taken to be a possible model for the cantilever portion of the DI tip assembly magnetised as in the Transverse Case.

Note that the magnetic film coating the cantilever model was 120nm thick, 3 times the thickness of the film coating the tip model (see Section 5.3.1 for possible explanations for this). We now briefly consider the character of the stray field from cantilever model *CT_2*.

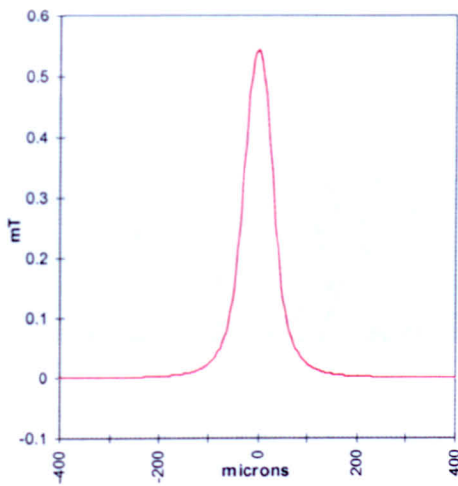
Fig. 5.20(a) shows a field scan (of the component of field normal to the plane of reconstruction) calculated directly from the cantilever model *CT_2* at the reconstruction plane. Fig. 5.20(b) shows a corresponding field scan (of the component of field normal to the plane of reconstruction) calculated directly from the tip model (magnetised as in fig. 5.17(a)) at the reconstruction plane.

In the vicinity of the peak tip field (i.e. on the reconstruction plane) the cantilever field is again less than 1mT and varies by less than 0.1mT. The peak tip field on the reconstruction plane is -46mT. Thus, the models again suggest that (similar to the Axial Case) the cantilever field on the reconstruction plane is small (being less than of 2% of the peak tip field) and effectively constant.

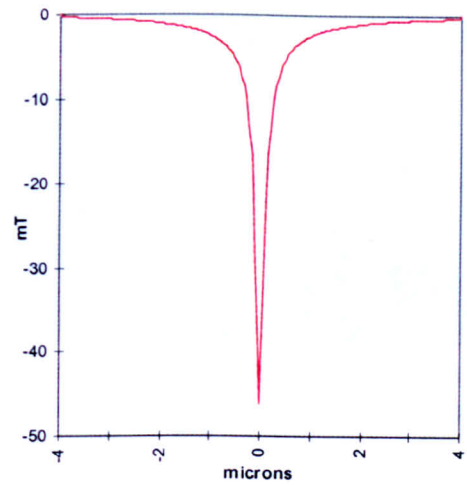
Now consider the horizontal axes on the graphs shown in fig. 5.20. Once again note that in fig. 5.20(a) the field scan calculated from the cantilever model is 800 μ m in length, while the scan in fig. 5.20(b) calculated from the tip model is 8 μ m in length.

We therefore conclude that the tip field immediately in front of the tip dominates over the field from the cantilever. However, the large spread of the

cantilever field ensures its field integrals are significant as figs. 5.17(b) and (c) show. Furthermore, since the tip field tends to zero at infinity faster than the field from the cantilever, the field from the cantilever becomes the dominant contribution to the stray field at distances of greater than approximately $20\mu\text{m}$ from the tip. We now consider possible magnetisation distributions for the substrate film magnetised as in the Axial and Transverse Cases.



(a) Field scan calculated directly from the cantilever model at the reconstruction plane.

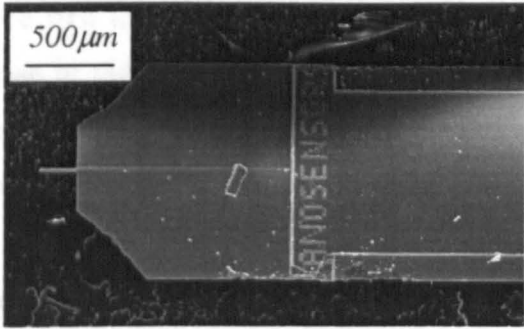


(b) Field scan calculated directly from the tip model at the reconstruction plane.

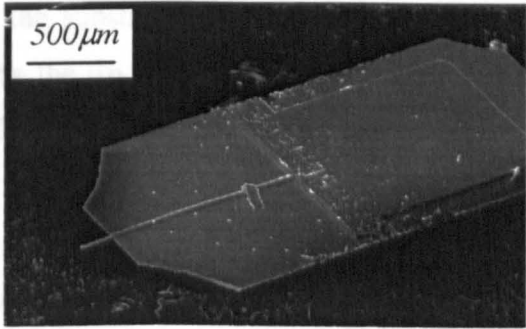
Fig. 5.20: Field scan components calculated in the plane of reconstruction from the cantilever model CT_2 and the tip model in fig. 5.17.

5.4 Substrate Contribution to the Experimental Deflection Data Set Generated by a MFM Tip Assembly

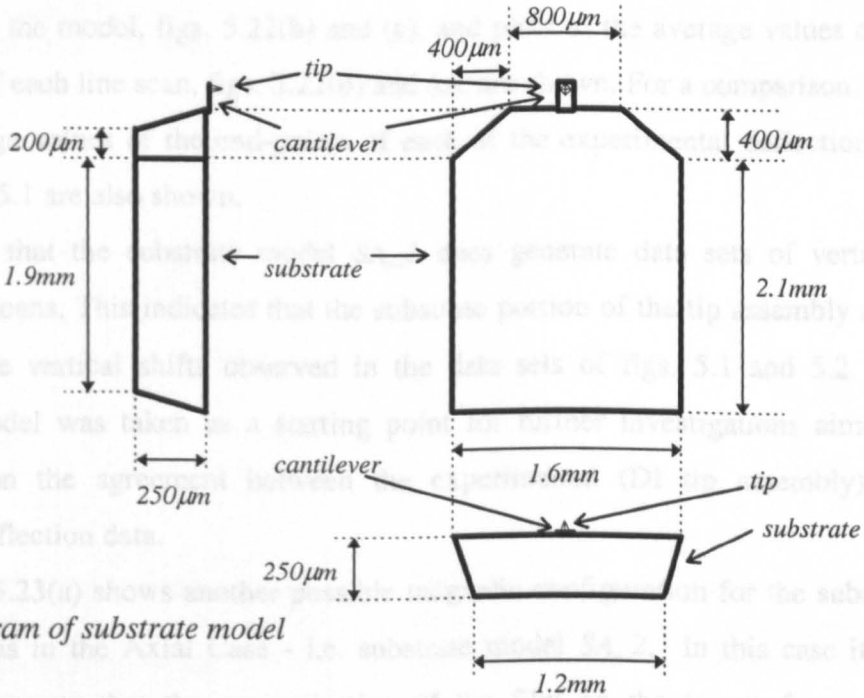
From the models considered in the previous sections the implication is that the vertical offset of the scans in figs. 5.1 and 5.2 must originate from the magnetic material attached to the substrate portion of the tip assembly. Figs. 5.21(a) and (b) show SEM images of the substrate from which the dimensions of a model were determined - see figs. 5.21(c).



(a) SEM image of the cantilever and substrate. View looking down onto top surface of the substrate.



(b) Another SEM image of the cantilever and substrate. View looking down onto the top surface of the substrate.



(c) Diagram of substrate model

Fig. 5.21: SEM images of the substrate portion of the tip assembly and the substrate model determined from them.

In all the following calculations the top surface and sides of the substrate are coated with a film of 120nm thickness. The film is the same CoCr alloy as used in the previous tip and cantilever models. The method used to calculate the stray field from the thin films attached to the substrate model is similar to the method described in section 4.2.

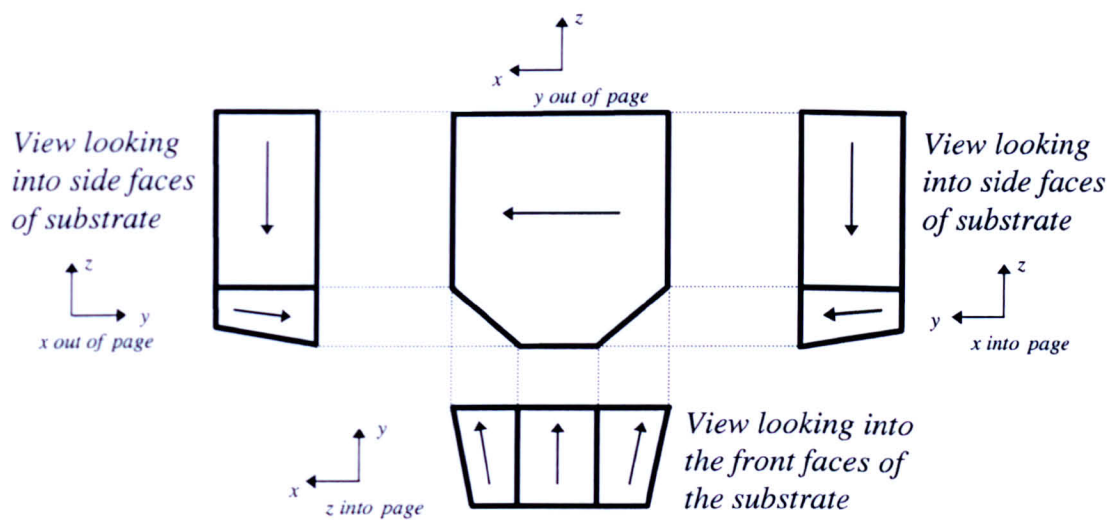
5.4.1 Substrate Portion of the Tip Assembly Magnetised as in the Axial Case

We first investigated possible models for the substrate film magnetisation for the case of the magnetising field directed along the tip axis. For each substrate model constructed it was assumed that the individual films which make up the model were magnetised in the plane of the film.

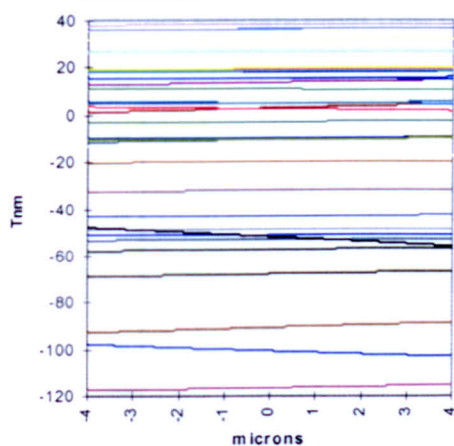
The first substrate model - *SA_1* - which generated a distribution of integrated field line scans comparable to the vertical distribution of the experimental deflection line scans in fig. 5.1 is shown in fig. 5.22(a). The magnetisation distribution of this model was estimated by taking into account the geometry of the model and the direction of the magnetising field. The integrated field line scans generated by the model, figs. 5.22(b) and (c), and plots of the average values of the end-points of each line scan, figs. 5.22(d) and (e), are shown. For a comparison, plots of the average values of the end-points of each of the experimental deflection line scans in fig. 5.1 are also shown.

Note that the substrate model *SA_1* does generate data sets of vertically shifted line scans. This indicates that the substrate portion of the tip assembly is the source of the vertical shifts observed in the data sets of figs. 5.1 and 5.2. This substrate model was taken as a starting point for further investigations aimed at improving on the agreement between the experimental (DI tip assembly) and simulated deflection data.

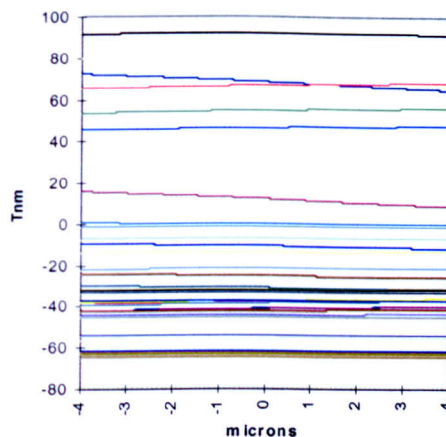
Fig. 5.23(a) shows another possible magnetic configuration for the substrate magnetised as in the Axial Case - i.e. substrate model *SA_2*. In this case it was decided to assume that the magnetisation of the film on the top surface of the substrate was in a flux closure configuration; therefore there are no free magnetic



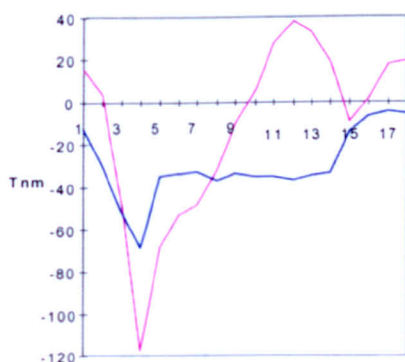
(a) Exploded plan view of model SA_1 - magnetising field directed along positive y direction.



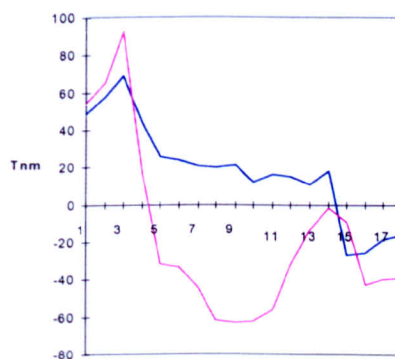
(b) Integrated field line scans (sensitive to induction normal to the plane of reconstruction) generated by the substrate model.



(c) Integrated field line scans (sensitive to induction in the plane of reconstruction) generated by the substrate model.

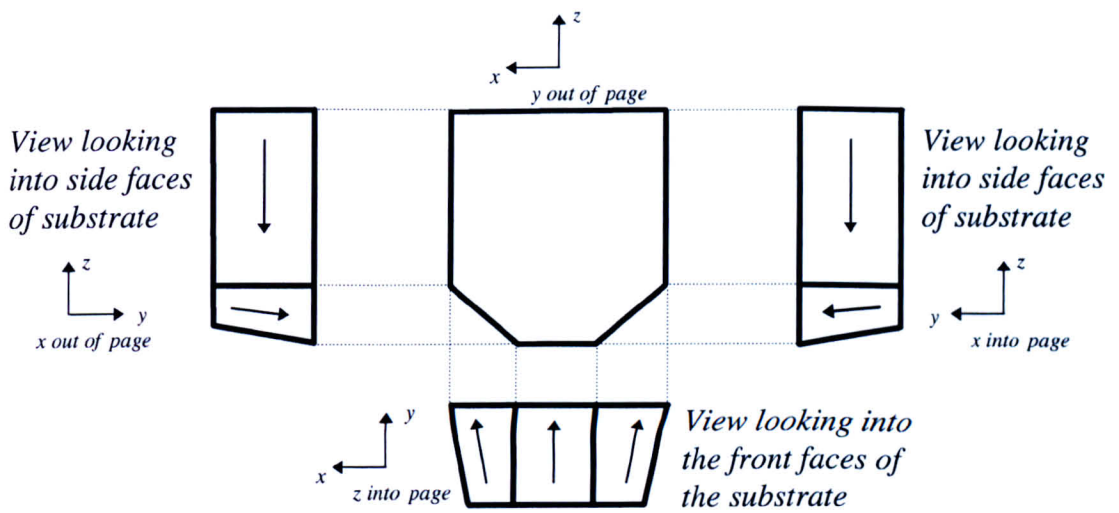


(d) Plots of the average value of the end-points of each scan in (b) and of the experimental scans in fig. 5.1(a)

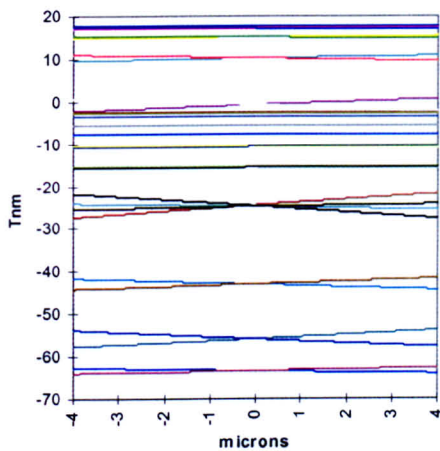


(e) Plots of the average value of the end-points of each scan in (c) and of the experimental scans in fig. 5.1(b)

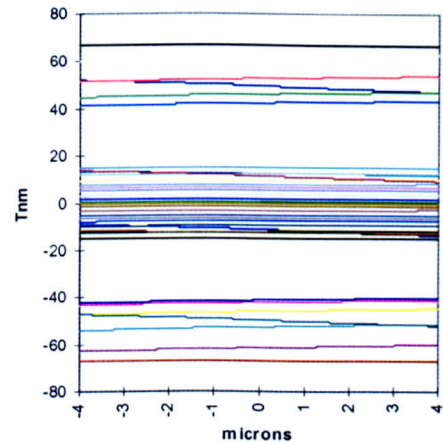
Fig. 5.22: A possible model for the substrate portion of the tip assembly magnetised as in the Axial Case. In (d) and (e), pink scans plot the average value of the end-points of the simulated scans, while blue scans plot the average value of the end-points of the experimental deflection line scans shown in fig. 5.1.



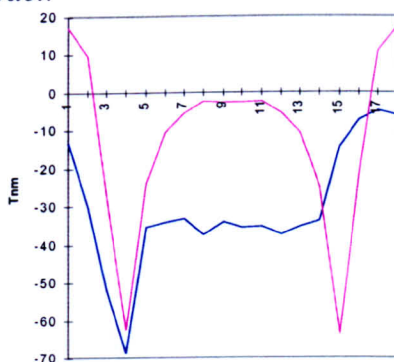
(a) Exploded plan view of model SA_2 - magnetising field directed along positive y direction. Note: the magnetisation of the film on the top surface of the substrate is in a flux closure configuration (therefore there are no free magnetic poles on this film).



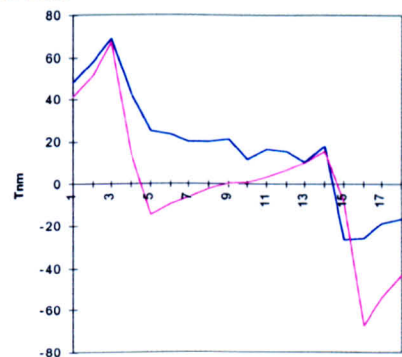
(b) Integrated field line scans (sensitive to induction normal to the plane of reconstruction) generated by substrate model.



(c) Integrated field line scans (sensitive to induction in the plane of reconstruction) generated by substrate model.

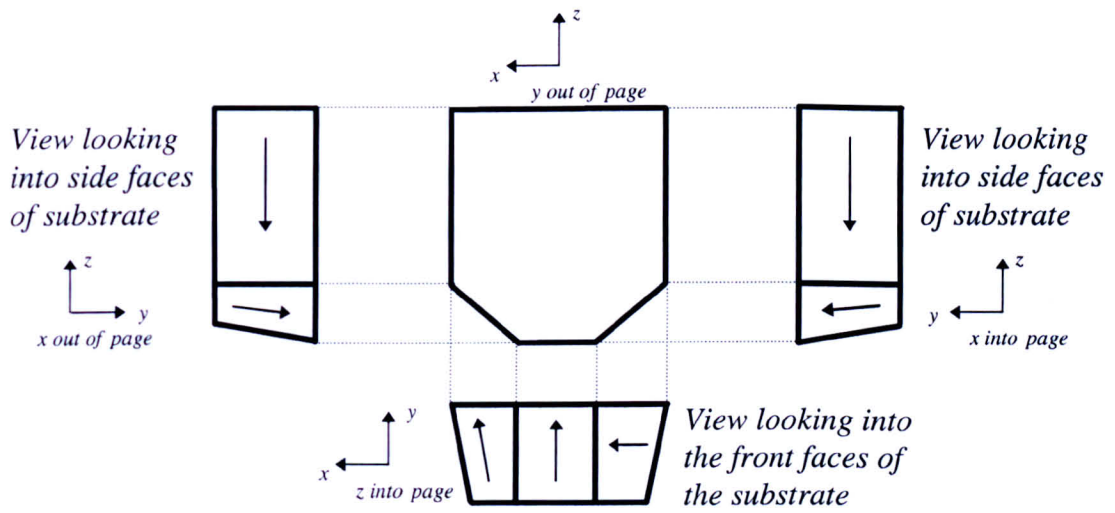


(d) Plots of the average value of the end-points of each scan in (b) and of the experimental scans in fig. 5.1(a)

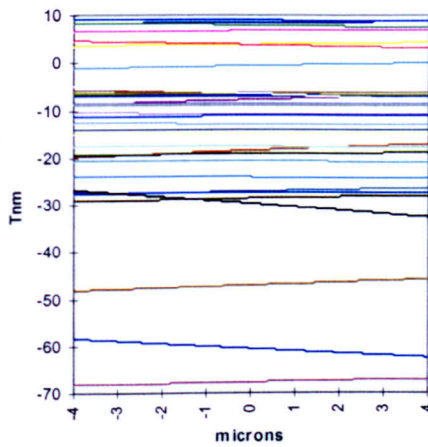


(e) Plots of the average value of the end-points of each scan in (c) and of the experimental scans in fig. 5.1(b)

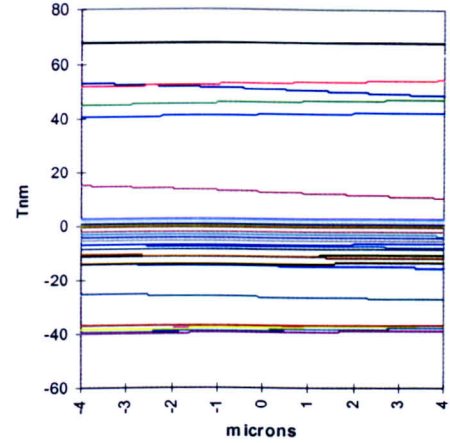
Fig. 5.23: Another possible model for the substrate portion of the tip assembly magnetised as in the Axial Case. In (d) and (e), pink scans plot the average value of the end-points of the simulated scans, while blue scans plot the average value of the end-points of the experimental deflection line scans shown in fig. 5.1



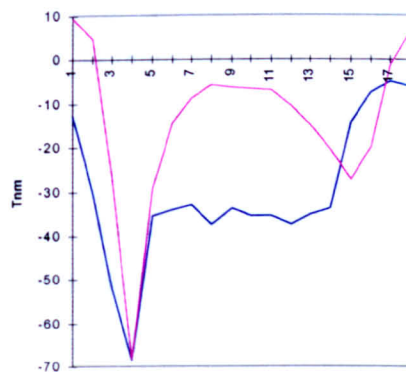
(a) Exploded plan view of model SA_3 - magnetising field directed along positive y direction. Again the magnetisation of the film on the top surface of the substrate is in a flux closure configuration (therefore there are no free magnetic poles on this film).



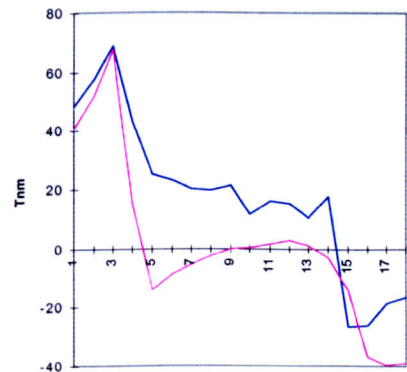
(b) Integrated field line scans (sensitive to induction normal to the plane of reconstruction) generated by substrate model.



(c) Integrated field line scans (sensitive to induction in the plane of reconstruction) generated by substrate model.



(d) Plots of the average value of the end-points of each scan in (b) and of the experimental scans in fig. 5.1(a).



(e) Plots of the average value of the end-points of each scan in (c) and of the experimental scans in fig. 5.1(b).

Fig. 5.24: Another model for the substrate portion of the tip assembly magnetised as in the Axial Case. In (d) and (e), pink scans plot the average value of the end-points of the simulated scans, while blue scans plot the average value of the end-points of the experimental deflection line scans shown in fig. 5.1.

poles on this film. This is a feasible assumption since the magnetising field is directed perpendicular to the plane of the film on this surface. The integrated field line scans generated by the model, figs. 5.23(b) and (c), and plots of the average value of the end-points of each of the simulated and experimental deflection line scans (in fig. 5.1), see figs. 5.23(d) and (e), are also shown.

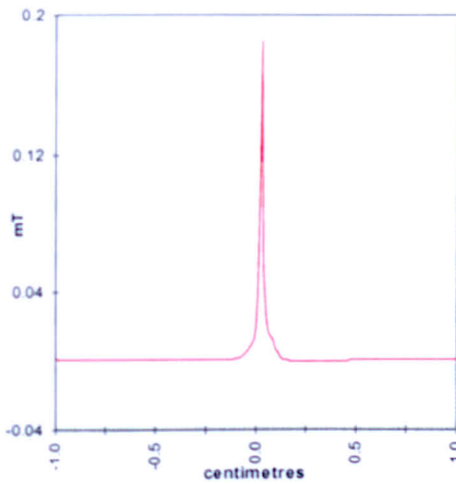
Once again the vertical distribution of the simulated line scans does compare reasonably with the experimental deflection data. This reinforces the suggestion that the substrate portion of the tip assembly is the source of the large variable vertical shift character of the experimental deflection line scans.

Using model SA_2 as a starting point and with the aim of improving the agreement between the simulated and experimental deflection data, several further models were constructed. Fig. 5.24(a) shows one these models - i.e. substrate model SA_3. Once again we assumed that the magnetisation of the film on the top surface of the substrate is in a flux closure configuration (and therefore there are no free magnetic poles on this film). The integrated field line scans generated by the model are shown in figs. 5.24(b) and (c), as are plots of the average values of the end points of the simulated and experimental deflection line scans in figs. 5.24(d) and (e).

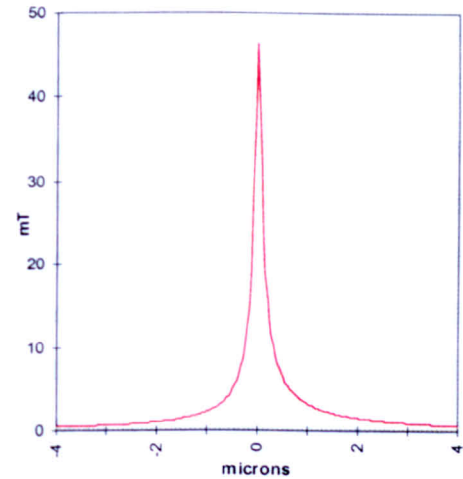
Note that model SA_3 generates a vertical distribution of simulated line scans which gives the closest agreement with the experimental deflection line scans in fig. 5.1. However, the agreement between the simulated and experimental deflection data could be improved by 1) including the contribution to the simulated deflection data sets from the tip and cantilever portions of the tip assembly, and 2) modifying the magnetic domain structure of the model substrate film since the existing model domains are larger than we might expect in a practical situation^[1]. Nevertheless, we conclude that the substrate model SA_3 is a possible model for the substrate portion of the tip assembly magnetised as in the Axial Case. We now consider the character of the stray field generated by substrate model SA_3.

Fig 5.25(a) shows a field scan (of the component of field normal to the plane of reconstruction) calculated directly from the substrate model SA_3 at the reconstruction plane. Fig. 5.25(b) shows a corresponding field scan (again of the component of field normal to the plane of reconstruction) calculated directly from model Tip1 (see fig. 4.5) at the reconstruction plane.

In the vicinity of the peak tip field (i.e. on the reconstruction plane) the substrate field is found to be of the order of 2×10^{-1} mT and varies by less than 10^{-2} mT. The peak tip field on the reconstruction plane is approximately 46 mT. Thus the suggestion is that in the vicinity of the tip, the field from the substrate portion of the tip assembly is small (being only a fraction of one percent of the peak tip field) and effectively constant (since changes in the substrate field of the order of than 10^{-2} mT are insignificant in a practical experiment).



(a) Field scan calculated directly from the substrate model at the reconstruction plane.



(b) Field scan calculated directly from the tip model at the reconstruction plane.

Fig. 5.25: Field scan components calculated in the plane of reconstruction from the substrate model SA_3 model and model Tip1.

Now consider the horizontal axes on the graphs shown in fig. 5.25. Note that in fig. 5.25(a) the field scan calculated from the substrate model is 2cm in length. While the scan in fig. 5.25(b), calculated from the tip model, is again only $8\mu\text{m}$ in length. Thus, the tip field immediately in front of the tip dominates over the field from the substrate. However, the large spread of the substrate field ensures its field integrals are significant as figs. 5.24(b) and (c) show. In Chapter 6 we consider the effect that the substrate (and cantilever) contribution to the tip assembly's deflection

data sets has on the accuracy of the reconstructed tip field. Firstly however, we consider possible magnetisation distributions for the practical substrate film magnetised as in the Transverse Case.

5.4.2 Substrate Portion of the Tip Assembly Magnetised as in the Transverse Case

Several models were constructed for the substrate portion of the tip assembly magnetised as in the Transverse Case. Fig. 5.26(a) shows one of these possible magnetic configurations for the substrate film - substrate model *ST_1*. As in the previous section it was assumed that the magnetisation of each of the magnetic films which make up the substrate model were magnetised in the plane of the film. A plausible magnetisation for the model was then estimated by taking into account the geometry of the model and the direction of the magnetising field. Note that the integrated field line scans generated from the model *ST_1* are shown in figs. 5.26(b) and (c) as well as plots of the average values of the end-points of the simulated line scans in figs. 5.26(d) and (e) (for comparison plots of the average values of the end-points of the experimental line scans in figs. 5.2 are also shown).

Once again note that the line scans generated by substrate model *ST_1* are vertically shifted by a variable amount. This again reinforces the suggestion that the substrate portion of the tip assembly is indeed the source of the vertical shift character of the scans in the experimental deflection data sets of figs. 5.1 and 5.2. Furthermore, note from both figs. 5.26(d) and (e) that a comparison of the average values of the end points of the simulated line scans with the average values of the end points of the experimental line scans in fig. 5.2 indicates that the vertical distribution of the simulated scans does compare favourably with that of the experimental deflection line scans.

Again note that the agreement between the simulated and experimental deflection data could have been improved upon if the contribution to the simulated integrated field from the tip and cantilever portions of the tip assembly had been taken into account. Further modification of the large domain configurations of the model substrate film may also have improved the agreement between the simulated

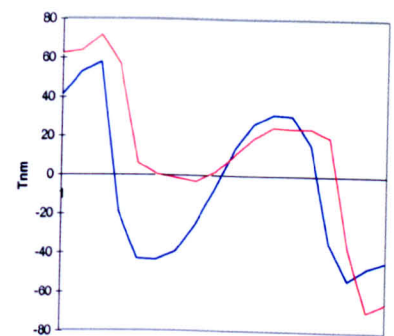
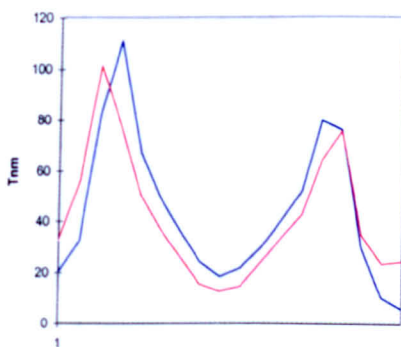
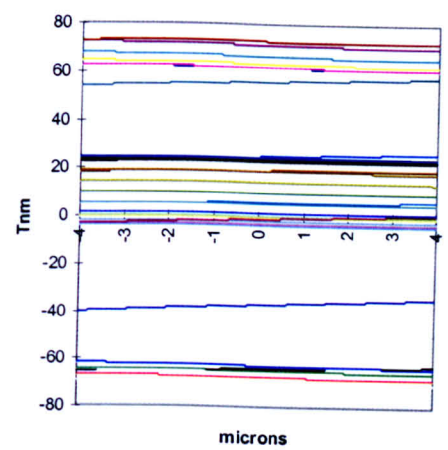
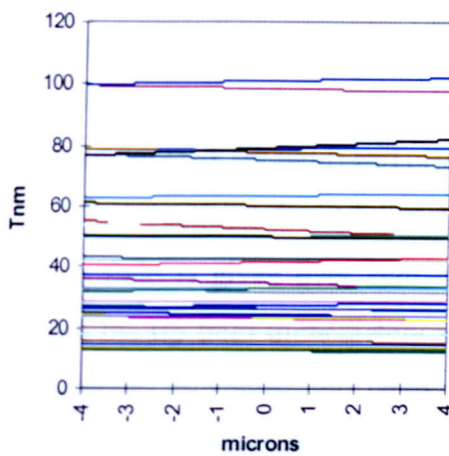
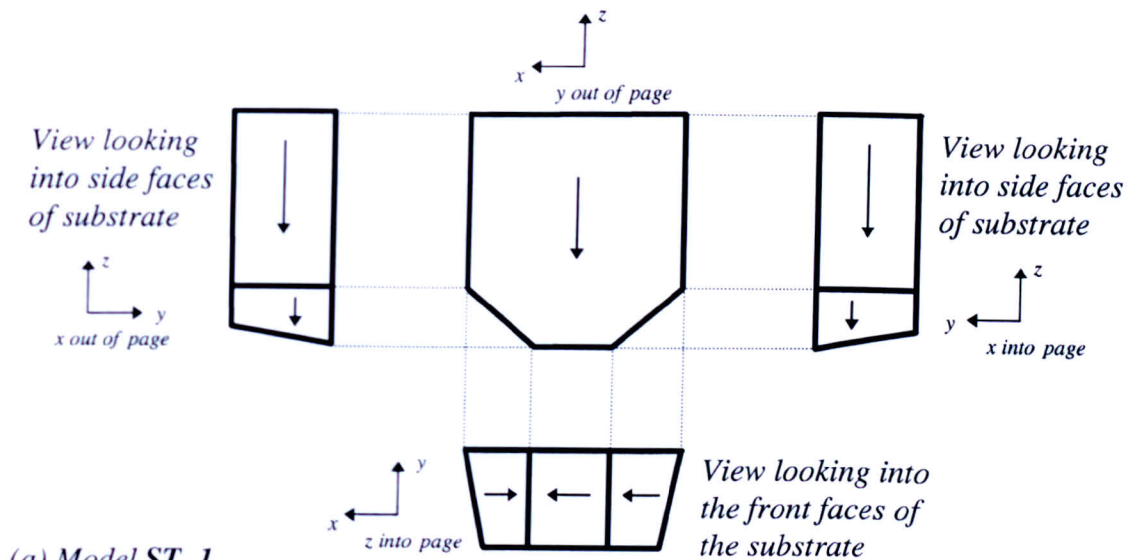


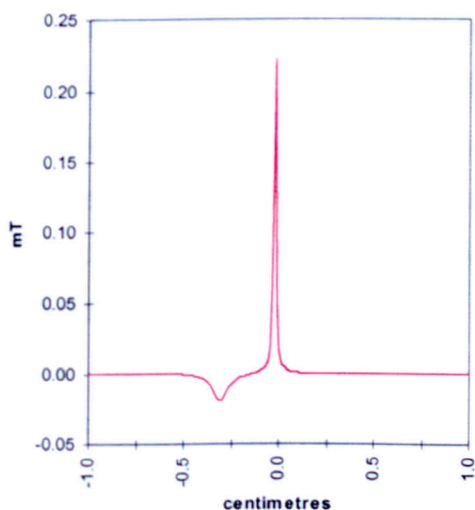
Fig. 5.26: A possible model for the substrate portion of the tip assembly magnetised as in the Transverse Case. In (d) and (e), red scans plot the average value of the end-points of simulated line scans, while blue scans plot the average value of the end-points of the experimental deflection line scans shown in fig. 5.2.

and experimental deflection data. Nevertheless, substrate model *ST_1* is taken to be a possible model for the substrate portion of the DI tip assembly magnetised as in the Transverse Case. We now briefly consider the character of the stray field from this model.

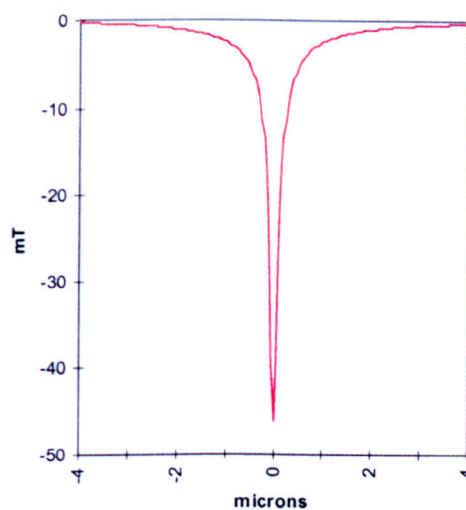
A field scan (of the component of field normal to the plane of reconstruction) calculated directly from the substrate model *ST_1* at the reconstruction plane is shown in fig. 5.27(a). Fig. 5.27(b) shows a corresponding field scan (of the component of field normal to the plane of reconstruction) calculated directly from the tip model (magnetised as in the fig. 5.17(a)) at the reconstruction plane.

Note that once again in the vicinity of the tip the field from the substrate is of the order of 2×10^{-1} mT and varies by less than 10^{-1} mT. Thus the models again suggest that in the vicinity of the tip the substrate field is small (being only a fraction of one percent of the peak tip field) and effectively constant.

Now consider the horizontal axes on the graphs in fig. 5.27. Once again the substrate field is given over 2cm, while the tip field is given over $8 \mu\text{m}$. Thus as expected the tip field immediately in front of the tip dominates over the field from the substrate. However, the large spread of the substrate field ensures its field integrals are significant as figs. 5.27(b) and (c) show.



(a) Field scan calculated directly from the substrate model at the reconstruction plane.



(b) Field scan calculated directly from the tip model at the reconstruction plane.

Fig. 5.27: Field scan components calculated in the plane of reconstruction from the substrate model *ST_1* and the tip model in fig. 5.17.

5.5 Summary

The deflection data sets generated by the DI MFM tip magnetised in the Axial and Transverse Cases were presented in this chapter. The vertical shift character of these deflection line scans was not predicted by the tip models considered in Chapter 4 and therefore the implication was that this variable vertical shift character originated from the magnetic material attached to the cantilever and substrate portions of the tip assembly.

Several possible models for the magnetic configuration of the cantilever and substrate portions of the tip assembly were constructed. These suggested that although the cantilever contribution to the deflection data sets is significant, it is the substrate portion of the DI tip assembly which is responsible for the vertical shifts of the experimental deflection line scans.

Investigations into the character of the stray field from each of the cantilever and substrate portions found that in the vicinity of the peak tip field, the cantilever and substrate fields are small (being less than 2% and 1% of the peak tip field respectively) and effectively constant. In fact we find that the tip field immediately in front of the tip dominates over the combined cantilever and substrate field. However, the small cantilever and substrate fields are spread over a large distance which results in large cantilever and substrate field integrals. In the following chapter (Chapter 6) we investigate the effect on the accuracy of the (ART and RTM) reconstructed tip stray fields of this large contribution from the cantilever and substrate to the tip assembly deflection data sets (i.e. to the input data sets for tomographic reconstruction).

Note that in the pursuit of suitable models for the substrate portion of the tip assembly magnetised as in the Axial and Transverse Cases, the $8\mu\text{m}$ line scans in the deflection data sets in figs. 5.1 and 5.2 were used as a guide. Calculations from the models of the substrate portion of the tip assembly magnetised as in the Axial and Transverse Cases suggest that the stray field from the substrate extends over a

distance of the order of 10^{-2} m. Thus, the line scan deflection data sets in figs. 5.1 and 5.2 only give a very small section of the substrate's field integral as a guide for determining possible magnetic configurations of the substrate. Therefore wider deflection line scans would better facilitate the search for possible models of the substrate portion of the tip assembly.

References

- [1] Private communication with Prof. R. P. Ferrier

Chapter 6

Investigation of the Effect on the Reconstructed Stray Field of the Cantilever and Substrate Contribution to the Tip Assembly's Line Scan Deflection Data Sets

6.1 Introduction

For a DI MFM tip assembly, the measured deflection line scans contain a large background contribution which investigations indicate originates from the cantilever and substrate portions of the assembly (see Sections 5.3 and 5.4). Further investigations have also indicated that the field from the cantilever and substrate portions is small in the immediate vicinity of the tip where the tip field dominates. However the long range nature of the stray fields from the cantilever and substrate ensures that their field integrals are not insignificant. It is the aim of this chapter to investigate the effect that the cantilever and substrate contribution to the tip assembly's deflection data sets has on the accuracy of the reconstructed field when we use line scans taken over the relatively small spatial range necessary to ensure the required spatial resolution of approximately 25nm in the tomographic determination of the MFM tip field. In the following section we investigate the accuracy with which stray field is reconstructed (using the RTM method) from 'well behaved' line scan deflection data sets (containing line scans which decrease to approximately zero at their extremes) generated by the tip portion of the tip assembly. In Section 6.3 we consider the accuracy of the field reconstructed from 'non-well behaved' deflection data sets generated by the cantilever and substrate portion of the assembly.

Subsequently, in Section 6.4 the accuracy with which the field is reconstructed from the entire model tip assembly is investigated. Following this the stray field reconstructed from the experimental deflection data sets generated by the DI tip assembly is considered (Section 6.5) and then a simple method for reducing the error in the reconstructed field values is described (Section 6.6). In Section 6.7 we consider the accuracy of stray field reconstructed using the ART method. Finally we investigate the error introduced into the reconstructed field from the finite size of the electron probe (Section 6.8) and from possible misalignment of line scans in the input deflection data sets (Section 6.9).

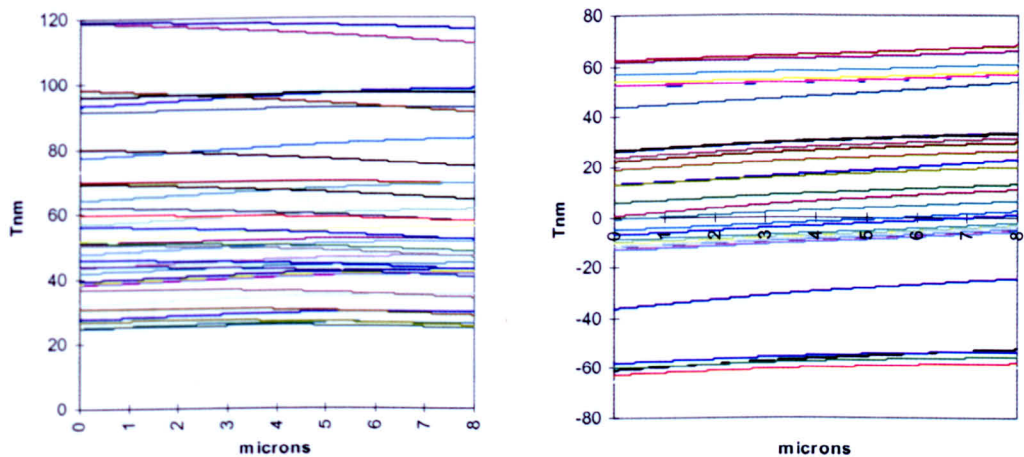
6.2 Comparison of the Calculated and Reconstructed Stray Fields from the Model Tip

Recall from Section 4.3.1.3 that a comparison of the average stray field reconstructed from each of the orthogonal simulated integrated field line scan data sets generated by model Tip1 (in figs. 4.8(c) and (d)) was found to be effectively identical to the field calculated directly from the tip model. This comparison of the calculated and reconstructed fields serves as a proof that the RTM reconstruction technique does produce an accurate representation of a self consistent three dimensional stray field provided the input deflection data sets contain 'well behaved' line scans which (approximately) decrease to zero at their extremes.

6.3 Comparison of the Calculated and Reconstructed Stray Fields from the Combined Cantilever and Substrate Model

Now consider figs. 6.1(a) and (b) which show the simulated rotation data sets of orthogonal components of integrated field generated by the combined cantilever and

substrate model which resembles most closely the tip assembly magnetised as in the Transverse Case (i.e. the cantilever model magnetised as in fig. 5.17(a) and the substrate model magnetised as in fig. 5.26(a)). It has already been established that the field from the cantilever alone extends over a distance of approximately $800\mu\text{m}$, while the field from the substrate extends over a distance of approximately 2cm . However, the integrated field line scans which are used to reconstruct the combined cantilever and substrate field are only $8\mu\text{m}$ wide. Thus, using the data sets in fig. 6.1 as the input data sets for tomographic reconstruction means that only a relatively small section of the combined cantilever and substrate integrated field is used to reconstruct its stray field (note that for an accurate reconstruction of a stray field, both the ART and RTM methods require input deflection line scans which decrease to zero at their extremes). It is therefore the aim of this section to investigate the accuracy with which the combined cantilever and substrate field is reconstructed from these ‘truncated’ data sets and consequently to assess the error in the reconstructed field arising from the use of truncated data in a practical reconstruction. We first consider the accuracy of the average stray field reconstructed from both rotation data sets before considering the accuracy of the field reconstructed from each individual rotation data set.



(a) Scans sensitive to induction normal to the plane of reconstruction.

(b) Scans sensitive to induction in the plane of reconstruction.

Fig. 6.1: Simulated rotation data sets of orthogonal integrated field components generated by the combined cantilever and substrate models magnetised as in the Transverse Case.

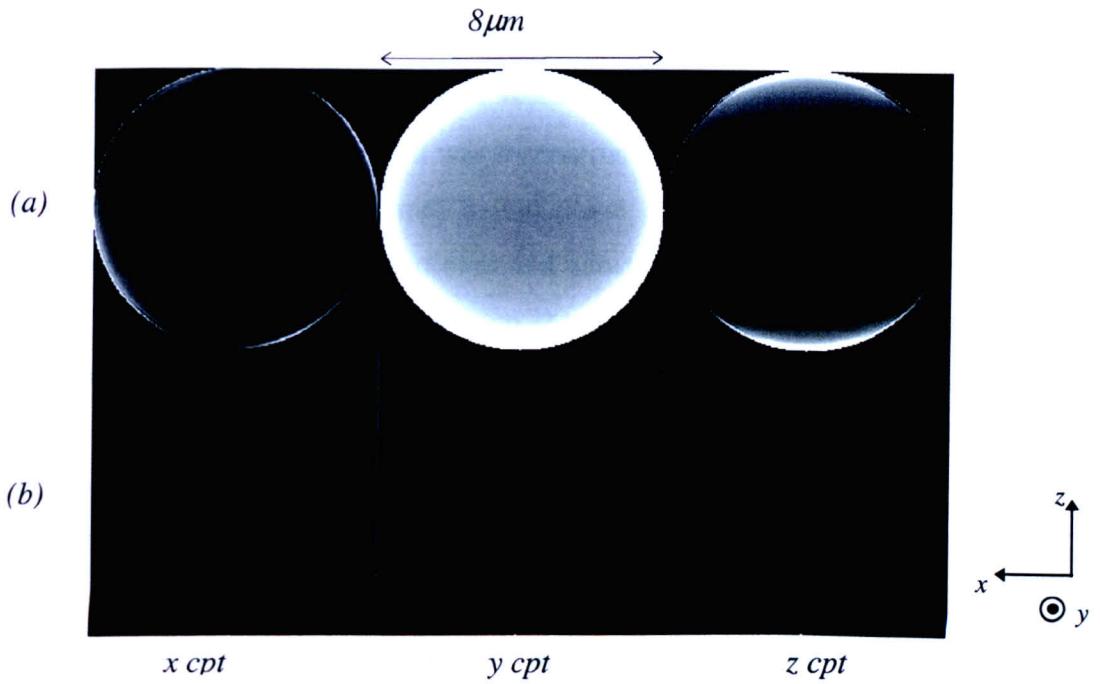
6.3.1 Average Stray Field Reconstructed from the Two Rotation Data Sets

Consider the average three dimensional stray field shown in fig. 6.2(a) which was reconstructed from the two rotation data sets of orthogonal components of integrated field generated by the combined cantilever and substrate model. The three dimensional stray field calculated directly from the cantilever and substrate model at the reconstruction plane is also shown in fig. 6.2(b). Note that the reconstructed field plane is bounded by a circle of diameter equal to the width of the deflection line scans, while the field calculated directly from the combined cantilever and substrate model is shown over the whole plane.

A visual comparison of the corresponding field components in fig. 6.2 indicates that there are significant differences between the calculated and reconstructed fields. Most notably the contrast at the edges of the reconstructed field plane bears no resemblance to the corresponding calculated field. As a further comparison line scans were taken across the calculated and reconstructed field planes and a selection are shown in figs. 6.2(c) and (d).

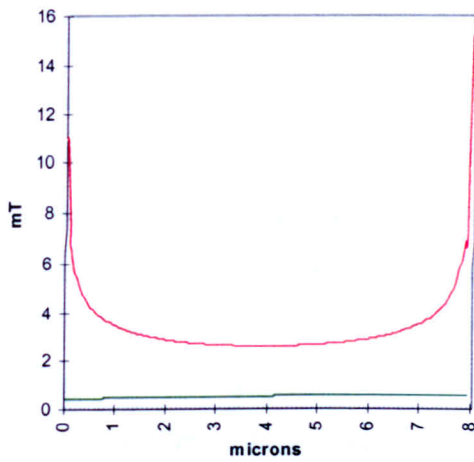
Fig. 6.2(c) shows horizontal scans taken across the normal component (y component) of the calculated and reconstructed fields. From these scans it is found that the reconstructed field values are at least five times larger than the calculated field. Note that a similar disagreement is also found between the corresponding in-plane components of the calculated and reconstructed fields - for example see fig. 6.2(d).

We therefore conclude that the average of the stray fields reconstructed from each of the 'truncated' data sets generated by the combined cantilever and substrate model does not compare favourably with the calculated field (this is expected due to the fact that the input deflection line scans do not decrease to zero at their extremes). However it was noted that the behaviour of each component of the reconstructed field differed depending on which data set was used in the RTM reconstruction technique. Hence a more detailed examination of the accuracy with which each field component is reconstructed from each of the orthogonal data sets is justified.

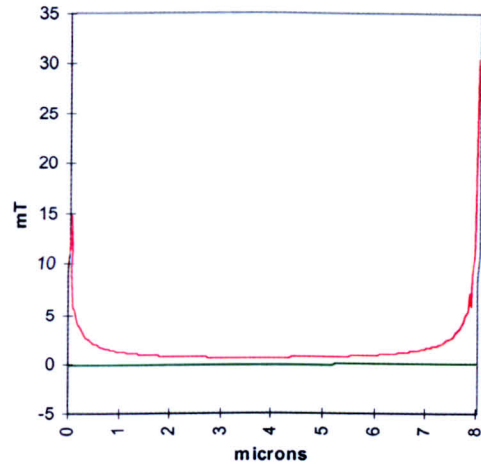


(a) Average stray field reconstructed from the simulated deflection data sets generated by the combined cantilever and substrate model.

(b) Stray field calculated directly from the combined cantilever and substrate model.



(c) Horizontal scans taken across the y components of the calculated and reconstructed fields above.



(d) Scans taken across the z components of the calculated and reconstructed fields above.

Fig. 6.2: Average stray field reconstructed from the rotation data sets in fig. 6.1, and the stray field calculated directly from the cantilever and substrate model. Also shown are field scans taken across the calculated and reconstructed fields in (a) and (b).

Note that the *red scans are taken across the reconstructed fields in (a)* while the *green scans are taken across the calculated fields in (b)*.

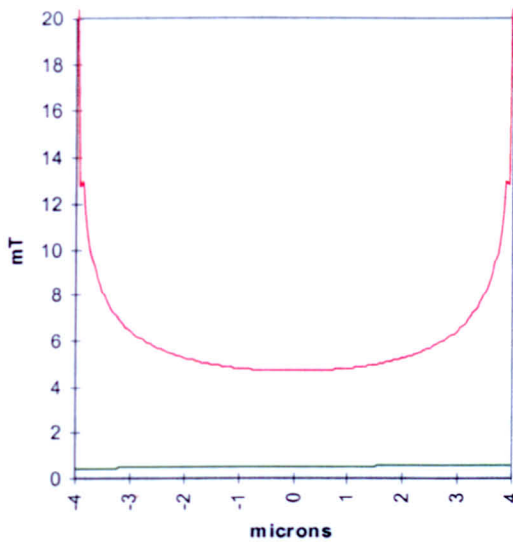
6.3.2 Stray Field Reconstructed from the Rotation Data Set Sensitive to Induction Normal to the Plane of Reconstruction

The three dimensional stray field was reconstructed from the simulated rotation data set sensitive to induction normal to the plane of reconstruction (see fig. 6.1(a)) generated by the combined cantilever and substrate model. The three dimensional field was also calculated directly from the cantilever and substrate model at the reconstruction plane. These three dimensional stray fields are not shown here, instead field scans were taken across the calculated and reconstructed field planes and are shown in fig. 6.3.

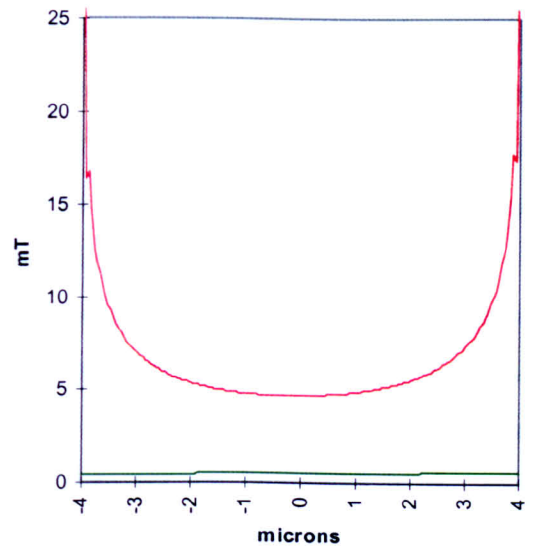
The horizontal and vertical field scans taken across the normal component of the calculated and reconstructed fields, shown in figs. 6.3(a) and (b), indicate that the normal component of the reconstructed field does not compare favourably with the corresponding field component calculated directly from the combined cantilever and substrate model. The normal component of the reconstructed field is at least 5-6mT larger than the corresponding calculated field values (which are less than 1mT). Figs. 6.3(c) and (d) however, clearly show a very good agreement between the field scans taken across the corresponding in-plane components of the calculated and reconstructed field. In fact the in-plane components of the reconstructed field are found to agree with the calculated field values within approximately 0.1mT. Note that the rapidly oscillating field values at the edges of the reconstructed field scans are not real effects but instead are artefacts of the RTM reconstruction technique due to the integrated field line scans not going to zero at their extremes.

We therefore conclude that the truncated nature of the line scan rotation data set (sensitive to induction normal to the plane of reconstruction) does effect the accuracy of the normal component of the reconstructed field. However, the accuracy of the in-plane components of the reconstructed field are not significantly effected in this case.

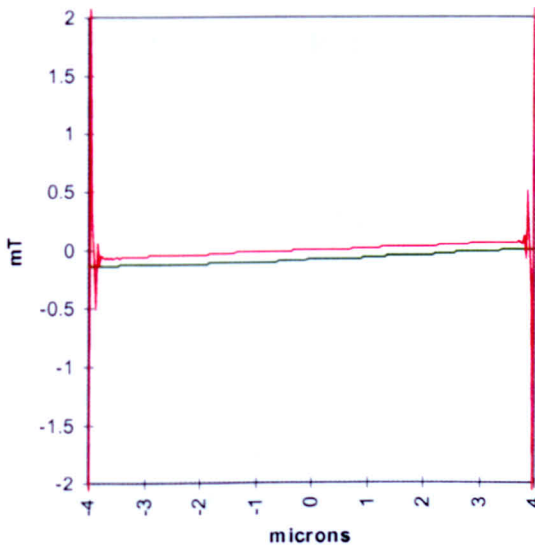
Note that the input rotation data set (sensitive to induction normal to the plane of reconstruction) is a measure of the normal component of field integrated along several thousand microns of the electron beam trajectory. However, the RTM method (incorrectly) assumes that all the field contributions to this rotation data set are contained in the area defined by the reconstruction plane (i.e. an $8^2 \mu\text{m}^2$ plane in



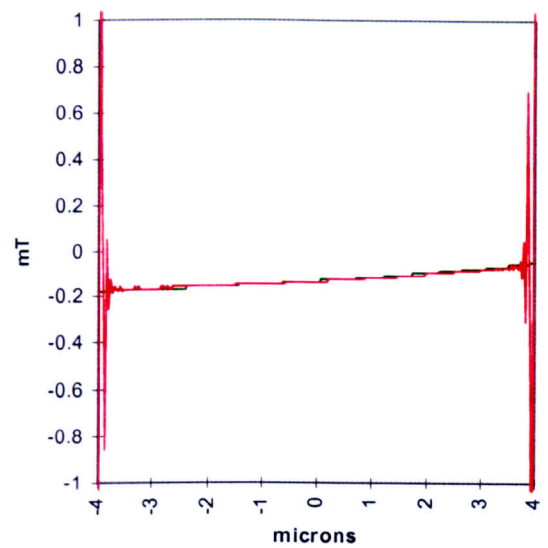
(a) Scans taken (horizontally) across the normal components (y components) of the calculated and reconstructed cantilever and substrate field.



(b) Scans taken (vertically) across the normal components (y components) of the calculated and reconstructed cantilever and substrate field.



(c) Scans taken across the (in-plane) x components of the calculated and reconstructed field.



(d) Scans taken across the (in-plane) z components of the calculated and reconstructed fields.

Fig. 6.3: Comparison of field scan components calculated directly from the combined cantilever and substrate model (see fig. 6.2(b)) with scans taken across the stray field reconstructed from the simulated rotation data set (sensitive to induction normal to the plane of reconstruction in fig. 6.1(a)).

Note that the x, y and z components referred to above correspond to the components in fig. 6.2.

Also note that the *red scans are taken across the reconstructed cantilever and substrate field*, while the *green scans are taken across the field calculated directly from the cantilever and substrate model*.

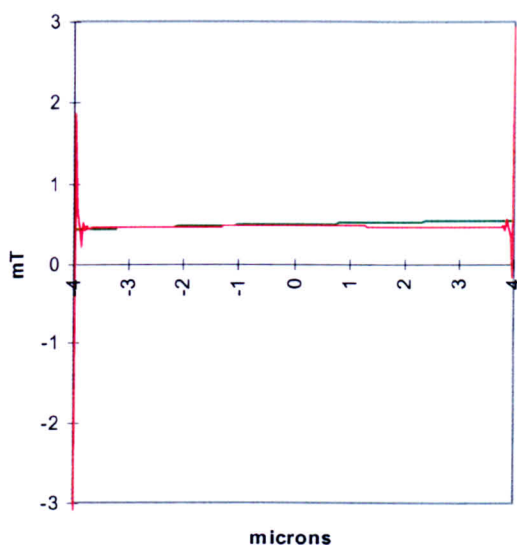
front of the tip). Therefore the normal component of field reconstructed using the RTM method (reconstructed over an $8^2\mu\text{m}^2$ plane) contains all the cantilever and substrate contributions to the input rotation data set. This is the reason that the normal component of the reconstructed field is not an accurate representation of the normal component of the combined cantilever and substrate field.

Furthermore, the rotation data set (sensitive to induction normal to the plane of reconstruction) does not contain any direct information on the in-plane components of the stray field. Therefore the assumption that all the normal component field contributions to the rotation data set are contained in the area defined by the reconstruction plane does not effect the in-plane components of the reconstructed field. Therefore the in-plane components of the reconstructed field are accurate representations of the in-plane components of the cantilever and substrate field.

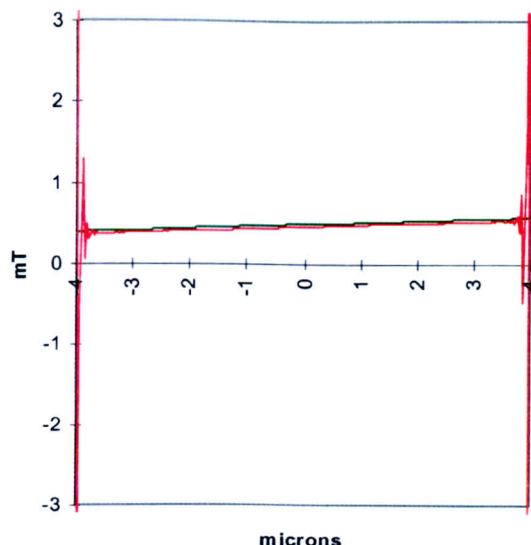
6.3.3 Stray Field Reconstructed from the Rotation Data Set Sensitive to Induction in the Plane of Reconstruction

We now consider the three dimensional stray field reconstructed from the rotation data set sensitive to induction in the plane of reconstruction (i.e. the data set in fig. 6.1(b)). The three dimensional field was again calculated directly from the cantilever and substrate model at the reconstruction plane. Once again these three dimensional stray fields are not shown here - instead field scans taken across the calculated and reconstructed field planes are shown in fig. 6.4.

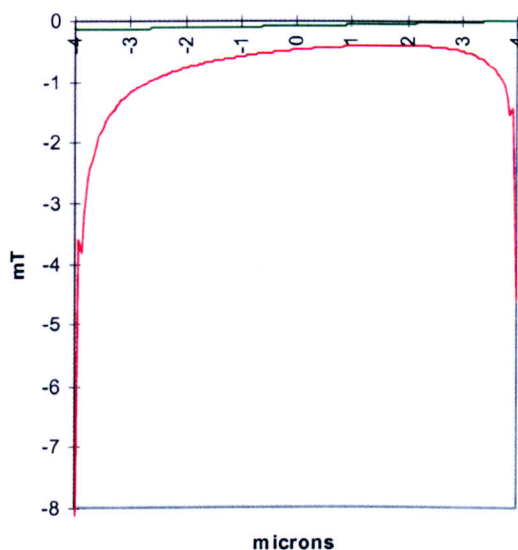
Figs. 6.4(a) and (b) show horizontal and vertical scans taken across the normal component (y component) of the calculated and reconstructed fields. Clearly there is excellent agreement between the calculated and reconstructed fields. In fact the normal component of reconstructed field is found to agree with the calculated field values within approximately 0.15mT. Again note that the rapidly oscillating field values at the edges of the field scans are not real effects but are an artefact of the RTM reconstruction technique due to the integrated field line scans not going to zero at their extremes. Figs. 6.4(c) and (d) show scans taken across the in-plane components (x and z components) of the calculated and reconstructed fields. In this case the agreement between the calculated and reconstructed field values is not good.



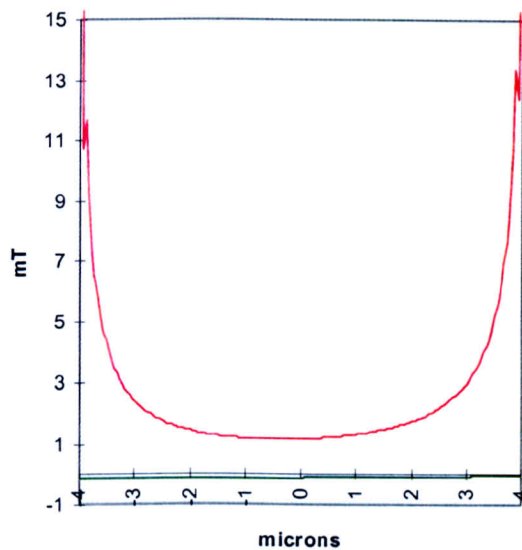
(a) Scans taken (horizontally) across the normal components (y components) of the calculated and reconstructed cantilever and substrate field.



(b) Scans taken (vertically) across the normal components (y components) of the calculated and reconstructed cantilever and substrate field.



(c) Scans taken across the (in-plane) x components of the calculated and reconstructed field.



(d) Scans taken across the (in-plane) z components of the calculated and reconstructed fields.

Fig. 6.4: Comparison of field scan components calculated directly from the combined cantilever and substrate model (see fig. 6.2(b)) with scans taken across the stray field reconstructed from the simulated rotation data set (sensitive to induction in the plane of reconstruction in fig. 6.1(b)).

Note that the x, y and z components referred to above correspond to the components in fig. 6.2.

Also note that the red scans are taken across the reconstructed cantilever and substrate field, while the green scans are taken across the field calculated directly from the cantilever and substrate model.

Thus the conclusion is that the truncated nature of the line scan rotation data set (sensitive to induction in the plane of reconstruction) affects the accuracy of the in-plane components of the reconstructed field. However, the accuracy of the normal component of the reconstructed field is not affected.

Once again note that the input rotation data set (sensitive to induction in the plane of reconstruction) is a measure of the in-plane components of field integrated along several thousand microns of the electron beam trajectory. However, the RTM method (incorrectly) assumes that all the field contributions to this rotation data set are contained in the area defined by the reconstruction plane. Therefore the in-plane components of field reconstructed using the RTM method (reconstructed over an $8\mu\text{m}^2$ plane) contain all the cantilever and substrate contributions to the input rotation data set. This is the reason that the in-plane components of the reconstructed field are not an accurate representation of the in-plane components of the combined cantilever and substrate field.

Furthermore, the rotation data set (sensitive to induction in the plane of reconstruction) does not contain any direct information on the normal component of the stray field. Therefore the assumption that all the in-plane component field contributions to the rotation data set are contained in the area defined by the reconstruction plane does not effect the normal component of the reconstructed field. Therefore the normal component of the reconstructed field is an accurate representation of the normal component of the cantilever and substrate field.

We have found that the average stray field reconstructed from the ‘truncated’ rotation data sets of orthogonal integrated field components generated by the combined cantilever and substrate model does not compare favourably with the field calculated directly from the model. However further investigations (for example see Section 6.4) have also found that the accuracy with which each field component is reconstructed is significantly better from one rotation data set than from the other. This suggests that by selecting the different components from the two reconstructions of the three dimensional stray field we can achieve a much more accurate determination of the field. In the following section we investigate the accuracy with which stray field from the model tip assembly can be reconstructed from ‘truncated’ data sets using this approach.

6.4 Comparison of the Calculated and Reconstructed Stray Fields from the model Tip Assembly

Figs. 6.5(a) and (b) show the simulated rotation data sets of orthogonal integrated field components generated by the model tip assembly magnetised as in the Transverse Case (i.e. the tip and cantilever models magnetised as in fig. 5.17(a), and the substrate model magnetised as in fig. 5.26(a)). In previous studies^[1] the experimentalists have tended to present the reconstructed field as the average of the field reconstructed from both the orthogonal line scan data sets. Hence in this section we will first consider the accuracy of the average stray field reconstructed from both rotation data sets before considering the accuracy of the field reconstructed from each individual rotation data set.

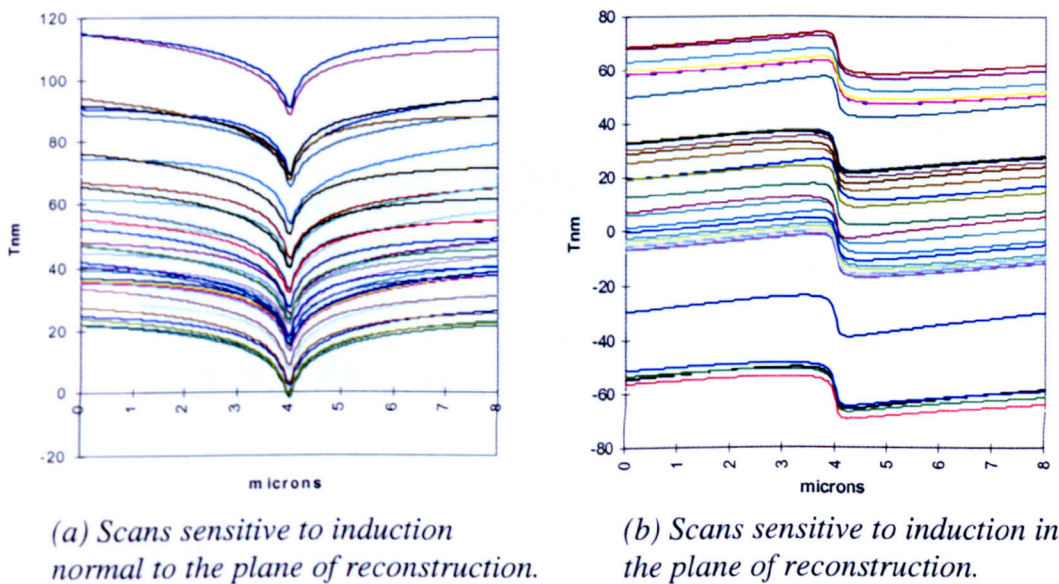


Fig. 6.5: Simulated rotation data sets of orthogonal integrated field components generated by the model tip assembly magnetised as in the Transverse Case.

6.4.1 Average Stray Field Reconstructed from both Rotation Data Sets

Consider fig. 6.6(a) which shows the average of the stray field reconstructed from each of the rotation data sets shown in fig. 6.5. The three dimensional stray field calculated directly from the model tip assembly at the reconstruction plane is also shown in fig. 6.6(b).

Once again note from a visual comparison of the corresponding field components in fig. 6.6 that the contrast at the edges of the reconstructed field planes is not observed in the calculated field. This again suggests that at least at the periphery of the reconstructed area there is a significant difference between the calculated and the reconstructed field components. Field scans taken across each of the field components are shown in fig. 6.7.

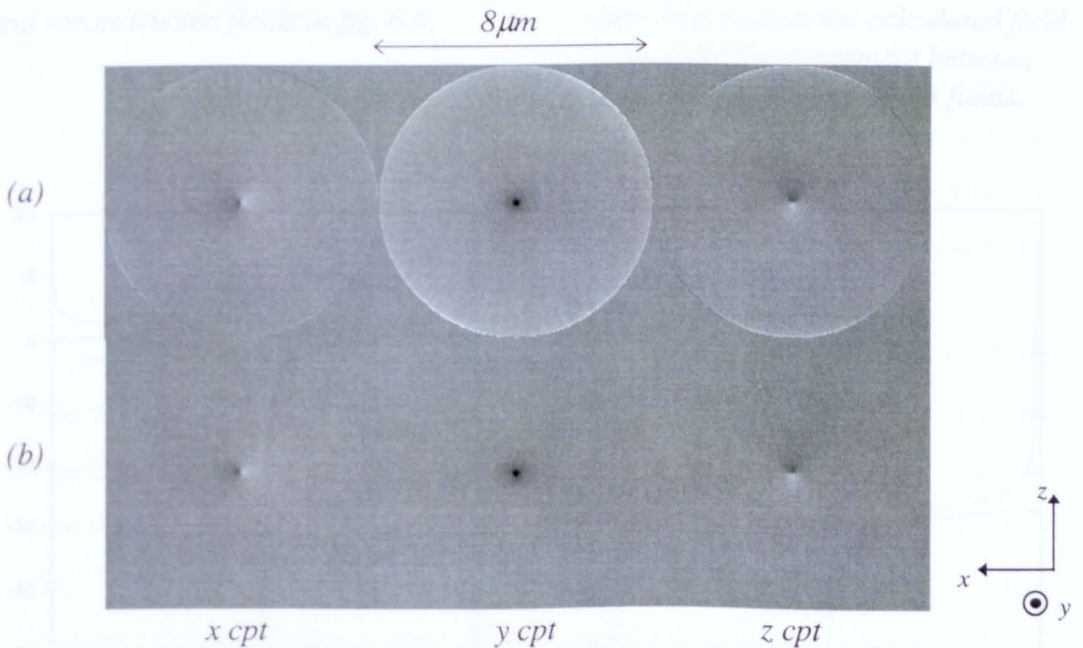
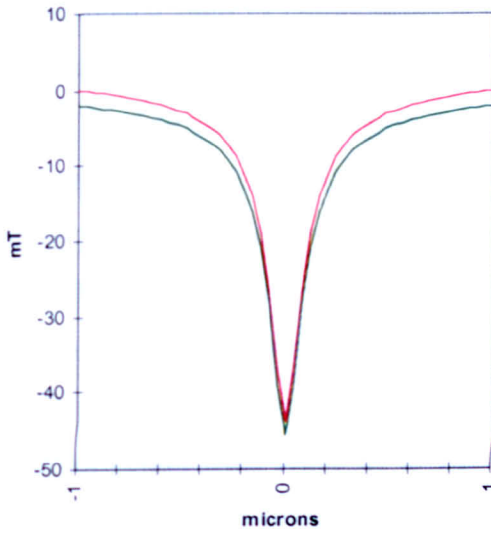
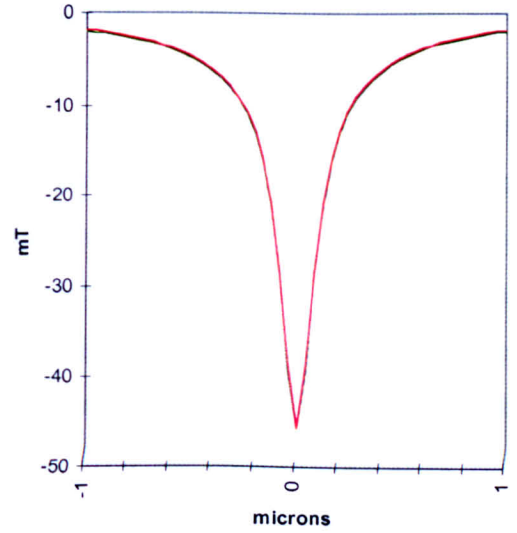


Fig. 6.6: (a) Average of the stray field reconstructed from the simulated rotation data sets generated by the model tip assembly magnetised as in the Transverse Case. (b) Stray field calculated directly from the model tip assembly magnetised as in the Transverse Case.

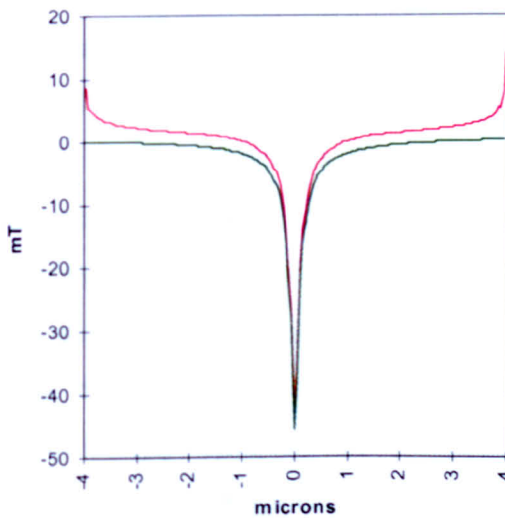
In fig. 6.7(a) the scans were taken horizontally across the components of stray field normal to the plane of reconstruction (y component) and are $2\mu\text{m}$ in length. The FWHM of the calculated field scan is found to be 218nm , while the FWHM of the



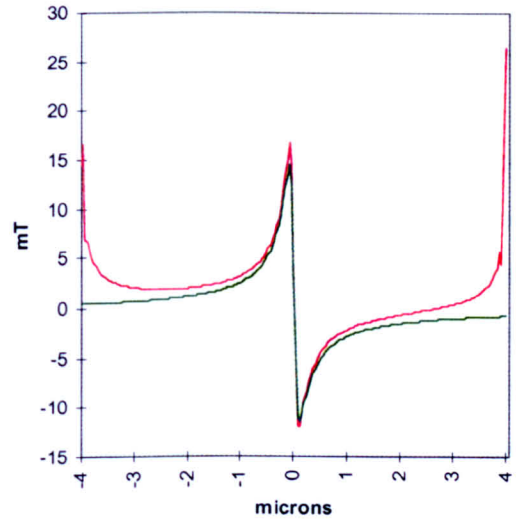
(a) Horizontal scans ($2\mu\text{m}$ in length) taken across the y components of the calculated and reconstructed fields in fig. 6.6.



(b) Same field scans as in (a) but with the reconstructed field scan superimposed on the calculated field scan. Note the agreement between the spatial definition of the fields.



(c) Horizontal scans ($8\mu\text{m}$ in length) taken across the y components of the calculated and reconstructed fields in fig. 6.6.



(d) Scans ($8\mu\text{m}$ in length) taken across the z components of the calculated and reconstructed fields in fig. 6.6.

Fig. 6.7: Scans taken across the calculated and reconstructed field components in fig. 6.6.

Note that the *red scans* are taken across the *average reconstructed tip assembly field*, while the *green scans* are taken across the field calculated directly from the model tip assembly.

reconstructed field scan is 217nm. Also, the peak value of the normal component of the calculated field (y component) is 46mT, while the corresponding reconstructed field value is 44mT.

Thus in the central region of the reconstructed field plane, the cantilever and substrate contribution to the tip assembly's rotation data sets does not effect the accuracy of the spatial definition of the average normal component of reconstructed field. However the cantilever and substrate contribution does result in an almost constant error (of approximately 5% of the peak tip field) in the field values of the normal component of reconstructed field in this central region. Fig. 6.7(b) shows the same horizontal field scans as in fig. 6.7(a) but with the reconstructed field scan superimposed on the corresponding calculated field scan. The fact that it is difficult to separate the calculated and reconstructed field scans highlights the excellent agreement between the spatial definition of the normal component of the calculated and reconstructed fields in the central region of the reconstructed field plane.

Now consider the field scans shown in figs. 6.7(c) and (d) which were taken across the full 8 μ m height and width of the reconstruction plane. Note that the difference between the calculated and reconstructed field values is greatest at the ends of these field scans.

The conclusion is that away from the central 'peak field' region of the reconstructed plane (i.e. further than approximately 1 μ m from the position of the peak field) the cantilever and substrate contribution to the tip assembly's rotation data sets does significantly effect the accuracy of the average field reconstructed from the data sets. However in the central 'peak field' region (i.e. within approximately 1 μ m of the position of the peak field) the accuracy of the reconstructed field is much improved - giving an almost constant (5% of the peak tip field) error in the reconstructed field values - and is considered unlikely to be significant in a practical experiment where random noise effects will mask errors of such magnitude. Nevertheless we now consider the accuracy of the stray fields reconstructed separately from each of the rotation data sets in fig. 6.5.

6.4.2 Stray Field Reconstructed from Each of the Orthogonal Rotation Data Sets

The three dimensional stray field reconstructed from the rotation data set sensitive to induction normal to the plane of reconstruction (see fig. 6.5(a)) using the RTM reconstruction technique is shown in fig. 6.8(a). The three dimensional field reconstructed from the rotation data set sensitive to induction in the plane of reconstruction (see fig. 6.5(b)) is shown in fig. 6.8(b), while the three dimensional field calculated directly from the model tip assembly at the reconstruction plane is shown in fig. 6.8(c).

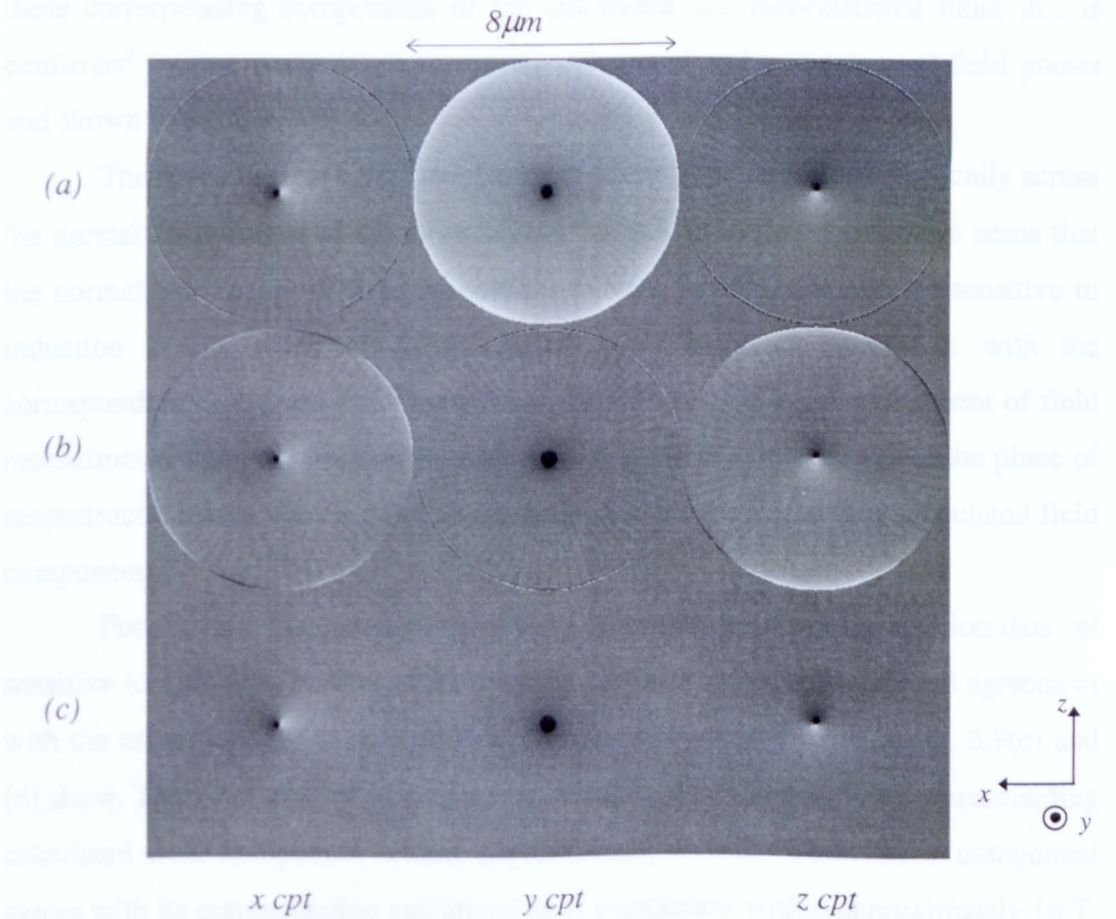


Fig. 6.8: (a) Stray field reconstructed from the simulated rotation data set sensitive to induction normal to the plane of reconstruction (see fig. 6.5(a)) generated by the model tip assembly magnetised as in the Transverse Case.

(b) Stray field reconstructed from the simulated rotation data set sensitive to induction in the plane of reconstruction (see fig. 6.5(b)) generated by the model tip assembly magnetised as in the Transverse Case.

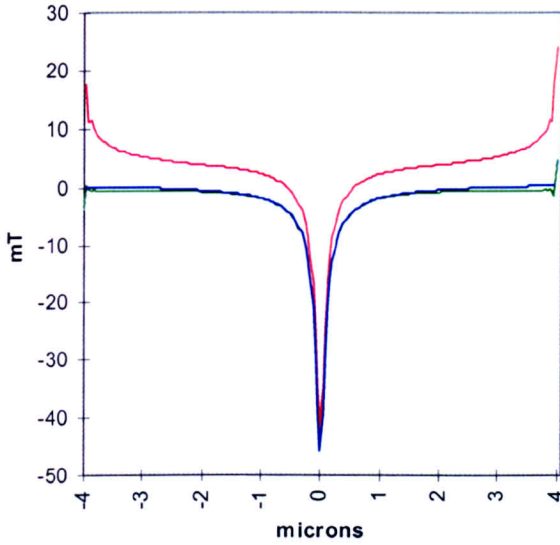
(c) Stray field calculated directly from the model tip assembly magnetised as in the Transverse Case.

Note that the normal component (y component) of the reconstructed field in fig. 6.8(a), and the in-plane components (x and z components) of the reconstructed field in fig. 6.8(b) all display contrast about the edges of the reconstructed field plane which is not observed in the calculated field - see fig. 6.8(c). This contrast at the edges of the reconstruction plane is due to the RTM method (incorrectly) assuming that all the field contributions to the rotation data sets are contained in the area defined by the reconstruction plane (i.e. an $8^2\mu\text{m}^2$ plane in front of the tip).

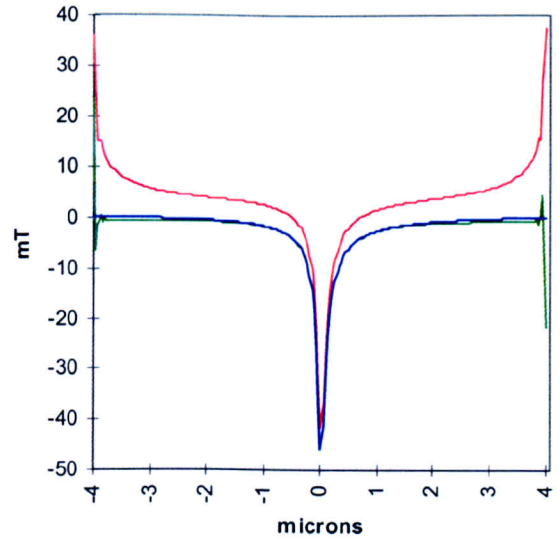
A visual comparison of the in-plane components of the reconstructed field in fig. 6.8(a), and the normal component of the reconstructed field in fig. 6.8(b), with the calculated field in fig. 6.8(c) suggests that there is excellent agreement between these corresponding components of the calculated and reconstructed field; this is confirmed by line scans taken across the calculated and reconstructed field planes and shown in fig. 6.9.

The scans in figs. 6.9(a) and (b) were taken horizontally and vertically across the normal components of the stray field in fig. 6.8. It is clear from these scans that the normal component of field reconstructed from the rotation data set sensitive to induction in the plane of reconstruction is in excellent agreement with the corresponding calculated field component. However, the normal component of field reconstructed from the rotation data set sensitive to induction normal to the plane of reconstruction does not compare favourably with the corresponding calculated field component.

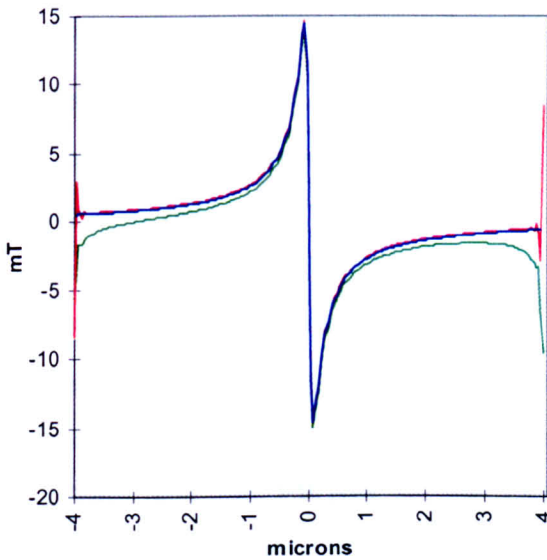
For the in-plane components of field reconstructed from the rotation data set sensitive to induction normal to the plane of reconstruction, there is good agreement with the corresponding calculated field components - as the scans in fig. 6.9(c) and (d) show. The x component of this reconstructed field agrees with the corresponding calculated field component within approximately 0.5mT, while the z component agrees with its corresponding calculated field component within approximately 1mT. The field scans in figs. 6.9(c) and (d) also show that the in-plane components of field reconstructed from the rotation data set sensitive to induction in the plane of reconstruction do not compare favourably with the corresponding calculated field components.



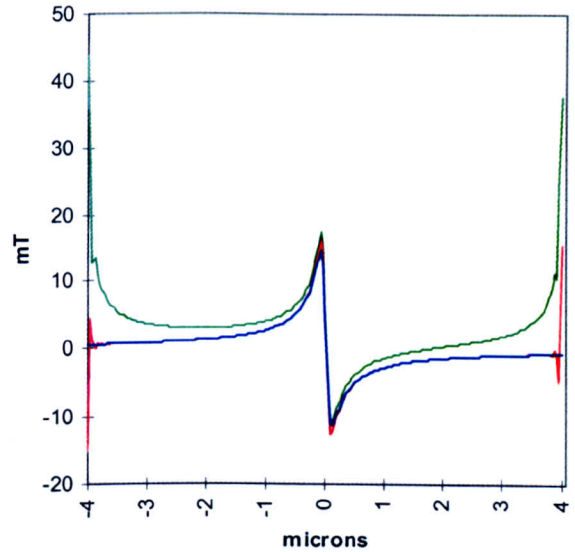
(a) Scans taken (horizontally) across the normal components (y components) of the calculated and reconstructed model tip assembly field.



(b) Scans taken (vertically) across the normal components (y components) of the calculated and reconstructed model tip assembly field.



(c) Scans taken across the (in-plane) x components of the calculated and reconstructed field.



(d) Scans taken across the (in-plane) z components of the calculated and reconstructed field.

Fig. 6.9: Comparison of field scan components calculated directly from the model tip assembly magnetised as in the Transverse Case (see fig. 6.6(b)) with scans taken across the stray field reconstructed from each of the simulated rotation data sets in fig. 6.5. Note that the x, y and z components referred to above correspond to the components in fig. 6.6.

Also note that the red scans are taken across the field reconstructed from the simulated rotation data set sensitive to induction normal to the plane of reconstruction in fig. 6.5(a). The green scans are taken across the field reconstructed from the simulated rotation data set sensitive to induction in the plane of reconstruction in fig. 6.5(b). And the blue scans are taken across the field calculated directly from the model tip assembly.

The results above are consistent with the results discussed in Section 6.3. The conclusion, therefore, is that for an accurate representation of the stray field from a MFM tip assembly we must reconstruct each of the stray field components from only one of the orthogonal rotation data sets. In particular, the normal component of field reconstructed from the rotation data set sensitive to induction in the plane of reconstruction, and the in-plane components of field reconstructed from the rotation data set sensitive to induction normal to the plane of reconstruction give the most accurate representation of the 3-D tip assembly stray field (reconstructed from non 'well behaved' line scan deflection data sets using the RTM method). In Section 6.5 we will consider the stray field reconstructed from the experimental deflection data sets in fig. 5.2 generated by the DI MFM tip. However, prior to this a simple check for the consistency of the orthogonal line scan rotation data sets is described.

6.4.3 Simple Check for the Consistency of Orthogonal Rotation Data Sets

Consider the scans in fig. 6.9(a) taken horizontally across the normal components of the stray field in fig. 6.8. The FWHM of the calculated field scan (taken across the y component in fig. 6.8(c)) is 218nm, while the FWHM of the reconstructed field scans (taken across the y components in fig. 6.8(a) and (b)) are 222nm and 217nm (respectively). In fig. 6.9(b) the scans were taken vertically across the normal components of field in fig. 6.8. In this case the FWHM of the calculated field scan is 222nm and the FWHM of the reconstructed field scans (taken across the y components in figs. 6.8(a) and (b)) are 220nm and 223nm (respectively).

The important point to note from above is that in the central region of the reconstruction plane (i.e. approximately $1\mu\text{m}$ from the peak field), the spatial definition of each of the reconstructed normal components of field compares favourably with the corresponding calculated field component. Therefore in a practical experiment, a simple check to ensure that the orthogonal rotation data sets are consistent with one another, is to compare the spatial distribution of the normal component of field reconstructed from each of the two data sets. Anything less than a

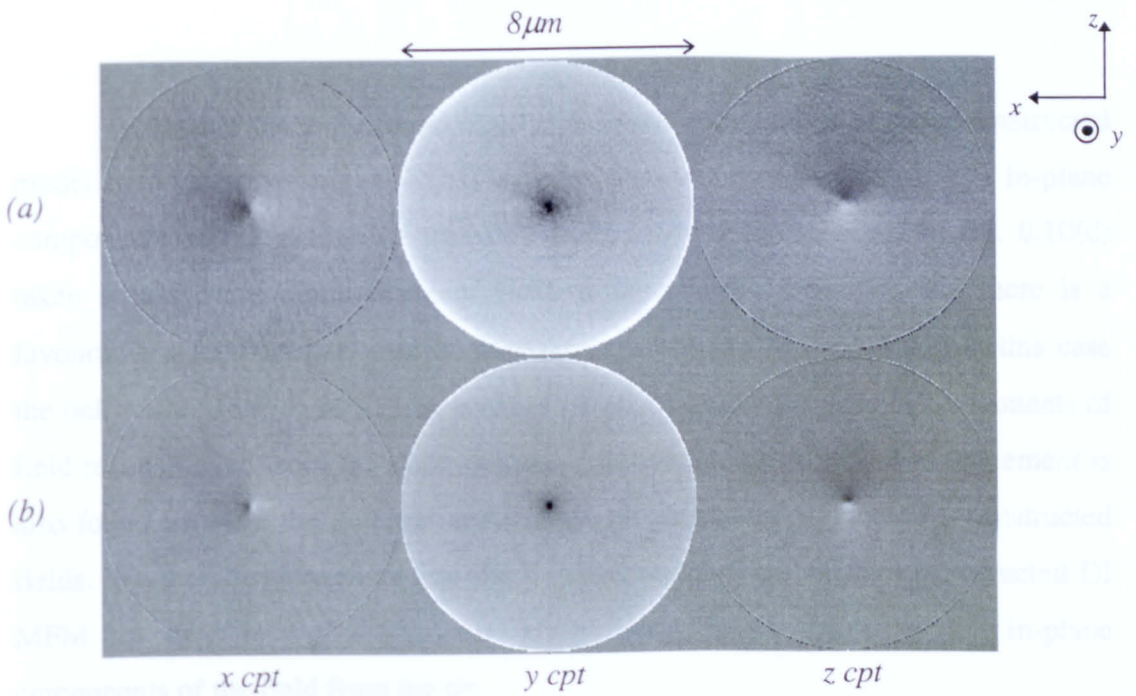
close agreement between the spatial character of the reconstructed field components suggests an error in the experimental set-up or in the recording of data.

6.5 Consideration of the Stray Fields Reconstructed from the Deflection Data Sets Generated by the DI MFM Tip

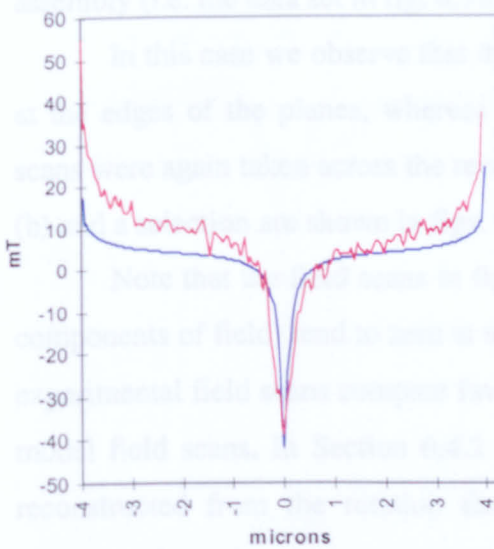
The DI MFM tip assembly's three dimensional stray field was reconstructed from the line scan deflection data set sensitive to induction normal to the plane of reconstruction (i.e. the data set in fig. 5.2(a)) and is shown in fig. 6.10(a). The three dimensional field reconstructed from the corresponding simulated deflection data set generated by the model tip assembly magnetised as in the Transverse Case (i.e. the data set in fig. 6.5(a)) is also shown in fig. 6.10(b).

Note that the normal components (y components) of the reconstructed fields in figs. 6.10(a) and (b) display contrast at the edges of the planes, whereas the in-plane components of the reconstructed fields (x and z components) do not. For a further comparison, scans were taken across each of the reconstructed field components in figs. 6.10(a) and (b) and a selection are shown in figs. 6.10(c) and (d).

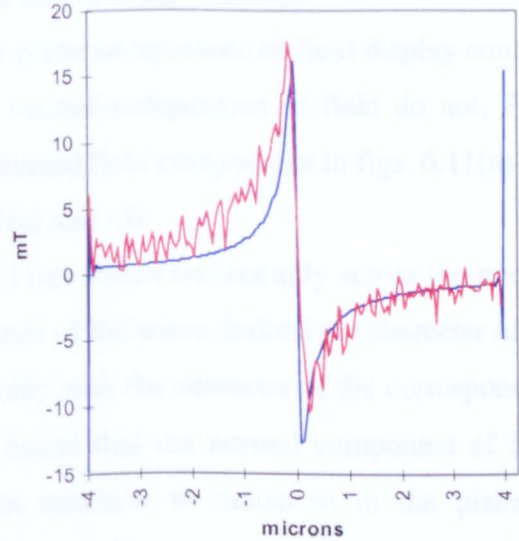
It is clear that the field values of the scans in fig. 6.10(c) (taken horizontally across the normal components of field) increase towards the ends of the scans. From previous investigations of the model tip assembly's stray field (in Chapters 4 to 6) we know that this is not a character of the model field but is instead a character of the normal component of field reconstructed from a truncated rotation data set (sensitive to induction normal to the plane of reconstruction) using the RTM reconstruction technique. Since the rotation data set (generated by the DI MFM tip and shown in fig. 5.2(a)) used to reconstruct the field in fig. 6.10(a) is also of a truncated nature, we therefore conclude that the increasing field values towards the ends of the experimental field scan in fig. 6.10(c) is not a character of the DI MFM tip field.



(a) Stray field reconstructed from the rotation data set (sensitive to induction normal to the reconstruction plane) in fig. 5.2(a) generated by the DI MFM tip.
 (b) Stray field reconstructed from the simulated rotation data set (sensitive to induction normal to the reconstruction plane) in fig. 6.5(a) generated by the model tip assembly.



(c) Horizontal scans taken across the y components of the reconstructed fields above.



(d) Scans taken across the z components of the reconstructed fields above.

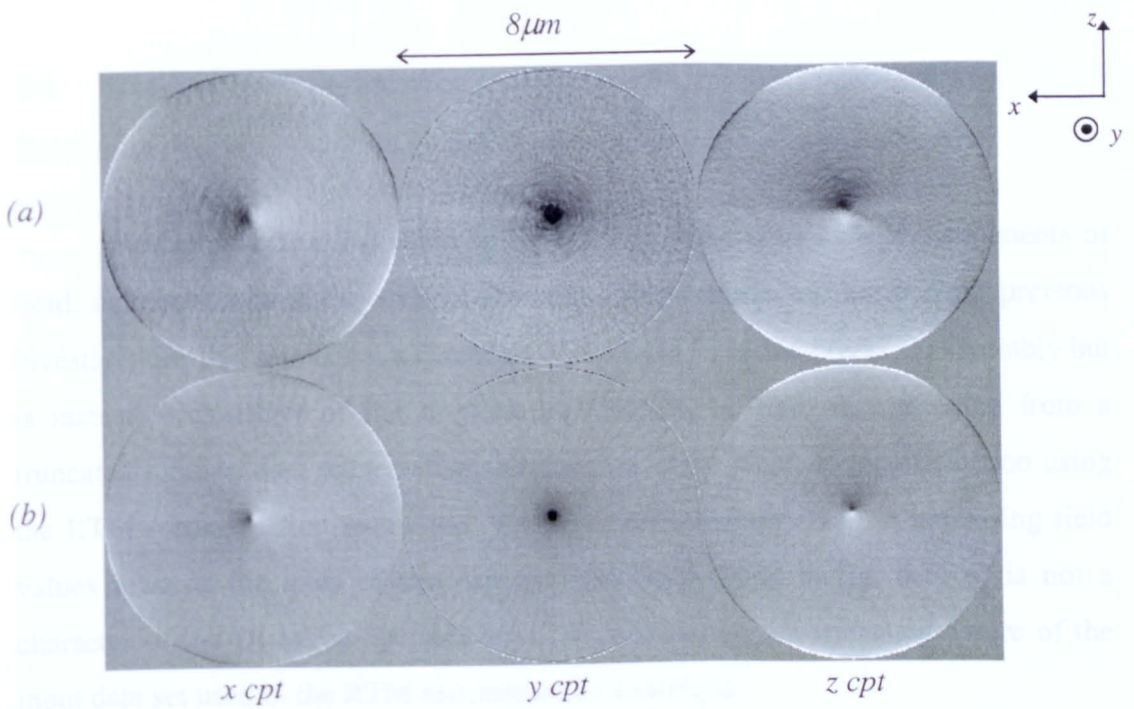
Fig. 6.10: Three dimensional stray fields reconstructed from the rotation data sets (sensitive to induction normal to the plane of reconstruction) generated by the DI MFM tip (in fig. 5.2(a)) and the model tip assembly (in fig. 6.5(a)). Also shown are field scans taken across the reconstructed fields in (a) and (b).

In Section 6.4.2 we found that the in-plane components of the reconstructed model field (shown in fig. 6.10(b)) were an accurate representation of the in-plane components of the model tip assembly field. Note from the scans in fig. 6.10(d) taken across the z components of field in figs. 6.10(a) and (b), that there is a favourable agreement between the experimental and model field scans. In this case the field values tend to zero at the ends of the scans unlike the normal components of field reconstructed from the same rotation data sets. A similar level of agreement is also found between the x components of the experimental and model reconstructed fields. We therefore conclude that the in-plane components of the reconstructed DI MFM tip field in fig. 6.10(a) are an accurate representation of the in-plane components of the field from the tip.

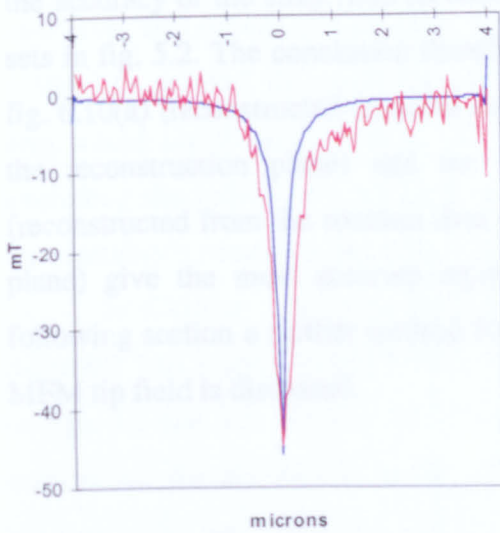
Now consider the DI MFM tip field reconstructed from the line scan deflection data set sensitive to induction in the plane of reconstruction (i.e. the data set in fig. 5.2(b)) shown in fig. 6.11(a). The three dimensional field reconstructed from the corresponding simulated deflection data set generated by the model tip assembly (i.e. the data set in fig. 6.5(b)) is shown in fig. 6.11(b).

In this case we observe that the in-plane components of field display contrast at the edges of the planes, whereas the normal components of field do not. Field scans were again taken across the reconstructed field components in figs. 6.11(a) and (b) and a selection are shown in figs. 6.11(c) and (d).

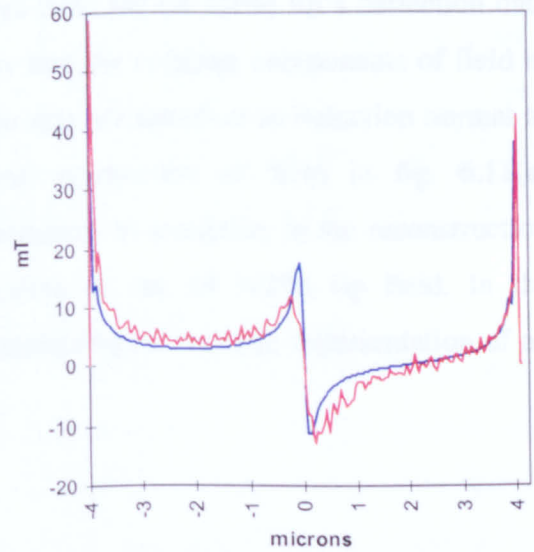
Note that the field scans in fig. 6.11(c) (taken horizontally across the normal components of field) tend to zero at the ends of the scans. Indeed the character of the experimental field scans compare favourably with the character of the corresponding model field scans. In Section 6.4.2 we found that the normal component of field reconstructed from the rotation data set sensitive to induction in the plane of reconstruction, gave the most accurate representation of the normal component of the field. We therefore conclude that the normal component of the reconstructed DI MFM tip field in fig. 6.11(a) is an accurate representation (within experimental errors) of the normal component of the DI MFM tip field over all but the very extremes of the reconstructed field plane.



- (a) Stray field reconstructed from the rotation data set (sensitive to induction in the reconstruction plane) in fig. 5.2(b) generated by the DI MFM tip.
- (b) Stray field reconstructed from the simulated rotation data set (sensitive to induction in the reconstruction plane) in fig. 6.5(b) generated by the model tip assembly.



(c) Horizontal scans taken across the y components of the reconstructed fields above.



(d) Scans taken across the z components of the reconstructed fields above.

Fig. 6.11: Three dimensional stray fields reconstructed from the rotation data sets (sensitive to induction in the plane of reconstruction) generated by the DI MFM tip (in fig. 5.2(b)) and the model tip assembly (in fig. 6.5(b)). Also shown are field scans taken across the reconstructed fields in (a) and (b).

Further note that the scans in fig. 6.11(d) taken across the z components of field, increase towards the ends of the scans. Once again, we know from previous investigations that this is not a character of the field from the model tip assembly but is instead a character of the in-plane components of field reconstructed from a truncated rotation data set sensitive to induction in the plane of reconstruction using the RTM reconstruction technique. We therefore conclude that the increasing field values towards the ends of the experimental field scans in fig. 6.11(d) is not a character of the DI MFM tip field but is instead due to the truncated nature of the input data set used in the RTM reconstruction technique.

We have therefore found that the character of the stray fields reconstructed from the DI MFM tip's deflection data sets is very similar to that of the fields reconstructed from the model tip assembly's deflection data sets. This has allowed us (through investigations in Sections 6.1 to 6.4) to comment with some authority on the accuracy of the stray field reconstructed from the DI MFM tip's deflection data sets in fig. 5.2. The conclusion therefore is that the in-plane components of field in fig. 6.10(a) (reconstructed from the rotation data set sensitive to induction normal to the reconstruction plane) and the normal component of field in fig. 6.11(a) (reconstructed from the rotation data set sensitive to induction in the reconstruction plane) give the most accurate representation of the DI MFM tip field. In the following section a further method for determining an accurate representation of an MFM tip field is discussed.

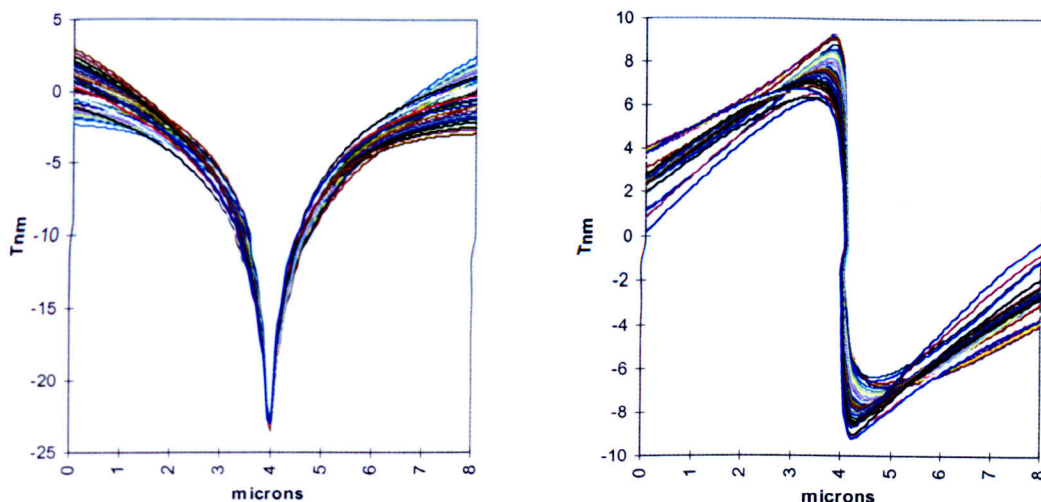
6.6 Method to Reduce the Error in the Average Stray Field Reconstructed from Both the Rotation Data Sets Generated by the Tip Assembly

As stated previously, in Section 6.4, experimentalists have tended to present the reconstructed field as the average of the field reconstructed from each orthogonal line scan data set. Our investigations have determined that this procedure does not yield an accurate representation of the three dimensional MFM tip field. However, a simple method to reduce the error in the average reconstructed field is described in the following.

Recall (from Sections 5.3.2 and 5.4.2) that the field calculated from the combined cantilever and substrate model (magnetised as in the Transverse Case) was found to be almost insignificant ($<1\text{mT}$) relative to the peak tip field. Also, recall (from Sections 6.2 and 6.4.1) that the error in the average reconstructed model tip assembly field (reconstructed from both the orthogonal line scan rotation data sets generated by the model tip assembly in fig. 6.5) was almost entirely due to the cantilever and substrate contribution to the tip assembly's rotation data sets. Thus a method to subtract the cantilever and substrate contribution from the rotation data sets would significantly reduce the error in the average reconstructed field while excluding the (effectively insignificant) cantilever and substrate contribution to the tip assembly's reconstructed stray field.

In Chapter 5 we concluded that the tip portion of the practical MFM tip assembly was largely responsible for the shape character of the deflection line scans in figs. 5.1 and 5.2. We also concluded that the cantilever and substrate portion was responsible for the vertical shifts of the same deflection line scans. Thus, for the rotation data sets generated by the model tip assembly magnetised as in the Transverse Case (see fig. 6.5) we decided to approximate the removal of the cantilever and substrate contribution to subtracting a constant deflection value from each scan in order that the average value of the extremities of each scan was zero, see fig. 6.12. From a visual comparison of the modified deflection line scans in fig. 6.12 with the line scans generated by model Tip1 in Chapter 4 (see fig. 4.8(c) and

(d)) it is clear that the shape of the modified line scans varies to a much greater degree than the shape of the unmodified scans from Tip1. This highlights the approximate nature of the removal of the cantilever and substrate contribution from the tip assembly rotation data sets which we consider.

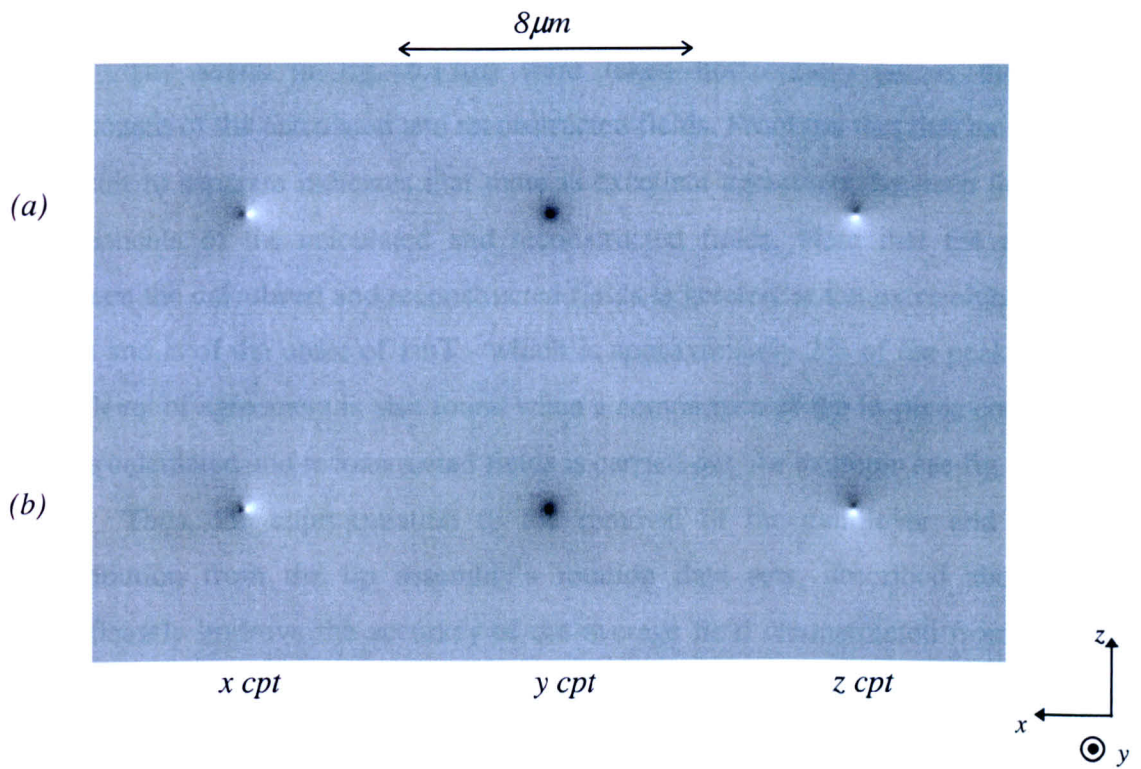


(a) Scans sensitive to induction normal to the plane of reconstruction.

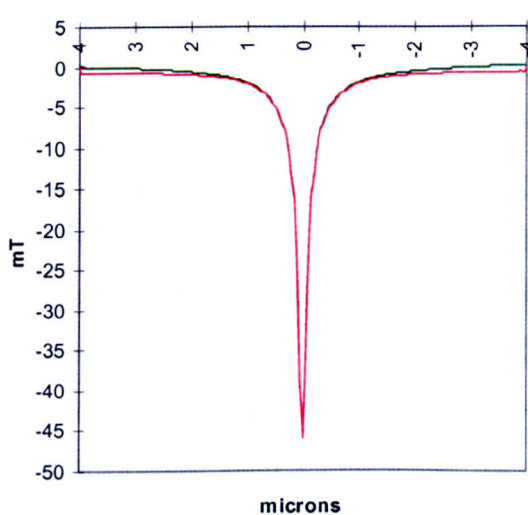
(b) Scans sensitive to induction in the plane of reconstruction.

Fig. 6.12: Modified rotation data sets of orthogonal integrated field components generated by the model tip assembly magnetised as in the Transverse Case. Note each line scan has had a constant deflection value subtracted from it.

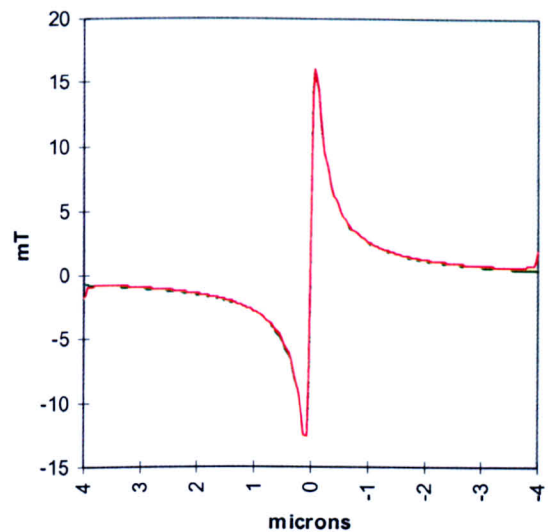
The three dimensional stray field was reconstructed from each of the modified rotation data sets (in fig. 6.12) and the average is shown in fig. 6.13(a). The stray field calculated directly from the model tip assembly at the reconstruction plane is also shown in fig. 6.13(b). A visual comparison of the corresponding field components suggests that there is a very good agreement between the calculated and reconstructed fields. Note that the average reconstructed field does not display contrast at the edges of the reconstructed plane - unlike the field in fig. 6.6(a) reconstructed from the unmodified data sets. Once again, as a further comparison, field scans were taken across each of the calculated and reconstructed field components and a selection are shown in fig. 6.13(c) and (d).



(a) Average stray field reconstructed from the modified rotation data sets in fig. 6.12 generated by the model tip assembly.
 (b) Stray field calculated directly from the model tip assembly.



(c) Horizontal scans taken across the y components of the calculated and the reconstructed fields above.



(d) Scans taken across the z components of the calculated and the reconstructed fields above.

Fig. 6.13: Three dimensional stray fields reconstructed from the modified rotation data sets in fig. 6.12 and calculated directly from the model tip assembly. Also shown are field scans taken across the reconstructed fields in (a) and (b). Note that the red scans were taken across the reconstructed field in (a), while the green scans were taken across the calculated fields in (b).

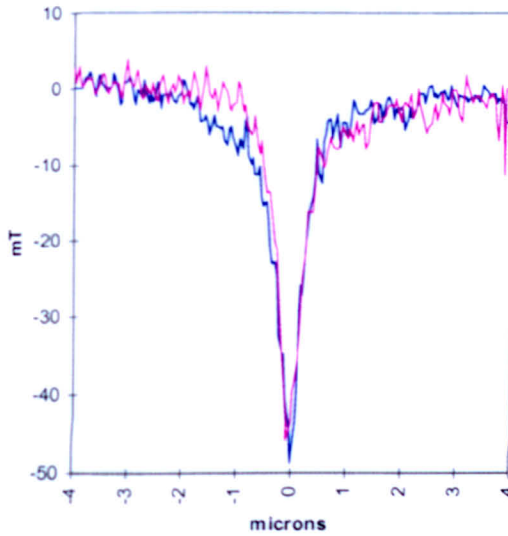
The scans in fig. 6.13(c) were taken horizontally across the normal component of the calculated and reconstructed fields. From the fact that the scans are difficult to separate indicates that there is excellent agreement between the normal components of the calculated and reconstructed fields. Note that the difference between the calculated and reconstructed fields is greatest at the extremities of these scans and is of the order of 1mT - which is approximately 2% of the peak tip field. This level of agreement is also found when a comparison of the in-plane components of the calculated and reconstructed fields is carried out, for example see fig. 6.13(d).

Thus, the approximation to the removal of the cantilever and substrate contribution from the tip assembly's rotation data sets, described above, does significantly improve the accuracy of the average field reconstructed from the data sets. We now consider the application of this method to the deflection data sets generated by the DI MFM tip in fig. 5.2.

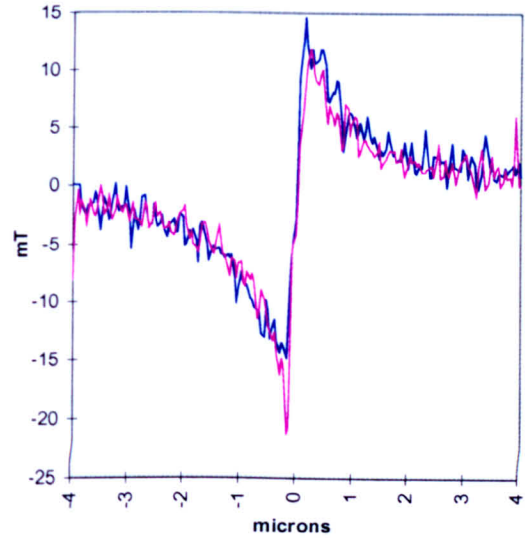
In this case, each line scan in the experimental deflection data sets in fig. 5.2 (generated by the DI MFM tip) had a constant deflection value subtracted from it so that the average value of the extremities of each line scan was approximately zero. The three dimensional stray field was then reconstructed from each of the modified experimental deflection data sets and the average was taken. This three dimensional stray field is not shown here, instead scans were taken across the field components and a selection are shown in fig. 6.14. For comparison scans taken across the in-plane components of the field in fig. 6.10(a) (reconstructed from the unmodified experimental deflection data set in fig. 5.2(a) sensitive to induction normal to the plane of reconstruction), and the normal component of the field in fig. 6.11(a) (reconstructed from the unmodified experimental deflection data set in fig. 5.2(b) sensitive to induction in the plane reconstruction) are also shown. These reconstructed field components have been determined to be the most accurate representation of the tip field - see Sections 6.3 and 6.4.

Note that the field scan components in fig. 6.14, reconstructed from the modified deflection data sets, decrease to approximately zero at their extremes. This is consistent with what we expect of the MFM tip stray field. Also note that corresponding field scan components in fig. 6.14 compare favourably with one another. This suggests that the average of the fields reconstructed from each of the

modified deflection data sets does give an accurate representation of the three dimensional DI MFM tip stray field.



(a) Scans taken across the normal components (y components) of the reconstructed fields.



(b) Scans taken across the (in-plane) z components of the reconstructed fields.

Fig. 6.14: Comparison of field scan components reconstructed from the modified and unmodified deflection data sets generated by the DI MFM tip.

Note that the x, y and z components referred to above correspond to the components in fig. 6.13.

Also note that the pink scans are taken across the field reconstructed from the unmodified deflection data sets, while the blue scans are taken across the field reconstructed from the modified deflection data sets.

We therefore conclude that the different methods described in this section and in Section 6.4 both produce accurate representations of the MFM tip field (within experimental errors) using the RTM reconstruction technique. We now consider the accuracy of the stray field reconstructed using the ART reconstruction technique.

6.7 Stray Fields Reconstructed Using ART

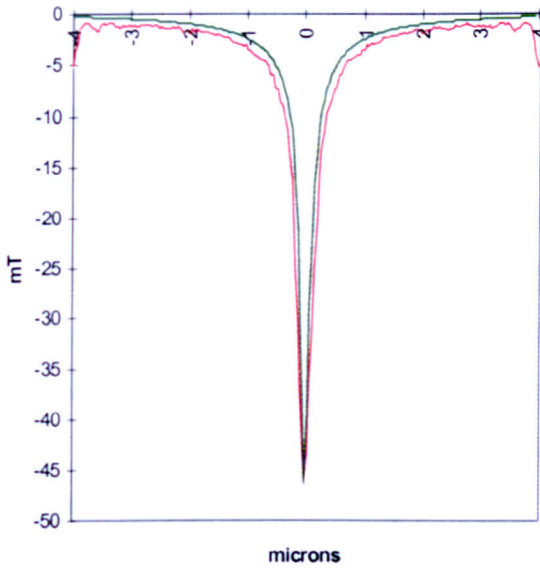
It has now been clearly proven in this Chapter that the RTM reconstruction technique is a proficient tool for the accurate determination of three dimensional stray field from line scan deflection data sets of a truncated nature. In this section we now consider the accuracy with which stray field is reconstructed using the ART reconstruction technique. We first consider the model tip field reconstructed using ART then we consider the field reconstructed from the deflection data sets generated by the model tip assembly.

6.7.1 Consideration of the Accuracy of the ART Reconstructed Model Tip Field

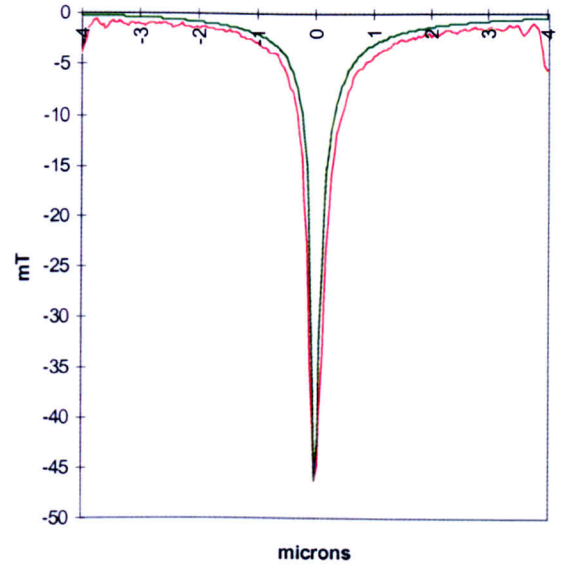
We first consider the stray field reconstructed using ART from the rotation data sets generated by the tip model magnetised as in the Transverse Case (see fig. 5.17(a)) - recall from Chapter 3 that ART uses both orthogonal deflection data sets for a combined determination of the three dimensional stray field. The three dimensional field was also calculated directly from the tip model at the reconstruction plane. These three dimensional stray fields are not shown here, instead field scans were taken across the calculated and reconstructed field planes and are shown in fig. 6.15.

From an inspection of the field scans in fig. 6.15 it is clear that the ART reconstructed field is not as accurate a determination of the tip field as the RTM reconstructed field was found to be - cf fig. 6.9. In fact for the scans in fig. 6.15(a) taken horizontally across the normal components of field, we find that the FWHM of the calculated field scan is 220nm, while the FWHM of the reconstructed field scan is 355nm. For the scans in fig. 6.15(b) taken vertically across the same components of field the FWHM of the calculated field scan is 225nm, while the FWHM of the reconstructed field scan is 360nm.

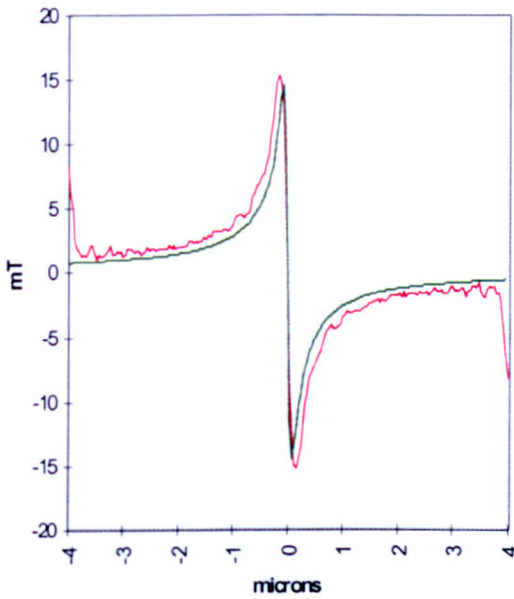
The peak value of the normal component of the calculated field is 46mT, while the corresponding reconstructed field value is 45mT. Thus although there is only a small error in the magnitude of the ART reconstructed field (less than 2%) there is a large error (approximately 50%) in the spatial definition of the ART



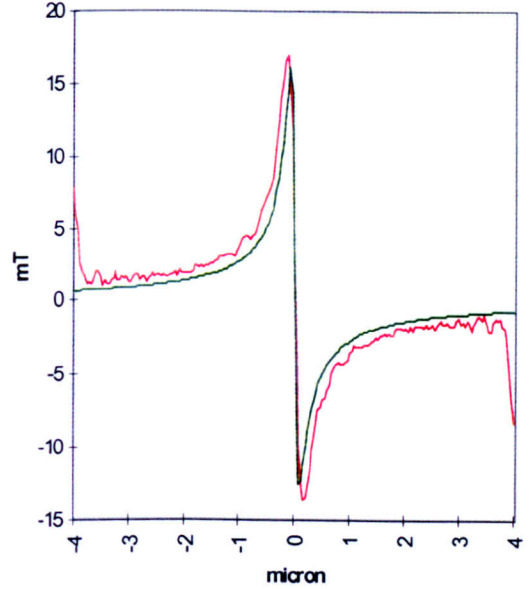
(a) Scans taken (horizontally) across the normal components (y components) of the calculated and ART reconstructed fields.



(b) Scans taken (vertically) across the normal components (y components) of the calculated and ART reconstructed fields.



(c) Scans taken across the (in-plane) x components of the calculated and ART reconstructed fields.



(d) Scans taken across the (in-plane) z components of the calculated and ART reconstructed fields.

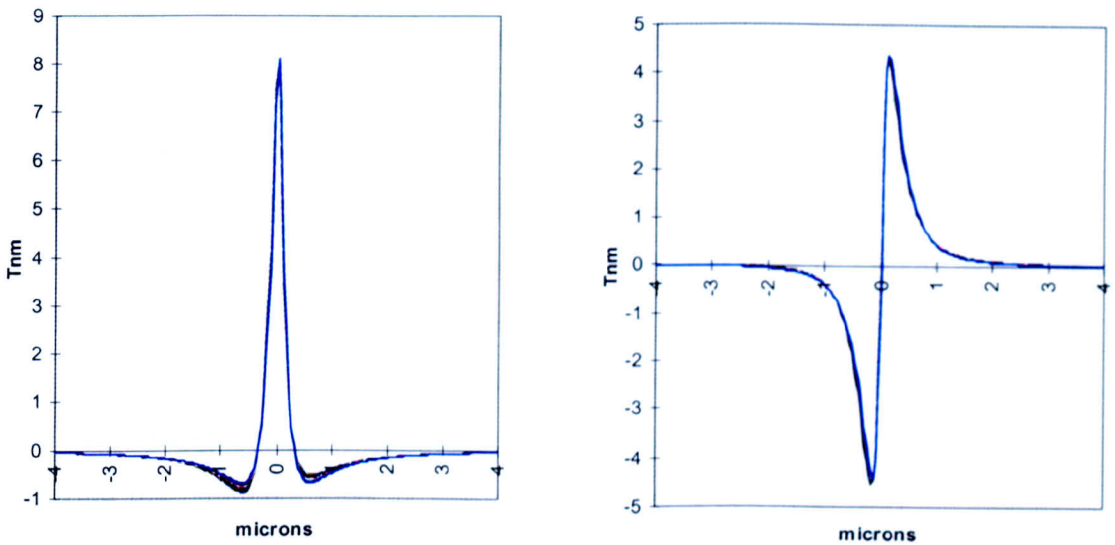
Fig. 6.15: Field scans taken across the calculated and ART reconstructed model tip fields.

Note that the x , y and z components referred to above correspond to the components in figs. 6.6 and 6.8.

Also note that the *red scans are taken across the ART reconstructed fields* and the *green scans are taken across the calculated fields*.

reconstructed field. We therefore conclude that ART does not produce a more accurate representation of the stray field than is available from the RTM reconstruction technique.

The inaccuracy of the ART reconstructed tip field was initially thought to be due to the truncated nature of the model tip's rotation data sets (see figs. 4.8(c) and (d) - notice that the line scans in both data sets do not go to zero at their extremes). We therefore decided to investigate the accuracy of the stray field reconstructed from orthogonal rotation data sets which were not of a truncated nature. Fig. 6.16 shows just such a data set pair generated by a model tip of height $0.5\mu\text{m}$; the line scans are approximately zero at the edges.



(a) Scans sensitive to induction normal to the plane of reconstruction.

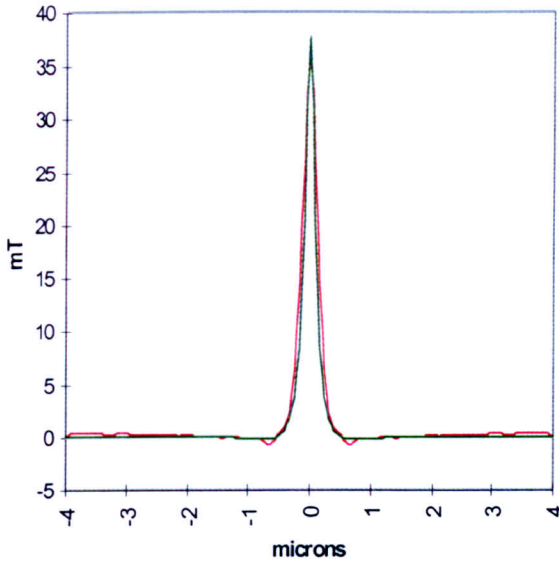
(b) Scans sensitive to induction in the plane of reconstruction.

Fig. 6.16: Simulated rotation data sets of orthogonal integrated field components generated by a model tip of height $0.5\mu\text{m}$.

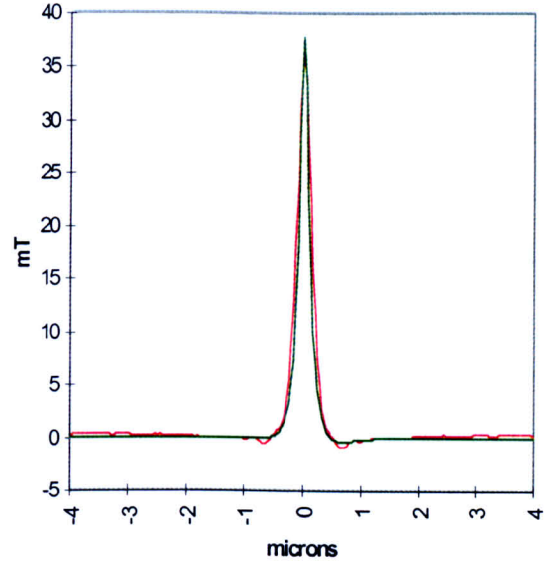
The stray field was reconstructed from these rotation data sets using ART. The stray field was also calculated directly from the tip model at the reconstruction plane. Once again these three dimensional stray fields are not shown here, instead field scans were taken across the calculated and reconstructed field planes and are shown in fig. 6.17.

Notice (from the scans in fig. 6.17) that there are still significant differences between the calculated and ART reconstructed fields. This suggests that even with 'well behaved' input data sets the ART method does not produce as accurate a representation of the stray field as is obtained from the RTM reconstruction technique. In fact we find that the error in the ART reconstructed field is of a similar magnitude to the error in the previous ART tip field reconstruction. For the scans in fig. 6.17(a) taken horizontally across the normal components of field we find that the FWHM of the calculated field scan is 177nm, while the FWHM of the reconstructed field scan is 268nm. For the scans in fig. 6.17(b) taken vertically across the same components of field the FWHM of the calculated field scan is 179nm, while the FWHM of the reconstructed field scan is 270nm.

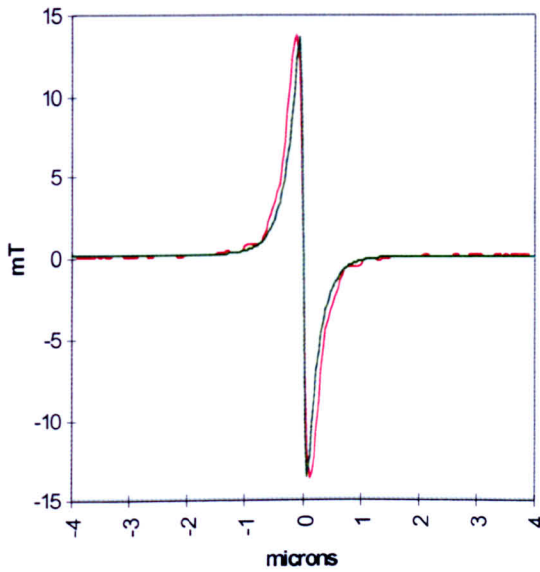
The peak value of the normal component of the calculated field is 38mT, while the corresponding reconstructed field value is 36mT. Thus in this case we again find that although there is only a small error in the magnitude of the ART reconstructed field (again less than 2%) the error in the spatial definition of the ART reconstructed field is large (being again approximately 50%). We therefore again conclude that ART does not produce a more accurate representation of the stray field than is available from the RTM reconstruction technique. We now consider the stray field reconstructed from the truncated rotation data sets generated by the model tip assembly.



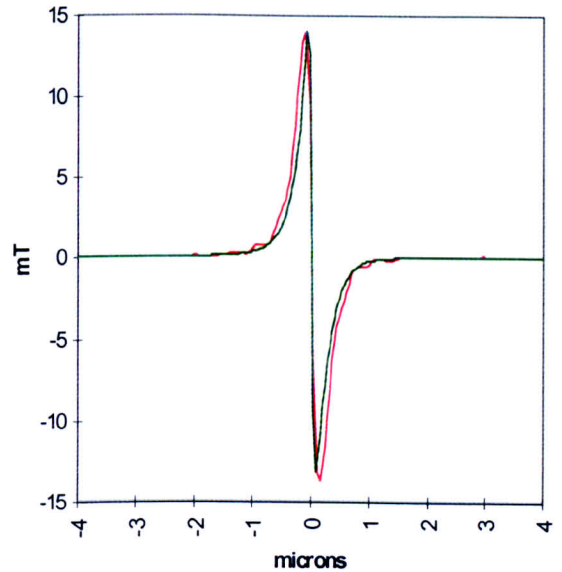
(a) Scans taken (horizontally) across the normal components (y components) of the calculated and ART reconstructed fields.



(b) Scans taken (vertically) across the normal components (y components) of the calculated and ART reconstructed fields.



(c) Scans taken across the (in-plane) x components of the calculated and ART reconstructed fields.



(d) Scans taken across the (in-plane) z components of the calculated and ART reconstructed fields.

Fig. 6.17: Field scans taken across the calculated and ART reconstructed model tip (of height $0.5\mu\text{m}$) stray fields.

Note that the x, y and z components referred to above correspond to the components in figs. 6.6 and 6.8.

Also note that the *red scans* are taken across the ART reconstructed fields and the *green scans* are taken across the calculated fields.

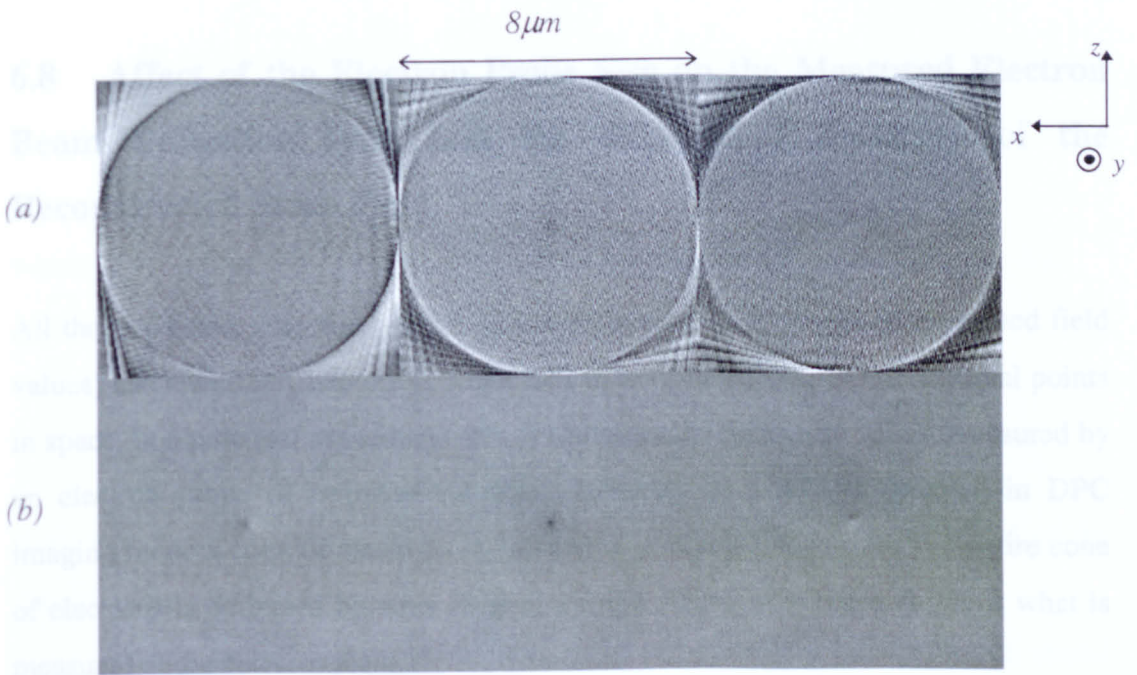
6.7.2 Consideration of the Accuracy of the ART Reconstructed Model Tip Assembly Stray Field

Fig. 6.18(a) shows the stray field reconstructed using the ART method from the deflection data sets (in fig. 6.5(a) and (b)) generated by the model tip assembly magnetised as in the Transverse Case. Fig. 6.18(b) shows the field calculated directly from the tip assembly model.

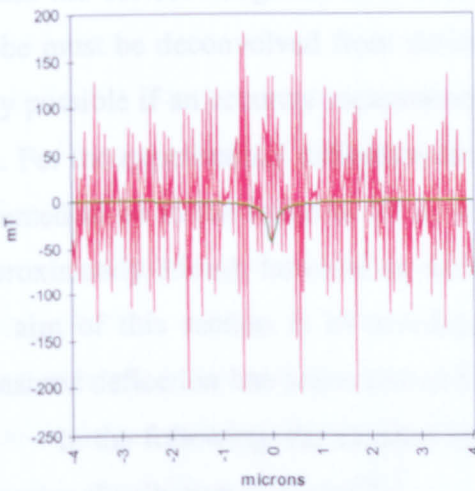
Clearly there is no agreement between the reconstructed field and the calculated field and the field scans in figs. 6.18(c) and (d) taken across the calculated and reconstructed field components reinforce this fact.

We therefore conclude that ART does not produce an accurate representation of stray field, and in fact the accuracy of the ART reconstructed field decreases as the input deflection data sets become more truncated in character - thus the RTM reconstruction technique is preferred for reconstructing MFM tip stray field.

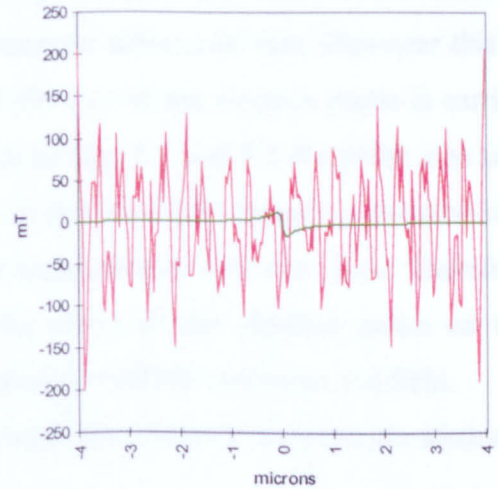
We now consider an unavoidable source of error in experimental deflection line scans (such as in figs. 5.1 and 5.2).



- (a) Stray field reconstructed using ART from the simulated rotation data sets generated by the model tip assembly magnetised as in the Transverse Case in fig. 6.5.
- (b) Stray field calculated directly from the model tip assembly.



(c) Horizontal scans taken across the y components of the reconstructed fields above.



(d) Scans taken across the z components of the reconstructed fields above.

Fig. 6.18: Comparison of the three dimensional stray field reconstructed using ART from the rotation data sets generated by the model tip assembly with the field calculated directly from the model tip assembly. Also shown are field scans taken across the reconstructed fields in (a) and (b).

6.8 Affect of the Electron Probe Size on the Measured Electron Beam Deflection Data and the Subsequent Accuracy of the Reconstructed Stray Field

All the simulated stray field values (and consequently the simulated integrated field values) calculated in Chapters 4, 5 and 6 have been calculated at infinitesimal points in space. In a practical experiment this is analogous to deflection values measured by an electron probe of infinitesimal size. However, in a STEM operated in DPC imaging mode a cone of electrons is focused to a disk of finite size. The entire cone of electrons is deflected by stray field in a finite region of space and this is what is measured at the detector plane.

If we assume that the cone of electrons is predominately deflected by stray field in the region of the focused electron disk then the experimental deflection line scans in figs. 5.1 and 5.2 can be approximately considered to represent a convolution of the shape of the focused electron probe with the DI MFM tip's integrated field. To obtain the correct integrated field from the tip assembly the shape of the electron probe must be deconvolved from the experimental deflection data. However this is only possible if an accurate measurement of the size of the electron probe is carried out. For the experimental deflection data sets in figs. 5.1 and 5.2 the probe size was assumed to be in the range of 20 to 40nm in diameter (the sampling distance was approximately 35nm); however an accurate measurement was not made. Therefore the aim of this section is to investigate the effect of the electron probe on the measured deflection line scans and on the subsequent RTM reconstructed field.

In the following, the electron probe was approximated to a one dimensional Gaussian distribution given by^[2],

$$f(x) = \frac{1}{\sqrt{2\pi}\sigma} \exp\left[-x^2 / 2\sigma^2\right] \quad (6.1)$$

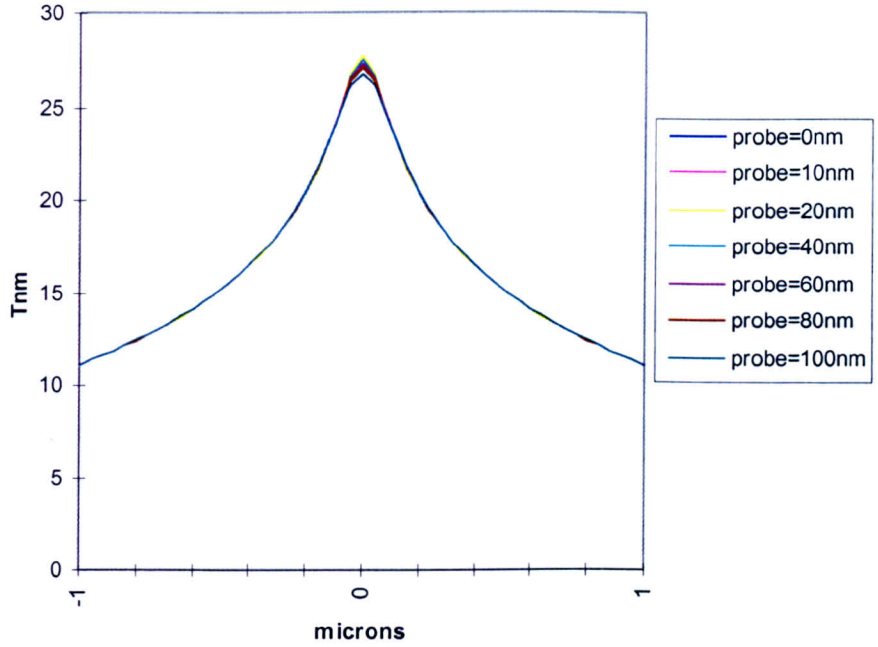
where $\sigma = FWHM/\sqrt{\ln 256}$ and the multiplying factor $\frac{1}{2\pi} \frac{1}{\sigma}$ was chosen so that

$$\int_{-\infty}^{\infty} f(x)dx = 1 \quad (6.2)$$

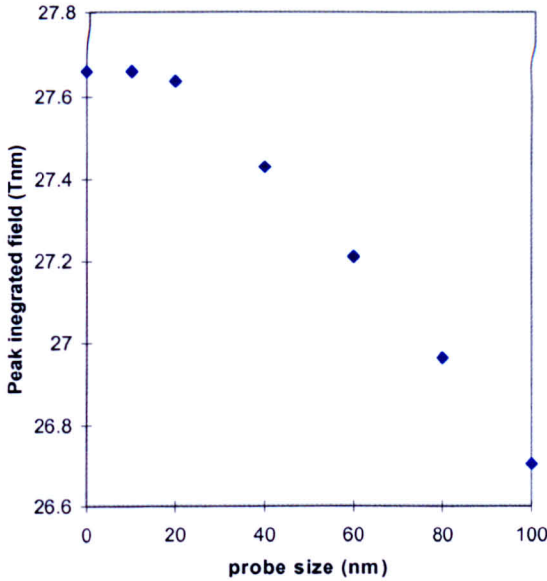
Note that the probe 'size' can be considered to be equivalent to the FWHM of the Gaussian distribution.

The integrated field line scans in the orthogonal data sets generated by model Tip1 in Chapter 4 (see fig. 4.8(c) and (d)) were convolved with various sized probe functions to simulate the integrated field measured in a STEM. Fig. 6.19(a) shows the central 2 μ m portion of one integrated field line scan convolved with a variety of probe sizes. From the fact that it is difficult to separate the individual scans suggests that the probe size has little effect on the measured deflection data. Nevertheless fig. 6.19(b) shows a plot of the peak integrated field values of the scans in fig. 6.19(a), while fig. 6.19(c) shows a plot of the FWHM of the scans.

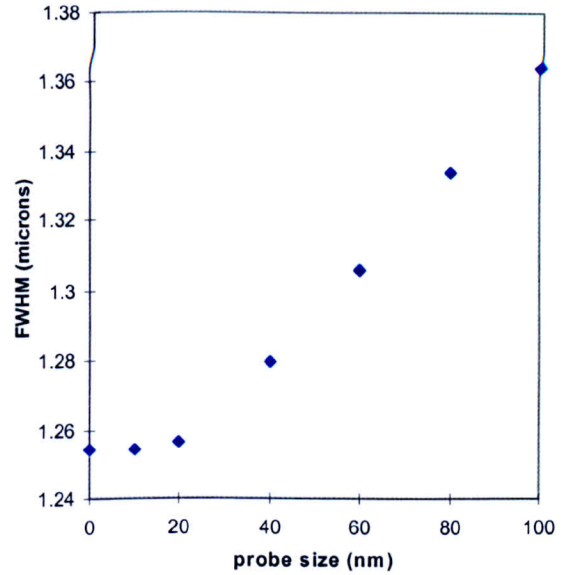
If the assumption that the electron probe used for the measurement of the deflection line scans in figs. 5.1 and 5.2 was approximately 20 to 40nm in diameter is correct, then the graphs in fig. 6.19 suggest that the magnitude of the measured peak deflection values (of the scans in figs. 5.1 and 5.2) can be expected to be approximately 2-3% lower than the deflection values that would be measured by an ideal (infinitesimally small) probe. Also the FWHM of the deflection line scans (in figs. 5.1 and 5.2) can be expected to be 3-4% larger than the FWHM of the scans measured by an ideal probe. Clearly as the probe size increases the effect on the magnitude and spatial character of measured deflection line scans will be more significant.



(a) A simulated integrated field line scan convolved with simulated probe functions of varying size. Only central $2\mu\text{m}$ of the scans are shown.



(b) Plot of the peak integrated field values of the scans in (a).



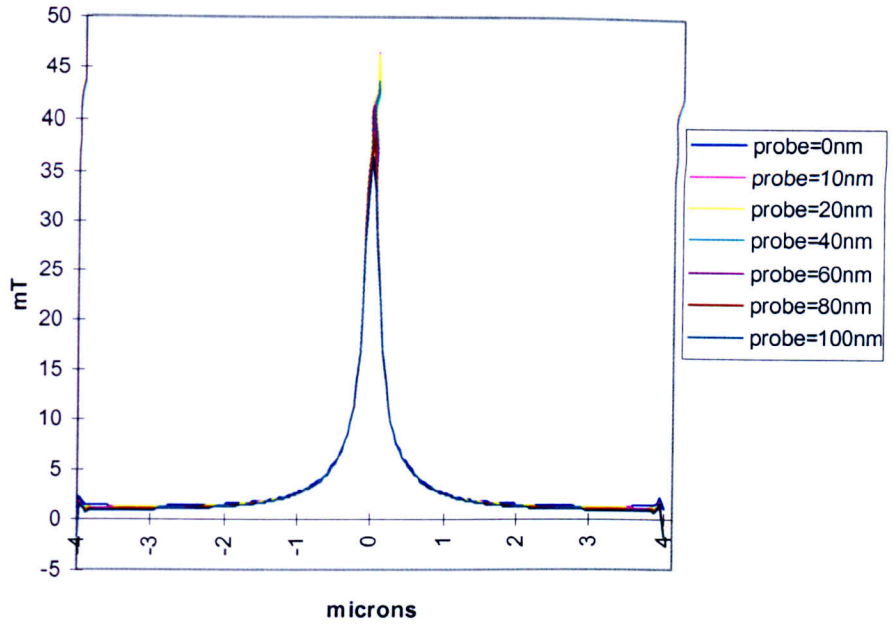
(c) Plot of the FWHM of the scans in (a).

Fig. 6.19: A simulated integrated field line scan convolved with various sized probe functions. Also shown are plots of the peak values and the FWHM of the scans.

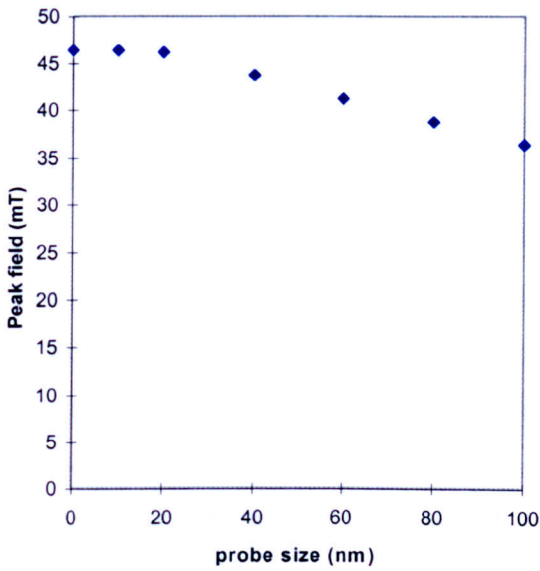
The three dimensional fields reconstructed from the 'measured' simulated deflection data sets are now considered. Field scans taken across the components of field normal to the reconstruction plane (reconstructed from the deflection data set sensitive to induction in the plane of reconstruction since this has been determined to be the most accurate representation of the normal component of stray field) are shown in fig. 6.20(a). Fig. 6.20(b) shows a plot of the peak field values of the scans, while fig. 6.20(c) shows a plot of the FWHM of the scans.

These graphs indicate the effect that a finite sized electron probe has on the accuracy of the stray field reconstructed from line scan deflection data sets measured in a STEM. Once again, if the diameter of the electron probe (used to measure the experimental deflection data in figs. 5.1 and 5.2) is 20 to 40nm, then we can expect the magnitude of the stray fields reconstructed from these data sets (in figs. 5.1 and 5.2) to be approximately 6-7% smaller than the correct stray field. Also, the spatial definition (FWHM of the normal component of field) of the reconstructed stray field can be expected to be 7-8% wider than that of the correct stray field. Again, as the probe size increases, the effect on the magnitude and spatial character of the experimental reconstructed field will be more significant.

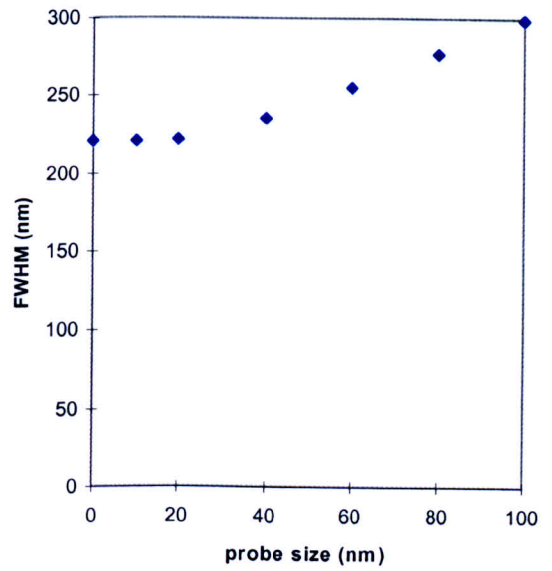
Hence the finite size of the focused electron probe will effect the precision of the stray field reconstructed from measured deflection line scans. However, provided that 1) the electron probe is of a similar size, or smaller than the sampling distance, and 2) the cone of electrons in the STEM is predominately deflected by stray field in the immediate vicinity of the focused electron disk, then the effect is expected to be small.



(a) Field scans taken across the component of the reconstructed field normal to the plane of reconstruction. The stray fields were reconstructed from the integrated field line scans convolved with varying sizes of probe function.



(b) Plot of the peak field values of the scans in (a).



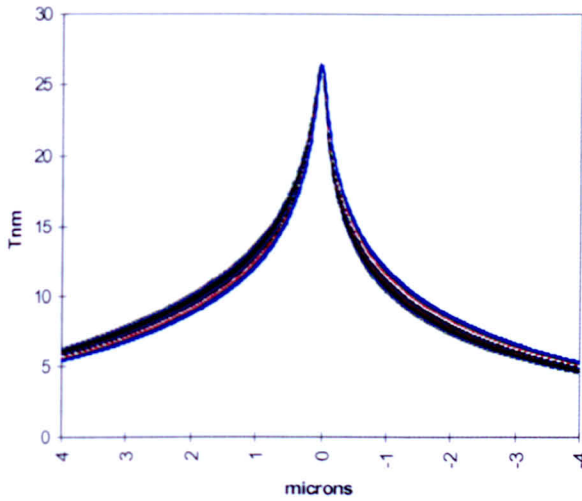
(c) Plot of the FWHM of the scans in (a).

Fig. 6.20: Field scan components reconstructed from integrated field line scan rotation data sets convolved with varying sizes of probe function. Also shown is plots of the peak field and the FWHM of the scans.

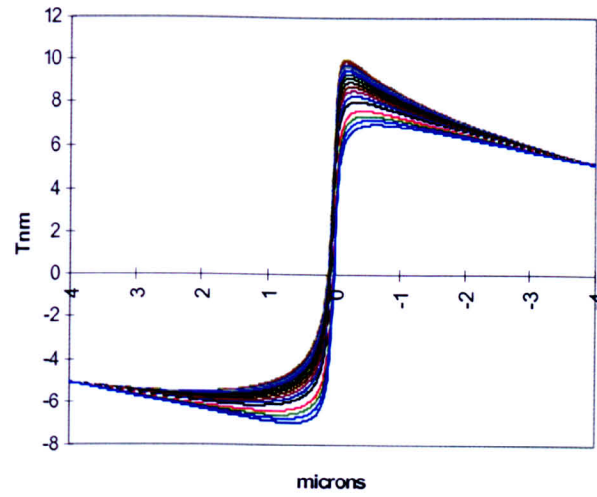
6.9 Stray Field Reconstructed From Incorrectly Aligned Integrated Field Line Scans

A further possible source of error in the stray field reconstructed from an experimental line scan deflection data set arises from the alignment of the line scans in the data set. When the rotation data sets are collected (using DPC imaging) it is impossible to set the position of the tip in the images with sufficient accuracy to establish a common axis. Thus the individual line scans are frequently aligned manually about a common peak deflection value prior to tomographic reconstruction. This therefore assumes that the peak deflection value of each scan occurs at the same position on the line scan. However this is not always a valid assumption as the integrated field line scans generated by Tip2 in Chapter 4 show; see fig. 6.21(a) and (b). We find that the position of the peak integrated field values of the scans in fig. 6.21(a) varies by up to 35nm on the horizontal axis - fig. 6.21(c) shows the central 500nm of the scans in fig. 6.21(a), from which the variation in the peak value position is clearer. In this section we consider the effect that this horizontal misalignment of line scans within a data set has on the accuracy of the reconstructed field.

The stray field was reconstructed from the correctly aligned line scans shown in fig. 6.21(a) and (b) generated by Tip2. The field was also reconstructed from the same line scans but with a horizontal misalignment so that the position of the peak integrated field values coincide (see fig. 6.21(d) which shows the central 500nm of the scans sensitive to induction normal to the plane of reconstruction). The line scans sensitive to induction in the plane of reconstruction were incorrectly aligned by an equal amount. These three dimensional reconstructed stray fields are not shown here. Instead horizontal and vertical field scans were taken across the components of field normal to the plane of reconstruction and are shown in fig. 6.22.

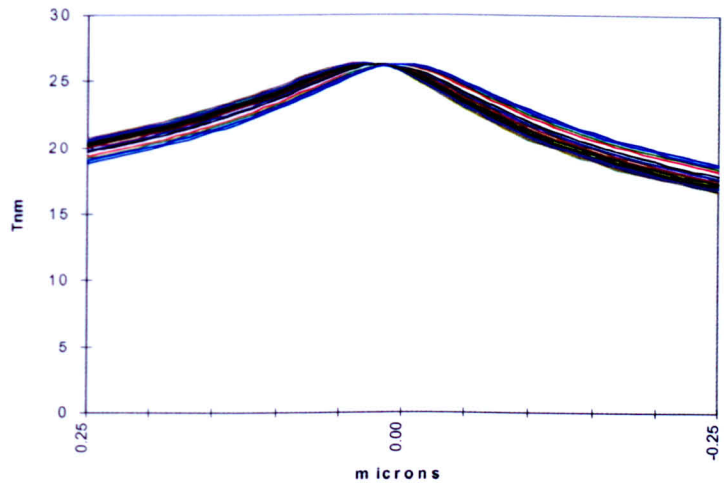


(a) Integrated field line scans generated by Tip2 sensitive to induction normal to the plane of reconstruction.



(b) Integrated field line scans generated by Tip2 sensitive to induction in the plane of reconstruction.

(c) Central 500nm portion of the correctly aligned line scans in (a). Notice the varying position of the peak integrated field value.



(d) Central 500nm of the same line scans as above but this time the scans have been incorrectly aligned about the same integrated field value position.

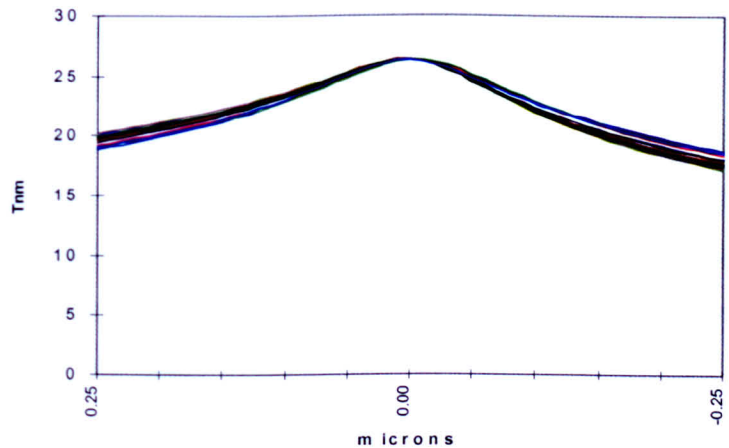
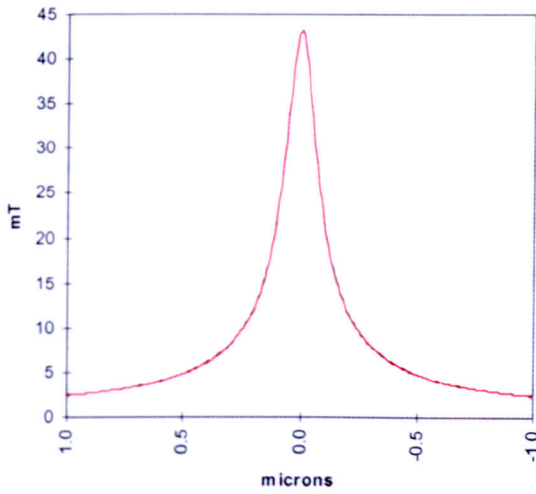
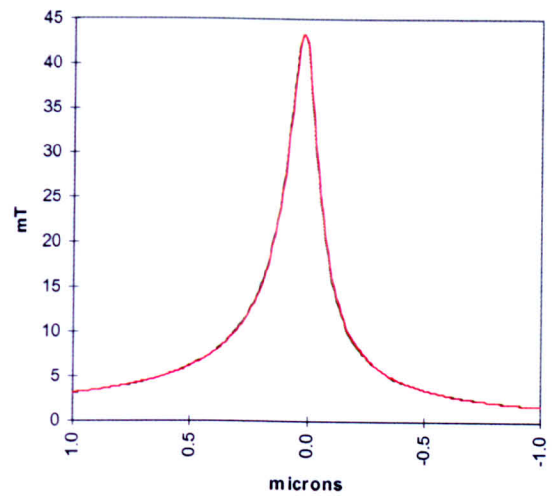


Fig. 6.21: Integrated field line scans generated by Tip2 in Chapter 4 (see fig. 4.5(b) for diagram of Tip2). Also shown is the central 500nm portions of the correctly and incorrectly aligned line scans sensitive to induction normal to the reconstruction plane.



(a) Horizontal field scans taken across the normal components of field.



(b) Vertical field scans taken across the normal components of field.

Fig. 6.22: Scans taken across the normal component of the stray field reconstructed from the correctly and incorrectly aligned line scan rotation data sets.

Note that the *red scans are taken across the field reconstructed from the correctly aligned line scans*, while the *green scans are taken across the field reconstructed from the incorrectly aligned line scans*.

The fact that it is difficult to separate the field scans in figs. 6.22(a) and (b) indicates that there is an excellent agreement between the reconstructed fields. In fact we find that the FWHM of the horizontal field scans in fig. 6.22(a) are 204nm for the field reconstructed from the correctly aligned line scans and 202nm for the field reconstructed from the incorrectly aligned line scans - effectively an insignificant error. Further, the vertical field scans in fig. 6.22(b) are both found to have FWHM of 200nm, while the peak value of the component of field over which the scans are taken is found to be 43mT in both cases.

We therefore conclude that an error in the horizontal alignment of the line scans (such as above) within an experimental deflection data set will not significantly effect the accuracy of the reconstructed stray field.

6.10 Discussion and Summary

Two methods for obtaining an accurate reconstruction of the 3-D MFM tip stray field from non 'well behaved' input deflection data sets (i.e. deflection data sets containing line scans which do not decrease to zero at their extremes - similar to the experimental deflection data sets presented in Chapter 5) using the RTM reconstruction method were demonstrated in this chapter.

The first method (see Sections 6.3 and 6.4) involved reconstructing the 3-D stray field from each of the tip assembly's orthogonal deflection data sets. The in-plane components of field reconstructed from the deflection data set sensitive to induction normal to the plane of reconstruction, and the normal component of field reconstructed from the deflection data set sensitive to induction in the plane of reconstruction were found to be accurate representations of the tip assembly's three stray field components.

The second method for accurate reconstruction of the tip field from the non 'well behaved' deflection data sets using the RTM reconstruction technique required a modification of the input deflection data sets (see Section 6.6). In this case a constant deflection value was subtracted from each deflection line scan so that the average value of the ends of each line scan were approximately zero. This is an approximate method for subtracting the cantilever and substrate contribution from the tip assembly's deflection data sets. The 3-D stray field was reconstructed from each of the modified orthogonal deflection data sets and the average was taken. This method also gives an accurate representation of the MFM tip field.

In Section 6.7 an investigation into the accuracy of the stray field reconstructed using the ART method was carried out. It was found that stray field reconstructed from 'well behaved' line scan deflection data sets using the ART reconstruction technique was not as accurate a representation of the tip field as the field reconstructed from the same deflection data sets using the RTM technique. In fact the less 'well behaved' the input deflection data sets to the ART reconstruction technique were, then the less accurate the (ART) reconstructed field was found to be. We therefore conclude that the RTM reconstruction technique is the most accurate reconstruction technique tested in this chapter (for reconstructing stray field from

'well behaved' and non 'well behaved' deflection data sets) and is therefore preferred for investigations of MFM tip stray fields.

References

- [1] Liu, Y (1996), '*Electron Beam Tomography of Recording Head Fields*' PhD Thesis
- [2] Private communication with Dr. S. McVitie

Chapter 7

Characterisation of the Stray Field from Two Further MFM Tips

7.1 Introduction

The tip models considered in Chapters 4, 5 and 6 were all constructed with the intention of simulating the stray field from one specific DI MFM tip (recall that we considered the DI tip magnetised in the Axial and Transverse Cases). In this chapter we now consider two further MFM tips, each of different type from the previous DI tip and each constructed with the intention of generating stray field of a specific character. In Section 7.2 we consider a DI tip partially coated with thin film. This tip was produced with the purpose of maximising the resolution achievable from the DI tip. In Section 7.3 we consider another thin film tip but in this case the tip has a groove made by ion milling at its apex. The purpose of the groove is to encourage the remanent tip magnetisation to align in a direction perpendicular to the groove and in the plane of the cantilever. This arrangement allows the tip to be sensitive to components of induction parallel to the surface of a specimen in the MFM.

7.2 The Partially Coated DI MFM Tip

The first generation of MFM tips employed in magnetic force microscopy were fine, electrochemically etched wires such as iron, nickel and cobalt^[1]. Several studies^{[2][3]} of these tips found that the radius of curvature of the tip and the tip-specimen separation are the main factors which limit the achievable resolution in the MFM. Thus the magnetic volume of the tip is important in defining the resolution. Since higher spatial resolution magnetic imaging is always desirable, it follows that MFM tips of lower magnetic volume are required. This led to the introduction of thin film MFM tips. We now consider one practical method proposed for maximising the spatial resolution achievable from a thin film MFM tip by minimising the magnetic volume of the tip.

A silicon Nanoprobe tip from DI was partially coated with a Co thin film by Tom Pfaffelhuber of Regensburg University in Germany. The magnetic film was evaporated from a point source with the intention that only two faces of the tip (as well as parts of the cantilever and substrate) be coated - see fig. 7.1. The tip was then magnetised by the application of a large field directed along the tip axis and a full deflection line scan rotation data set was taken.

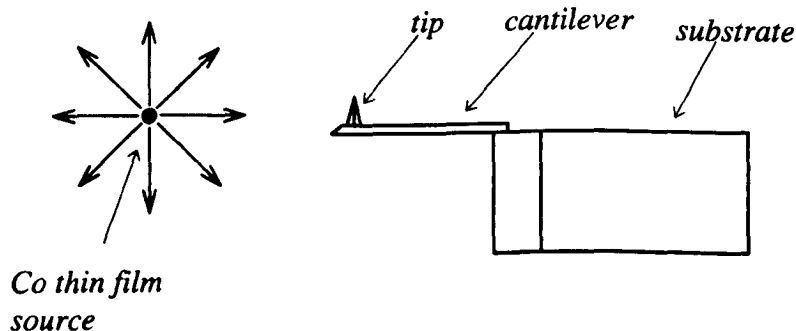


Fig. 7.1: Diagram illustrating the directional evaporation of Co thin film onto the tip assembly structure. Only the surfaces of the tip assembly which are directly exposed to the source will be coated with film.

To determine whether a partially coated DI tip mounted in a MFM can achieve a higher spatial resolution than is possible from an identical DI tip entirely coated with film, we require to compare the character of the stray fields generated by each tip. A comparison of the stray field from the partially coated DI tip with the field reconstructed from the deflection data sets in fig. 5.1 (generated by a separate DI tip entirely coated with film and magnetised as in the Axial Case) would have been carried out but for the fact that the thickness of film coating each tip is not known precisely and this influences the peak field and the spatial character of a tip's stray field (see Section 4.5). Instead an extensive theoretical investigation comparing the stray fields generated from a model tip partially coated with film and the field from a tip entirely coated with film of the same thickness is required. However, prior to this, a comparison of the deflection line scans generated by the partially coated DI tip with simulated integrated field line scans generated by a model of this DI tip is conducted.

Fig. 7.2 shows a diagram of a possible model for the DI tip partially coated with thin film. For this model it was assumed that the film evaporated onto the DI tip coated the front two faces only. Note that this model will subsequently be referred to as the Two Sided Tip. Also note that the effective geometry of the model tip is identical to that of Tip 3 in Chapter 4.

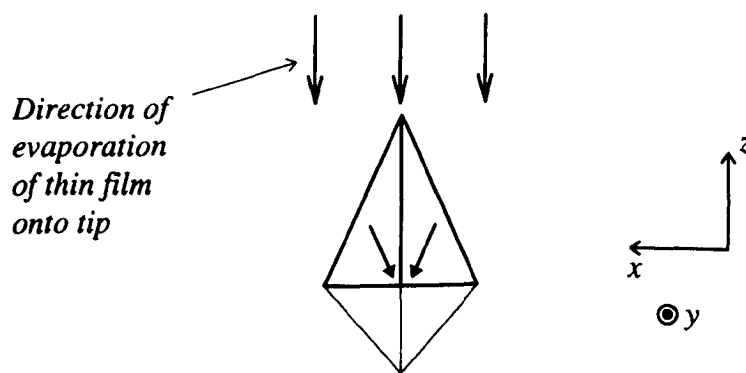
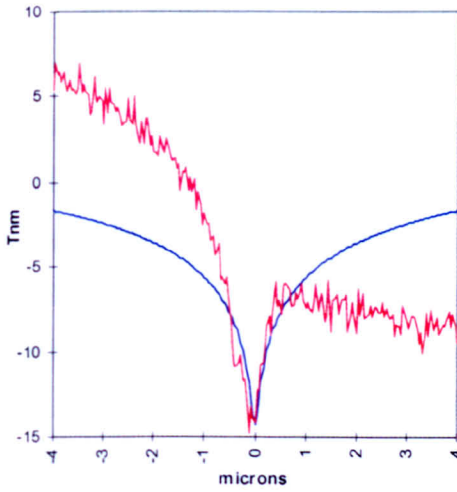


Fig. 7.2: Diagram of a model for the partially coated DI MFM tip. Note that the geometry of the model is identical to that of Tip 3 in Chapter 4 (see fig. 4.5).

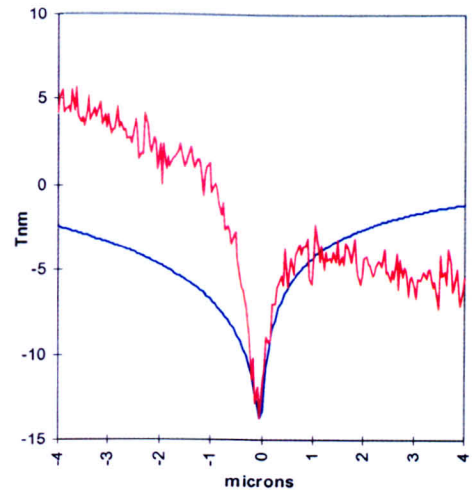
A full integrated field line scan rotation data set was calculated from this tip model and a selection of these line scans are shown in fig. 7.3. Also shown are the corresponding experimental deflection line scans generated by the partially coated DI MFM tip. Note that the deflection line scans generated by the DI tip have been modified by the subtraction of a large variable vertical shift value from each scan.

Figs. 7.3(a) and (b) show a comparison of simulated and experimental deflection line scans sensitive to induction normal to the plane of reconstruction. There is reasonable agreement between corresponding scans. A similar level of agreement is also found between the simulated and experimental line scans sensitive to induction in the plane reconstruction, see figs. 7.3(c) and (d). Note that the contribution to the experimental deflection data sets from the cantilever and substrate portions of the partially coated DI tip assembly have not been taken into account in the model. This is a possible reason that the agreement between the simulated and experimental deflection line scans is not better.

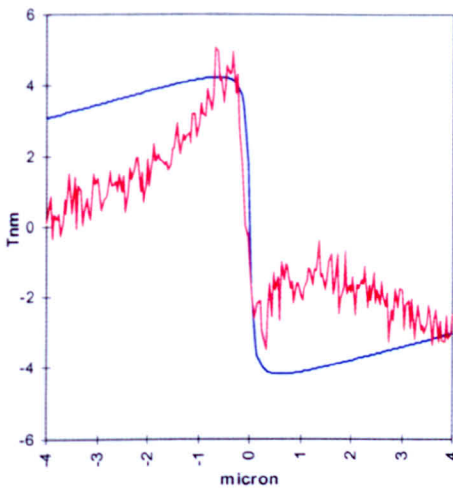
The agreement between the simulated and experimental deflection line scans justifies the use of the Two Sided Tip model to investigate the character of the partially coated DI tip field. We now compare the stray fields and integrated stray fields generated by the Two Sided Tip with that from model Tip3 in Chapter 4 (note that model Tip3 is coated with a film of equal thickness and represents a DI tip entirely coated with film). In the following, model Tip3 will be referred to as the Four Sided Tip.



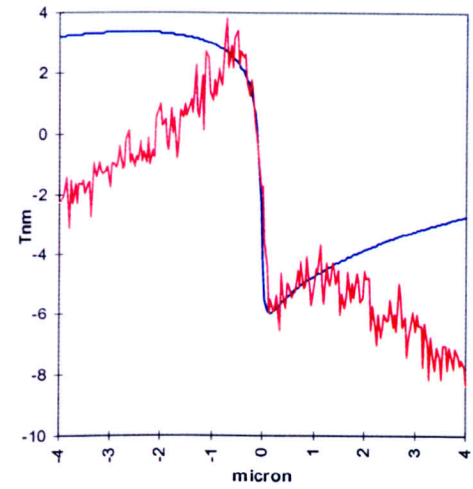
(a) Scans sensitive to induction normal to the plane of reconstruction.



(b) Scans sensitive to induction normal to the plane of reconstruction. Scans separated from the scans in (a) by 90° about the rotation axis.



(c) Scans sensitive to induction in the plane of reconstruction.



(d) Scans sensitive to induction in the plane of reconstruction. Scans separated from the scans in (c) by 90° about the rotation axis.

Fig. 7.3: Comparison of a selection of deflection line scans generated by the partially coated DI MFM tip with simulated integrated field line scans generated by the Two Sided Tip.

Note that the scans in (a) are separated by 90° about the rotation axis from the scans in (b). The same is true of the scans in (c) and (d).

Also note that the experimental deflection line scans generated by the DI tip have had a constant deflection value subtracted from them. The value subtracted was the average value of the end-points of the scans.

Further note that the red scans were generated by the partially coated DI tip, while the blue scans were generated by the Two Sided Tip model.

Full simulated integrated field line scan rotation data sets were calculated from each tip model and a scan taken from each data set (sensitive to induction normal to the plane of reconstruction) is shown in fig. 7.4. The magnitude and the FWHM of the scan generated by the Two Sided Tip is 14Tnm and 1200nm respectively. The corresponding magnitude and FWHM of the scan generated by the Four Sided Tip is 23Tnm and 850nm. Thus, as expected (due to the fact that the Two Sided Tip is coated in a significantly smaller volume of magnetic material than the Four Sided Tip), the magnitude of the integrated field generated by the Two Sided Tip is smaller than that from the Four Sided Tip. Also note that the FWHM of the integrated field generated by the Four Sided Tip is significantly smaller than the FWHM of the integrated field from the Two Sided Tip. This is due to the fact that Four Sided Tip model contains a larger amount of negatively polarised magnetic charge planes than the Two Sided Tip - these tend to reduce the FWHM of the integrated field. These points are generally expected and tell us little about any difference between the character of the stray fields from the Two and Four Sided Tips.

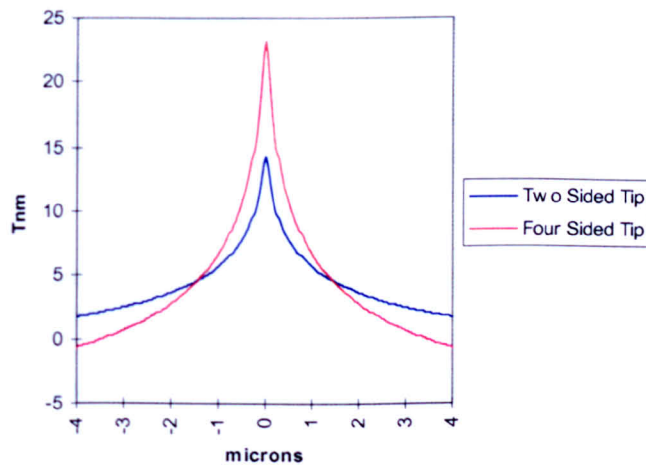


Fig. 7.4: Simulated integrated field line scans (sensitive to induction normal to the reconstruction plane) generated by the Two and Four Sided Tips.

The stray field was therefore reconstructed from the two orthogonal rotation data sets generated by the Two Sided Tip and the average was taken. The average three dimensional field reconstructed from the two orthogonal rotation data sets generated by the Four Sided Tip was also determined. The spatial distribution of these 3-D fields was comparable but the fields are not shown here. Instead horizontal and vertical scans were taken across the components of field normal to the reconstruction plane and are shown in fig. 7.5.

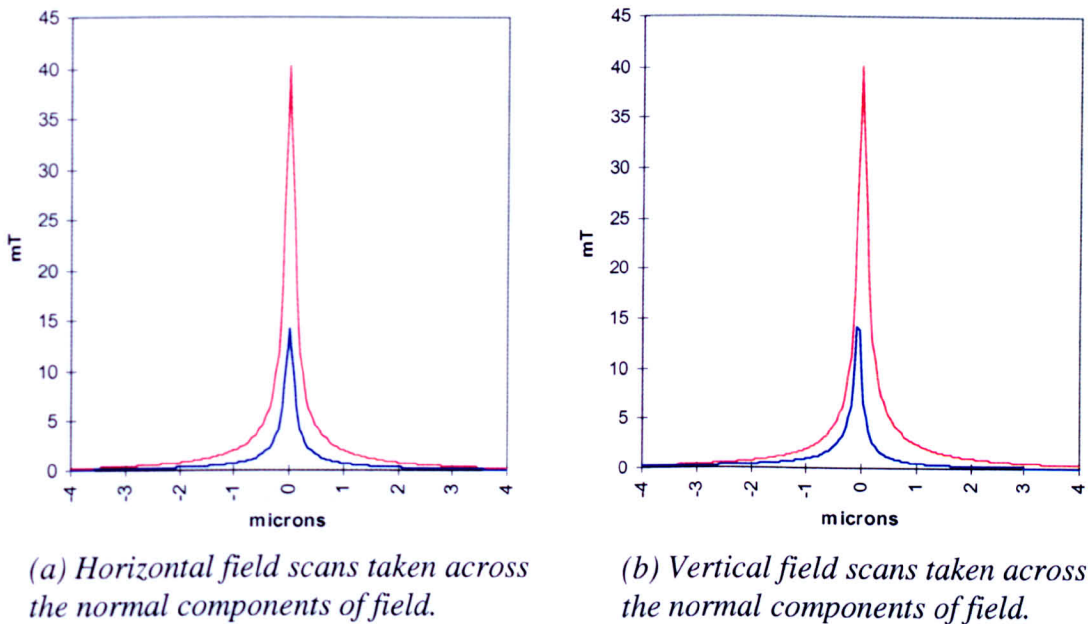


Fig. 7.5: Scans taken across the normal components of the Two and Four Sided Tip Model reconstructed stray fields. Note that red scans have been taken across the normal component of the Four Sided Tip field, while blue scans have been taken across the normal component of the Two Sided Tip field.

The peak value of the normal component of field from the Two Sided Tip is found to be 14mT, while the corresponding peak value of the field from the Four Sided Tip is 40mT. Further, in fig. 7.5(a) the FWHM of the field scans were found to be 218nm

for the Two Sided Tip, and 220nm for the Four Sided Tip. In fig. 7.5(b) the FWHM of the scan taken across the field from the Two Sided Tip was found to be 214nm, while the corresponding FWHM of the scan taken across the field from the Four Sided Tip was found to be 225nm.

Thus the magnitude of the stray field generated by the Two Sided Tip is significantly smaller than the field generated by the Four Sided Tip. Also, although the FWHM of the Two Sided Tip field is smaller than the field from the Four Sided Tip the difference is small - being less than approximately 5%. This suggests that the spatial resolution available from a partially coated DI MFM tip (of comparable geometry to the model) will be only marginally higher than the resolution available from a DI tip entirely coated with thin film. Other methods exist for increasing the spatial resolution achieved in Magnetic Force Microscopy such as sharper MFM tips and lowering the tip-specimen separation^{[4][5]}. However it is a combination of these methods as well as reducing the volume of magnetic material coating the MFM tip which need to be implemented to increase the spatial resolution significantly. We now consider one further MFM tip.

7.3 The Seagate Grooved Tip

Recall from Section 2.4 that a MFM image represents a two dimensional map of a convolution of the tip magnetisation and the sample stray field. Due to the Theory of Reciprocity^[6] we can alternatively regard a MFM image as a map of a convolution of the tip stray field and the specimen magnetisation. Thus, to determine quantitatively a specimen's magnetisation from a MFM image, we must deconvolve the tip stray field from the image. It therefore follows that for quantitative MFM imaging a tip with a known stray field distribution is required.

We have previously considered MFM tips (i.e. the DI tip magnetised as in the Axial and Transverse Cases and the partially coated DI tip considered in Section 7.2) which have been found to be predominately magnetised along the tip axis (even after the application of a large field directed along the cantilever axis for the DI tip

magnetised as in the Transverse Case). In this section we now consider a MFM tip which was specifically designed so that a large component of its remanent magnetisation be directed perpendicular to the tip axis (i.e. in the plane of the cantilever). This was required to give a field which could be used to investigate the spatial variation of the magnetoresistive (MR) sensitivity over the area of an MR sensor designed for data read back from hard disks^[7]. The tip was manufactured by Seagate and had a groove ion milled at its apex. The groove was measured from SEM images to extend approximately $6\mu\text{m}$ down the tip and to be approximately 200nm wide. The bottom of the groove is assumed to be parallel to the sides of the tip. A magnetic film was sputtered onto the structure after the groove was formed (the thickness of this magnetic film is not known). The tip was designed with the intention that a series of magnetic dipoles be set up across the groove (when exposed to a magnetising field) thereby generating the required stray field distribution.

The Seagate MFM tip was magnetised in three different ways and for each a full line scan rotation data set was taken. A model of the Seagate tip was constructed - see fig. 7.6 - for the purpose of assisting in the determination of possible magnetisation distributions for the three cases. We now consider the deflection data sets and consequent reconstructed stray fields generated by the Seagate tip.

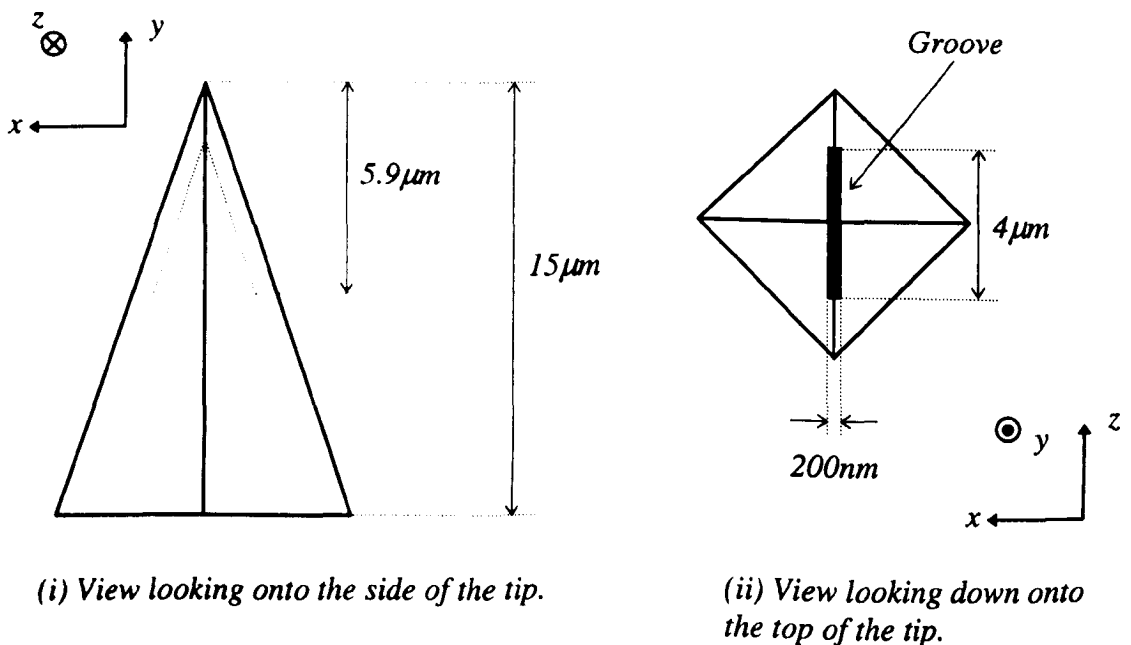


Fig. 7.6: Diagram of the model of the Seagate tip. Note that the geometry of the model is the same as Tip1 in Chapter 4 (see fig. 4.5).

7.3.1 The Seagate Tip Magnetised by a Large Field Directed in the Plane of the Cantilever and Normal to the Groove

We first consider the Seagate tip magnetised by the application of a large field directed normal to the cantilever axis and in the plane of the cantilever (i.e. directed normal to the groove). This will subsequently be referred to as the Normal Case. Several possible models for the magnetic configuration of the Seagate tip were constructed and are shown in fig. 7.7. Full simulated integrated field line scan rotation data sets were calculated from each tip model but are not shown here. Instead a selection of line scans generated by the tip model *GT_1* (see fig. 7.7(a)) are shown in fig. 7.8. Also shown are the corresponding deflection line scans generated by the Seagate tip. Note that the experimental deflection line scans have again been modified by the subtraction of a large variable vertical shift value from each scan.

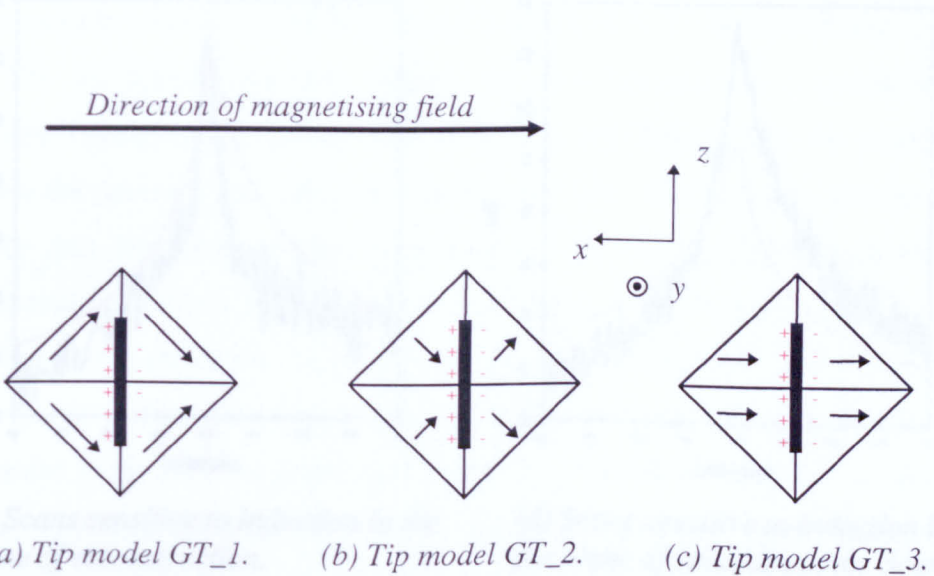
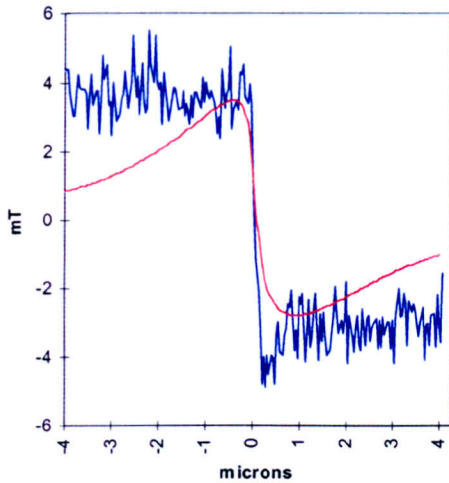
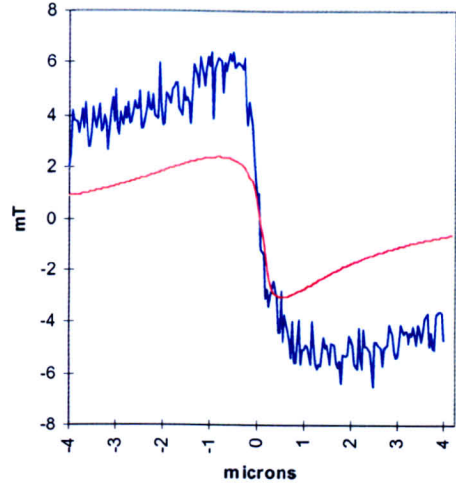


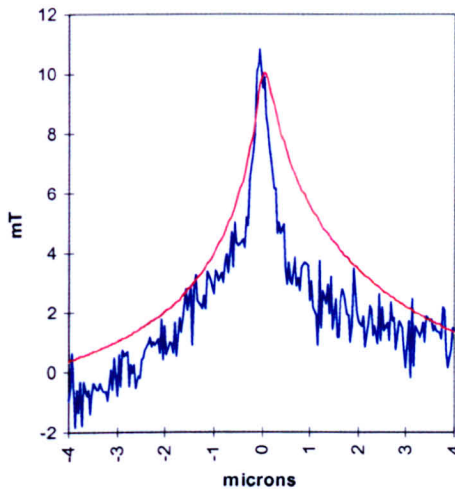
Fig. 7.7: Three possible magnetic configurations of the Seagate tip magnetised as in the Normal Case. Note that each individual film is magnetised in the plane of the film. Also note that the +’s and -’s indicate the directions of the series of dipoles set up across the groove.



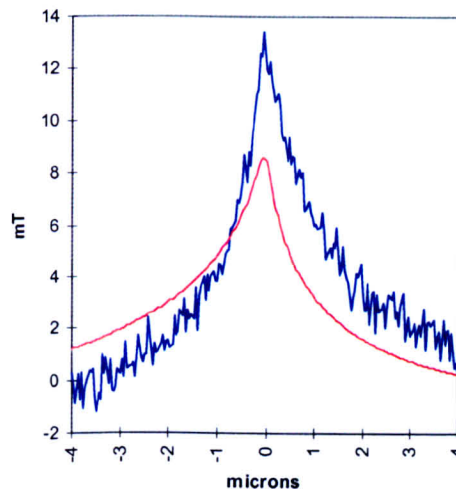
(a) Scans sensitive to induction normal to the plane of reconstruction.



(b) Scans sensitive to induction normal to the plane of reconstruction. Scans separated from the scans in (a) by 90° about the rotation axis.



(c) Scans sensitive to induction in the plane of reconstruction.



(d) Scans sensitive to induction in the plane of reconstruction. Scans separated from the scans in (c) by 90° about the rotation axis.

Fig. 7.8: Comparison of a selection of deflection line scans generated by the Seagate tip magnetised as in the Normal Case with the simulated integrated field line scans generated by tip model GT_1 (see fig. 7.7(a)).

Note that the scans in (a) and (c) are separated from the corresponding scans in (b) and (d) by 90° about the rotation axis.

Also note that the deflection line scans generated by the Seagate tip have had a constant deflection value subtracted from them. The value subtracted was the average value of the end-points of the scans.

Further note that the blue scans were generated by the partially coated DI tip, while the red scans were generated by the Two Sided Tip model.

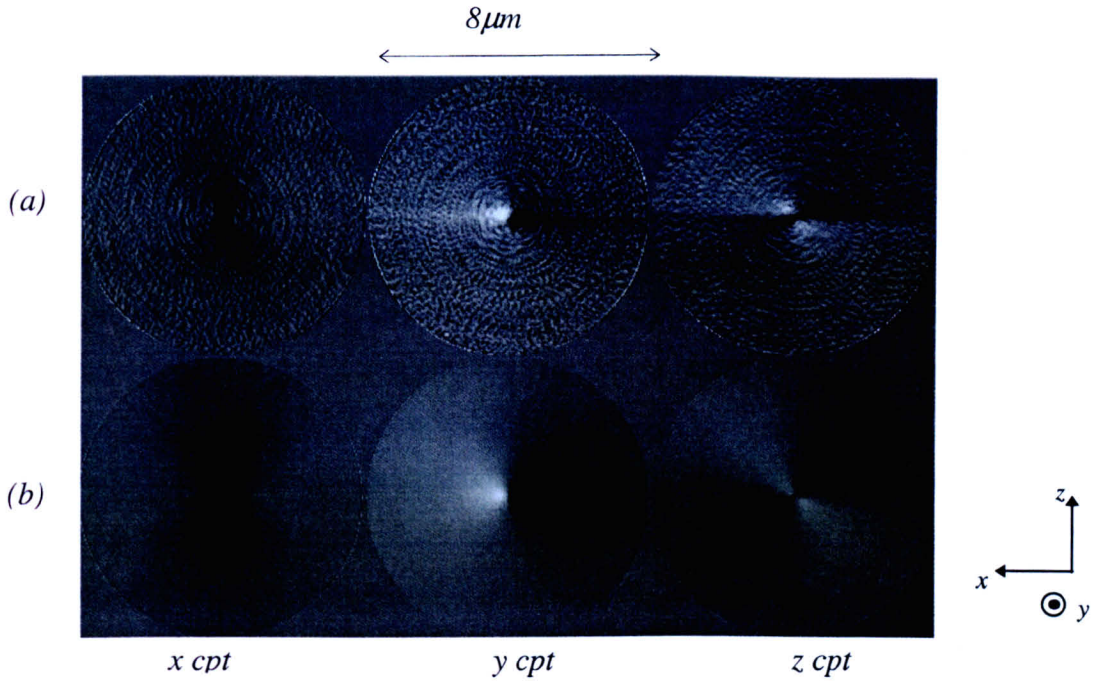
Figs. 7.8(a) and (b) show a comparison of experimental and simulated line scans sensitive to induction normal to the plane of reconstruction. It is clear from a visual comparison of the corresponding line scans that there is reasonable agreement between the character of the simulated and experimental deflection data. This is also found for a comparison of simulated and experimental deflection line scans sensitive to induction in the plane of reconstruction, see figs. 7.8(c) and (d). Therefore the suggestion is that tip model *GT_1* is a possible model for the Seagate tip magnetised in the Normal Case.

Note that in the absence of detailed information on the Seagate tip film thickness, a similar level of agreement can also be achieved for comparison of these experimental deflection line scans with the simulated deflection data generated by tip models *GT_2* and *GT_3*. However, the thickness of film coating each tip model must be modified accordingly (to ensure the tip models generate stray field of comparable magnitude to the experimental tip field). Therefore the tip models *GT_2* and *GT_3* are also possible models for the Seagate tip magnetised in the Normal Case.

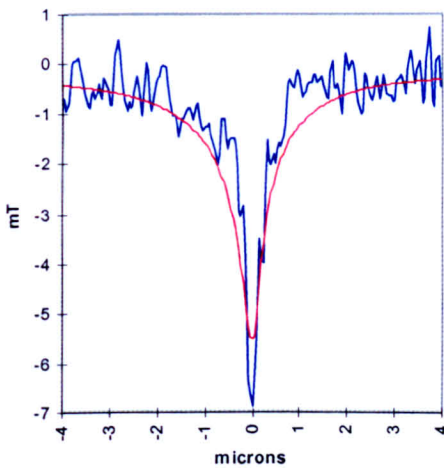
The tip models therefore suggest that the Seagate tip is predominately magnetised normal to the groove (however it is not clear which tip model best resembles the practical tip). We now consider the stray field reconstructed from the deflection data sets generated by the Seagate tip and make a comparison with the fields reconstructed from the rotation data sets generated by the tip models.

Fig. 7.9(a) shows the 'best fit' three dimensional field reconstructed from the orthogonal deflection data sets generated by the Seagate tip (i.e. the in-plane components have been reconstructed from the deflection data set sensitive to induction normal to the plane of reconstruction, while the normal component of field is reconstructed from the deflection data set sensitive to induction in the plane of reconstruction - see Sections 6.3 and 6.4). Fig. 7.9(b) shows the corresponding three dimensional field reconstructed from the simulated rotation data sets generated by tip model *GT_1*.

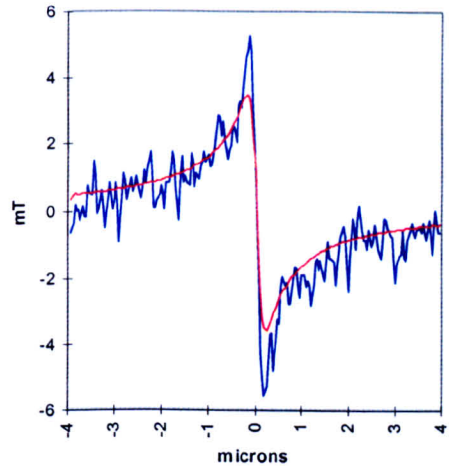
A visual comparison of the corresponding field components clearly suggests that the experimental and simulated reconstructed fields are very similar. Field scans were taken across each of these field components and a selection are shown in figs. 7.9(c) and (d). From these scans it is clear that there is good agreement between the



(a) Stray field reconstructed from the deflection data sets generated by the Seagate tip magnetised as in the Normal Case.
 (b) Stray field reconstructed from the simulated deflection data sets generated tip model GT_1 (see fig. 7.7(a)).



(c) Vertical scans taken across the *x* components of the reconstructed fields above.



(d) Horizontal scans taken across the *y* components of the reconstructed fields above.

Fig. 7.9: Stray fields reconstructed from the rotation data sets generated by the Seagate tip magnetised as in the Normal Case and the tip model GT_1 (see fig. 7.7(a)).

Also shown are scans taken across the reconstructed fields in (a) and (b). Note that the blue scans are taken across the reconstructed fields in (a), while the red scans are taken across the reconstructed fields in (b).

simulated and experimental reconstructed fields. Note that a similarly favourable agreement can also be obtained from a comparison of the experimental reconstructed field with the field reconstructed from the rotation data sets generated by tip models *GT_2* and *GT_3* (however the thickness of each model tip film must be modified accordingly to achieve agreement with the experimental deflection data).

In Section 5.2.2 we concluded that the DI MFM tip magnetised as in the Transverse Case was still predominately magnetised along the tip axis even after the application of a large field directed along the cantilever axis. In this section we conclude that a groove ion milled at the tip apex does encourage the tip magnetisation to settle in the plane of the cantilever and normal to the groove. Note however, that without a measure of the Seagate tip film thickness it is not clear which of the tip models in fig. 7.7 best represents the Seagate tip magnetisation. We now consider the Seagate tip re-magnetised by the application of a large field directed in the plane of the cantilever and parallel to the cantilever axis.

7.3.2 The Seagate Tip Magnetised by a Large Field Directed Along the Cantilever Axis

The Seagate tip was re-magnetised by the application of a large field directed along the cantilever axis (i.e. in the groove direction). This will subsequently be referred to as the Transverse Case.

Several possible models for the magnetic configuration of the Seagate tip magnetised as in the Transverse Case were constructed and are shown in fig. 7.10. Full line scan rotation data sets were again calculated from each tip model but are not shown here. A comparison of the line scan deflection data sets generated by the Seagate tip with the data sets generated by the tip models (*GT_4*, *GT_5* and *GT_6*) was carried out as was a comparison of the experimental and simulated fields reconstructed from these data sets (these comparisons are not shown here). The agreement between the experimental and the simulated data was poor and this indicated that the tip models (in fig. 7.10) did not represent possible magnetisation distributions for the Seagate tip film in this case.

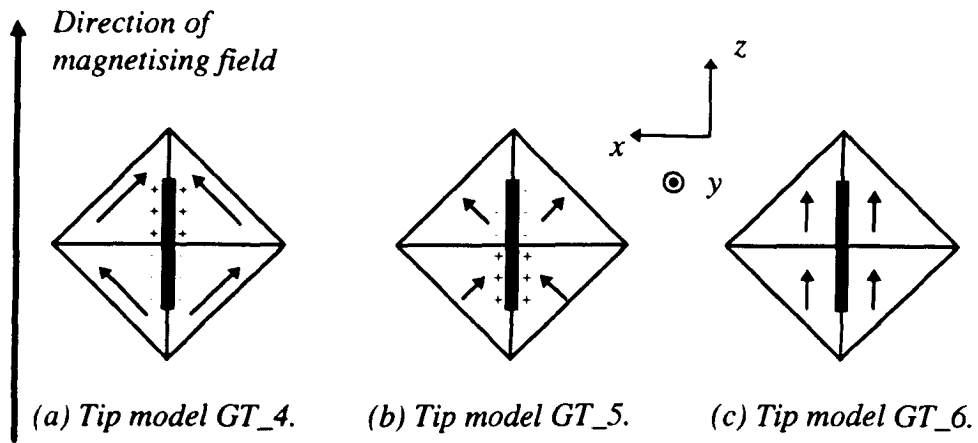
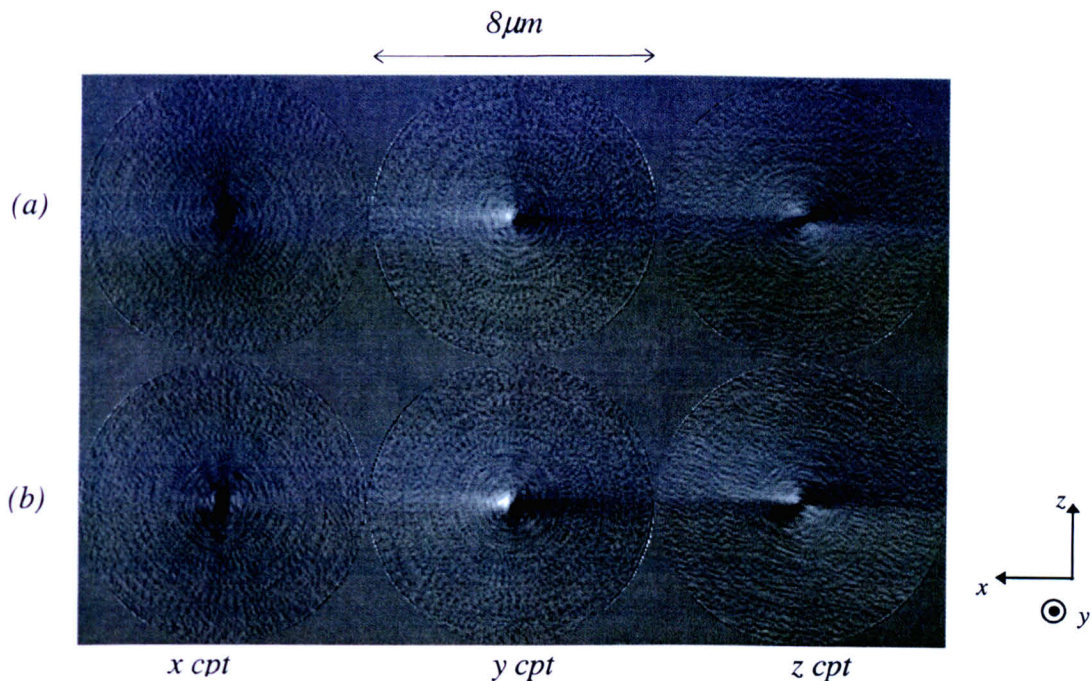


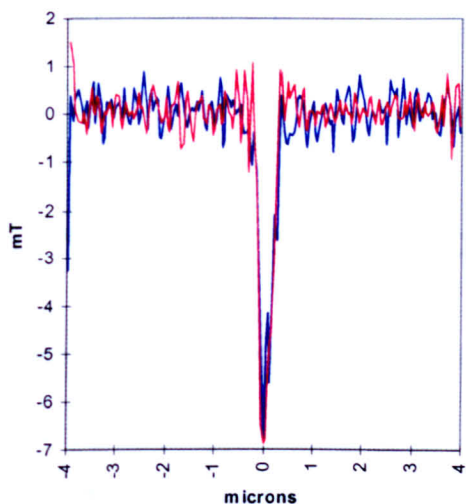
Fig. 7.10: Three possible magnetic configurations of the Seagate tip magnetised as in the Transverse Case. Note that each individual film is magnetised in the plane of the film. Also note that the '+'s and '-'s indicate the directions of the series of dipoles set up across the groove.

However, it was observed that the stray field from the Seagate tip magnetised as in the Transverse Case was very similar to the field from the same tip magnetised as in the Normal Case (i.e. the tip considered in Section 7.3.1), see figs. 7.11(a) and (b). As a further comparison, field scans were again taken across each of the field components and a selection are shown in figs. 7.11(c) and (d). It is clear from these scans that there is excellent agreement between the experimental reconstructed fields. Note that a comparison of corresponding deflection line scans generated by the Seagate tip magnetised as in the Normal and Transverse Cases were also found to give good agreement, see fig. 7.12.

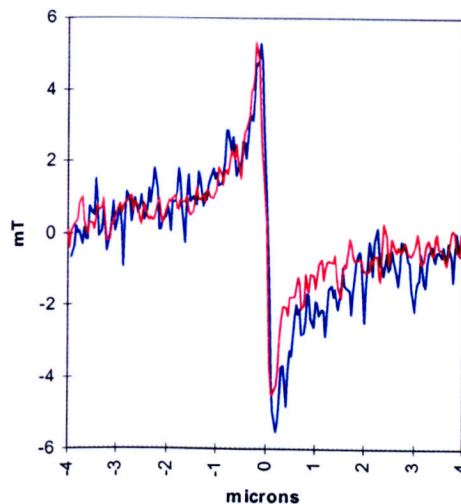
We therefore conclude that the magnetisation of the Seagate tip magnetised in the Transverse Case is still predominately directed in the plane of the cantilever and normal to the groove, despite the application of a large field directed along the cantilever axis. It follows that the tip models in fig. 7.7 (i.e. *GT_1*, *GT_2* and *GT_3*) represent possible magnetisation distributions for the Seagate tip film magnetised in



(a) Stray field reconstructed from the deflection data sets generated by the Seagate tip magnetised as in the Normal Case.
 (b) Stray field reconstructed from the deflection data sets generated by the Seagate tip magnetised as in the Transverse Case.

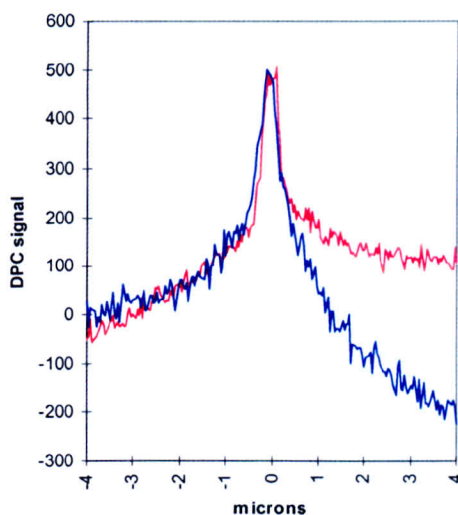


(c) Horizontal scans taken across the x components of the reconstructed fields above.

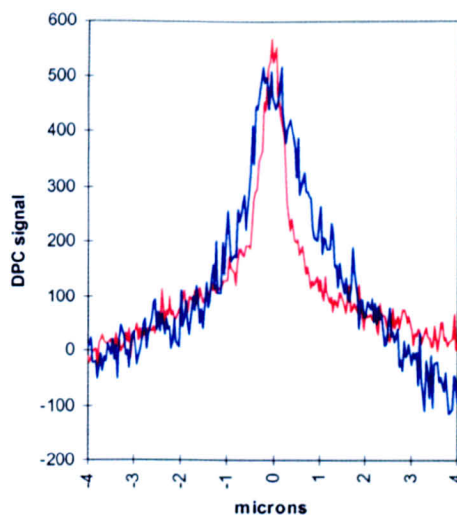


(d) Horizontal scans taken across the y components of the reconstructed fields above.

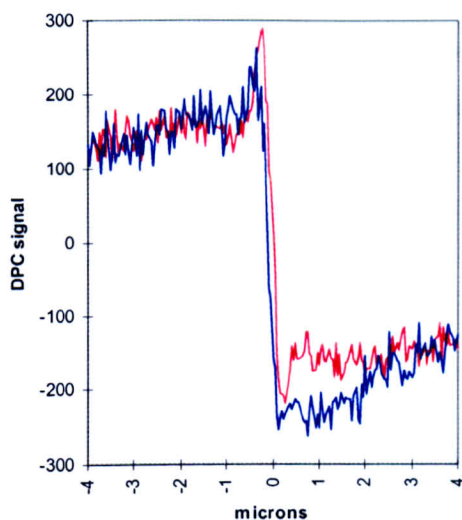
Fig. 7.11: Stray fields reconstructed from the rotation data sets generated by the Seagate tip magnetised as in the Normal and Transverse Cases. Also shown are field scans taken across the reconstructed fields in (a) and (b). Note that the blue scans are taken across the reconstructed fields in (a), while the red scans are taken across the reconstructed fields in (b).



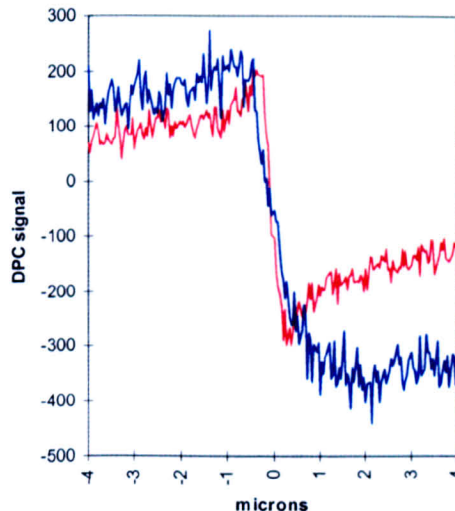
(a) Scans sensitive to induction in the plane of reconstruction.



(b) Scans sensitive to induction in the plane of reconstruction. Scans separated from the scans in (a) by 90° about the rotation axis.



(c) Scans sensitive to induction normal to the plane of reconstruction.



(d) Scans sensitive to induction normal to the plane of reconstruction. Scans separated from the scans in (c) by 90° about the rotation axis.

Fig. 7.12: Comparison of a selection of corresponding deflection line scans generated by the Seagate tip magnetised as in the Normal and Transverse Cases. Note that the scans in (a) and (c) are separated from the corresponding scans in (b) and (d) by 90° about the rotation axis.

Also note that all the deflection line scans have had a constant deflection value subtracted from them. The value subtracted was the average value of the end-points of the scans.

The red scans were generated from the Seagate magnetised as in the Transverse Case, while the blue scans were generated from the Seagate tip magnetised as in the Normal Case.

this case. However, in the absence of detailed information on the Seagate film thickness it is again not clear which tip model best represents the experimental tip. We now consider the Seagate tip re-magnetised by the application of a large field directed normal to the plane of the cantilever.

7.3.3 The Seagate Tip Magnetised by a Large Field Directed Along the Tip Axis

The Seagate tip was re-magnetised by the application of a large field directed along the tip axis. This will subsequently be referred to as the Axial Case. A possible model for the Seagate tip magnetised in this manner is shown in fig. 7.13. A full integrated field line scan rotation data set was calculated from the model but is not shown here. Instead a comparison of a selection of simulated deflection line scans (sensitive to induction normal to the plane of reconstruction) generated by the tip model *GT_7* with the corresponding experimental deflection line scans generated by the Seagate tip is shown in fig. 7.14.

Note that the scans do not match perfectly with the corresponding scans in fig. 7.14 about the rotation axis. Also note that the experimental deflection line scans have had a constant offset value subtracted from them. The value subtracted was the average value of the start points of the scans.

The red marks were generated by the tip model *GT_7* and the blue marks were generated by the experimental data.

It is noted that the experimental data in fig. 7.14 that the \pm signs of the simulated deflection line scans are in complete agreement with the experimental deflection data.

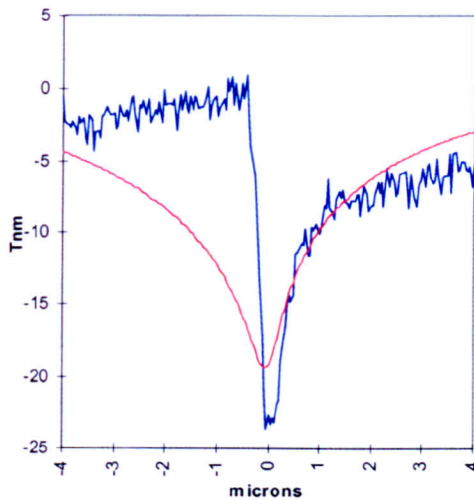
The simulation of corresponding simulated and experimental deflection line scans relative to rotation in the plane of reconstruction, but as not shown here. The figure also shows the Seagate tip

Fig. 7.13: A possible magnetic configuration of the Seagate tip magnetised as in the Axial Case. Note that each individual film is magnetised in the plane of the film. Also note that the +’s indicate polarity of the magnetic charge density at the groove edges.

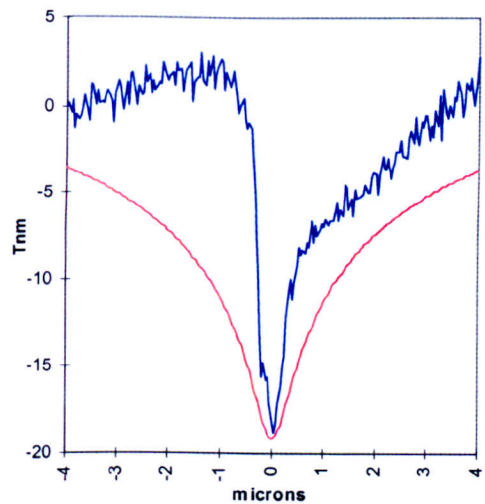
The red marks were generated by the tip model *GT_7* and the blue marks were generated by the experimental data.

The red marks were generated by the tip model *GT_7* and the blue marks were generated by the experimental data.

The red marks were generated by the tip model *GT_7* and the blue marks were generated by the experimental data.



(a) Scans sensitive to induction normal to the plane of reconstruction.



(b) Scans sensitive to induction normal to the plane of reconstruction. Scans separated from the scans in (a) by 90° about the rotation axis.

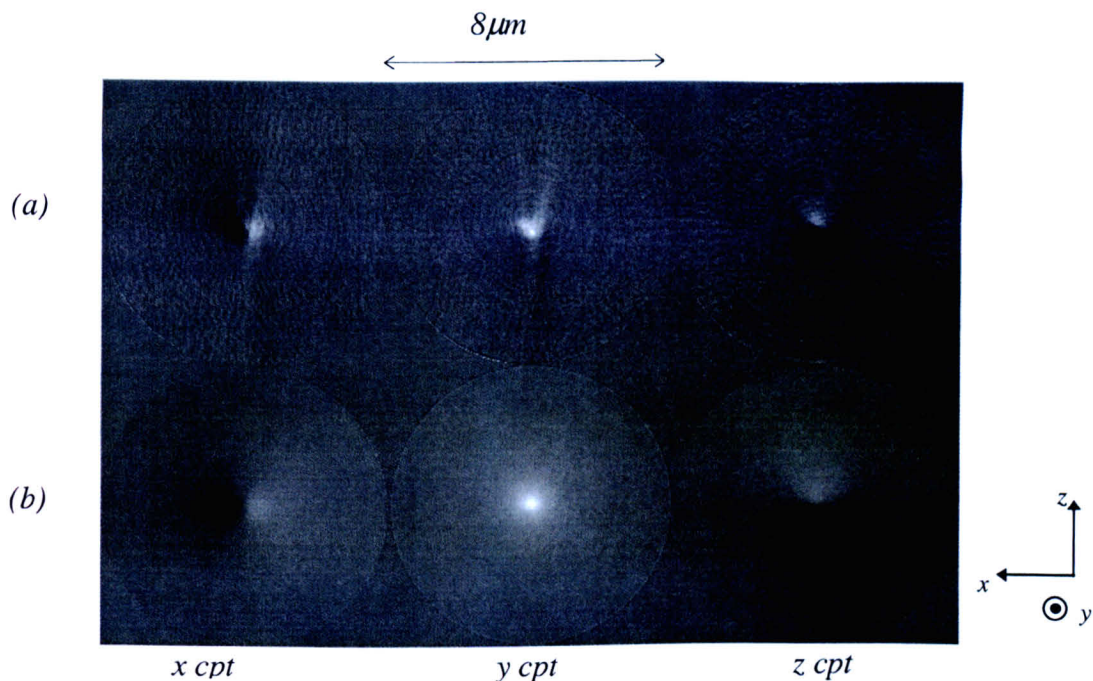
Fig. 7.14: Comparison of a selection of deflection line scans (sensitive to induction normal to the plane of reconstruction) generated by the Seagate tip magnetised as in the Axial Case with simulated deflection line scans generated by tip model *GT_7*. Note that the scans in (a) are separated from the corresponding scans in (b) by 90° about the rotation axis. Also note that the experimental deflection line scans have had a constant deflection value subtracted from them. The value subtracted was the average value of the end-points of the scans. The red scans were generated from the Seagate magnetised as in the Axial Case, while the blue scans were generated from the tip model *GT_7*.

It is clear from a visual comparison of the corresponding line scans in fig. 7.14 that the character of the simulated integrated field does not compare favourably with the experimental deflection data. This was also found for a comparison of corresponding simulated and experimental deflection line scans sensitive to induction in the plane of reconstruction but is not shown here. This suggests that the Seagate tip magnetised in the Axial Case is not entirely magnetised along the tip axis - even after it has been exposed to a large field applied along that direction. We now consider the stray field reconstructed from the deflection data sets generated by the Seagate tip and make a comparison with the corresponding field from the tip model *GT_7*.

Fig. 7.15(a) shows the 'best fit' three dimensional field reconstructed from the deflection data sets generated by the Seagate tip. Fig. 7.15(b) shows the corresponding three dimensional field reconstructed from the simulated rotation data sets generated by tip model *GT_7*.

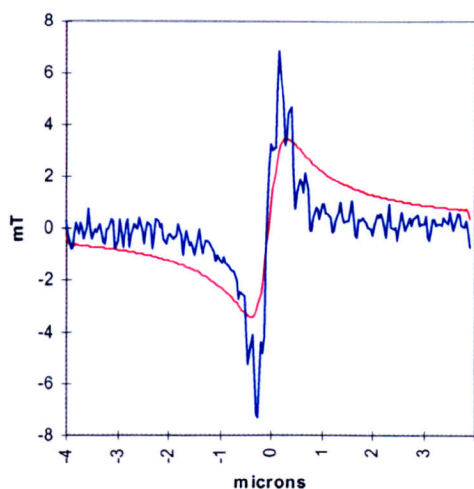
A visual comparison of the corresponding field components clearly suggests that the character of the simulated and experimental reconstructed fields are very similar. Field scans were again taken across each of the corresponding field components and a selection is shown in figs. 7.15(c) and (d). From these scans it is clear that there is agreement between the simulated and experimental reconstructed fields. However the experimental reconstruction indicates a sharper field directed along the tip axis.

Recall from Section 4.4 that the tip film coating approximately the top 1 to $3\mu\text{m}$ of the tip (depending on the magnetic configuration of the tip) was found to be the most important for defining the character of the tip stray field. Thin film coating the tip beyond $3\mu\text{m}$ from the apex was found to have little influence on the character of the field immediately in front of the tip. However this portion of the magnetic film was found to influence significantly the character of the integrated field generated by the tip. Thus, the implication from the fact that there is good agreement between the simulated and experimental reconstructed fields is that at least the top 1 to $3\mu\text{m}$ of the Seagate tip film is predominately magnetised along the tip axis. The poor agreement between the simulated and experimental deflection line scans, however, suggests that the film beyond $3\mu\text{m}$ from the apex of the Seagate tip is not predominately magnetised along the tip axis.

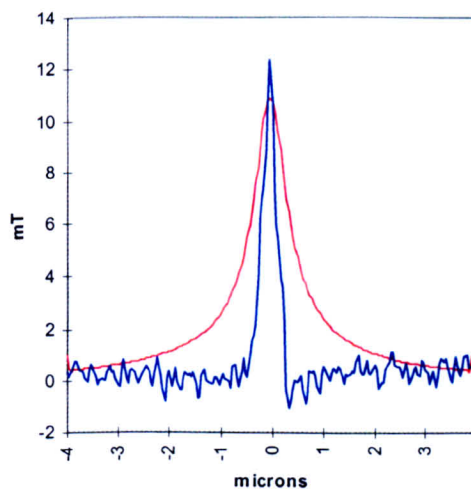


(a) Stray field reconstructed from the deflection data sets generated by the Seagate tip magnetised as in the Axial Case.

(b) Stray field reconstructed from the simulated deflection data sets generated tip model GT_7 (see fig. 7.13).



(c) Scans taken across the x components of the reconstructed fields above.



(d) Horizontal scans taken across the y components of the reconstructed fields above.

Fig. 7.15: Stray fields reconstructed from the rotation data sets generated by the Seagate tip magnetised as in the Axial Case and the tip model GT_7 (see fig. 7.13). Also shown are field scans taken across the reconstructed fields in (a) and (b). Note that the blue scans were taken across the reconstructed fields in (a), while the red scans were taken across the reconstructed fields in (b).

We now consider another possible model for the Seagate tip magnetised in the Axial case, see fig. 7.16. The film coating the top $3\mu\text{m}$ of the tip model is magnetised axially, while the rest of the film is magnetised in the plane of the cantilever and normal to the groove (similar to the Seagate tip magnetised in the Normal and Transverse cases). A full integrated field line scan rotation data set was calculated from the tip model. A selection of these simulated line scans with the corresponding experimental deflection line scans generated by the Seagate tip are shown in fig. 7.17.

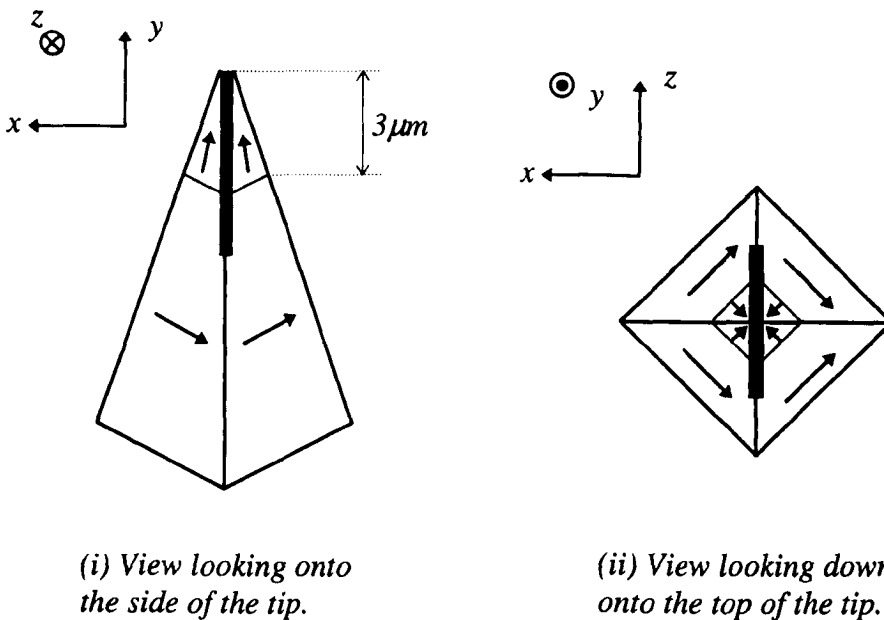
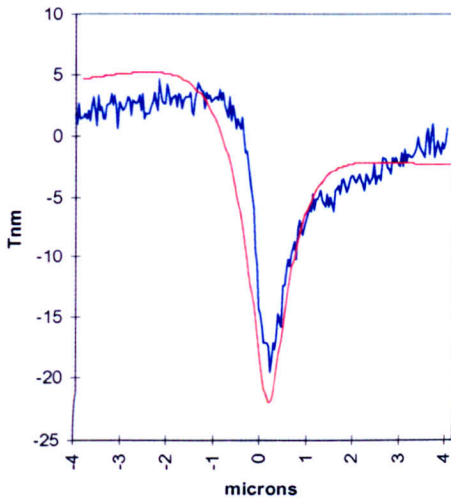
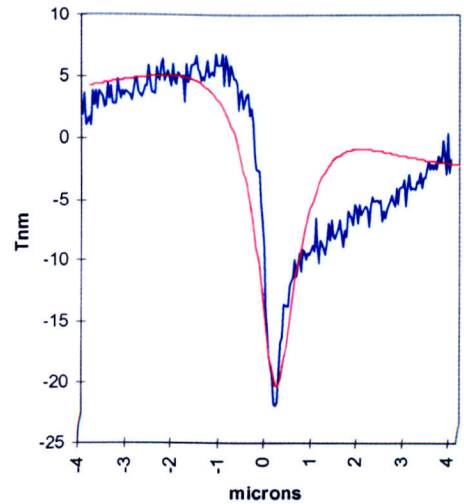


Fig. 7.16: Another possible magnetic configuration of the Seagate tip magnetised as in the Axial Case. Note that the top $3\mu\text{m}$ of the tip film is magnetised axially, while the rest of the tip film is magnetised in the plane of the cantilever and normal to the groove.

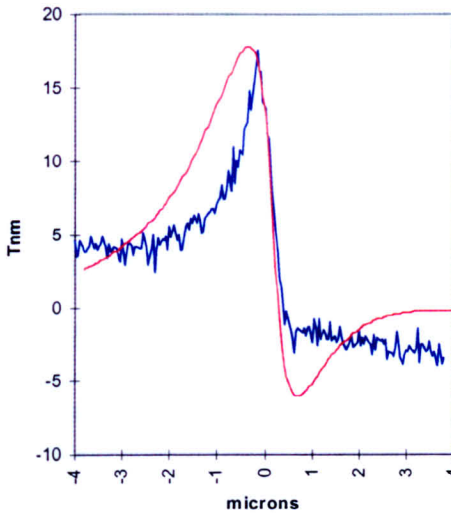
A visual comparison of the corresponding line scans in fig. 7.17 indicates that there is some agreement between the simulated and experimental line scans. However there are also some significant differences in the character between corresponding scans. This may be due to the fact that the contribution to the experimental deflection data sets from the cantilever and substrate portions of the Seagate tip assembly has not been taken into account in the model.



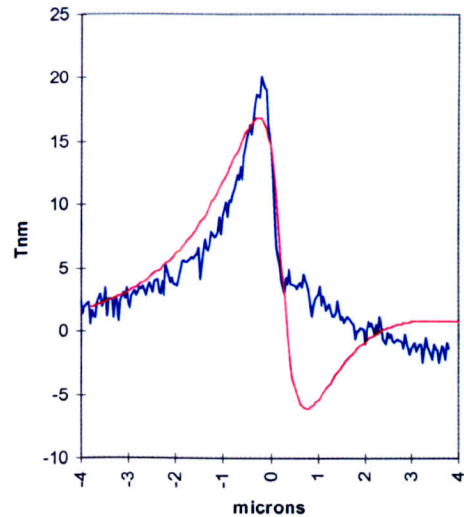
(a) Scans sensitive to induction normal to the plane of reconstruction.



(b) Scans sensitive to induction normal to the plane of reconstruction. Scans separated from the scans in (a) by 60° about the rotation axis.



(c) Scans sensitive to induction in the plane of reconstruction.



(d) Scans sensitive to induction in the plane of reconstruction. Scans separated from the scans in (c) by 60° about the rotation axis.

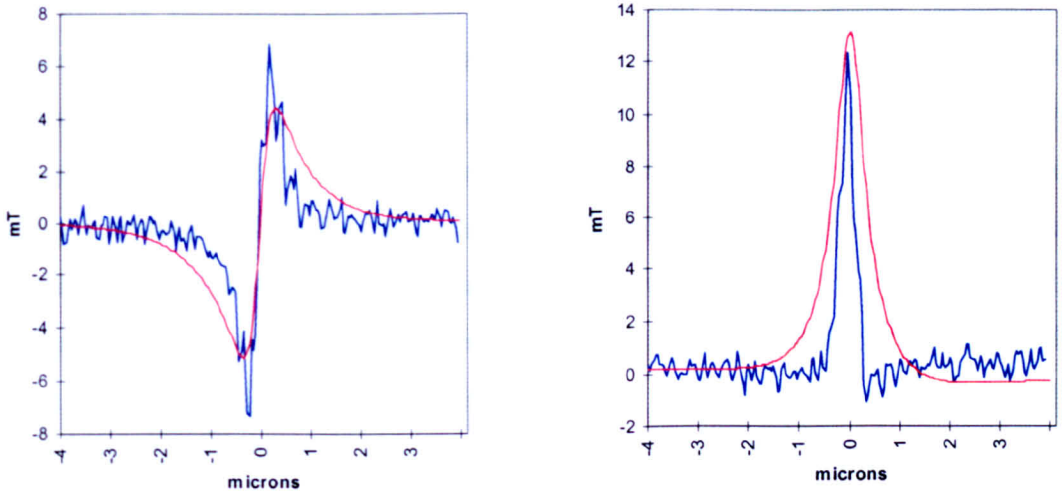
Fig. 7.17: Comparison of a selection of deflection line scans generated by the Seagate MFM tip magnetised in the Axial case with simulated integrated field line scans generated by the tip model GT_8.

Note that the scans in (a) are separated by 60° about the rotation axis from the scans in (b). The same is true of the scans in (c) and (d).

Also note that the experimental deflection line scans generated by the Seagate tip have had a constant deflection value subtracted from them. The value subtracted was the average value of the end-points of the scans.

Further note that the red scans were generated by the Seagate tip, while the blue scans were generated by the tip model GT_8.

The character of the stray fields reconstructed from the simulated and experimental line scan deflection data sets were found to compare favourably - as the field scans in fig. 7.18 show. We therefore conclude that tip model *GT_8* is a possible model for the Seagate tip magnetised in the Axial case.



(a) Horizontal scans taken across the (in-plane) x components of the reconstructed fields.

(b) Horizontal scans taken across the normal components (y components) of the reconstructed fields.

Fig. 7.18: Comparison of field scan components reconstructed from the line scan deflection data sets generated by the Seagate tip magnetised in the Axial case and the tip model *GT_8*.

Note that red scans have been taken across the field generated by the tip model *GT_8*, while blue scans have been taken across the field generated by the Seagate tip magnetised in the Axial case.

It has been shown that the magnetisation of the experimental Seagate tip is predominately in the plane of the cantilever and normal to the groove provided the magnetising field is directed in the plane of the cantilever. Since the grooved character of the Seagate tip is the only significant physical difference to the DI tips considered in earlier sections, we conclude that the groove does facilitate the remanent magnetisation settling in the plane of the cantilever and normal to the groove.

7.4 Summary and Conclusions

The models considered in Section 7.2 suggest that similar spatial resolution is achievable from a DI MFM tip either partially coated or entirely coated with magnetic film. However the magnitude of the stray field from the partially coated tip is significantly smaller than that from a fully coated tip. Therefore a partially coated DI tip (mounted in an MFM) will alter a sample magnetisation to a lesser extent than an identical tip fully coated with magnetic material (while still achieving a similar spatial resolution). It follows that the partially coated DI MFM tip will be useful for imaging 'softer' magnetic materials (i.e. materials for which the large field from the fully coated DI tip effects the specimen magnetisation significantly).

In Section 7.3, the grooved character of the Seagate tip was found to facilitate the remanent magnetisation settling in the plane of the cantilever and normal to the groove (provided the magnetising field is directed in the plane of the cantilever).

References

- [1] Martin Y and Wickramasinghe H K, (1987), *Applied Physics Letters*, 50, pp 1455
- [2] Rugar D, Mamin H J, Guether P, Lambert S E, Stern J E, McFadyen I and Yogi T, (1990), *Journal of Applied Physics*, 68, pp1169
- [3] Schonberger C and Alvarado S F, (1990), *Z. Phys. B* 80, pp 373
- [4] Wadas A and Grutter P, (1989), *Phys. Rev. B*, 39, pp 12013
- [5] Wadas A and Guntherodt H J, (1990), *Phys. Lett.*, 146, pp 277
- [6] Wright C D and Hill E W, (1995), *Appl. Phys. Lett.*, 67, pp 433
- [7] Song D, van Ek J, Amin N, Mao S, Louder D and Schultz A, (1999), *IEEE Trans. Mag.*, 35, pp 667-670

Chapter 8

Conclusions and Future Work

8.1 Conclusions

The work described in this thesis was concerned with a theoretical characterisation of the stray field from a MFM tip and the structure on which it is built. We also investigated the accuracy of practical methods (i.e. electron beam tomographic reconstruction methods) for characterising the tip field.

The experimental line scan deflection data sets generated by a DI MFM tip assembly were presented in this thesis. Possible tip, cantilever and substrate models for the DI tip assembly were constructed. These models indicated that in the vicinity of the tip, the tip field dominates over the combined cantilever and substrate field. However the small cantilever and substrate field (relative to the peak tip field) is spread over a far larger distance than the tip field. The large spread of the cantilever and substrate field ensures that their field integrals are large and therefore the cantilever and substrate contribution to the tip assembly's deflection data sets is significant. With regard to the experimental line scan deflection data sets generated by the DI MFM tip (see figs. 5.1 and 5.2), the models suggest that the tip portion of the DI tip assembly is predominately responsible for the shape character of the deflection line scans, while the cantilever and substrate portion is responsible for the large vertical shifts of the experimental scans.

Both the ART and RTM reconstruction methods require 'well behaved' input deflection data sets containing line scans which decrease to zero at their extremes to

produce an accurate reconstruction of the 3-D tip stray field. The large cantilever and substrate contribution to the experimental deflection data sets was therefore expected to effect the accuracy of the reconstructed tip assembly field. However, two methods for obtaining an accurate reconstruction of the 3-D MFM tip stray field from non 'well behaved' input deflection data sets using the RTM reconstruction technique were demonstrated.

The first method involved reconstructing the 3-D stray field from each of the tip assembly's orthogonal deflection data sets. The in-plane components of field reconstructed from the deflection data set sensitive to induction normal to the plane of reconstruction, and the normal component of field reconstructed from the deflection data set sensitive to induction in the plane of reconstruction were found to be accurate representations of the tip assembly's three stray field components.

The second method for accurate reconstruction of the tip field from the non 'well behaved' deflection data sets using the RTM method required a modification of the input deflection data sets. In this case a constant deflection value was subtracted from each deflection line scan so that the ends of each line scan were approximately zero (this is an approximate method for subtraction of the cantilever and substrate contribution to the tip assembly deflection data sets). The average of the 3-D stray field reconstructed from each of the modified orthogonal deflection data sets also gives an accurate representation of the MFM tip field.

Investigations into the accuracy of the stray field reconstructed using the ART technique were also undertaken. It was found that stray field reconstructed from 'well behaved' line scan deflection data sets using the ART method was not as accurate a representation of the tip field as the field reconstructed from the same deflection data sets using the RTM technique. In fact the less 'well behaved' the input deflection data sets to the ART method were, then the less accurate the reconstructed field was found to be.

In conclusion, the RTM method is the most accurate reconstruction technique tested in this thesis (for reconstructing field from 'well behaved' and non 'well behaved' line scan deflection data sets) and is therefore preferred for investigations of MFM tip stray fields.

8.2 Future Work

In this section possible future work is discussed.

1. A theoretical investigation into the effect of the electron probe size on the measured deflection data was undertaken in Section 6.8. We concluded that provided 1) the cone of electrons in the STEM is predominately deflected by stray field in the immediate vicinity of the focused electron disk, and 2) the focused electron probe is of a similar size or smaller than the sampling distance, then the effect on the measured deflection data is small. An extension of this work would be to formulate a technique for deconvolution of the electron probe from the measured deflection data (by approximating the electron probe to be a 2-D Gaussian distribution). Therefore a smaller sampling distance could be used in a practical experiment and the original deflection data could be deconvolved from the measured deflection data and consequently a higher spatial resolution achieved.
2. Using existing tip, cantilever and substrate models and by constructing specimen models, the tip-specimen interaction could be simulated. With knowledge of the initial model tip and specimen magnetisation distributions, an iterative technique for deconvolution of the tip stray field from the simulated MFM images should be sought.
3. Possible magnetisation distributions for the tip portion of the DI tip assembly were investigated briefly using the *LLG Micromagnetics Simulator*^[1] (this package solves the Landau-Lifshitz-Gilbert^[2] equations using finite difference methods). The relatively large scale of the tip structure means that realistic tip models require several days (even weeks) computation to determine a suitable remanent tip magnetisation. However, small portions of the tip film can be modelled separately provided suitable boundary conditions are used. Preliminary investigations modelling the top 0.5 μm portion of the tip film (from the tip apex) have shown promise. Further investigations are warranted.

References

- [1] Licensor: Micheal R. Scheinfein, 2008 E. Aspen Drive, Tempe, AZ 85282, USA
- [2] Brown (1963), *Micromagnetics*, John Wiley & Sons.

Appendix I

In Chapter 4 the equations required for the calculation of the magnetic field from a uniformly magnetised block were given. The three components of \underline{H} are now calculated from equations (4.2) and (4.3) and the following notation is used,

$$\begin{aligned}
 x - x' &= \alpha & z - z' &= \gamma \\
 x - L_1 &= a_- & y - L_2 &= b_- & z - L_3 &= c_- & (1) \\
 x + L_1 &= a_+ & y + L_2 &= b_+ & z + L_3 &= c_+
 \end{aligned}$$

Equation (4.2) is now used to give the three components of \underline{H} .

Component H_x

The expression for H_x using the substitutions in (1) is,

$$H_x = \frac{M_s}{4\pi} \left[\int_{a_-}^{a_+} \int_{c_-}^{c_+} \frac{\alpha d\alpha d\gamma}{[\alpha^2 + b_-^2 + \gamma^2]^{3/2}} - \int_{a_-}^{a_+} \int_{c_-}^{c_+} \frac{\alpha d\alpha d\gamma}{[\alpha^2 + b_+^2 + \gamma^2]^{3/2}} \right] \quad (2)$$

These are two very similar integrals and we consider one only with the substitutions $\omega = \alpha^2 + b^2 + \gamma^2$ and $d\omega = 2\alpha d\alpha$ then,

$$\int_{c_-}^{c_+} d\gamma \int_a^a \frac{d\omega}{2\omega^{3/2}} = - \int_{c_-}^{c_+} \left[\frac{1}{[\alpha^2 + b^2 + \gamma^2]^{1/2}} \right]_a^{a_+} d\gamma \quad (3)$$

this integral is easily solved as,

$$\int_{c_-}^{c_+} \frac{d\gamma}{[a^2 + b^2 + \gamma^2]^{\frac{3}{2}}} = \left[\ln(\gamma + [a^2 + b^2 + \gamma^2]^{\frac{1}{2}}) \right]_{c_-}^{c_+} \quad (4)$$

Thus the complete expression for H_x is calculated as the sum of several terms like equation (4) and is given by,

$$\begin{aligned} H_x = \frac{M_x}{4\pi} & \left\{ \ln\left(c_+ + [a_-^2 + b_-^2 + c_+^2]^{\frac{1}{2}}\right) - \ln\left(c_+ + [a_+^2 + b_-^2 + c_+^2]^{\frac{1}{2}}\right) \right. \\ & - \ln\left(c_- + [a_-^2 + b_-^2 + c_-^2]^{\frac{1}{2}}\right) + \ln\left(c_- + [a_+^2 + b_-^2 + c_-^2]^{\frac{1}{2}}\right) \\ & - \ln\left(c_+ + [a_-^2 + b_+^2 + c_+^2]^{\frac{1}{2}}\right) + \ln\left(c_+ + [a_+^2 + b_+^2 + c_+^2]^{\frac{1}{2}}\right) \\ & \left. + \ln\left(c_- + [a_-^2 + b_+^2 + c_-^2]^{\frac{1}{2}}\right) - \ln\left(c_- + [a_+^2 + b_+^2 + c_-^2]^{\frac{1}{2}}\right) \right\} \quad (5) \end{aligned}$$

Component H_y

From equation (4.2) the expression for H_y using the notation described in equation (1) is,

$$H_y = \frac{M_y}{4\pi} \left[b_- \int_{c_-}^{c_+} \int_{a_-}^{a_+} \frac{d\alpha d\gamma}{[\alpha^2 + b_-^2 + \gamma^2]^{\frac{3}{2}}} - b_+ \int_{c_-}^{c_+} \int_{a_-}^{a_+} \frac{d\alpha d\gamma}{[\alpha^2 + b_+^2 + \gamma^2]^{\frac{3}{2}}} \right] \quad (6)$$

Again we have two double integrals with the basic form being,

$$\int_{c_-}^{c_+} d\gamma \int_{a_-}^{a_+} \frac{d\alpha}{[a^2 + b^2 + \gamma^2]^{\frac{3}{2}}} \quad (7)$$

Integrating this with respect to the variable α is a standard integral which leaves,

$$\int_{c_-}^{c_+} \left[\frac{\alpha}{(b^2 + \gamma^2)(\alpha^2 + b^2 + \gamma^2)^{\frac{1}{2}}} \right]_{a_-}^{a_+} d\gamma \quad (8)$$

Solving this integral is complicated and requires several substitutions - the first being $\gamma = u \tan \vartheta$ with $u^2 = \alpha^2 + b^2$ and $d\gamma = u \sec^2 \vartheta d\vartheta$, so that the terms of equation (8) are of the form,

$$\begin{aligned} & \int_{c_-}^{c_+} \frac{u \sec^2 \vartheta d\vartheta}{[u^2 - \alpha^2 + u^2 \tan^2 \vartheta][u^2 + u^2 \tan^2 \vartheta]^{\frac{1}{2}}} \\ &= \int_{c_-}^{c_+} \frac{\sec \vartheta d\vartheta}{[u^2 \sec^2 \vartheta - \alpha^2]} = \int_{c_-}^{c_+} \frac{\cos \vartheta d\vartheta}{[u^2 - \alpha^2 \cos^2 \vartheta]} \end{aligned} \quad (9)$$

using basic trigonometric rules. This equation can be further simplified by,

$$= \int_{c_-}^{c_+} \frac{\cos \vartheta d\vartheta}{[u^2 + b^2 - \alpha^2 \cos^2 \vartheta]} = \int_{c_-}^{c_+} \frac{\cos \vartheta d\vartheta}{[b^2 + \alpha^2 \sin^2 \vartheta]} \quad (10)$$

and now the substitution $v = \alpha \sin \vartheta$ with $dv = \alpha \cos \vartheta d\vartheta$ means that,

$$= \frac{1}{\alpha} \int_{c_-}^{c_+} \frac{dv}{[b^2 + v^2]} = \frac{1}{\alpha} \left[\frac{1}{b} \tan^{-1} \left(\frac{v}{b} \right) \right]_{c_-}^{c_+} \quad (11)$$

on substituting the variables back in this gives,

$$= \frac{1}{\alpha b} \tan^{-1} \left(\frac{\alpha}{b} \sin \left[\tan^{-1} \left(\frac{\gamma^2}{[\alpha^2 + b^2]^{\frac{1}{2}}} \right) \right] \right) \Big|_{c_-}^{c_+} \quad (12)$$

This cumbersome expression is the basic form of the component H_y which from equation (6) is,

$$\begin{aligned} H_y = \frac{M_s}{4\pi} & \left\{ \tan^{-1} \left(\frac{a_+}{b_-} \sin \left(\tan^{-1} \left(\frac{c_+}{(a_+^2 + b_-^2)^{\frac{1}{2}}} \right) \right) \right) \right. \\ & - \tan^{-1} \left(\frac{a_+}{b_-} \sin \left(\tan^{-1} \left(\frac{c_-}{(a_+^2 + b_-^2)^{\frac{1}{2}}} \right) \right) \right) - \tan^{-1} \left(\frac{a_-}{b_-} \sin \left(\tan^{-1} \left(\frac{c_+}{(a_-^2 + b_-^2)^{\frac{1}{2}}} \right) \right) \right) \\ & + \tan^{-1} \left(\frac{a_-}{b_-} \sin \left(\tan^{-1} \left(\frac{c_-}{(a_-^2 + b_-^2)^{\frac{1}{2}}} \right) \right) \right) - \tan^{-1} \left(\frac{a_+}{b_+} \sin \left(\tan^{-1} \left(\frac{c_+}{(a_+^2 + b_+^2)^{\frac{1}{2}}} \right) \right) \right) \\ & + \tan^{-1} \left(\frac{a_+}{b_+} \sin \left(\tan^{-1} \left(\frac{c_-}{(a_+^2 + b_+^2)^{\frac{1}{2}}} \right) \right) \right) + \tan^{-1} \left(\frac{a_-}{b_+} \sin \left(\tan^{-1} \left(\frac{c_+}{(a_-^2 + b_+^2)^{\frac{1}{2}}} \right) \right) \right) \\ & \left. - \tan^{-1} \left(\frac{a_-}{b_+} \sin \left(\tan^{-1} \left(\frac{c_-}{(a_-^2 + b_+^2)^{\frac{1}{2}}} \right) \right) \right) \right\} \quad (13) \end{aligned}$$

Component H_z

The calculation of H_z from equation (4.2) involves solving the following integral,

$$H_z = \frac{M_s}{4\pi} \left[\int_{c_-}^{c_+} \int_{a_-}^{a_+} \frac{\gamma d\alpha d\gamma}{[\alpha^2 + b_-^2 + \gamma^2]^{\frac{3}{2}}} - \int_{c_-}^{c_+} \int_{a_-}^{a_+} \frac{\gamma d\alpha d\gamma}{[\alpha^2 + b_+^2 + \gamma^2]^{\frac{3}{2}}} \right] \quad (14)$$

the similarity between equations (2) and (14) is clear. In fact the calculations are identical with γ replacing α so that the full expression for H_z is given as,

$$\begin{aligned}
 H_z = \frac{M_z}{4\pi} \left\{ \ln\left(a_+ + [a_+^2 + b_-^2 + c_-^2]^{1/2}\right) - \ln\left(a_+ + [a_+^2 + b_-^2 + c_+^2]^{1/2}\right) \right. \\
 - \ln\left(a_- + [a_-^2 + b_-^2 + c_-^2]^{1/2}\right) + \ln\left(a_- + [a_-^2 + b_-^2 + c_+^2]^{1/2}\right) \\
 - \ln\left(a_+ + [a_+^2 + b_+^2 + c_-^2]^{1/2}\right) + \ln\left(a_+ + [a_+^2 + b_+^2 + c_+^2]^{1/2}\right) \\
 \left. + \ln\left(a_- + [a_-^2 + b_+^2 + c_-^2]^{1/2}\right) - \ln\left(a_- + [a_-^2 + b_+^2 + c_+^2]^{1/2}\right) \right\} \quad (15)
 \end{aligned}$$